INFRARED LASER SPECTROSCOPY: INSTRUMENTATION, METHODS,

APPLICATIONS, AND NEW TRENDS WITH FREQUENCY COMBS

A Dissertation

by

RUQAYYAH F M H H ASKAR

Submitted to the Office of Graduate and Professional Studies of
Texas A&M University
in partial fulfillment of the requirements for the degree of

DOCTOR OF PHILOSOPHY

| | |
|---|---|
| Chair of Committee, | Hans A. Schuessler |
| Committee Members, | Olga Kocharovskaya |
| | Alexandre A. Kolomenski |
| | Philip Hemmer |
| Head of Department, | Grigory Rogachev |

December 2020

Major Subject: Physics

ABSTRACT

The demand for highly sensitive infrared spectroscopic measurements has been a strong motive towards developing high-sensitivity instruments. This demand ranges from environmental and atmospheric necessities to study, analyze, and predict the concentrations of various greenhouse gases, to medical applications in diagnosis based on the content of breath samples. Newly developed infrared laser sources with record output powers, ultra-broad spectral coverage, and efficient nonlinear conversion opened the door for high accuracy broadband absorption measurements.

My research is devoted to laser absorption spectroscopy in the mid-infrared spectral region and is divided into two parts. In the first part, an overview of the field is presented, and some of the developments are summarized. The content is prepared to form a basis for a graduate course on infrared spectroscopy. The course is primarily on instrumentation, methods, and applications of infrared laser spectroscopy with a particular focus on infrared optical frequency comb sources.

The outline of this work can serve as an outline for the course. An introduction to absorption spectroscopy is presented, followed by a review of the principles of molecular spectroscopy and the characteristic absorption features in the mid-infrared region. Several infrared sources and generation methods are discussed, and a historical overview of photodetection and its concepts are provided. The concepts behind many experimental elements used in laser spectroscopy are covered briefly, and experimental demonstrations of two techniques are presented.

Frequency combs are powerful broadband sources and are excellent for obtaining precise measurements of the absorption spectra of gases in short periods of time. In the second part of my work, two powerful spectroscopic techniques based on infrared frequency comb sources are discussed. The first one is cavity ringdown spectroscopy (CRDS), which is capable of providing highly sensitive measurements. Second, we investigated and measured methane concentration in the surrounding air in our laboratory based on 250 MHz mid-infrared fiber frequency combs. We used a multipass cell to enhance the length of interaction between the laser beam and the molecules in the air to 580 m, which improved the sensitivity by orders of magnitude. We measured a concentration of 1.5 ppmv for methane in the air in 80 ms with a very high sensitivity of $7.6\times10^{-7}$ cm$^{-1}$. Our results demonstrate the advantages of mid-infrared dual frequency comb spectroscopy for trace gas detection and sensing applications.

# ACKNOWLEDGEMENTS

# NOMENCLATURE

P                   Power

I                   Intensity

R                   Reflectivity

T                   Transmission

IR                  Infrared

Mid-IR              Mid-Infrared

CW                  Continuous Wave

SNR                 Signal-to-Noise Ratio

NEP                 Noise Equivalent Power

HITRAN              High-Resolution Transmission Molecular Absorption Database

PNNL                Pacific Northwest National Laboratory

MPC                 Multi-Pass Cell

DAS                 Direct Absorption Spectroscopy

EO                  Electro-Optic

AO                  Acousto-Optic

AOM                 Acousto-Optic Modulator

PZT                 Piezoelectric Transducer

EDFA                Erbium-Doped Fiber Amplifier

QWP                 Quarter Wave Plate

HWP                 Half Wave Plate

| | |
|---|---|
| HNLF | Highly Non-linear Fiber |
| VDL | Variable Delay Line |
| WDM | Wavelength Division Multiplexer |
| COL | Collimator |
| FCP | Frequency Conversion Processes |
| OPG | Optical Parametric Generation |
| OPO | Optical Parametric Oscillation |
| OPA | Optical Parametric Amplification |
| DFG | Difference Frequency Generation |
| SFG | Sum Frequency Generation |
| SHG | Second Harmonic Generation |
| HHG | High Harmonic Generation |
| SR | Synchrotron Radiation |
| SLS | Synchrotron Light Source |
| SR-IRMS | Synchrotron Radiation Infrared Micro-Spectroscopy |
| LINAC | Linear Accelerator |
| QCL | Quantum Cascade Laser |
| SMSR | Side-Mode Suppression Ratio |
| FP-QCL | Fabry-Pérot Quantum Cascade Laser |
| DFB-QCL | Distributed Feedback Quantum Cascade Laser |
| EC-QCL | External Cavity Quantum Cascade Laser |
| BPM | Birefringent-Phase-Matching |

QPM             Quasi-Phase-Matching

ZBLAN           Fluoride Glass based on $ZrF_4$, $BaF_2$, $LaF_3$, $AlF_3$, and NaF

OP              Orientation-Patterned

PO              Periodically Poled

CPBC            Coherent Polarization Beam Combining

PBS             Polarizing Beam Splitter

QWP             Quarter Wave Plate

VOC             Volatile Organic Compounds

T1D             Type 1 Diabetes

PD              Photo-Detector

MCT             Mercury-Cadmium-Telluride

APD             Avalanche Photo-Detector

IR-FPA          Infrared Focal Plane Arrays

QWIP            Quantum Well Infrared Photodetector

CCD             Charged-Coupled Devices

HR              Highly-Reflective

FSR             Free Spectral Range

RF              Radio-Frequency

FID             Free Induction Decay

GVD             Group Velocity Dispersion

CE-AS           Cavity-Enhanced Absorption Spectroscopy

CRDS            Cavity Ring-Down Spectroscopy

TABLE OF CONTENTS

LIST OF FIGURES

xiii

xv

LIST OF TABLES

# 1. INTRODUCTION

## 1.1 Absorption Spectroscopy

Global warming and environmental health issues have brought attention to the necessity of accurate monitoring of trace gases [1]. The increasing emissions of greenhouse gases, such as methane and carbon dioxide, with insufficient monitoring can take this planet to a point where environmental-related issues form the largest concern. In order for such issues to be contained, regular and reliable monitoring should take place worldwide using efficient monitoring systems. This, along with increasing public awareness and adjusting global gas emission policies, will take us forward to a future with controllable gas-emission rates related to human-activities.

Various techniques have been employed to measure and monitor trace gas concentrations in the environment [2, 3, 4, 5]. Among them, absorption spectroscopy is one of the most powerful techniques with high sensitivity.

Molecular absorption spectroscopy rely on the concept of absorption of electromagnetic radiation by molecules. This concept is illustrated in Figure 1. The molecules present in a sample absorb the electromagnetic radiation at certain wavelengths depending on the spacing between the energy levels of the molecules.
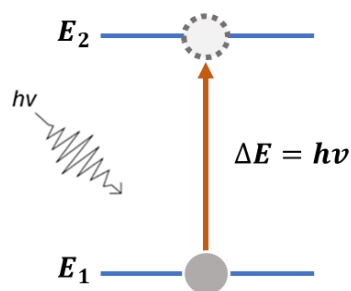
Figure 1 The energy level diagram for absorption of electromagnetic radiation.

Absorption spectroscopy is widely used in different scientific fields to study the molecules and their concentrations in a gas, a liquid, or a solid sample. It has been used in a wide range of spectroscopic measurements in molecular physics, astronomy, chemistry, biomedicine, and environmental studies [2, 6, 7].

In chemistry and life sciences, the term spectrophotometry is commonly used for measurements of reflection or transmission properties of materials as a function of wavelength with particular interest in the visible and ultraviolet (UV) regions. In biology and medicine, absorption spectroscopy is applied to study living systems based on characterization of the structure and the function of macromolecular and molecular systems.

Clinical diagnosis is another field with interest in absorption spectroscopy as a technique for analyzing and monitoring breath samples [6, 8]. With sensitive spectroscopic measurements and low detection limits, the prospect for early clinical diagnosis of several diseases has increased over the last years. More is discussed in Section 1.4.

Depending on the gas and particular technique used, the sensitivity of concentration measurements is determined in parts per million (ppm), parts per billion (ppb), and parts per trillion (ppt) all in volume (v) as shown in Table 1.

Table 1 Common Terms for Sensitivities.

| Parts Per Million by Volume | ppmv | $10^{-6}$ |
|---|---|---|
| Parts Per Billion by Volume | ppbv | $10^{-9}$ |
| Parts Per Trillion by Volume | pptv | $10^{-12}$ |
| Parts Per Quadrillion by Volume | ppqv | $10^{-15}$ |

## 1.2 Overview of Techniques and Applications

The simplest method of absorption measurements is direct absorption spectroscopy (DAS), which determines the absorption in a sample from the incoming and outgoing spectral intensities. In addition, several other spectroscopic techniques based on direct and indirect light absorption were developed. Among them are cavity-enhanced absorption spectroscopy [9, 10] and dual frequency comb spectroscopy that uses dual-beam detection [11, 12, 13].

Examples of indirect absorption techniques are cavity ring-down spectroscopy (CRDS) [9, 14, 15], photoacoustic spectroscopy (PAS) [16, 17], and Faraday rotation spectroscopy (FRS) [18].

Spectroscopic techniques that rely on long absorption path lengths are implemented using a multipass optical cell [12, 19] or a high finesse optical cavity [2, 8, 10, 15]. Both techniques require cavity mirrors with a very high reflectivity in the spectral region of interest.

In a multipass cell, the beam experiences multiple reflections before it exits the cell through a hole in one of the mirrors. Some geometries use one hole as an entrance and exit for the laser beam, while other geometries use two holes. The multiple reflections inside the cell provide a long path length over which the light-matter interaction takes place, resulting in a strong absorption signal. Multipass cells are discussed in detail in Section 2.5, and a dual frequency comb system based on a multipass cell can be found in the experimental part in Section 4.2.

In a high finesse cavity, the light bounces between the highly reflective mirrors until the intra-cavity signal builds up to reach a threshold level. This method requires careful optimization to match the cavity mode with the laser mode. The light leaking out of the cavity is detected to obtain the absorption spectrum of the gas sample inside the cavity. Section 2.5 describes high finesse cavities in more detail, and Section 4.1 discusses an experiment in the near infrared that utilizes a high finesses cavity.

## 1.3 Detection Limit and Precision of Spectroscopic Measurements

According to atmospheric and climate change studies, the global warming will continue to increase rapidly [1, 20]. Carbon dioxide emission rates keep increasing as people burn more and more fossil fuel. Methane and carbon dioxide are the major

4

greenhouse gases that contribute to global warming [20, 21]. Accordingly, the efforts toward sensitive atmospheric monitoring should intensify, and high sensitivities need to be achieved for reliable gas concentration measurements.

Gas sensing systems which depend on spectroscopic measurements are usually characterized by the detection limit in terms of a minimum detectable concentration or minimum absorption coefficient [18]. To perform the gas detection with a high sensitivity, it is important to improve the signal-to-noise ratio (SNR). This can be achieved through multiple signal enhancement approaches along with employing noise reduction schemes. Werle *et al* used Allan variance analysis to characterize signal size and the instrumental limitations of signal averaging, and achieved a detection limit of 10 pptv in 25 seconds for $NO_2$ under laboratory conditions [22].

The precision of the measurements with spectroscopic systems, determined by the variations of measurement results, is also limited by the signal-to-noise ratio. A major factor affecting the precision is the stability of the system. The accuracy of the measurements is determined by systematic errors and different uncertainties including the uncertainties in the pressure $P$, the temperature $T$, and the absorption path length $L$ [18]. Uncertainties in temperature $T$ and pressure $P$ can be minimized by stabilization of these parameters.

The effective absorption path length ( $L_{eff}$ ) is the path length in which the light-matter interaction occurs and where the molecules absorb light at certain wavelengths. Measuring this length for an optical cavity depends on the reflectivity of the mirrors used in the cavity and the cavity length, which is discussed in Section 2.5. An exact

5

measurement of $L_{eff}$ is necessary for high accuracy in experiments involving an open-path as well as multi-pass cell measurements, which can also be written as "multipass." In open-air experiments, the presence of atmospheric aerosols that scatter light could strongly affect the effective absorption path length [3, 23, 24]. In addition, air turbulence has to be taken into account [25, 26]. Examples of aerosols in the atmosphere include dust, fog, smoke, particular air pollutants, and sulfate aerosols [24].

When comparing the sensitivity of different techniques of spectroscopy, we should take into account the purpose of the experiment and the spectral region under study. Continuous wave (CW) lasers can be used to obtain highly sensitive absorption measurements. However, it might take up to several hours to scan a desired spectral range because of the narrow bandwidth of CW lasers. The spectral coverage of a broadband laser source exceeds that of a CW laser source. For simultaneous detection of various molecules at short periods of time, a broadband spectroscopic system with sufficient optical intensity per detection channel is required. Nowadays, many broadband techniques are applied to perform quantitative spectroscopic measurements of several trace gas species simultaneously [3, 9, 14, 19, 27, 28].

## 1.4 Breath Analysis and Trace Gas Detection

### 1.4.1 Application of Infrared Absorption spectroscopy to Breath Analysis

Many research studies are conducted towards diagnosis and monitoring of different diseases [6, 15, 29, 30]. Absorption spectroscopy is one of the powerful techniques that allows sensitive qualitative and quantitative measurements of different

compounds in a sample that are considered biomarkers of diseases. This potential has been a driving force towards inventing and establishing new and more sensitive spectroscopic approaches for medical applications over the last few decades. Human breath analysis is one of the fields that witnesses such an improvement [31, 32]. Thorpe *et al* studied $CO, CO_2, H_2O, CH_4$, and $NH_3$ for breath analysis using cavity-enhanced frequency-comb spectroscopy in the 1.5 $\mu m$ – 1.7 $\mu m$ range [8]. Their system's minimal sensitivity for $NH_3$ is higher than the limit of detectable ammonia in a normal human breath, but is sufficient for detecting increased concentrations of $NH_3$ for diagnosis of renal failure at early stages. Acetone and methane concentrations in exhaled breath were investigated by Bicer and co-workers based on a near infrared spectroscopic system with a high finesse cavity [15]. The concentration of acetone in human breath can be used to indicate certain types of diseases such as heart diseases and diabetes [33].

Other fields of scientific research focus on diseases that involve metabolic processes [30]. Siegel and Daneshkhah *et al* conducted a study on breath samples from patients with type 1 diabetes (T1D). They used gas chromatography along with mass spectrometry to analyze the volatile organic compounds (VOCs) present in the breath samples [29]. These compounds are used to identify the metabolic processes that lead to low levels of blood glucose. In their work, they tried to replicate the detection ability of diabetes alert dogs (DADs) so that more patients can get the benefits of breath sample monitoring. The results indicate sufficient sensitivity and the possibility to differentiate hypoglycemic breath samples from other samples. Recent results on these technologies improved our understanding of metabolism in humans [30, 34, 35]. However, the systems

they use are large and complex with long measurement times. This is because mass spectrometry is often used in parallel with gas chromatography. Even though it is extremely sensitive, this approach has difficulty to differentiate between different molecules present in the sample. Therefore, attention have been paid in recent years to optical measurement systems, and in particular to IR spectroscopy techniques, which allow to investigate several biomarkers simultaneously with lower costs, shorter times, and higher system flexibility [8, 31, 32].

### 1.4.2    *Application of Infrared Absorption Spectroscopy to Trace Gas Detection*

In trace gas detection, the concentration of molecules can be revealed from the measurement of the absorption coefficient. Those measurements are also used to optimize the performance of the spectroscopic system. The absorption of gas molecules per unit length $cm^{-1}$ is equal to:

$$\alpha = n\, S_i\, g$$

where $g$ is the line-shape, n is the gas concentration per unit volume, and $S_i$ is the line-intensity. The environmental conditions where the experiment is conducted alter the line shape. Therefore, it is vital to consider the pressure, temperature, and humidity level when the measurements are taken. Whereas, the line intensity can be found from the available molecular databases like HITRAN [36]. Measuring the absorption $\alpha$ experimentally, we can retrieve the concentration (n) of the molecular species in the sample. This is the fundamental concept behind absorption spectroscopy and its applications. Diverse fields of infrared spectroscopy applications are shown in the chart in Figure 2.
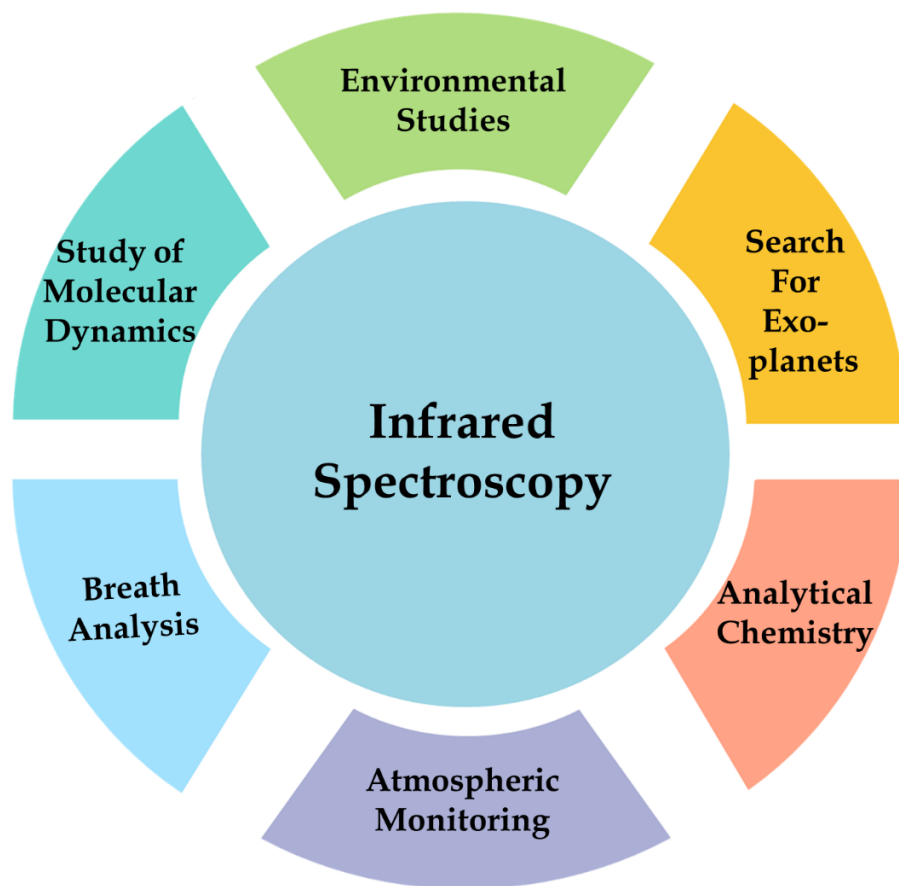
Figure 2 A variety of applications of infrared spectroscopy.

## 1.5 The Interest in the Infrared Spectral Region

Due to the availability of several techniques and sources of infrared radiation in the last few decades, the infrared spectral region has received perceptible attention from many fields in industry [37, 38], environmental research [4, 5, 12, 39, 40], medical diagnosis [8, 31, 32], astronomical instrumentation [41, 42], and scientific research [43, 44].

Infrared spectroscopy is overtaking Raman spectroscopy in industrial applications because of the flexibility of preparing the samples for infrared absorption spectroscopy applications either in laboratories or in the field [13, 39, 45]. In addition, the development of new broadband infrared sources allows the detection of the absorption spectra of various molecules with a single measurement [5, 9, 19, 27, 28]. Several detection systems that utilize the capabilities and advantages of recently developed infrared sources have been demonstrated [3, 9, 46, 47, 48].

A detailed discussion of the characteristics of the infrared region is provided in Section 2.1, and several types of sources of infrared radiation are covered in Section 2.2. A brief history and description of photodetection methods and techniques are presented in Section 2.3. Section 2.4 reviews the principles of optical ray tracing, which is essential in many applications to characterize optical systems or analyze signals and images. The chapter concludes with high finesse cavities and multipass cells, which are often used in spectroscopy to increase the light-matter interaction length. Then in Chapter 3, the concepts behind many instruments used in laser spectroscopy experiments are explained. For the experimental part, two different techniques were implemented based on infrared frequency combs, and are discussed in Chapter 4. In general, this work primarily focuses on mid-infrared spectroscopy and its elements, although many topics are related to the infrared and terahertz (THz) regions in general.

## 2. THEORETICAL DESCRIPTION AND OVERVIEW

### 2.1 Principles of Infrared Spectroscopy

#### 2.1.1 The Infrared Region

The experiment performed by Sir William Herschel in 1800 to study sunlight using a prism was the starting point for the development of infrared spectroscopy [49, 50]. When he observed a peak temperature at the invisible range beyond the red color, he named it "infrared".

Infrared spectroscopy is a field of spectroscopy that studies the spectra of molecules in the infrared region of the electromagnetic spectrum. The infrared (IR) region is between the visible and the microwave regions, as can be seen in Figure 3, and it extends from around 780 nm to 1 mm.
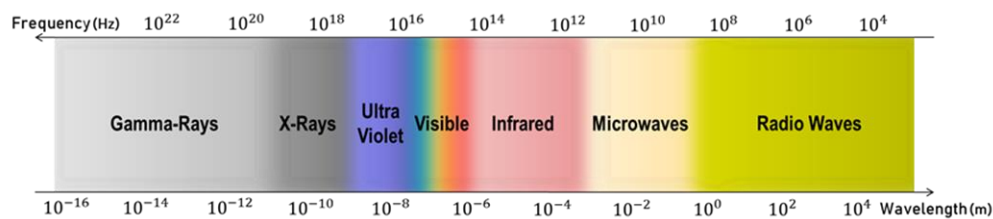


Figure 3 The electromagnetic spectrum.

Since the propagation speed of electromagnetic radiation in vacuum is constant $c = 2.997925 \times 10^8 \ m/s$, light of higher frequencies has shorter wavelengths and vice versa.

The subdivision of the IR spectral region is slightly different for different fields of science. This mostly depends on the available detectors and applications for each range of wavelengths. In astronomy, the infrared is subdivided into near infrared (Near IR), mid-infrared (Mid-IR), and far-infrared (Far-IR), as shown in Figure 4.
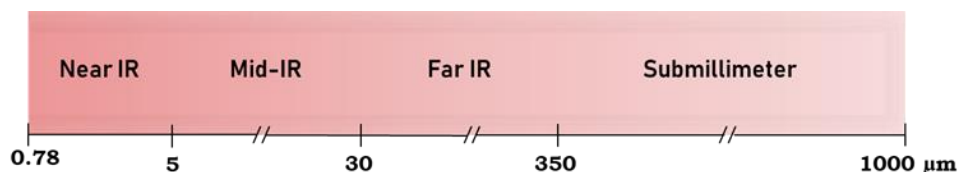


Figure 4 The subdivisions of the infrared spectral region used in Astronomy.

Rogalski uses the subdivision illustrated in Figure 4 to characterize the different kinds of infrared detectors [51, 52, 53]. He divides the infrared into near infrared (NIR), short wavelength infrared (SWIR), medium wavelength infrared (MWIR), long wavelength infrared (LWIR), very long wavelength infrared (VLWIR), and far infrared (FIR) followed by submillimeter (SubMM) spectral range. The difference in the divisions mainly arise from the difference in optical materials and instruments used in each field.

Fundamental rotational-vibrational transitions in molecules result in strong absorption bands in the mid-IR region $3 - 25\,\mu m$. Therefore, this spectral region is referred to as the "molecular fingerprint region" [28, 31, 48, 54], as illustrated in Figure 5.
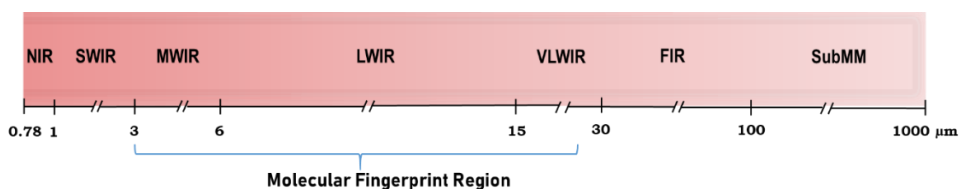
Figure 5 The subdivisions of the infrared spectral region used for detector characterization.

Since the IR radiation is not visible to the human eye, it requires special techniques and methodologies to deal with it. Over the years, different detection methods were implemented to study and analyze light in this range [27, 51, 53, 55]. A brief historical overview of detection methods and discussions of various detectors are given in Section 2.3.

Advances in prism manufacturing and materials and the use of diffraction gratings allowed further improvements in spectral measurements. Using diffraction-based spectrometers is common in experiments with broadband laser sources. Diffraction gratings are treated explicitly in Section 3.1.

Instrumentation techniques for IR spectroscopy were developed in the 1940s following an instrument by Lehrer around 1937 [56]. In 1946, the first catalog for analytical studies based on infrared absorption spectroscopy was published. Michelson is the one who used an interferometer for spectroscopy, and his name is well-known for this technique [57]. After 1960, commercial interferometers became available.

The fast Fourier transform (FFT) algorithm was discovered around 1965, which opened the door for Fourier Transform Infrared Spectroscopy (FT-IR). With the progress

in computer technology, the task of obtaining and analyzing the Fourier transform (FT) of an interferogram became easier and faster. As a result, commercial FT-IR systems are dominant these days for analytical purposes in various fields.

Advances in the various techniques of IR laser spectroscopy strongly depends on the availability of efficient IR sources. The key characteristics of a highly efficient laser source suitable for spectroscopic applications include high optical power and broad spectral coverage. This necessity led to the development of different kinds of IR sources over the years [27, 44, 58-64]. In Section 2.2, the primary sources of radiation relevant to IR spectroscopy are summarized.

*2.1.2   Molecular Excitation by Absorption of Infrared Radiation*

When we shine light from a radiation source on a material or a gaseous sample, light-matter interaction takes place. Consider a photon of energy equal to the energy difference between two levels or orbitals. When an electron in the ground state absorbs this photon, it gets excited to a higher energy level, as illustrated in part (a) of Figure 6. Spontaneous emission takes place when an electron in an excited state relaxes to a ground state and emits a photon of an energy determined by the two levels, as part (b) of Figure 6 shows. Laser emission depends on the stimulated emission process shown in part (c) of Figure 6. In this process, an electron in an excited state responds to an incoming photon by moving to a lower energy state and emitting a photon identical to the incoming one. For this to happen, obtaining a population inversion is required.

14
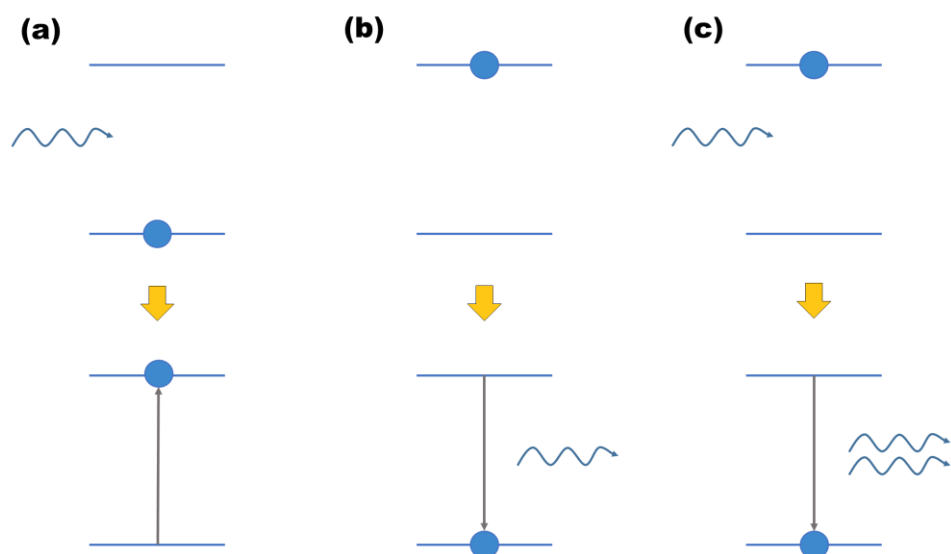
Figure 6 The energy level diagrams for three different processes. (a) Absorption of electromagnetic radiation occurs when the incident photon is absorbed and the electron is excited to a higher level, (b) spontaneous emission involves an electron in a higher state moving to a lower one and emitting a photon, and (c) stimulated emission takes place when the electron is in excited state and a photon is incident. The electron moves to a lower state and emits a photon of the same energy as the incident one.

Different atoms and molecules have different energy levels that are unique and defines the properties of the atom or molecule. In an absorption process, the type of the transition between energy levels in a molecule depends on the wavelength of the electromagnetic radiation incident on the molecule. The basic types of transitions are shown in Figure 7. An electronic transition is a transition between two electronic states, and it takes place by absorption of UV, visible, or near IR radiation. A molecule can also undergo a pure rotational transition when it absorbs microwave radiation. Whereas, IR radiation probes the absorption of energy in molecules corresponding to molecules transitioning between vibrational levels of the same electronic state, or between rotational

levels of different vibrational states in the same electronic state. The transitions in the latter case are also called rotational-vibrational, or "ro-vibrational" transitions [65]. Vibrational transitions require much less energy than electronic transitions, as can be inferred from the figure.
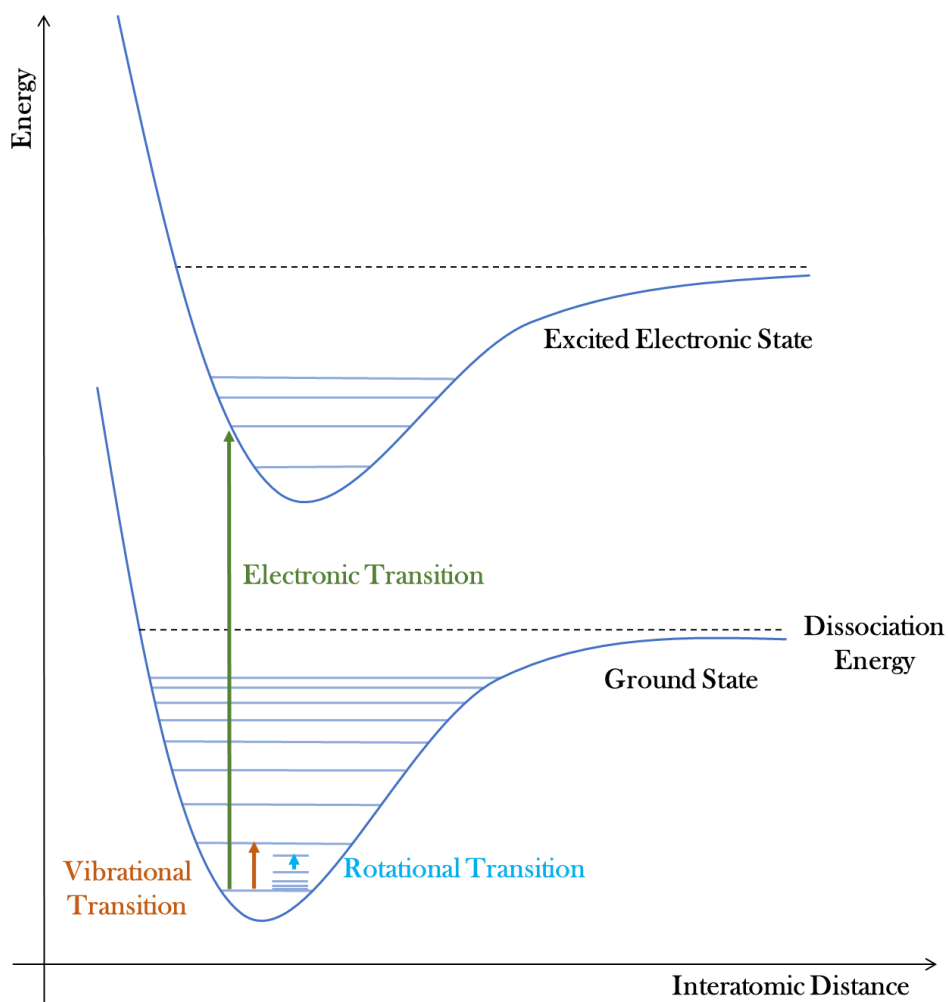


Figure 7 A schematic showing electronic transitions, which correspond to the visible or UV regions, vibrational transitions, which correspond to the IR region, and pure rotational transitions, which correspond to the microwave region.

In a molecule, bonds between atoms have different strengths ranging from strong bonds to weak bonds. Strong bonds tend to correspond to higher vibrational energies in comparison with weak bonds. Molecular vibrations can be stretching or bending. Stretching of molecules composed of three atoms or more can be symmetric, when the length of the bonds changes by the same amount and in symmetry, or asymmetric, when the vibration involves bonds that get shorter and other bonds that get longer. Bending vibrations include changes in the angle between different bonds, and can be in the form of scissoring, rocking, wagging, and twisting, as shown in part (b) of Figure 8. An example of vibrational modes is given in part (a) of Figure 8 for a triatomic nonlinear molecule. Some vibrational mods can also be seen as internal rotation, such as the fourth mode in part (a) of the Figure 8.
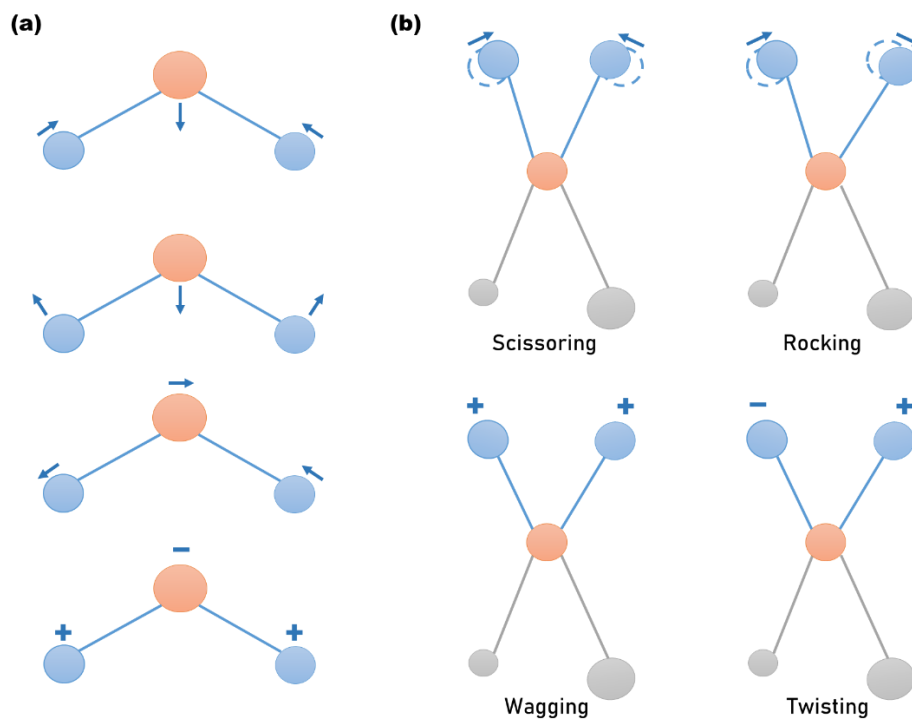
Figure 8 (a) Modes of vibration for a nonlinear molecule of three atoms. (b) An example of different types of bending vibrations for a molecule. The negative and positive signs indicate in- and out-of-plane vibrations.

Examples of some of the important bonds in the IR region are displayed in Figure 9. In chemistry and other absorption spectroscopy applications, these vibrational bonds are used to determine the molecular structure and the chemical composition of different compounds.
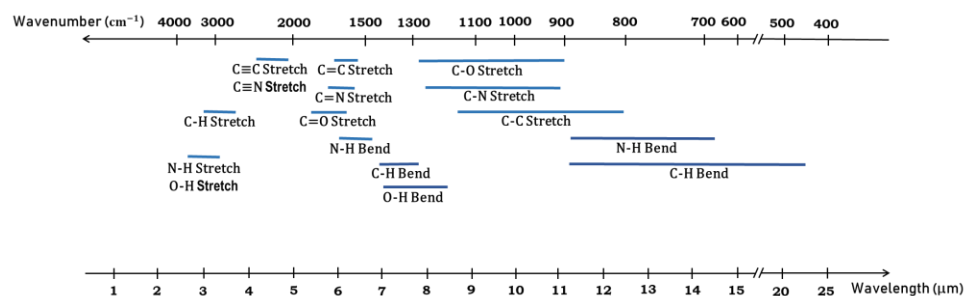
Figure 9 Group vibrations of different bonds in the group frequency and the fingerprint regions of the infrared.

The absorption of IR radiation leads to transitions between rotational levels in different vibrational bands, as illustrated in Figure 10. These rotational-vibrational transitions result in three sets of absorption lines known as branches. The selection rules of the P-branch transitions are $\Delta v = +1$ between the vibrational levels and $\Delta J = -1$ between the rotational levels. The Q-branch transitions have the selection rules $\Delta v = +1$ and $\Delta J = 0$, and for the R-branch transitions, the selection rules are $\Delta v = +1$ and $\Delta J = +1$ [65, 66].
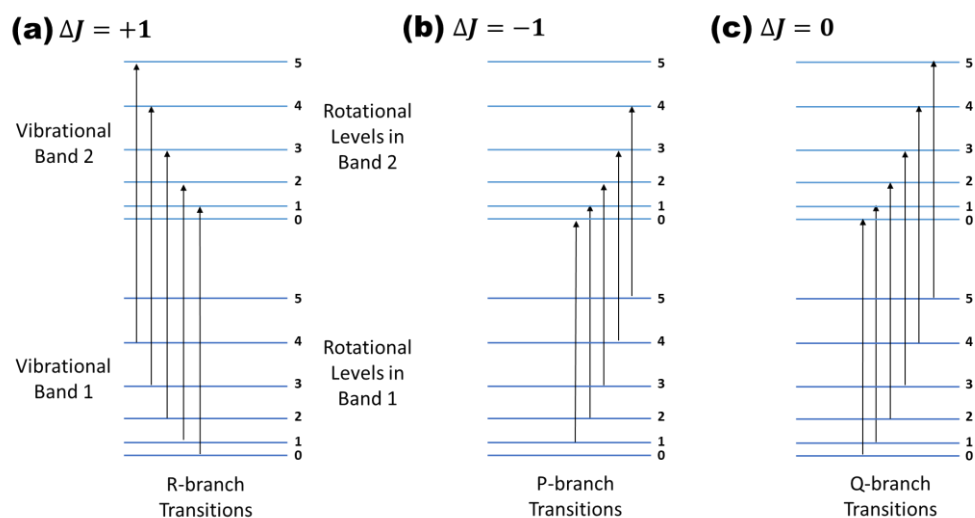
Figure 10 Transitions between rotational levels of different vibrational bands are (a) R-branch with ΔJ=1, (b) P-branch with ΔJ=-1, and (c) Q-branch with ΔJ=0.

In considering molecular vibrations, let us take the simple case of a diatomic molecule as an example. When the bond between the two atoms compresses, its compression is limited by the repulsion force between the atoms. Stretching is also limited, and the stretch bond breaks at some point. Therefore, bonds between the atoms in the molecule act as an anharmonic oscillator. Figure 11 illustrates the difference between a harmonic oscillator potential and anharmonic oscillator potential for a diatomic molecule. The allowed vibrational transitions are for $\Delta\upsilon=\pm1, \pm2, \pm3, ...$ comparing to $\Delta\upsilon=\pm1$ in the harmonic oscillator case [66].
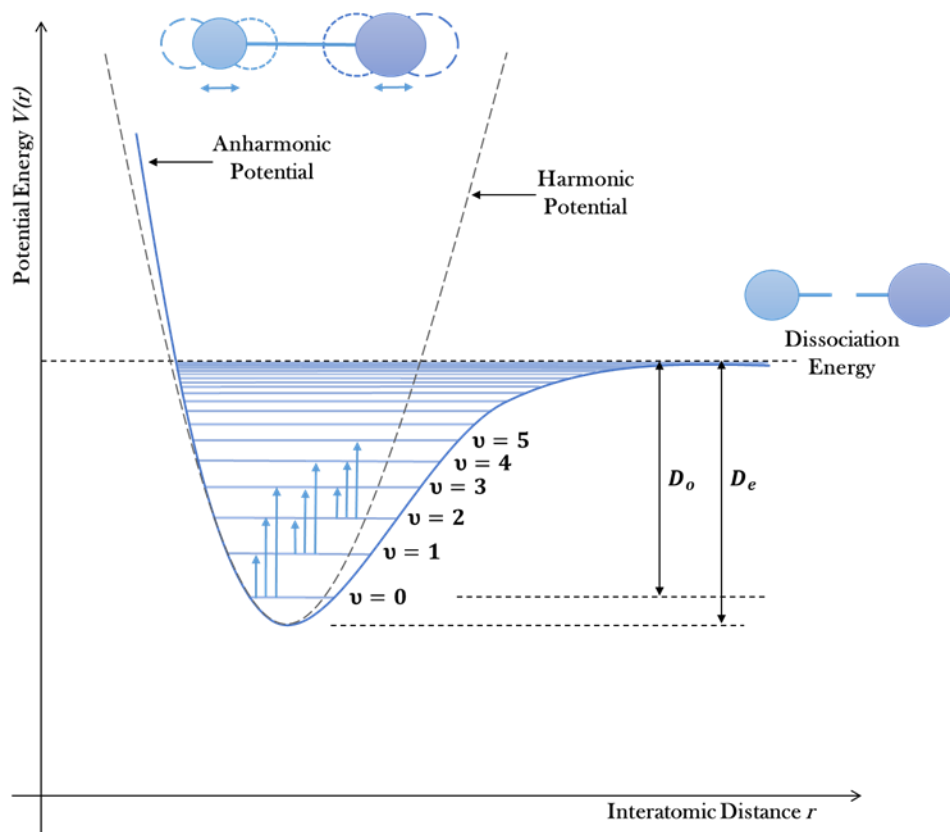
Figure 11 The anharmonic potential energy curve (Morse-type) and energy levels for a diatomic molecule in comparison to a harmonic potential (Hooke's law). Some allowed transitions between the energy levels are shown. $D_o$ is the dissociation energy relative to the vibrational energy at $\upsilon$=0, and $D_e$ is the dissociation energy relative to the minimum of the curve.

When a molecule interacts with IR radiation, it absorbs the radiation and gets excited to a higher vibrational level only when there is a change in the dipole moment associated with this transition [65]. In such case, the transition is allowed and is called "IR-active." In other words, the absorption of IR radiation occurs if two conditions are met. First, the molecular vibration involves a change in the dipole moment, which induces a changing electric field that interacts with the electric field of incident radiation. Second,

the frequency of the incident radiation matches the frequency of a transition between two vibrational levels. Note here that the first vibrational level $\upsilon=0$ has non-zero energy, as can be seen in Figure 11.

On the other hand, molecular vibrational transitions that do not involve a change in the dipole moment are called "IR-inactive" or forbidden transitions [66]. Table 2 includes some examples of molecules that demonstrate this requirement.

Table 2 Examples of IR-active and IR-inactive transitions
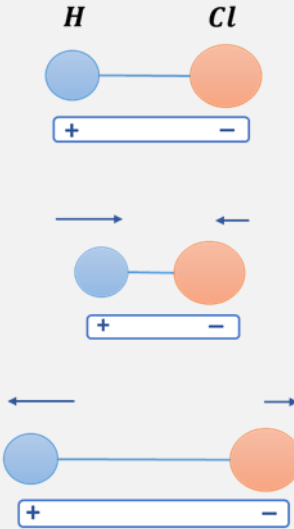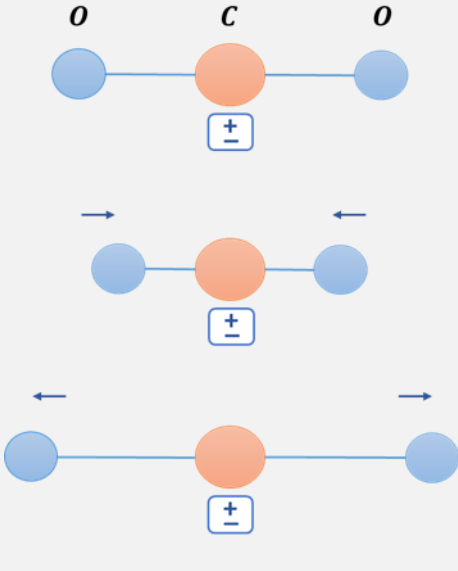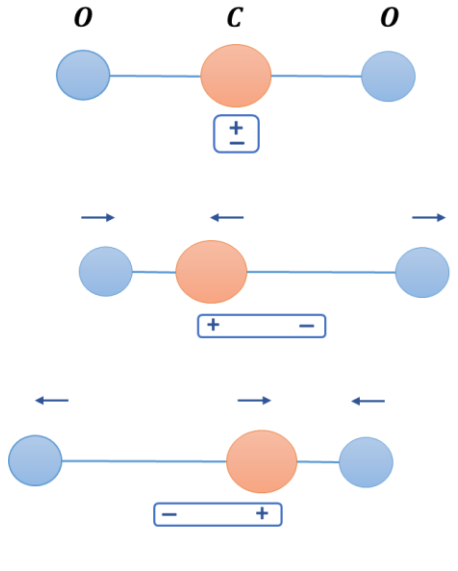
| Molecule | Vibration | Characterization |
|---|---|---|
| $HCl$ |  | IR-active |

Table 2 Continued.

| Molecule | Vibration | Characterization |
|----------|-----------|------------------|
| $CO_2$<br><br>Symmetric Vibration |  | IR-inactive |
| $CO_2$<br><br>Antisymmetric<br><br>Vibration |  | IR-active |

Recall that the dipole moment is a product of the charge and the distance between the two charges μ=qr, in the simplest case. Vibrations of diatomic molecules like $HCl$, $HF$, and $CO$ result in a changing dipole moment due to changes in the distance between the

23

atoms. Therefore, these molecules are IR-active. However, IR radiation is not absorbable by symmetrical molecules such as $H_2$, $O_2$, and $Cl_2$ because they do not have a dipole moment.

Antisymmetric vibrations in symmetric molecules like $CO_2$, $NH_2$, and $CH_2$ are IR-active even though the molecules do not have a dipole moment at the equilibrium state. The change in the dipole moment by the antisymmetric vibration arises from the oscillations of negative and positive centers of charges [66]. Whereas, symmetric vibration of the same molecule is IR-inactive, because the two identical atoms are displaced by the same amount to opposite directions, which does not yield a change in the dipole moment, as Table 2 shows.

IR spectroscopy is one of the primary techniques employed in the monitoring of trace gases, as we mentioned in the first chapter. An essential application is the quantitative measurements of atmospheric greenhouse gases. Observations by climate change centers in the last couple of decades have brought a considerable concern towards the rapid increase of concentrations of greenhouse gases in the atmosphere [1], and its effects on human health and the environment.

Most of the solar energy absorbed by the Earth each day is released in the form of heat or IR radiation. Oxygen ($O_2$) and nitrogen ($N_2$) are the most abundant atmospheric gas molecules, but they are IR-inactive, so no IR absorption takes place. On the other hand, other certain gas molecules that are abundant in the atmosphere are IR-active, such as methane ($CH_4$), carbon dioxide ($CO_2$), nitrous oxide ($N_2O$), and chlorofluorocarbons. Therefore, these molecules can absorb the IR-radiation emitted from the surface and re-

emit it in different directions. In this way, the IR-active gas molecules in the atmosphere act similar to the glass of a greenhouse by increasing the inside temperature.

An increase of $1.9 \, ppm$ per year for $CO_2$ was recorded between 1995 and 2005. This growth rate in atmospheric $CO_2$ concentration is the largest to be recorded over the last two centuries. Based on the correlation of $CO_2$ levels and fossil fuel usage along with industrial activities, spectroscopic studies have been conducted to measure, monitor, and predict levels and sources of $CO_2$ in the environment. Vibrational modes of $CO_2$, illustrated in Figure 12, are used in IR-spectroscopy measurements to investigate its concentration and isotope ratios, which require IR sources and detectors that operate at the desired wavenumber range. The same concept applies to spectroscopic measurements of other IR-active greenhouse molecules.

**(a)** $CO_2$ Stretching

**(b)** $CO_2$ Bending
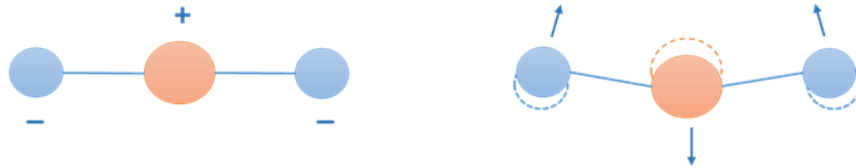
Figure 12 An illustration of the vibrational modes of carbon dioxide. (a) The symmetrical stretching mode on the left, corresponding to $1340\ cm^{-1}$ or $7.5\ \mu m$, and the antisymmetric stretching mode on the right, corresponding to $2350\ cm^{-1}$ or $4.3\ \mu m$. (b) The scissoring-bending modes, corresponding to $666\ cm^{-1}$ or $15\ \mu m$. The two equal-energy bending vibrations are identical except that one bending mode is perpendicular to the plane of the paper, and the other is along the plane of the paper.

*2.1.3   The Beer-Lambert Law*

The absorption coefficient is $\alpha{=}n\sigma$, where $n$ is the number of absorbing molecules in molecules/cm$^3$, and $\sigma$ is the absorption cross-section in cm$^2$/molecule. When the light passes through the sample, a portion of the incident light will be absorbed by the molecules present in the sample. As a result, the intensity of the transmitted light $I$ is less than the intensity of the incident light $I_0$. The Beer-Lambert law describes the relation between $I$ and $I_0$ in terms of $\alpha$ and the interaction length $L$:

$$\frac{I}{I_o} = e^{-\alpha L}$$

26

The absorbance $A$ at a frequency $\nu$ is obtained from this law [18], and is given by:

$$A(\nu) = ln\left(\frac{I_0(\nu)}{I(\nu)}\right) = n\sigma(\nu)L$$

The absorbance $A$ is proportional to the density of molecules. A sufficiently long effective path-length $L_{eff}$ is required, in order to enhance the light-matter interaction and therefore improve the sensitivity of measurements.

The proportionality of the absorbance in material to its thickness was first discovered by Bouguer in 1729 [67] and formulated by Lambert in 1760 [68]. The thickness of the material indicates the absorption path length $L$. In 1852, Beer discovered another proportionality that relates the absorbance in a material to the number of attenuating species in that material [69]. The Beer-Lambert law, which combines both factors, has been used for a long time in different fields of science, atmospheric studies, and industrial applications [70]. A modified version of the Beer-Lambert law that considers the presence of atmospheric aerosols is given in Appendix A.

## 2.2 Sources of Infrared Radiation

### 2.2.1 *Development of Infrared Sources and Detection Methods*

The initial discovery of IR radiation was in Germany by Herschel using thermometers [49, 50]. In Germany also, the first thermocouple was discovered in 1821 by the physicist J. Seebeck [52, 71]. The first thermopile was constructed by an Italian physicist L. Nobili in 1829 and was modified by Melloni in 1833 [72]. The bolometer followed in 1881 providing better sensitivity [52]. The English engineer W. Smith

discovered the photoconductive effect, and used selenium in an experiment in 1873. Years later, a high responsivity IR photoconductor was developed by Case in 1917, and Cs-O-Ag phototubes were developed in the 1930s [51, 53].

The first practical photoconductor was based on lead sulfide (PbS), which was discovered in Germany as a photoconductive material. The first lead sulfide photodetector was manufactured in Germany around 1934, and in the US and England a couple of years thereafter [53]. In the early 1950s, the transistor was developed and this was the starting point where the advances in semiconductor materials for IR detection took off. The mercury-cadmium-telluride (HgCdTe) was developed by Lawson and others [73] following the discovery of III-V compound semiconductor family. The 1980s witnessed the development of the second generation of mercury-cadmium-telluride systems, which is also known as "MCT," with the advantage of lower power dissipation. Soref was the first to use extrinsic Si in his work published in 1967 [74], followed by Boyle and Smith who used extrinsic Si in inventing charge-coupled devices (CCD) [75]. This imaging semiconductor circuit is commonly applied nowadays in spectroscopy as an IR sensor.

Developments in IR sources and detection techniques continued, which led to the advancement of IR technology that we see today [44, 51, 55, 66]. This section covers the most common sources of IR radiation starting from globar and synchrotron sources to semiconductor sources. Fiber lasers and lasers based on nonlinear processes are also discussed in detail. The section concludes with optical frequency combs and their characteristics. Principles and features of different detectors are described in the following section.

*2.2.2    Globar IR Sources and IR Synchrotron Radiation*

The synchrotron radiation (SR) is the radiation produced in large electron accelerator rings operated in relativistic conditions. When charged particles are accelerated to velocities close to the speed of light $c$, IR radiation can be extracted within a wide solid angle when the particles move between bending magnets [76]. Even though the emission of this radiation is not based on optical transitions, it produces a broadband IR beam of high brightness suitable for many spectroscopic applications. For this reason, a brief description of SR is given in this section.

Special facilities are built across the world to serve as sources of SR. The important parts of those facilities include a linear accelerator (linac), a synchrotron, a storage ring, a shielding wall, beamlines, and experimental areas [77]. A basic drawing of the structure of synchrotron research facilities is given in Figure 13 below. In the storage ring, an electric field is applied to accelerate the particles and a magnetic field is applied to support the circular motion in the ring. An accurate synchronization between the fields and the beam of traveling particles is maintained [78]. The National Synchrotron Light Source (NSLS-II) in New York and BESSY-II in Germany are two of many SR facilities that support different areas of research worldwide. The first research program, to use an IR beamline, was at Daresbury facility in England [79].

A significant advantage of the SR is the continuous emission range spanning the electromagnetic spectrum from the radio wave region to other regions that can extend to the gamma-ray region [78, 79]. This advantage opened the door for a vast variety of analytical applications. Furthermore, compared to the IR radiation emitted from normal

29

blackbodies and other continuum light sources, the infrared synchrotron radiation (IRSR) is more directional and has a considerably higher brightness, often called brilliance [80].

Globar is a source of electromagnetic radiation that emits near the IR region. It is typically a solid that is heated to a very high temperature to produce radiation. To be more specific, an IR globar is a blackbody at a temperature $T \sim 1300\ K$, and is used in commercial and experimental Fourier transform infrared spectrometers as a source with a broad spectral window $1 - 8\ \mu m$ [81, 82]. In a study by Carr and co-workers, they use a mid-IR globar source at $T \sim 1200\ K$, focus the flux, and predict the illuminated area in $\mu m^2$ using ray tracing [83]. The concepts of optical ray tracing are explained briefly in Section 2.4. In their study, Carr *et al* used $3\ \mu m$ aperture to compare the signal-to-noise (SNR) ratio of the spectra obtained from the globar versus the SR source, and found that it is 20 times higher when the SR is used [83]. To reach the same SNR with the globar, it requires 400 times longer averaging of the signal, which means a measurement time longer than a whole day with the globar comparing to 4 minutes with the SR. For micro-spectroscopy, they consider IRSR as a nearly ideal IR source. Using a $10\ \mu m$ pinhole, it has been found in a more recent study that the SR brightness exceeds that of a typical IR globar by 100 to 1000 times [82, 84].

Let us explain how IR radiation from synchrotron sources is used in experiments. The area around the storage ring in a synchrotron facility is divided into sections, and each section is dedicated to experiments within a specific domain of energy [76, 79, 80]. IR radiation is produced in one of those areas, as indicated in Figure 13, and is used with IR optics and spectrometers for different research studies. The IRSR can have a linear or

circular polarization, depending on the optical and geometrical beam characteristics, and can be produced in a pulsed structure, which depends on the intrinsic features of SR in that facility [76]. Conventional beamlines emitting IRSR in synchrotron facilities cover wavelengths from $1\ \mu m$ to $1\ mm$, which correspond to energies between $1\ eV$ to $1\ meV$ [80].
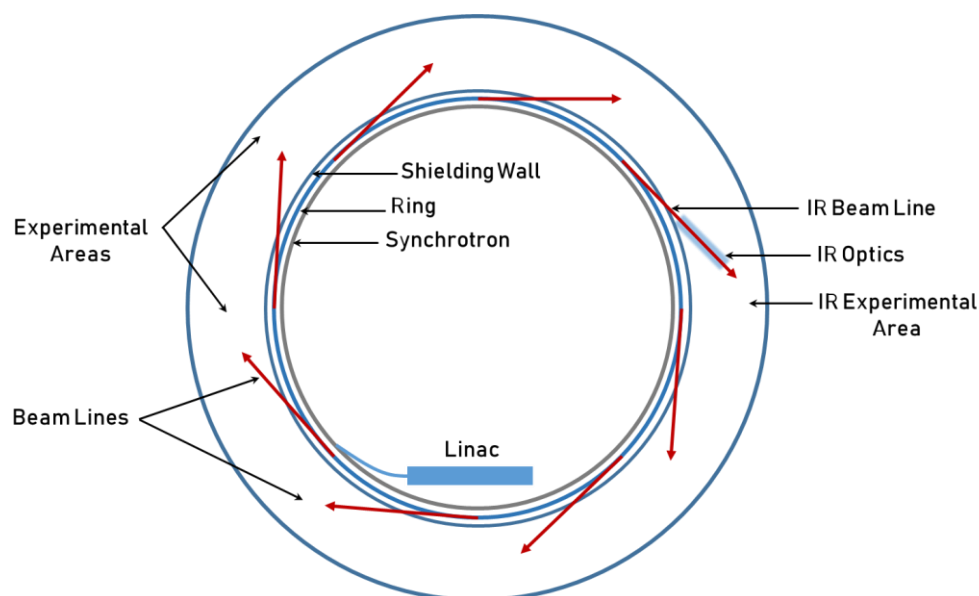


Figure 13 Basic schematic of a synchrotron radiation facility that produces several beamlines for scientific experiments.

Highly sensitive IR spectral measurements can be performed for cellular molecular markers in bio-samples, which utilize the diagnostic capabilities of different techniques based on IRSR [84]. In biology, synchrotron radiation infrared micro-spectroscopy (SR-IRMS) is a technique that enables the study of biological tissues as small as a single living cell [85]. Using a high power SR source and a focal plane array detection method,

individual cell imaging is achievable within a few minutes [86]. Following the development of high-current SR facilities [78, 80, 86] and the advances in sensitivity and spectral coverage of IR detectors [51, 55], resolutions in the micrometer and sub-micrometer scales will be possible for biomedical images in the near future [86].

### 2.2.3 *Laser Diodes and Quantum Cascade Lasers*

A quantum cascade laser (QCL) is based on a grown structure of multiple layers of semiconductors, and it emits radiation in the mid- and far IR regions. It was first demonstrated in 1994 by Faist and co-workers [87]. QCLs are coherent light sources, and the brightness of QCLs exceeds that of globar and synchrotron IR sources by several orders of magnitude.

The difference between QCLs and typical semiconductor lasers is mainly in the type of transitions between energy levels in the material. The photon emission in semiconductor lasers results from electron transitions between the valence and conduction bands, which are known as interband transitions. In contrast, the transitions in QCLs are "inter-subband" transitions that occur within the conduction band. This difference is presented in parts (a) and (b) of Figure 14.

In bulk semiconductor lasers, the size of the band gap determines the frequency of the emitted radiation $h\nu = E_g$. This limits light emission to a certain range of wavelengths, because the band gap size depends on the two materials used in the laser. Whereas in a QCL, the repeated series of thin semiconductor layers of altered materials form a cascade of quantum wells when an electric voltage is applied across the structure. The thickness

of semiconductor layers defines the width of quantum wells that are formed in the structure.

Light emission is attained from optical transitions of electrons between the quantized energy levels of the quantum wells, as shown in part (c) of Figure 14. Hence the wavelength or the frequency of emitted radiation depends on the thickness of those layers. Based on this, band gap engineers are capable of designing structures made from the same materials, but with different layer sizes, to achieve IR emission at different wavelengths. This advantage makes QCLs an attractive source of mid-IR radiation in the various fields relevant to molecular spectroscopy [88, 89]. According to Belkin and Capasso, the high performance and wide tunability of QCLs have made them the most commonly used IR sources in the last two decades [59].
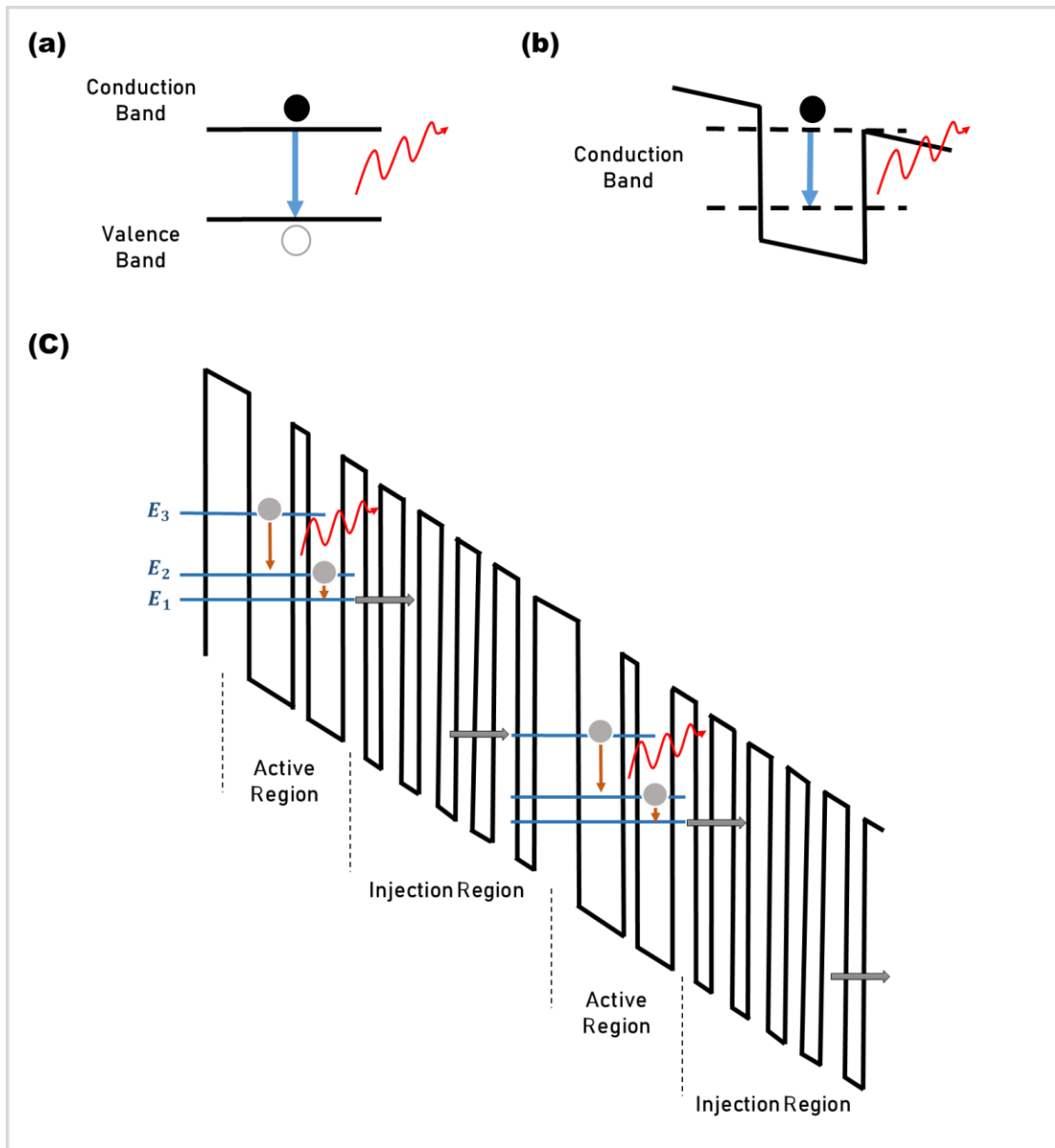
Figure 14 Emission of mid-IR radiation by (a) interband transitions in diode lasers and (b) inter-subband transitions in QCLs. (c) The quantum wells cascade enables multiphoton emission by a single electron via laser transitions in the active regions.

As can be seen in part I of the figure, the cascade process involves multiple steps. By applying an electric current, the electrons are injected into an energy level $E_3$. When

this energy level is more populated than a lower energy level $E_2$, population inversion is achieved. The cascade of an active region and injector pairs form the gain medium of QCLs. When a radiative transition between the two levels follows, a photon of energy $E_3 - E_2$ is emitted. An efficient and rapid transition from $E_2$ to $E_1$ serves to extract the electron from $E_2$. The injector of the next period of the structure can use the same electron and inject it into the next active region, and by the end of the cascade process this results in multiphoton emission by a single electron.

Available configurations of quantum cascade lasers are the Fabry-Pérot (FP-QCLs), the distributed feedback (DFB-QCLs), and the external cavity (EC-QCLs). The FP-QCLs have a multi-mode operation at high operating currents, and the laser emission supports wavelengths which are within the spectral gain curve of the QCL and meet the FP condition. The emission wavelength of the laser can be tuned by changing the temperature of the device. FP-QCLs are suitable for some spectroscopic applications that involve broad continuous absorption features, such as those targeting solids or liquids [89].

In general, FP-QCLs are not well suited for gas sensing and monitoring applications because these applications require a narrow linewidth comparing to the pressure broadened linewidth of the target gas at room temperature. Therefore, single-mode IR lasers which are tunable over a broad range of wavelengths are preferred for sensor technology and applications. Despite this, recent advances allowed Wang *et al* to extract high resolution ~ 15 $MHz$ spectral measurements employing a mid-IR absorption spectroscopy technique based on a broadband multimode FP-QCL source [90, 91].

The DFB-QCLs support a single-mode operation, and their structure incorporates a grating element, typically a Bragg grating [92]. Changing the operating temperature of the laser allows for spectral tuning. The structure of the DFB-QCL device sets a limit on the thermal tuning range, which is in the order of $10\ cm^{-1}$ at most [90]. Thus, IR applications that employ DFB-QCLs utilize a particular spectral range within the molecular fingerprint region. In analytical chemistry, this allows highly sensitive measurements of a characteristic rovibrational absorption line that does not interfere with the absorption lines of other gases and is specific to the analyte. Other potential applications of QCLs in many areas of chemistry and chemical physics are being developed [93].

Well-designed DFB-QC laser devices can have an excellent side-mode suppression ratio (SMSR). This ratio, expressed in decibels ($dB$), compares the power of the central longitudinal mode to that of the closest higher-order mode, as illustrated in Figure 15. In other words, a large SMSR indicates that most of the optical power is fed to the main mode.
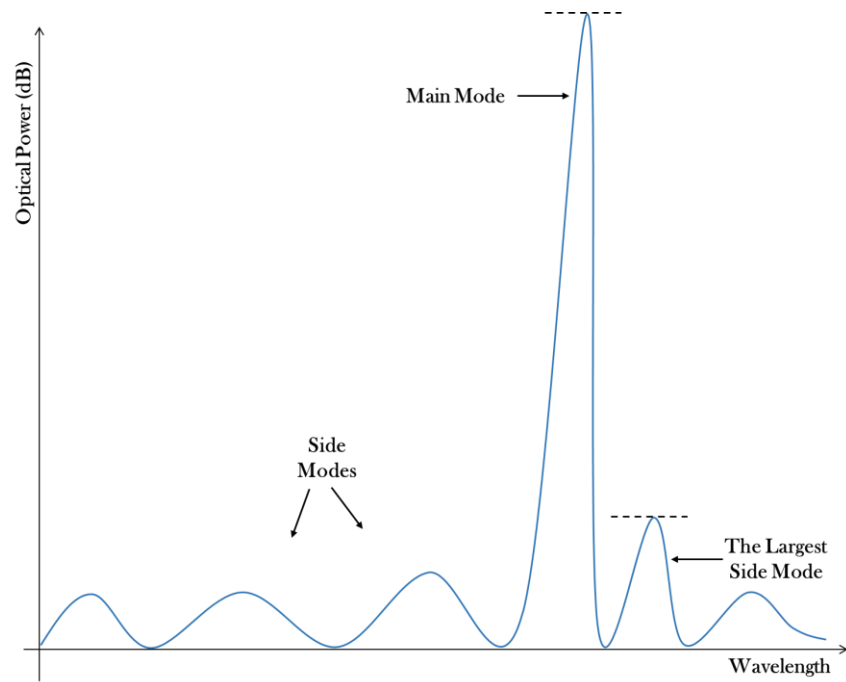
Figure 15 The side-mode suppression ratio (SMSR) is a measure of the ratio in the optical power in dB of the main laser mode to the largest higher-order mode. A high-quality CW laser has a large SMSR.

A value greater than $30 \, dB$ was achieved for SMSR by Yu and co-workers using a room temperature CW DFB-QC laser with a single-mode emission at wavelength $\lambda = 4.8 \, \mu m$ [94, 95]. The single-facet they obtained has a maximum output power $2.4 \, W$ at $T = 298 \, K$. A compact single-mode laser source, demonstrated by Lee *et al*, suits sensing application in the wavelength range $8.7 - 9.4 \, \mu m$ [96]. They fabricated on a chip an array of DFB-QCLs that provide very close emission wavelengths. Using this array makes the wavelength of their laser source continuously tunable between the two limits.

Broadband tuning of QCLs is achievable by using an external cavity and a frequency-selective element, typically a diffraction grating. This concept initiated the

development of EC-QCLs, which efficiently utilize the spectral gain of QC lasers. In this type, wavelength tuning does not require a temperature change, but involves a change of the grating angle instead. When the angle changes, the laser mode that meets the resonance condition changes. Therefore, different grating angles result in the amplification of different modes.

Hugi and co-workers constructed a room temperature external cavity QC laser tunable over $432\ cm^{-1}$ with $15\ mW$ average power [97]. The wavelength emission range is from $7.6$ to $11.4\ \mu m$, and the optical power of the peaks is around $1\ W$. Different designs of broadband QCLs and EC-QCLs, and a variety of ranges for wavelength tuning achieved by various types of IR QCL sources are reviewed and summarized by Yao *et al* [98].

Parallel to the development of QC lasers, a different type of semiconductor lasers that implement the cascading process was developed. These lasers, which are known as type-II cascade lasers, are also called "interband cascade lasers," or ICLs, because the transitions responsible for photon emission are in the active region between the valence and conduction bands [99, 100, 101]. Most implementations of ICLs design utilize a type-II band alignment in the active region. After electron-hole recombination, the electric voltage applied across the material accelerates the transfer of the electron from the valence band to the conduction band. Following this transfer, the type-II alignment in the active region allows the electron to re-tunnel efficiently to the conduction band [89]. Using the electron repeatedly is a characteristic that all types of cascade lasers have in common.

Applications of IR QCLs are found in a variety of fields including biomedical spectroscopy of clinically relevant molecular species [102], photonic systems for information technology [103], vibrational spectroscopy for atmospheric and chemical sensing [104, 105, 106], industrial monitoring and plasma diagnostics [38, 107], structural analysis of biomolecules in biology [108], and THz technology [109].

Compact and robust gas sensing portable systems based on QCLs are already being developed [110]. Areas of improvement for QCLs are mainly in increasing the optical power of the wavelength-emission peaks while maintaining a broad range of wavelength tuning at the same time.

### 2.2.4  Infrared Fiber Lasers

Guiding light in optical fibers is an idea that was successfully tested and applied by experimentalists in the l960s [111]. By the end of the century, material processing and fabrication methods have advanced and new types of pump sources have emerged. This opened the door for a wide variety of scientific, industrial, technological, and commercial applications of optical fibers and fiber-based laser sources [112, 113].

A fiber laser configuration, in principle, comprises a high-intensity pump laser, a single-mode or a multimode fiber, and two reflectors at the two ends of the fiber [114]. Figure 16 illustrates the basic configuration of a fiber laser [115]. The width of the core is typically in the same range of the wavelength of light propagating in the fiber, and the cladding area is normally larger than the core area. Therefore, the diameter of a single-

mode core area emitting in the IR can be few microns, and the total size of a mid-IR optical

fiber is almost the size of a human hair [116].
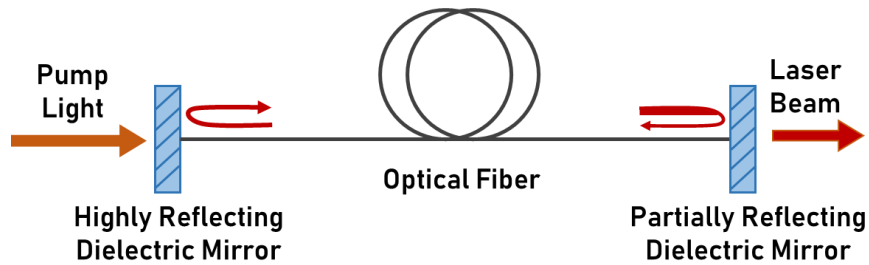


Figure 16 A schematic of the simplest configuration of a fiber laser. A single-mode fiber core doped with active ions forms the gain medium of the laser. The fiber resonator consists of a high reflectivity mirror to provide maximum feedback and a partially reflective mirror to transmit part of the light as an output signal (Reproduced with permission [115]).

Using a larger core diameter expands the mode area of the fiber but apparently

results in a multimode fiber, which is an undesired effect in many fiber applications [112].

However, it is possible to excite the fundamental mode by applying a mode matching

technique at the input of the fiber [117]. The higher order modes can be suppressed

through dissipation into guided modes [118], delocalization into the fiber cladding [119,

120], or other mode-filtering techniques [112, 121, 122].

In a single-mode fiber, the following condition is met [114]:

$$d \,.\, NA \ \leq \ 2.405 \, \frac{\lambda}{\pi}$$

where $d$ is the diameter of the core, $\lambda$ is the wavelength of light, and $NA$ is the numerical aperture of the fiber which can be written in terms of the refractive index $n$ and the acceptance angle of the fiber $\theta$ as:

$$NA = n\sin(\theta)$$

The maximum angle of acceptance allows incident light to be reflected totally inside the fiber. To couple the optical field efficiently into the single-mode core, a high brightness pump source is required. The brightness is said to be conserved if at any two points $A$ and $B$ along the beam path we have an equal product as follows [114]:

$$d_A \cdot (NA)_A = d_B \cdot (NA)_B$$

The primary factor that influenced the practical usage and popularity of fiber lasers is the double-clad configuration [123, 124]. Using this configuration allows for an output with higher intensity, which is an essential requirement for spectroscopic applications. A schematic is shown in Figure 17 for different types of optical fibers [116, 125].

Most of the early applications of optical fibers involved pumping light into the core of the fiber. However, lunching pump power into the cladding has spread widely since the development of double-clad fibers [126]. This is because the small size of the fiber core possesses a limit on the maximum peak intensity, which only allows for utilizing a restricted number of pump sources. On the other hand, the large area of the cladding enables the use of high-brightness pump sources, which in turns facilitates the output power of the fiber laser. As a consequence of the limited power allowed for core-pumping, the majority of the early developed IR fiber lasers operate in the CW regime, and pulsed fiber sources became popular years after [127, 128].
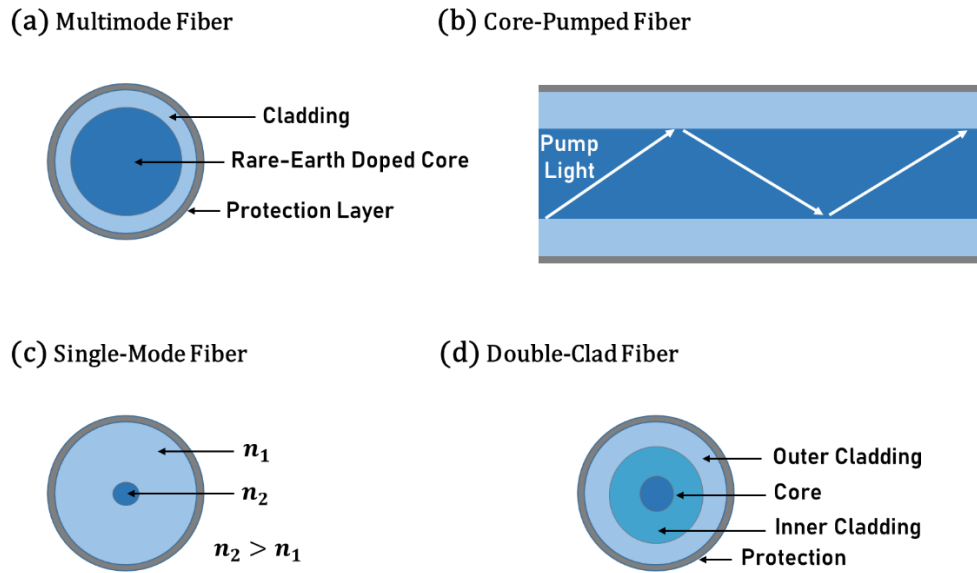
Figure 17 Schematics of different types of fibers and the core-pumping method. (a) A multimode fiber with a large core area. The protection layer, also called a fiber buffer, is an elastic material that prevents physical damage. (b) Core-pumping in optical fibers. (c) A single-mode fiber where the refractive index of the core $n_2$ is larger than that of the cladding $n_1$ to achieve total internal reflection, and the size of the core is in the same order of the wavelength ~ µm. (d) A double-clad fiber which enables cladding-pumping techniques (Reproduced after [116] and [125]).

In principle, the emission wavelength of the fiber laser is very much determined by the rare-earth ion used to dope the glass material, the transmission range allowed by the glass material, and the type of the laser used as the pump source. Using rare-earth ions as the active medium in fiber-based light sources was demonstrated for the first time in the early 1960s [129]. Snitzer reported an emission centered on $1.06 \, \mu m$ from a neodymium-doped barium crown glass in 1961 [111]. Since then, numerous materials and fabrication techniques have been developed.

Optical pumping in doped-fibers can be applied to the core or the cladding, as we discussed earlier. In general, the area of the cladding is at least two orders of magnitude larger than the area of the core [116, 130]. Therefore, cladding-pumping is more common nowadays as it can handle higher intensities. This feature has also led to the advent of several pumping techniques in optical fibers [64].

Temperature effects in optical fibers have been investigated as they contribute to the properties of the fiber and, consequently, of the laser beam emitted from the fiber laser [131, 132, 133]. Thermal effects arise in the case of double-clad fibers more than in single-clad fibers because the surface area in a single clad fiber is larger, which permits for effective heat dissipation [64, 134]. In IR fiber lasers operating with high intensities, heat dissipation is considered very seriously because it can have a negative impact on the quantum efficiency [135]. Yang *et al* conducted a numerical study of the thermal effects in a cladding-pumped fiber laser doped with $Tm^{3+}$ ions for different transitions of the pump [134]. They found an in-band pump transition that can reduce the heat generated in the process dramatically and provide a high quantum efficiency close to 95%.

Fiber lasers are available in the two regimes; CW and pulsed. When light runs in the fiber resonator freely, a CW output is obtained [136]. Whereas, light modulated using mode-locking or Q-switching results in a pulsed output of the fiber laser [137, 138, 139, 140] but still, the maximum allowed intensity is limited by the damage-threshold of the fiber. For this reason, literature shows that CW fiber lasers were dominant in the early years of fiber laser technology, and other types of lasers such as OPOs and crystalline lasers were dominant in the pulsed regime [64]. However, major advances in material

fabrication and high power fiber pumping schemes have contributed significantly to the various advances and developments in mid-IR pulsed fiber lasers in recent years [139, 141, 142, 143]. Luo *et al* demonstrated the first pulsed fiber laser tunable in the mid-IR region beyond $3.4\ \mu m$ [144]. Their system is based on a passively Q-switched fluoride fiber doped with erbium ions, and $Fe^{2+}:ZnSe$ crystal used as a saturable absorber. This pulsed fiber laser is tunable over the $3.4 - 3.7\ \mu m$ region with a maximum average output of $0.58\ W$.

The major difficulties facing the development of fiber-based applications in the mid-IR are the high fabrication costs and the large optical losses [64, 141]. As a result, many materials and several material processing techniques have been used to provide efficient gain media for fiber lasers.

The IR optical transparency of fiber materials is mainly determined by the band-gab size of the material and the cut-off of IR absorption [64, 145]. In the majority of available IR fibers, laser transitions occur in the 2-3 µm region [127]. For wavelengths larger than 3 µm, there is a limited number of materials that can be used as hosts of rare-earth ions, also known as lanthanide ions. As the host material; a glass or plastic, is doped with optically active ions, different chemical reactions happen yielding different oxidation states [64]. Undesired oxidation states can behave as impurities and impose unwanted optical effects. For this reason, a stable oxidation state is an essential requirement of the active ions used as dopants in fiber lasers [64, 127]. Consequently, this limits the number of active ions suitable for fiber-doping.

Lanthanide ions are commonly used for fibers in the visible and IR range. Doping fiber lasers with rare-earth ions, such as neodymium ion $Nd^{3+}$, ytterbium ion $Yb^{3+}$, erbium ion $Er^{3+}$, thulium ion $Tm^{3+}$, terbium ion $Tb^{3+}$, holmium ion $Ho^{3+}$, or dysprosium ion $Dy^{3+}$, gives special spectroscopic characteristics to the fiber material [64, 114]. In particular, doping with $Ho^{3+}$ and $Er^{3+}$ ions, and more recently $Tm^{3+}$ ions, allows for IR optical transitions that are significant for many applications.

Co-doping is another option in fiber fabrication; it can be defined as the process of using two different rare-earth ions to dope the host material of the fiber towards gaining access to specific laser transitions and improving the efficiency of the fiber laser [146, 147, 148, 149]. An example that describes the transitions in a co-doping situation is illustrated in Figure 18 below [141].
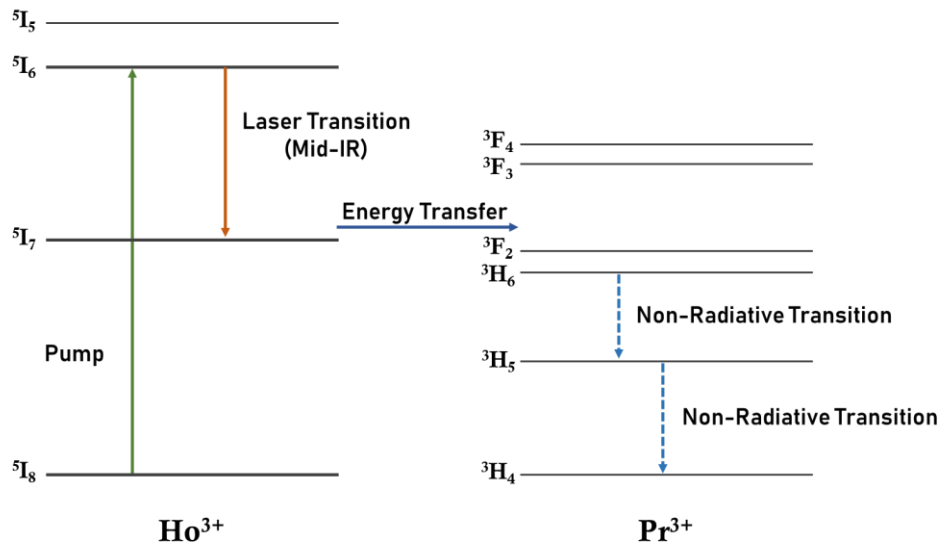
Figure 18 A simple version of the energy level diagram for co-doping with holmium and praseodymium rare-earth ions (Reproduced with permission from [141] copyright 2015 IEEE).

Robinson and Devor reported the emission of infrared light from erbium ions for the first time in 1967 [150]. In 1988, the first demonstration of an erbium-doped fiber laser was made by Brierley and France around 3 µm [151]. Progress in the field went on and these days we have high power fiber-based sources that can be tuned over broad spectral regions. Kulkarni *et al* demonstrated a mid-IR supercontinuum source tunable over the $1.9 - 4.5\ \mu m$ range based on a fluoride glass fiber and $Tm^{3+}$ doped fiber amplifier [152]. Photoluminescence emission over the $2 - 6\ \mu m$ range was observed from a mid-IR source based on $Pr^{3+}/Dy^{3+}$ co-doped glass fiber [149].

Thulium ($Tm^{3+}$) based fiber lasers can produce a laser beam with a very high power suitable for industrial applications [126, 153, 154]. Commercial applications of fiber oscillators in micromachining have a high demand for polarization-maintaining

fibers [112]. Furthermore, repetition rates between 1.7 and $10\ MHz$ are desirable for micromachining because this ensures that the plasma shielding effects at repetition rates $> 10\ MHz$ are avoided [155].

Fibers based on silica glass doped with rare-earth ions have quantum efficiencies in the range between 0.63 and 0.95, which depends on the ion, the wavelength of emission, and the pump source [114]. In silica fibers, the range of optical transparency is between $350\ nm$ and $2.4\ \mu m$ [112].

Recently, fiber materials based on fluoride glass doped with rare-earths have become available [127]. The development of this class of fibers with high purity and low losses enabled fiber laser operation to extend to the mid-IR [64]. Comparing to silica glass, which has an IR cut-off at around 2.2 µm, fluoride glass is transparent in the IR region up until 5 µm or even larger [156, 157]. A tunable mid-IR fluoride-glass based fiber laser doped with $Er^{3+}$ ion was demonstrated at room temperature with $1.45\ W$ of output power at $3.47\ \mu m$ [158]. Fiber laser systems based on rare-earth doped fluoride glasses are also cost-effective because traditional laser diodes that are commercially available can be used as pump sources in most of the systems [64, 159].

ZBLAN is so far the most widespread fluoride glass material for mid-IR fiber lasers, and it is a combination of five different heavy metal fluorides; $ZrF_4$, $BaF_2$, $LaF_3$, $AlF_3$, and $NaF$ [145, 157]. Many reasons are behind the popularity of the ZBLAN fiber material and the major one is the broad range of IR transmission, which extends from $0.2\ \mu m$ to $4.5\ \mu m$, with losses below $0.2\ dB/m$ [127, 141]. Furthermore, the optical properties of this fluoride glass can be manipulated by changing the concentration of each

element during the fabrication process or replacing a heavy metal fluoride element with another. For example, substituting the first element in ZBLAN by $HfF_4$ allows to push the IR cut-off from around $6 - 7 \, \mu m$ to around $7 - 8 \, \mu m$, and replacing the same element $ZrF_4$ by $ThF_4$ can extent IR transmission to around $8 - 9 \, \mu m$ [157].

Fiber materials made from chalcogenide glasses doped with rare-earth ions have a relatively high refractive index ~ 2.6 [127] and relatively low optical losses between 50 and 300 $dB/Km$ in the spectral region $2 - 9 \, \mu m$ [160]. The high refractive index results in large cross-sections of emission and absorption, which is a major benefit of using chalcogenide glasses besides their low toxicity and high nonlinearity [64, 161]. Chalcogenide glasses consist of different elements among which are the chalcogen elements $Te, Se$ and $S$ [162]. Sulfide glasses are among the most popular IR fiber materials of this type [64]. A mid-IR source based on selenide fiber doped with $Tb^{3+}$ ions is demonstrated by Sojka *et al* [163]. They recorded a maximum output power of $0.42 \, W$ from this source which is tunable in the $4.3 - 6 \, \mu m$ wavelength range.

A popular chalcogenide glass material is $Te - As - Se$, which can be fabricated with different combinations of each element giving rise to attractive optical properties in the IR region $2 - 18 \, \mu m$ [164]. Losses as low as $12 - 14 \, dB/Km$ were observed in arsenic-sulfide-glass fiber in the mid-IR range $3 - 5 \, \mu m$ [160]. Shiryaev *et al* reported optical losses in the $0.04 \, dB/m$ level for an optical fiber based on $Te_{25}As_{40}Se_{35}$ glass at a mid-IR wavelength $6.7 \, \mu m$ [165]. Sanghera and co-workers have achieved three orders of magnitude higher nonlinearities in chalcogenide-glass fibers comparing to that of silica-

glass fibers [162]. Large nonlinear coefficients are desirable in IR fiber materials since they allow for effective nonlinear conversion from near-IR to mid-IR and further.

Non-silica oxide glass-based fiber lasers utilizes tellurite, phosphate, and germanate non-silica oxide glasses. Advantages of using these glasses as host materials for rare-earth ions include high rare-earths solubility, large nonlinearity, and simplicity in design and handling [166]. The IR transmission windows are $0.2 - 2.5\ \mu m$ for silica, $0.2 - 4.3\ \mu m$ for phosphate, $0.3 - 4.0\ \mu m$ for germinate, and $0.4 - 5.0\ \mu m$ for tellurite [166]. Therefore, the emission of fiber lasers based on these materials can be extended to longer wavelengths in the mid-IR. The transmission spectra of different IR fiber materials can be seen in Figure 19 [116].

Tellurite glass has many key properties that make it suitable for mid-IR fiber lasers [167]. In addition to the aforesaid properties of non-silica oxide glasses, it provides low background losses, high efficiency of lasing, and a transparency range that reaches the $5\ \mu m$ region and beyond [146, 168]. Improvements in the fabrication of IR tellurite glasses have been made recently by using glass dehydration techniques and increasing the mode area of the fiber towards extending the nonlinear supercontinuum generation in tellurite-based fibers to longer mid-IR wavelengths [167]. Nguyen *et al* investigated the generation of a mid-IR supercontinuum from tellurite and chalcogenide fibers numerically [169]. Their simulation reveals the possibility of a highly coherent source tunable in the $0.78 - 8.3\ \mu m$ region.
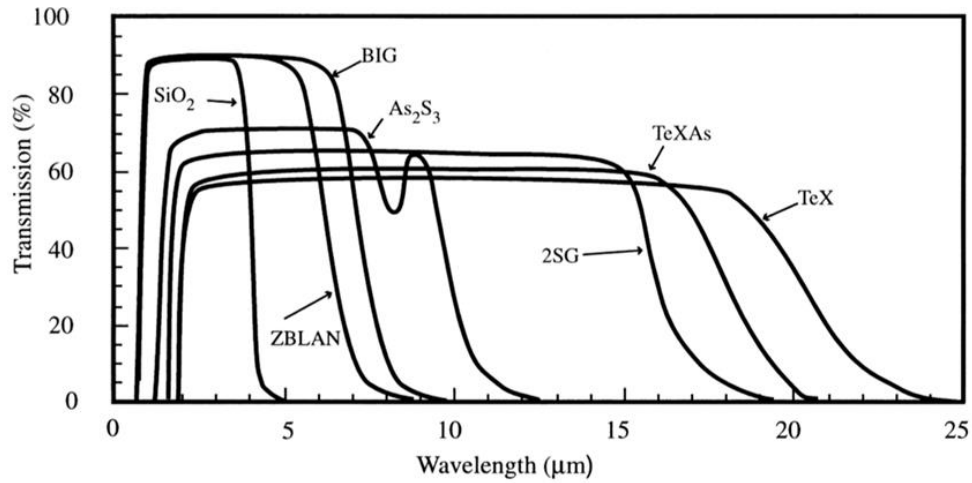
Figure 19 IR transmission windows of a number of glass materials that are commonly used in IR fibers. BIG and ZBLAN are fluoride glasses that combine different heavy-metal fluorides. 2SG represents glass materials based on selenium; it has the Sb, Se, Ga, Ge elements. TeX and TeXAs are tellurite glasses that combines Te, Se and $I_2$, and the later has As in addition (Reprinted with permission from [116] copyright 1999 Elsevier Science).

Ceramic-based fiber materials have several promising features [170]. Fibers based on crystalline materials and ceramics have the advantage that the cross-sections of emission and absorption are large, but also the disadvantage of relatively high optical losses [171, 172]. Ceramics are usually based on nano-crystallites; e.g. $Y_3Al_5O_{12}$ (YAG), $Y_2O_3$, $Sc_2O_3$, $YA_1O_3$(YAP), and $Lu_2O_3$, which allow for low fabrication costs and considerably high melting temperatures [64, 173]. Kang *et al* investigated a borosilicate glass-ceramic fiber material based on $NaYF_4$ nanocrystals and co-doped with $Er^{3+}$and $Ho^{3+}$ions [174]. They found that the co-doping allowed to extent the mid-IR emission from this ceramic-based material to the $2.6 - 2.95\ \mu m$ wavelength region, which promises high efficiency tunable mid-IR ceramic fiber lasers. Another ceramic material

suitable for mid-IR sources in the 2.7 $\mu m$ wavelength range is $Er{:}Y_2O_3$, which has been used in both CW [175] and pulsed [176] mid-IR ceramic lasers. Though, rare-earth doped glass fiber materials currently dominate the field of IR fiber lasers. Examples of rare-earth dope fiber-based mid-IR laser systems are given in Table 3.

Table 3 Parameters of Recent Examples of Mid-IR Sources based on Optical Fibers. Each Fiber System is Characterized by the Host Material of the Rare-Earth Ions, the Rare-Earth Ion Used for Doping, the Emission Wavelength of the Laser or the Tuning Range of Emission in case of Tunable Sources, and the Maximum Output Power.

| Fiber Host-Material | Rare-Earth Ion | Wavelength Tuning Range ($\mu m$) | $P_{out}$ ($Watt$) | Reference |
|---|---|---|---|---|
| $ZBLAN$ | $Ho^{3+} / Pr^{3+}$ | $2.825 - 2.975$ | 7.2 | [141] |
| $ZBLAN$ | $Tm^{3+}$ | $1.9 - 3.8$ | 21.8 | [177] |
| $ZBLAN$ | $Dy^{3+}$ | $2.8 - 3.4$ | 0.17 | [178] |
| $InF_3, ZrF_4$ | $Er^{3+}$ | $2.4 - 5.4$ | 0.214 | [179] |
| $ZBLAN$ | $Tm^{3+}$ | $1.9 - 4.5$ | 0.7 | [152] |
| $ZBLAN$ | $Ho^{3+}$ | $2.8 - 3.9$ | 0.411 | [180] |

Table 3 Continued.

| Fiber Host-Material | Rare-Earth Ion | Wavelength Tuning Range ($\mu m$) | $P_{out}$ ($Watt$) | Reference |
|---|---|---|---|---|
| $InF_3$ | $Ho^{3+}$ | 3.92 | 0.2 | [181] |
| $Ga_5Ge_{20}Sb_{10}S_{65}$ | $Pr^{3+}/Dy^{3+}$ | $2.2 - 5.5$ | – | [182] |
| $Ge - As - Ga - Se$ | $Pr^{3+}/Dy^{3+}$ | $2 - 6$ | – | [149] |
| $ZrF_4$ | $Er^{3+}$ | $3.4 - 3.7$ | 0.5837 | [144] |
| $InF_3$ | $Tm^{3+}$ | $1.96 - 4.6$ | 3 | [183] |
| $TeO_2 - BaF_2 - Y_2O_3$ | – | $0.947 - 3.934$ | 10.4 | [184] |
| $Ge - As - Ga - Se$ | $Tb^{3+}$ | $4.3 - 6$ | 0.42 | [163] |
| $ZrF_4$ | $Dy^{3+}$ | $3 - 3.3$ | 10.1 | [185] |
| $ZBLAN$ | $Er^{3+}$ | $4.012 - 4.198$ | 2.1 | [186] |

Other types of fiber lasers are the Raman fiber laser and fiber lasers based on combining beams from different sources. Because of the limited accessible lasing transitions in rare-earth doped materials, many regions are found in the IR spectrum where

fiber lasers based on rare-earth ions are absent [187, 188]. Therefore, new fiber laser technologies were developed to operate in those regions as an alternative to the rare-earth doped fiber laser technology.

Raman fiber lasers have the potential of power and wavelength scalability in the IR [177]. This kind of lasers rely on stimulated Raman scattering as the gain mechanism and utilizes the Raman gain spectrum of the glass material. In other words, pumping with a high power source results in a series of Raman-Stokes shifts which convert the wavelength of light to longer wavelengths. At the same time, an inhomogeneous broadening takes place in the glass material allowing for a broad emission over the longer wavelength region [189]. The spectra of Raman gain in different glasses can be seen in Figure 20 [187, 188].
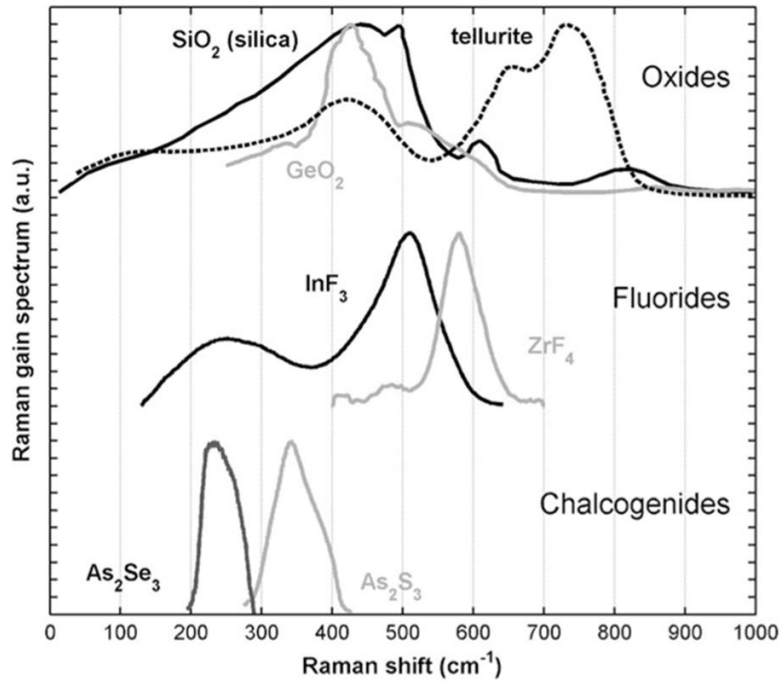
Figure 20 The Raman gain curves for glass materials commonly used in Raman fiber lasers (Reprinted with permission from [187] copyright 2015 The Optical Society, and [188] copyright 2017 Springer Nature).

Several Raman laser approaches have evolved in the last couple of decades. A $2.8\,m$ long fluoride glass fiber doped with erbium ions was used by Bernier and co-workers to pump a cascaded Raman cavity where the reflective elements are fiber Bragg gratings [190]. With this $3.005\,\mu m$ pump operating in a quasi-CW regime, they observed Stokes of first order at $3.34\,\mu m$ and Stokes of second order at $3.766\,\mu m$ with 8.3% efficiency. A simulation by Peng *et al* promised an output power of $0.269\,W$ at a wavelength $4.3\,\mu m$ in $As_2Se_3$ fiber using a mid-IR fiber laser pump source at $3.92\,\mu m$ with $1.5\,W$ of pump power [191]. The first realization of a $4.4\,\mu m$ Raman laser is reported by Gladyshev *et al* based on a hollow-core silica fiber filled with $H_2$ gas [192]. They

observed an output with a peak power close to $0.6\,kW$ and a conversion efficiency around 15%. The same research group demonstrated Raman generation at 2.9, 3.3, and 3.5 $\mu m$ in $H_2/D_2$ gas fiber, using the same $ns$ pulsed erbium-doped fiber laser as a pump, and achieved a maximum peak power of $0.9\,kW$ [193]. An ultrafast laser continuously tunable over the $2.1-2.7\,\mu m$ mid-IR region was implemented by Li and co-workers based on a germania-core fiber and a thulium-doped double clad fiber amplifier [194]. A very high peak power $\sim 9.5\,MW$ and a $113\,mW$ average power was obtained by Cao *et al* at wavelength 2.81 $\mu m$ from a Raman fiber laser filled with methane [195].

Techniques that combine laser beams from an array of several fiber lasers and/or amplifiers have evolved in recent years [159, 196]. The nonlinear effects in single-mode fibers, in which the optical field is highly confined and the interaction length is relatively long, allow for sufficiently high conversion efficiencies and low threshold levels. However, power scaling in optical fibers doped with rare-earth ions is not only limited by nonlinear effects but also by other factors. Those factors include the power saturation level, thermal effects, and the optical damage threshold [113]. Hence, combining laser beams from multiple sources has emerged recently as a new method that overcomes those limitations and promises potential power scaling [197, 198]. An example of a beam combination system is given in Figure 21.
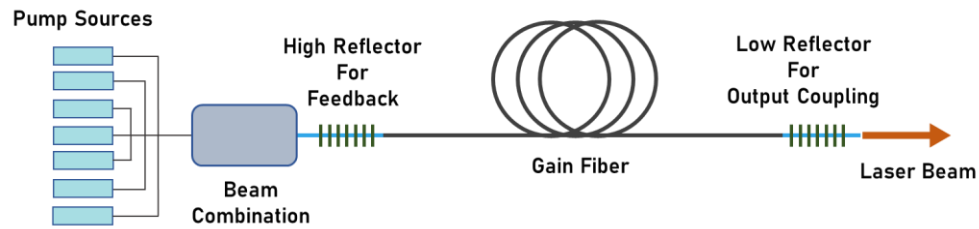
Figure 21 An example of a combination system used to add beams from multiple laser sources to provide higher optical intensities at longer IR wavelengths.

Beam combining is said to be coherent when the individual elements of the array of pump lasers operate in coherence with each other [198, 199]. Otherwise, the technique of beam combination is said to be an incoherent one [113, 200]. Coherent beam combination is more popular because it provides output beams of high intensities and high spectral purities, and allows for adjusting the shape of the wavefront [196]. It can be divided into two categories, active [201] and passive [202], depending on the applied combining technique. A passive combination is, in general, easier to achieve than an active combination [113]. However, different demonstrations of the later one have spread recently using, for example, phase modulators and feedback algorithms [203].

Coherent polarization beam combining (CPBC) is one of the most recent techniques in this area. Liu and co-workers employed the CPBC technique and achieved a beam combing efficiency of 90%, which yielded output powers in 570 to 1870 Watts range using different pump sources [204]. Lie *et al* obtained an output power of $14.1 \; kW$ by incoherent combination of seven beams from $2 \; kW$ lasers based on ytterbium-doped fibers [200]. They reported a large beam quality and estimated the transmission efficiency of this all-fiber system to be higher than 98.5%.

Gas fiber lasers are newly developed laser sources that overcome the difficulties with quantum and thermal limiting dynamics of doped fiber lasers and offer several advantages in the mid-IR region [205, 206]. This type of fiber lasers depends, in principle, on a hollow-core fiber filled with gas, and a suitable pump source. In addition to the advantage of guiding mid-IR light in optical fibers, it benefits from the well-established technology of fiber materials based on silicate [207]. The first demonstration of a mid-IR gas fiber laser was realized by Jones and co-workers by obtaining population inversion in a hollow-core fiber filled with $C_2H_2$ gas at $7\ torr$ [208]. The observed lasing at $3.12\ \mu m$ and $3.16\ \mu m$, and measured a pulse energy of $6\ nJ$ .

Progress in the field of gas fiber lasers continued with exploitation of the most recent pump sources and different filling gases to reach higher output powers and longer IR wavelengths. Cui *et al* achieved an output power of $82\ mW$ in a hollow-core silica fiber filled by $CO_2$ gas and pumped by a laser diode emitting at $2\ \mu m$ [209]. Their fiber laser operates in CW regime at room temperature and produces a mid-IR laser beam at $4.3\ \mu m$. A $1.1\ Watts$ of optical power was reported at $3.1\ \mu m$ by Xu and co-workers based on acetylene-filled fiber laser and a single-pass $Er^{3+}$ doped fiber amplifier [210]. They enhanced the optical gain in the fiber by using a hollow-core fiber of $31\ m$ length, and analyzed their results further towards understanding the molecular dynamics in fiber systems. A tunable pump source at $1.5\ \mu m$ was used by Zhou *et al* to implement a CW mid-IR hollow-core fiber laser filled by acetylene and tunable in the wavelength range $3.09 - 3.21\ \mu m$ with a maximum power close to $0.77\ W$ [211]. Mid-IR emission at $4.6\ \mu m$ based on $R$ and $P$ branch lasing transitions was observed by Aghbolagh and co-

workers [212]. They used a hollow-core fiber $45\ cm$ in length with a core size of $85\ \mu m$ filled with $N_2O$ gas. Gladyshev *et al* suggested that coupling the pump power into hollow-core fibers using bulk materials imposes some limitations on the laser system [207]. In their work, they use a new approach to demonstrate a Raman fiber laser based on a hollow-core silica fiber emitting at $4.42\ \mu m$ with a high average power. Pulsed all-fiber mid-IR laser systems based on hollow-core gas-filled fibers are also under scientific investigation [213].

The simplicity and design flexibility of tunable IR fiber lasers, comparing to other tunable mid-IR laser sources, promoted them to be used in robust and compact technological applications [143]. In contrast to solid state lasers, all-fiber tunable laser sources do not suffer from cavity misalignment effects, and the output power can be largely amplified with the available fiber amplifiers [114]. Diffraction effects in the laser beam are also limited if a single-mode fiber is used. All of those advantages make ultrafast fiber lasers more attractive for applications in telecommunication in comparison to ultrafast solid-state lasers [214, 215].

The generation of high power IR supercontinua over broad IR intervals is a major area where fiber lasers are significant [177, 216, 217]. Petersen and co-workers demonstrated a mid-IR supercontinuum spanning the $1.4 - 13.3\ \mu m$ region with a $2.29\ MW$ of coupled peak power in a chalcogenide fiber [54]. Additionally, broadband mid-IR optical frequency combs based on ultrafast fiber lasers, with high peak powers and short pulse widths, are powerful laser sources that open the door for more applications in spectroscopy and frequency metrology [2, 43, 218, 219, 220].

The need for IR fiber lasers with high-brightness and excellent beam quality have escalated in the last decade in parallel with the increasing accuracy and proficiency demands of IR fiber-laser applications. This comes as a result of the widespread applications of fiber lasers in various fields such as sensing [164, 221, 222], micromachining [112], communications [154], and medicine [129, 223]. For example, a widely tunable fiber-based source in the $2.2 - 5.5~\mu m$ IR region demonstrated by Ari and co-workers was used in gas sensing, and concentration measurements were obtained with detection sensitivities around $15~ppm$ and $300~ppm$ for $CO_2$ and $CH_4$, respectively [182]. According to this high demand of mid-IR fiber lasers and the variety of its applications, further improvements in material quality, fabrication methods, fiber configurations, spectral beam purity, and generated power are expected to follow [224, 225].

## 2.2.5 *Mid-IR Sources Based on Frequency Conversion Processes*

Mid-infrared laser-based sensors have been used as the major technological tool for gas analysis and monitoring in a large number of applications in industry, environmental sciences, medical diagnostic, agricultural emissions, and for security purposes [226]. As mentioned in Section 2.1, most of the organic and inorganic molecules exhibit strong absorption features in the mid-IR spectral region. This advantage of the IR region, as well as the increasing complexity of IR laser applications, both motivated the development of novel narrow-band infrared laser sources with broad wavelength tunability [227].

59

Mid-infrared quantum cascade lasers, discussed in Section 2.2.3, are versatile laser sources with a design flexibility that allows access to different regions of the IR from 3 to 25 $\mu m$, and to the terahertz region. However, the wavelength tuning ranges of early QCL devices were limited to a few wavenumbers [59, 98, 227]. Furthermore, the unavailability of IR laser sources with broad and continuous tunability in the region between 2.8 $\mu m$ and 4 $\mu m$, and the lack of active laser materials in that region, have both initiated the search and the development of new IR laser techniques and fabricated materials since the beginning of this century [227, 228].

One of the powerful approaches for the implementation of efficient tunable IR sources is using frequency conversion processes in nonlinear materials. If an electric field incident on a nonlinear material is strong enough, it induces a polarization in the material. In other words, an electric dipole moment results from the separation of charges in the material due to interacting with the strong input field, meaning that the material is polarized. The dipole oscillations in the dielectric material are responsible for the emission of optical waves at new frequencies [229, 230]. This mechanism, which employs available frequencies to produce new frequencies, is considered the key advantage of nonlinear processes. In the year 1961, Franken *et al* observed the first nonlinear effect in which the second harmonic of the incident light was generated in a dielectric medium using a ruby laser [231].

The nonlinear optical processes are mainly second harmonic generation (SHG), optical parametric generation (OPG), and sum- and difference-frequency generation, (SFG) and (DFG) respectively. All of these processes involve a conversion of the

frequency of the input light to a different frequency or frequencies at the output, as summarized in Table 4. In the case of difference and sum frequency mixing, two input beams, known as the pump and the signal beams, are required [227]. The generated light beam in the DFG and SFG processes is often called the idler. However, differences in the nomenclature are found in the literature for the input and output beams of nonlinear processes [60].
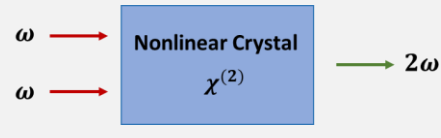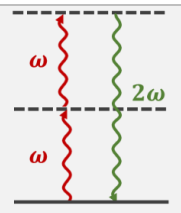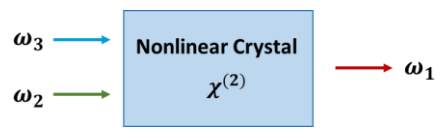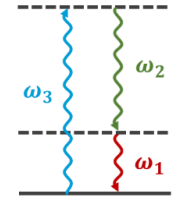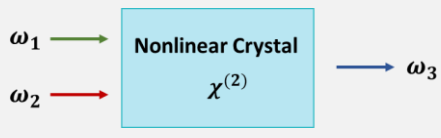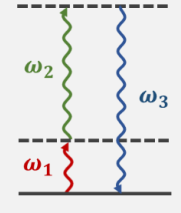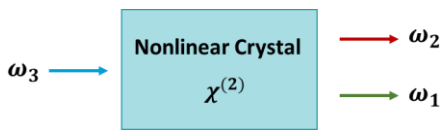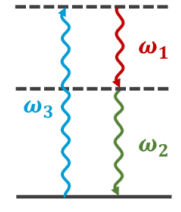
For all of the nonlinear processes in Table 4, the conservation of energy is met, where $\hbar$ is Plank's constant [232]:

$$\hbar\omega_1 + \hbar\omega_2 = \hbar\omega_3$$

The condition expressing momentum conservation provides the greatest emission in frequency conversion processes, and it can be achieved in practice through perfect phase-matching such that [233]:

$$k_1 + k_2 = k_3$$

Table 4 Frequency Conversion Processes in Second-Order Nonlinear Materials.

| Nonlinear Process | Schematic | Process Description | Energy Diagram |
|---|---|---|---|
| SHG | $\omega \longrightarrow$ Nonlinear Crystal $\chi^{(2)}$ $\omega \longrightarrow$ $\longrightarrow 2\omega$ | $\omega + \omega = 2\omega$ | |
| DFG | $\omega_3 \longrightarrow$ Nonlinear Crystal $\chi^{(2)}$ $\omega_2 \longrightarrow$ $\longrightarrow \omega_1$ | $\omega_3 - \omega_2 = \omega_1$ | |
| SFG | $\omega_1 \longrightarrow$ Nonlinear Crystal $\chi^{(2)}$ $\omega_2 \longrightarrow$ $\longrightarrow \omega_3$ | $\omega_1 + \omega_2 = \omega_3$ | |
| OPG | $\omega_3 \longrightarrow$ Nonlinear Crystal $\chi^{(2)}$ $\longrightarrow \omega_2$ $\longrightarrow \omega_1$ | $\omega_3 \rightarrow \omega_2 + \omega_1$ | |

In the simple case, the general mathematical expressions of nonlinear processes can be discussed by starting with the material polarization $\mathcal{P}$. The polarization is the dipole moment per unit volume, and it has a linear part $\mathcal{P}_{lin}$ and a nonlinear part $\mathcal{P}_{nonlin}$ as follows [234]:

$$\mathcal{P} = \mathcal{P}_{lin} + \mathcal{P}_{nonlin}$$

$$\mathcal{P}_{lin} = \varepsilon_o \chi^{(1)} E$$

$$\mathcal{P}_{nonlin} = \varepsilon_o \chi^{(2)} E^2 + \varepsilon_o \chi^{(3)} E^3 + \varepsilon_o \chi^{(4)} E^4 + \cdots$$

where $\varepsilon_o$ is the free space permittivity, $\chi^{(1)}$ is the linear susceptibility which depends on the refractive index $n$ of the material $\chi^{(1)} = n^2 - 1$, $E$ is the incident electric field, and $\chi^{(m)}$ are the nonlinear susceptibilities of order $m$, where $m$ is an integer greater than 1. Ignoring other higher order terms of the nonlinear polarization and using the tensor representation, the second-order polarization can be written in the following form [227]:

$$\mathcal{P}_i^{(2)} = \varepsilon_o \chi_{ijk}^{(2)} E_j E_k$$

where the indices $i, j$, and $k$ represent the axes of space. As can be seen, $\chi_{ijk}^{(m)}$ depends on the direction of propagation of the electric field $E$.

The description of nonlinear optical processes is often in terms of the nonlinear coefficients $d_{ijk}$, where $d_{ijk} = \frac{1}{2} \chi_{ijk}^{(2)}$ in the tensor notation [232]. In this manner, the second-order polarization can be written as:

$$\mathcal{P}^{(2)} = 2 \varepsilon_o d E E$$

Using this representation and the effective nonlinear coefficient $(d_{eff})$, one can explicitly arrive at the following expressions for the second-order nonlinear polarizations [235]:

$$\mathcal{P}_s^{(2)} = 2 \varepsilon_o d_{eff} E_p E_{id}^*$$

$$\mathcal{P}_{id}^{(2)} = 2 \varepsilon_o d_{eff} E_p E_s^*$$

$$\mathcal{P}_p^{(2)} = 2 \varepsilon_o d_{eff} E_s E_{id}$$

The tensor elements of the nonlinear coefficient $d_{ijk}$ can be found by first introducing an appropriate system of coordinates. A variety of coordinate systems are found in the literature because choosing the suitable one depends on the nonlinear material, which is used for the frequency conversion process, and in particular on the structural symmetries of the crystal [227]. There exit a large selection of nonlinear optical materials which can be used to access different regions of the IR. Table 5 shows examples of nonlinear materials with large IR transparency, as well as examples of the common values for their nonlinear coefficients within the corresponding range [227, 229, 236].

Table 5 Examples of Nonlinear Materials Used in Frequency Conversion Processes. The Selected Materials have Wide Transparency Windows in the IR.

| Nonlinear Material | Nonlinear Coefficient $d_{ij}$ $(pm\ V^{-1})$ | Transparency Range $(\mu m)$ | Ref. |
|---|---|---|---|
| Lithium Niobate ($LiNbO_3$) | $d_{33} = 19.5$ | $0.35 - 5.2$ | [237, 238, 239] |
| $\beta$-Barium Borate ($\beta$-$BaB_2O_4$) | $d_{22} = 2.2$ | $0.19 - 3.3$ | [238, 240, 241] |
| KTA ($KTiOAsO_4$) | $d_{31} = 3.27$ | $0.35 - 5.5$ | [242, 243, 244] |
| LT ($LiTaO_3$) | $d_{33} = 10.3$ | $0.28 - 5.5$ | [237] |

Table 5 Continued.

| Nonlinear Material | Nonlinear Coefficient $d_{ij}$ $(pm\ V^{-1})$ | Transparency Range $(\mu m)$ | Ref. |
|---|---|---|---|
| Silver Gallium Selenide $(AgGaSe_2)$ | $d_{36} = 39.5$ | $0.78 - 18$ | [237, 245] |
| BGS $(BaGa_4Se_7)$ | $d_{36} = 13$ | $2.6 - 10.4$ | [246, 247] |
| Zinc Germanium Phosphide $(ZnGeP_2)$ | $d_{36} = 73$ | $0.72 - 12.3$ | [248, 249] |
| $LiGaTe_2$ | $d_{31} = 10$ | $0.52 - 15$ | [250] |
| $CdSiP_2$ | $d_{36} = 92$ | $1 - 6.5$ | [62, 63, 251] |
| Gallium Arsenide $(GaAs)$ | $d_{14} = 94$ | $4.5 - 10.7$ | [252] |
| Gallium Phosphide $(GaP)$ | $d_{36} = 70$ | $0.57 - 12$ | [253] |
| Gallium Selenide $(GaSe)$ | $d_{22} = 54$ | $4.2 - 16$ | [254, 255] |

### *2.2.5.1 Parametric IR Sources*

Optical parametric light generation, along with difference-frequency generation and second harmonics, are the most significant nonlinear optical processes that depend on

frequency conversion [229, 231, 256]. The generation of parametric waves depends on nonlinear optical effects, which usually requires a large input field. This input electric field is referred to as the pump. The frequency of the pump must be within the transparency window of the material, which was indicated for different materials in Table 5 above, and the photon energy should be less than the energy gap to avoid resonance conditions [229]. It is worth mentioning here that only after the laser was invented, it was possible to observe nonlinear effects experimentally [257].

To describe a nonlinear effect associated with mixing three optical waves in a second-order nonlinear process, one starts with the following Maxwell's wave equation [60]:

$$\frac{\partial^2 E}{\partial z^2} = \mu\varepsilon \frac{\partial^2 E}{\partial t^2} + \mu \frac{\partial^2 \mathcal{P}^{(2)}}{\partial t^2}$$

where $E$ is the electric field of the incoming wave and $\mathcal{P}^{(2)}$ is the second order polarization. For a propagating wave along the z-axis with a complex field amplitude $E(z)$, the electric field can be written as:

$$E = \frac{1}{2}\left[ E(z)\, e^{i(kz-\omega t)} + c.c. \right]$$

and the total field of the idler, signal, and pump optical waves involved in the parametric process is [60]:

$$E = E_{id}(\omega_{id}) + E_s(\omega_s) + E_p(\omega_p)$$

where $\omega_{id}$, $\omega_s$, and $\omega_p$ are the frequencies of the idler, signal, and pump waves, respectively.

For simplicity, monochromatic uniform plane waves are assumed for the fields, and slowly varying amplitudes with respect to the wavelength are considered here [60, 227]. In that case, the following coupled-wave equations:

$$\frac{\partial E_{id}(z)}{\partial z} = i \, \kappa_{id} \, E_p(z) \, E_s^*(z) \, e^{i(\Delta k)z}$$

$$\frac{\partial E_s(z)}{\partial z} = i \, \kappa_s \, E_p(z) \, E_{id}^*(z) \, e^{i(\Delta k)z}$$

$$\frac{\partial E_p(z)}{\partial z} = i \, \kappa_p \, E_{id}(z) \, E_s(z) \, e^{-i(\Delta k)z}$$

are the solution for Maxwell's wave equation, which applies to any second-order nonlinear process involving three-wave-mixing in a dielectric material [60, 230]. In the equations, $\Delta k = k_p - k_s - k_{id}$ is the phase-mismatch, and $\kappa = \omega \, d_{eff} / n \, c$, where $\omega$ is the frequency of the optical wave, $c$ is the speed of light, $d_{eff}$ is the effective nonlinear coefficient of the material, and $n$ is the refractive index along the direction of propagation. It can be seen from the coupled-wave equations that the field amplitudes are coupled through $d_{eff}$ [60].

The parametric gain factor is expressed in terms of $d_{eff}$, the pump intensity $I_p$, and other parameters as follows, assuming no pump depletion [235]:

$$\Gamma^2 = \frac{2}{c^3 \, \varepsilon_o} \frac{d_{eff}^2 \, \omega_s \, \omega_{id}}{n_p \, n_s \, n_{id}} \, I_p$$

where the pump intensity here is equal to $I_p(z = 0)$, $d_{eff}$ is the nonlinear coefficient that the light experiences as it propagates through the crystal, $\varepsilon_o$ is the vacuum permittivity, $c$

is the speed of light, $\omega_s$ and $\omega_{id}$ are the frequencies of the signal and idler, respectively, and $n$ symbolizes the refractive index.

The key advantage of optical parametric generation is the broad spectral range of light emission [230, 257]. The process involves a break-up of the pump photon to signal and idler photons of lower energies while maintaining the conservation of energy, as illustrated in Figure 22 below [229]. Given that the number of pump photons is large and the ways they can be divided are different, the lower energy photons are emitted over a broad band [230].
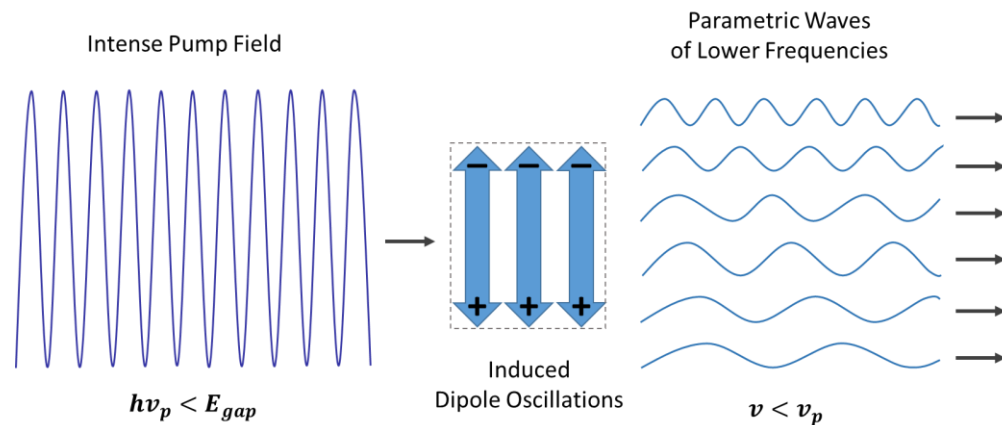


Figure 22 A simplified description of the parametric light generation process. An intense incident pump field induces dipole oscillations resulting in the generation of parametric waves at frequencies lower than the pump frequency. Possible combinations of generated parametric waves are shown for clarification.

Optical parametric amplification (OPA) is a primary step towards an efficient generation of coherent and directional optical parametric waves [229]. Optical amplification in parametric processes is achieved by phase-matching, which is considered

as the essential gain mechanism in nonlinear processes [230]. In the first phase-matching mechanism, the propagation of the parametric waves has to be synchronized with the propagation of the pump waves. This mechanism can be realized in a certain type of material known as the birefringent material [258]. In a typical material, waves of different frequencies travel at different velocities due to dispersion. However, wave propagation through a birefringent material depends on the propagation direction and the polarization [229]. Thus, when scientists and manufacturers implement OPA-based laser devices using birefringent crystals, they select the pump, polarization, propagation direction, and the material type such that the frequencies within a desired range are amplified [259].

The phase matching condition in a birefringent material is associated with the refractive index that the light experiences along the propagation direction [229]. By changing the direction of propagation in the crystal, a specific set of refractive indices becomes accessible. Therefore, the most common technique of birefringent-phase-matching (BPM) relies on this concept, and it is known as the angle-tuning technique [230]. In this technique, the rotation angle of the crystal is adjusted while keeping the propagation axis fixed. This allows for the amplification of desired frequencies over a broad continuous range. Tuning by changing the wavelength of one of the incident beams or changing the temperature of the crystal are other techniques for phase-matching, and are discussed briefly in the next section.

The most popular design for parametric devices is the optical parametric oscillator (OPO), which is shown in Figure 23. Placing the crystal in an oscillator allows for achieving higher output powers. The parametric oscillation process was demonstrated for

the first time in 1965 with a $LiNbO_3$ birefringent crystal [260]. In general, an OPO consists of three primary elements, a pump source, a nonlinear material, and an optical resonator [229]. To obtain an adequate optical growth in each pass through the material, high pump intensity is required. Adding to this, the material length is limited to few $mms$ or $cms$, and so is the gain in a single pass [60]. Thus, comparing to APGs and OPAs, OPOs use a resonator to overcome the single-pass gain limit and produce sufficient parametric growth.

On the other hand, the use of optical resonators always imposes unwanted effects of optical losses. In the parametric oscillation process, the losses take place in both directions whereas the nonlinear gain is only available in one direction [230]. This denotes that multiple passes through the nonlinear crystal are required before a certain threshold level can be reached. After surpassing the threshold, the OPO emits coherent light with broad tunability.
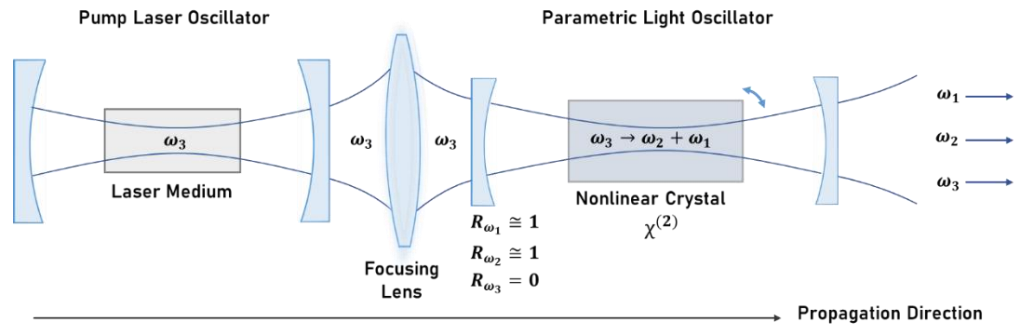


Figure 23 A Schematic of an optical parametric oscillator (OPO) based on a second-order nonlinear process. The pump light emitted from a strong laser source is focused and used to pump a nonlinear crystal of second-order susceptibility $\chi^{(2)}$. A frequency conversion process takes place in the crystal and parametric waves of lower frequencies are generated. The parametric waves oscillate until the threshold is reached and coherent light is emitted over an extended band.

A variation of OPO designs is available depending on the type on the pump source and the main purpose of the device or application [61]. Conversion efficiencies of 50% and higher are reported in the literature for OPO lasers of different configurations based on different nonlinear materials [260].

Quasi-phase-matching (QPM) in nonlinear crystals emerged as a substitute for birefringent phase-matching (BPM). This phase matching technique was proposed in 1962 [256], but it was not possible in practice until around 1992 after new technologies of material fabrication emerged [259, 261]. Now, the QPM technique dominates the field.

To understand the concept of QPM in nonlinear materials, let us recall the discussion of wave propagation in a dielectric medium from the previous section. As a result of dispersion, the relative phase of traveling waves slips by $180^o$ after a very short propagation distance (~ $\mu ms$) [229]. This distance is known as the "aperture length," or the "coherence length" $l_c$ [227]. After this distance, the amplitudes of generated waves decrease until reaching zero at a distance $2l_c$, as shown in part (a) of Figure 24 [60]. In other words, all of the generated waves become in-phase and then out-of-phase in a periodic manner, yielding zero intensity growth [229]. Thus, material fabrication was considered to override this obstacle and allow for intensity growth [262].

In QPM, a special technique is used to fabricate the nonlinear material such that the intensity will continue to build up after the $2l_c$ distance and integer multiples of it [229]. The intensity growth in QPM versus BPM can be seen in Figure 24 [227, 263]. This technique is known as "periodic poling" and is realized by applying high voltages ~ kV to ferroelectric materials [262].

71

In a periodically poled material, the dipole oscillations in each domain has a relative phase of $180^o$ with respect to the previous domain [229]. This means that the intensity will continue to build up in a quasi-continuous manner after traveling for a distance $\Lambda = 2l_c$, as in part (b) of Figure 24 [227, 263].
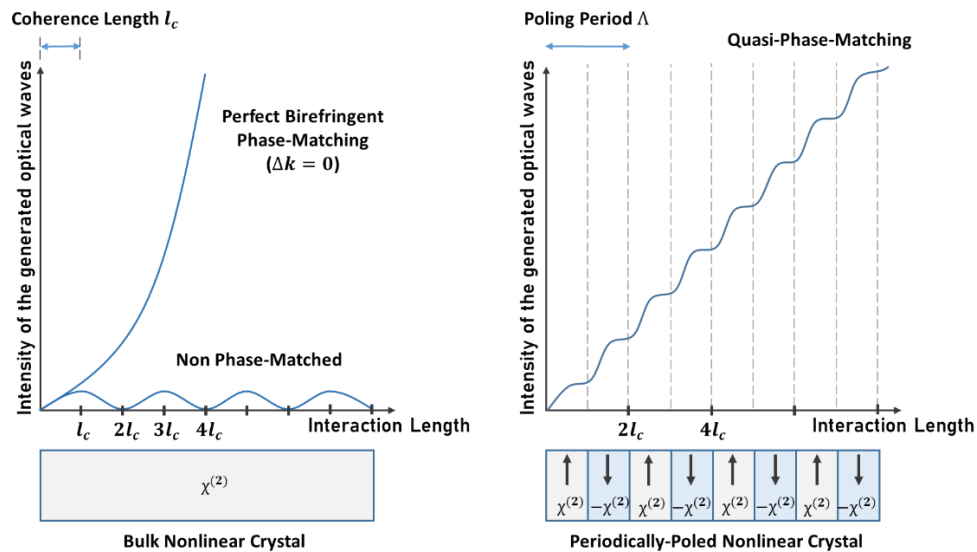


Figure 24 The growth of the idler intensity with quasi-phase-matching (QPM) comparing to birefringent-phase-matching (BPM) in a nonlinear material. The growth is the highest for perfect phase-matching ($\Delta k = 0$) in a birefringent material, but it is quasi-continuous in a periodically polled material with a poling period $\Lambda$. The arrows indicate the polarization direction, which is reversed after each $l_c$ in the periodically polled material.

Advances and breakthroughs in material sciences, design engineering, and poling technology have empowered the field of nonlinear optics by fabricating materials with broad transparencies and extreme capabilities [235]. Even though the BPM provides larger idler intensities, the use of QPM in periodically-structured nonlinear materials is preferred

for several reasons. First, the poling period $\Lambda$, which determines the transparency range of the material, can be freely chosen [229]. Second, the nonlinearity and the optical quality of semiconductors have improved dramatically. Thus, the material can be engineered as desired to operate in the deep mid-IR and far beyond [61, 236]. Third, the flexible selection of polarization and propagation direction allow access to the highest available nonlinearity in the material [230]. Furthermore, the QPM falls in the non-critical phase-matching category comparing to BPM, which can be critical or non-critical [227]. These differences are summarized in Table 6.

Table 6 A Comparison between Quasi-Phase-Matching and Birefringent-Phase-Matching in Nonlinear Optical Materials.

| Comparison Element | Quasi-Phase-Matching (QPM) | Birefringent-Phase-Matching (BPM) |
|---|---|---|
| Material | Periodically-poled (PP) | Birefringent |
| Intensity Growth | Quasi-continuous | Continuous |
| Material Characteristics | - Freely engineered<br>- Transparency window depends on the poling period | - Depends on material availability<br>- Transparency window is determined by the material |
| Nonlinear Coefficient | - Highest coefficient is accessible<br>- Polarization and propagation direction are flexible | - The highest accessible coefficient is limited<br>- Birefringence requires selecting a particular polarization and propagation direction |
| Phase-Matching Condition | Non-critical | Could be critical or non-critical |

The optical damage threshold is a crucial parameter of the nonlinear crystal, and it must be considered when operating an OPO system because of the high intensity requirement. Other important parameters to consider are the highest accessible nonlinear coefficient, transparency range, optical quality, scattering and absorption losses, thermal stability, and the phase-matching method [207]. In many OPOs, the only limiting factor for the tuning range is the optical transparency of the nonlinear crystal [219].

The last couple of decades witnessed significant improvement of optical components and nonlinear materials, which enhanced the performance of OPOs and extended their operation range to the mid-IR. Furthermore, the birth of new techniques of spectroscopy allowed for more applications of OPOs in various fields. Some of the new developments of mid-IR OPO sources and their applications in spectroscopy and sensing are summarized by Peng [236].

### 2.2.5.2 IR Sources Based on Difference Frequency Generation

Difference frequency generation (DFG) is one of the most prevalent nonlinear processes for the generation of tunable mid-IR radiation. The process involves mixing two laser beams; the pump and the signal, in a nonlinear material to produce an idler beam at a frequency equal to their difference. One of the very first spectroscopic applications based on DFG is the work established by Pine around 1974 [264]. In his work, he mixed two beams; one from $Ar^+$ laser and one from a tunable cw dye laser, in a $LiNbO_3$ crystal, and he used the output beam for high-resolution spectrometry in the $2.2 - 2.4\ \mu m$ region.

A major advantage of DFG systems is the ability to transfer the tunability of available laser sources to new regions within the infrared where conventional laser sources are absent [63]. For example, wavelengths between 5.9 and 6.6 $\mu m$ in the mid-IR are of interest for medical surgery because this region is suitable for the protein [265]. It has large water absorption which minimizes the side effects of laser-based human surgery. Hence, many DFG-and OPO-based laser systems have been developed in accordance with specific necessities.

A careful selection of the pump laser, signal laser, and nonlinear material is necessary so that the lasers are matched with the suitable nonlinear crystal [227]. When the material is considered, it is desired to use the highest possible nonlinear coefficient available at the wavelength of interest. Critical material parameters are the damage threshold of the crystal and the range of transparency. The output power, room-temperature operation, and wavelength tunability come into play when the laser sources are considered. In addition to that, it is significant to follow with the newly available nonlinear materials and laser types, as they allow for new combinations in the field of implementing frequency-conversion based laser sources [227, 229]. A selected set of recently reported mid-IR DFG systems are presented in Table 7, and the type of phase-matching used in each system is also included.

Table 7 Relevant Parameters of Recently Reported Mid-IR DFG Systems. Each DFG System is Characterized by the Nonlinear Material, the Wavelength of the Pump $\lambda_p$, the Wavelength of the Signal $\lambda_s$, the Wavelength of the Generated Idler Beam $\lambda_{id}$, and the Phase-Matching Type Used in the Difference Frequency Mixing Process.

| Nonlinear Material | $\lambda_p$ $(nm)$ | $\lambda_s$ $(nm)$ | $\lambda_{id}$ $(nm)$ | Phase Matching | Ref. |
|---|---|---|---|---|---|
| OP-$GaAs$ | 1950 | 2500 | $6700 - 12700$ | QPM | [266] |
| OP-$GaP$ | 1064 | $1609 - 1637$ | $3040 - 3132$ | QPM | [267] |
| $AgGaS_2$ | 1300 | $1670 - 2700$ | $2500 - 5890$ | QPM | [268] |
| OP-$GaP$ | 1064 | $1723 - 1827$ | $2548 - 2781$ | QPM | [269] |
| $BaGa_4Se_7$ | 1064 | $1360 - 1600$ | $3360 - 4270$ | BPM | [270] |

For optical gain to be realized in any nonlinear frequency conversion process, phase matching is a key issue and it has to be carefully considered, as previously mentioned. There are two types of birefringent phase matching; type I and type II, and there are two types of birefringent nonlinear materials where this phase matching can be achieved, positive and negative birefringent crystals [229].

Let us take an example of a type I phase matching technique in a DFG process using a positive birefringent material [227]. In collinear wave propagation, $|k| = \frac{nc}{\lambda}$ can be used for the wave-vectors [271], so we get:

$$\frac{n_{DFG}}{\lambda_{DFG}} = \frac{n_e(\omega_{id}, \Theta)}{\lambda_{id}} = \frac{n_o(\omega_p)}{\lambda_p} - \frac{n_e(\omega_s, \Theta)}{\lambda_s}$$

Using this expression and the following widely used equation of the ellipse, which describes the refractive index of uniaxial crystals:

$$\frac{1}{n^2(\Theta)} = \frac{\sin^2(\Theta)}{n_e^2} + \frac{\cos^2(\Theta)}{n_o^2}$$

one arrives at:

$$\frac{n_o(\omega_p)}{\lambda_p} - \frac{n_e(\omega_s, \Theta)}{\lambda_s} = \frac{1}{\lambda_i} \sqrt{\left( \frac{\sin^2(\Theta_{PM})}{[n_e(\omega_{id})]^2} + \frac{\cos^2(\Theta_{PM})}{[n_o(\omega_{id})]^2} \right)^{-1}}$$

where $\lambda_p$, $\lambda_s$, and $\lambda_{id}$ are the wavelengths of the pump, signal, and idler beams; respectively, $\Theta_{PM}$ is the phase-matching angle, $\Theta$ is the angle that the propagation path of the input beams make with the optical axis of the nonlinear crystal, $n_o$ is the ordinary refractive index of the perpendicularly-polarized light, and $n_e$ is the extraordinary refractive index defined as the refractive index of light with a polarization parallel to the optical axis.

The dependence of the refractive index on the angle of incidence $\Theta$, the parameters of the crystal, and the wavelengths of the incident beams, $\lambda_p$ and $\lambda_s$, provides several criterions for phase-matching realization [227]. This includes angle tuning, temperature tuning, and incident-wavelength tuning. The angle tuning technique is applied by means

of rotating the nonlinear crystal and searching for the angle at which the highest output power can be measured. Obtaining the highest power measurement for the idler beam indicates that the phase matching condition is satisfied. Adjusting the temperature of the crystal is a different approach to fulfill the phase matching condition. Another possible way is to use a tunable laser source as the pump or the signal laser in the DFG system. The mentioned mechanisms are convenient since synchronization is not required for this phase matching technique.

When the conversion efficiency losses are considered, phase matching conditions are also characterized by being critical or non-critical. Phase matching conditions which are highly sensitive such that any small deviation results in large efficiency losses, are known as critical conditions. On the other hand, if a high conversion efficiency is achievable even when there is a small mismatch, the phase matching condition is called a non-critical [227].

The conversion efficiency is the ratio of output intensity or power, after the conversion, to the incident one. In a difference frequency conversion process, there are two incident beams and therefore two efficiencies, $\eta_p = \frac{P_{out}}{P_p} = \frac{I_{out}}{I_p}$ for the pump and $\eta_s = \frac{P_{out}}{P_s} = \frac{I_{out}}{I_s}$ for the signal, where equal cross-sectional beam areas were assumed. For a DFG process with a perfect BPM, the efficiencies of conversion can be calculated using [227]:

$$\eta_p = \frac{2}{c^3 \, \varepsilon_o} \frac{\omega_{id}^2 \, d_{eff}^2 \, L^2}{n_p \, n_s \, n_{id}} I_s$$

$$\eta_s = \frac{2}{c^3\,\varepsilon_o}\,\frac{\omega_{id}^2\,d_{eff}^2\,L^2}{n_p\,n_s\,n_{id}}\,I_p$$

where $\eta_p$ is the conversion efficiency of the pump, $\eta_s$ is the conversion efficiency of the signal, $I_p$ is the intensity of the pump, $I_s$ is the intensity of the signal, $d_{eff}$ is the effective nonlinear coefficient, $\omega_{id}$ is the frequency of the idler, $\varepsilon_o$ is the permittivity of free space, $c$ is the speed of light, $n$ is the refractive index, and $L$ is the interaction length within the nonlinear crystal. In BPM, the coefficient $d_{eff}$ is determined by the orientation of the nonlinear crystal, the polarization direction, and apparently by the propagation direction within the crystal. If the phase matching is not perfect, i.e., if $\Delta k \neq 0$, an extra term of $sinc^2(\frac{\Delta k\,L}{2})$ appears in each expression.

The conversion efficiencies of the pump and the signal in the case of QPM can be found similarly [227]:

$$\left(\eta_p\right)_{qpm} = \frac{2}{c^3\,\varepsilon_o}\,\frac{\omega_{id}^2\,L^2}{n_p\,n_s\,n_{id}}\left(\frac{d_{qpm}}{m}\right)^2 I_s$$

$$\left(\eta_s\right)_{qpm} = \frac{2}{c^3\,\varepsilon_o}\,\frac{\omega_{id}^2\,L^2}{n_p\,n_s\,n_{id}}\left(\frac{d_{qpm}}{m}\right)^2 I_p$$

where $d_{qpm}$ is the QPM effective coefficient, and $m$ is the number of travelled coherence lengths $l_c$ before the threshold level is reached, and it is called the order of QPM.

Assuming equal Gaussian spot sizes for the three optical beams and no reduction in the pump intensity, the intensity generated from the DFG process can be written as follows:

$$\left(I_{DFG}\right)_{BPM} = \frac{2}{c^3\,\varepsilon_o}\,\frac{\omega_{id}^2\,L^2}{n_p\,n_s\,n_{id}}\,d_{eff}^2\,I_p\,I_s$$

$$(I_{DFG})_{QPM} = \frac{2}{c^3 \, \varepsilon_o} \frac{\omega_{id}^2 \, L^2}{n_p \, n_s \, n_{id}} \left(\frac{d_{qpm}}{m}\right)^2 I_p \, I_s$$

where $(I_{DFG})_{BPM}$ is the generated intensity in a perfect BPM process, and $(I_{DFG})_{QPM}$ is the generated intensity in a QPM process. It can be seen from the expressions that the output intensity can be increased by increasing the interaction length $L$ and improving the conversion efficiency $\eta$ [227]. Using a high power pump source is also an option for improving the idler intensity. However, it has unwanted effects from possible OPG and OPA processes such as linewidth broadening [272, 273].

Nonlinear processes in lasers enable many features that make them attractive for a variety of applications. The temporal and spectral characteristics of the output beam can be selected in advance by choosing the appropriate pump or pump/signal laser sources [60, 230]. For example, pulsed and ultrafast OPO laser sources have been implemented based on nanosecond and femtosecond pump lasers [61]. In addition, a wide tuning range is possible since it is dependent on the phase-matching condition which can be reached with different tuning techniques [246]. Thus, combing the suitable nonlinear crystal with the suitable pump source allows for coherent light emission within spectral regions that are inaccessible to traditional lasers, as we discussed earlier. These advantages of OPO, DFG, and other frequency-conversion-based lasers have opened the door for potential IR and THz applications and for practical compact laser designs [61, 235, 236, 274].

In a very recent work by Kolker and his colleagues, a broadly-tunable mid-IR OPO source based on $BaGa_4Se_7$ nonlinear crystal was demonstrated [246]. The $BaGa_4Se_7$ crystal they used has a large transparency range in the IR, which is over the whole region

from 0.47 $\mu m$ to 18 $\mu m$. They employed an angle-tuning technique as a phase-matching mechanism, and achieved a wide wavelength tunability for the generated idler beam that extends from 2.6 $\mu m$ to 10.4 $\mu m$. In summary, tunable IR laser sources based on frequency conversion in nonlinear materials offer a powerful alternative to conventional laser sources, which have a restricted spectral coverage. Table 8 summarizes the main features of the two categories [229, 235], and the next section includes examples of broadband IR sources based on DFG processes in nonlinear crystals [27, 44, 218].

Table 8 A Comparison between the Laser Sources based on Frequency Conversion Processes (FCP) in Nonlinear Materials and Traditional Laser Sources based on Stimulated Emission in Gain Media.

| Comparison Element | Traditional Lasers | FCP Lasers |
|---|---|---|
| Mechanism | Stimulated emission | Frequency conversion via dipole oscillations |
| Material | Gain medium | Nonlinear crystal |
| Output Wavelength | - Determined by the structure of the atomic or molecular energy levels<br>- Depends on the laser material | - Determined by the conservation of energy and momentum<br>- Depends on the wavelengths of the pump and the signal |
| Wavelength Tunability | Limited to $300 - 400\ nm$ at best | Broad and can extend to several $\mu m$s |

## 2.2.6 Optical Frequency Combs

Optical frequency combs were implemented in the late 1990s and have since been considered one of the most precise tools for time and frequency measurements [43, 44, 219, 275]. Using frequency comb laser sources in IR spectroscopic systems adds enhanced capabilities in terms of improving sensitivity, precision, and recording time. Such broadband sources also improve spectral bandwidth of the instrument [3, 5, 9, 19, 27, 41].

The optical frequency comb arises from well-stabilized sequence of short (femtosecond) coherent laser pulses temporarily separated by a time interval equal to the round-trip time ($T_R$) inside the laser cavity [219, 276]. The time $T_R$ is the required time for a laser pulse to circulate once through the cavity, and it is given as follows:

$$T_R = \frac{2\,L}{v_g}$$

where $v_g$ is the group velocity of the light in the cavity, which is defined by the intra-cavity dispersion, and $L$ is the length of the cavity [43].

An ultrashort laser pulse results in a broad spectrum in the frequency domain, as can be seen in part (a) of Figure 25. The shorter the laser pulse, the wider the spectrum. This is because the spectral width is inversely proportional to the width of the pulse envelop. However, when we have a train of ultrashort pulses, the regular spikes with equal intervals between them produce a spectrum with the shape of a comb, as in part (b) of Figure 25.
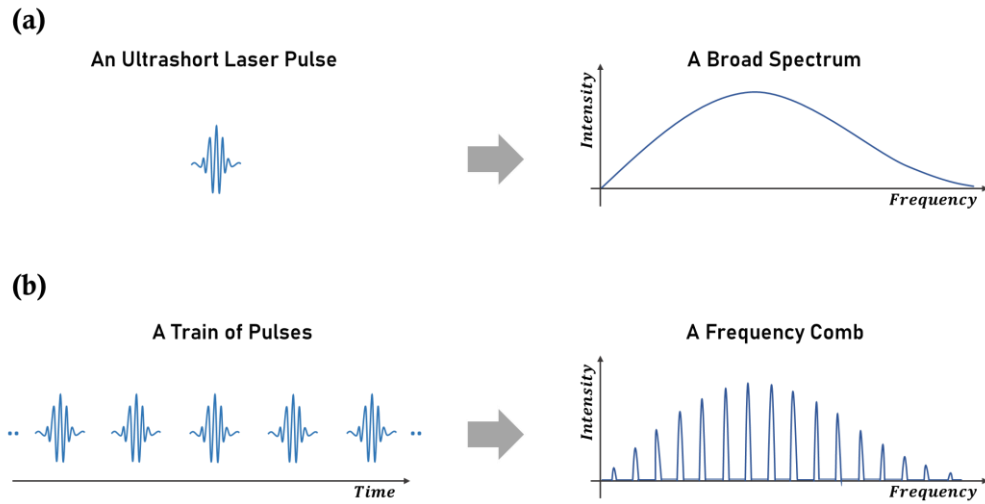
Figure 25 (a) The broad spectrum of an ultrashort laser pulse, and (b) the comb spectrum of a train of coherent stabilized lasers pulses.

The mode spacing of the comb is given by the repetition rate of the laser $f_r$, which is the inverse of the cavity round-trip time:

$$f_r = \frac{1}{T_R} = \frac{v_g}{2\,L}$$

The velocity of the carrier wave of the pulse is called the phase velocity $v_p$ and it is different from $v_g$ inside the laser cavity. The difference between the group velocity of the envelop and the phase velocity of the carrier wave results in a phase shift of the carrier with respect to the pulse envelop. This phase shift appears in the out-coupled electric field of the pulses. Taking a Fourier transform, this shift, which is shown in Figure 26, leads to an offset of the frequency comb due to the carrier-envelop offset frequency $f_0$. The frequencies of the comb modes are given by the following equation [44, 276]:

$$f_n = n\,f_r + f_0$$

In this expression, $n$ is a very large integer ( $10^5 - 10^6$ ), $f_r$ is the repetition rate of the frequency comb as defined previously, and $f_0$ is the carrier-envelop offset frequency which is connected to the phase shift $\Delta\varphi$ by the relation:

$$f_0 = \frac{1}{2\pi} f_r \Delta\varphi$$

**(a)**



**(b)**
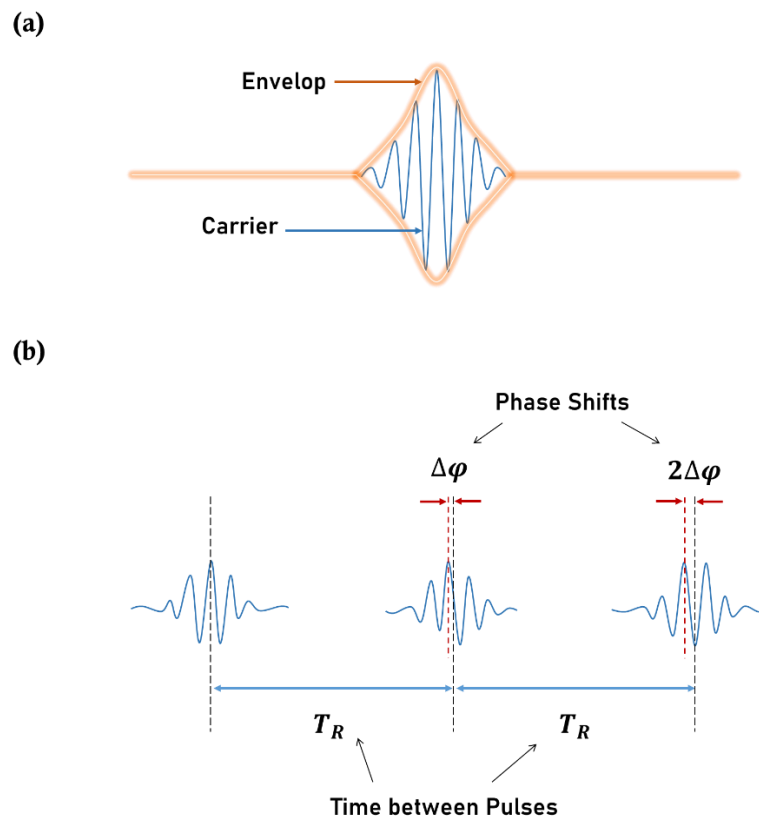


Figure 26 (a) The carrier and the envelop of a single laser pulse. (b) The phase difference between adjacent pulses due to the shift of the carrier with respect to the envelope after each round trip.

The short pulses oscillating in the laser cavity experiences dispersion, as it has been explained earlier, which is responsible for the shift $\Delta\varphi$ between adjacent emitted pulses. In each round trip, the pulse is out-coupled through the partially reflective mirror once, as illustrated in Figure 27. Only the modulo $2\pi$ part contributes to the pulse-to-pulse phase change. As a result, the carrier-envelop phase shift can be written as [219, 276]:

$$\Delta\varphi = \left(\frac{1}{v_g} - \frac{1}{v_p}\right) L\, \omega_c \, mod(2\pi)$$

where $\omega_c$ is the frequency of the carrier, $v_p$ and $v_g$ are the phase and group velocities, respectively, and $L$ is the length of the laser cavity.



**Pulsed Laser Oscillator**

**Output Laser Pulses**

**Laser Medium**

**Partially Reflective Mirror**
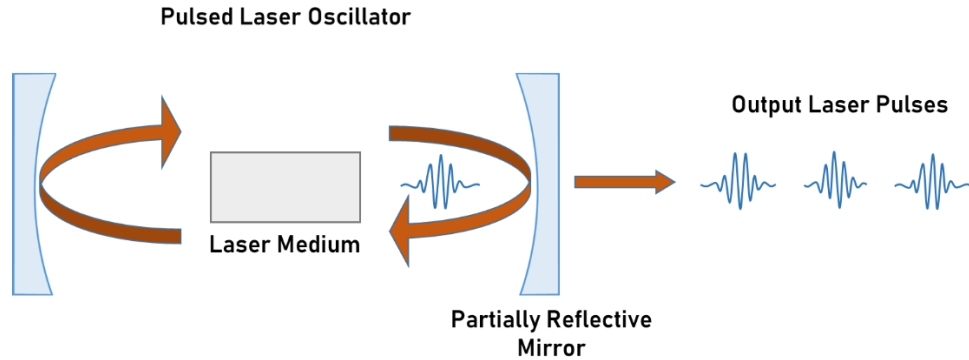
Figure 27 An illustration of the laser oscillator showing that a pulse is out-coupled after each round trip inside the cavity.

To understand the equation that describes the frequencies of the comb modes and its relation to the phase shift between pulses, let us consider the electric field of a single pulse at a fixed position in space, which can be written as:

$$E_1(t) = \hat{E}(t)\, e^{i(\omega_c t + \varphi_o)}$$

85

Then, for a pulse train, the electric filed can be written as:

$$E(t) = \sum_n \hat{E}(t - n\,T_R)\ e^{i(\omega_c t - n\omega_c T_R + n\,\Delta\varphi + \varphi_o)}$$

$$= \sum_n \hat{E}(t - n\,T_R)\ e^{i(\omega_c t + n(\Delta\varphi - \omega_c T_R) + \varphi_o)}$$

where $\hat{E}(t)$ is the envelop, $\varphi_o$ is the overall phase shift, $\omega_c$ is the frequency of the carrier, and $T_R$ is the round-trip time [277]. Taking the Fourier transform, we arrive at:

$$E(\omega) = \int \sum_n \hat{E}(t - n\,T_R)\ e^{i(\omega_c t + n(\Delta\varphi - \omega_c T_R) + \varphi_o)}\ e^{-i\omega t}\ dt$$

$$= \sum_n e^{i[n(\Delta\varphi - \omega_c T_R) + \varphi_o]} \int \hat{E}(t - n\,T_R)\,e^{-i(\omega - \omega_c)t}\ dt$$

Then, use $\tilde{E}(\omega) = \int \hat{E}(t)\,e^{-i\omega t}\ dt$ and recall the following formula:

$$\int f(x - a)\,e^{-i\beta x}\ dx = e^{-i\beta a}\int f(x)\,e^{-i\beta x}\ dx$$

to arrive at the following result [277]:

$$E(\omega) = \sum_n e^{i[n(\Delta\varphi - \omega_c T_R) + \varphi_o]}\ e^{-in(\omega - \omega_c)T_R}\ \tilde{E}(\omega - \omega_c)$$

$$= e^{i\varphi_o} \sum_n e^{in(\Delta\varphi - \omega T_R)}\ \tilde{E}(\omega - \omega_c)$$

There is an exponential term in the sum, hence coherent addition is obtained when the phases of two adjacent pulses; $n$ and $n + 1$, are different by $2\pi$ or a multiple of $2\pi$. This corresponds to $\Delta\varphi - \omega T_R = 2m\pi$, which can be rewritten as:

$$\omega_m = \frac{1}{T_R}\,(\Delta\varphi - 2m\pi)$$

Using $f_r = \frac{1}{T_R}$ and $f_0 = \frac{1}{2\pi} f_r \, \Delta\varphi$, we get the result that forms the basis of frequency combs $f_m = m \, f_r + f_0$, which is also illustrated in Figure 28.
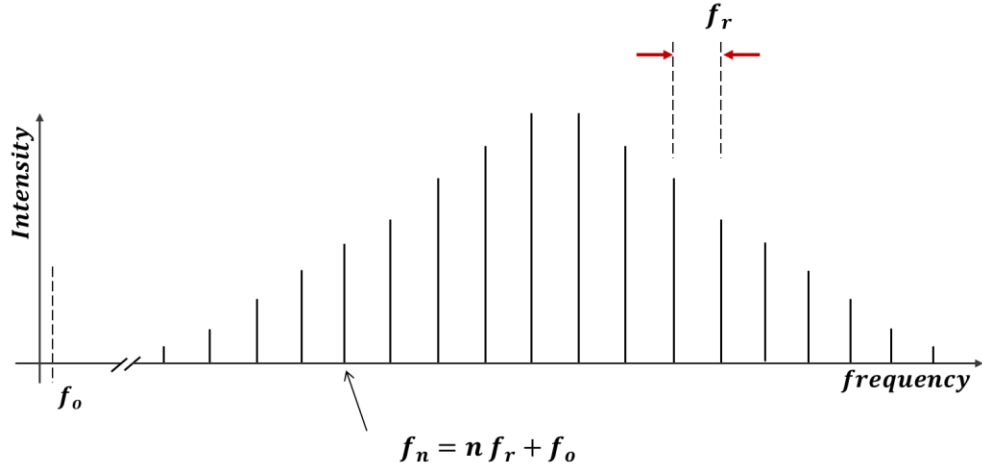


Figure 28 Characteristics of an optical frequency comb. The repetition rate $f_r$ is equal to the distance between two adjacent comb lines and $f_o$ is the carrier-envelop offset frequency resulting from intra-cavity dispersion. The frequencies $f_o$ and $f_r$ of the generated comb are determined by the mode-locked laser cavity.

The stabilization and control of $f_r$ and $f_0$ is required in many applications that depend on precision laser measurements [43, 44, 218, 276]. Both $f_o$ and $f_r$ , which characterizes a given optical frequency comb, are in the radio-frequency (RF) domain. Measuring the repetition rate of the comb can be simply achieved by using a fast photodiode, which detects the train of laser pulses emitted by the comb source. However, measuring the intensity does not reveal the phase relationship and thus an interferometric approach is often used to determine the offset frequency $f_o$.

An $f$-to-$2f$ heterodyne beating is a common technique that can be applied to measure $f_o$ if the spectrum of the frequency comb spans an octave. In other words, if the frequency of a comb line at the high-frequency edge of the comb is larger than the frequency of a comb line at the low-frequency edge of the comb by a factor of 2, then a beat signal can be obtained based on those two comb lines to provide a measurement of the offset frequency as follows [43]:

$$2f_n - f_{2n} = 2\left(n\,f_r + f_0\right) - \left(2\,n\,f_r + f_0\right) = f_0$$

Here, $f_n$ is the frequency at the lower edge of the comb spectrum and $f_{2n}$ is that at the higher edge, as described before. The $2f_n$ part can be obtained using a second harmonic nonlinear crystal, as explained in Figure 29. Given that the light from the comb itself is used as a reference, this approach is referred to as "self-referencing" and a variety of schemes were developed based on this approach [45, 276, 278].
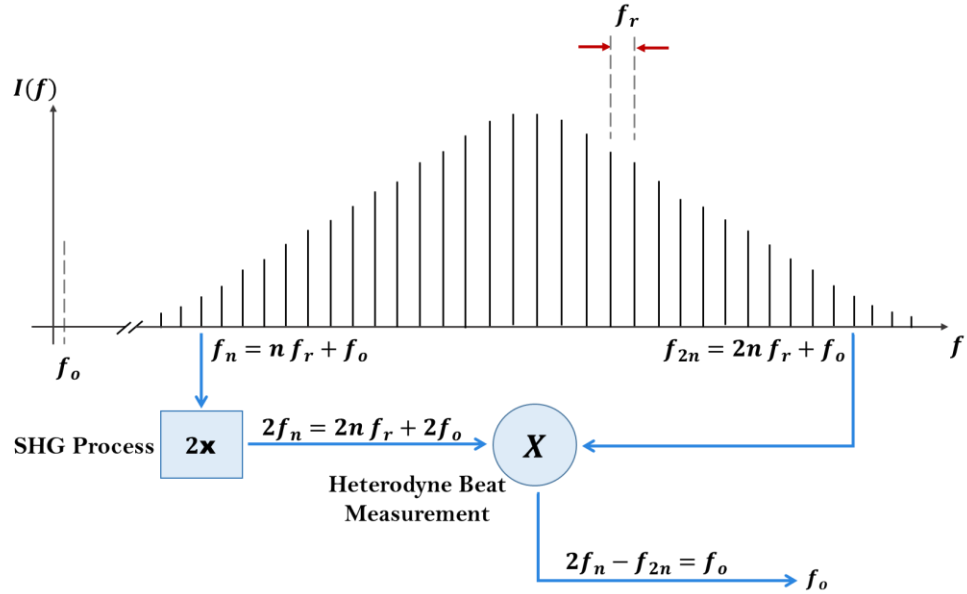
Figure 29 An illustration of the concept of self-referencing often used to determine the offset frequency by heterodyne detection. The frequency of the signal from the low-end of an octave-spanning comb is doubled in a nonlinear crystal and combined with the signal from the high-end at a photodetector. The beating provides a measurement of the offset frequency.

Heterodyne beating approach can also be applied to measure the absolute frequency of a CW laser in the case that its frequency is close to a spectral line $n$ of the comb and its second harmonic is close to a spectral line $2n$ [219]. This enables determining the CW frequency with a very high accuracy based on the following equation:

$$f_{2b} - f_{1b} = \left[2\, f_{cw} - \left(2\, n\, f_r + f_0\right)\right] - \left[f_{cw} - \left(n\, f_r + f_0\right)\right] = f_{cw} - n\, f_r$$

where $f_{1b} = f_{cw} - (n\, f_r + f_0)$ and $f_{2b} = 2\, f_{cw} - (2\, n\, f_r + f_0)$ are the beat frequencies, and $f_{cw}$ is the frequency of the CW laser [276].

It is beneficial to mention the different types of frequency comb sources before going into more detail with comb stabilization. Each type of frequency combs is

89

characterized based on the adapted concept of comb generation. For many years, it's been known that Ti:sapphire laser medium has the broadest gain bandwidth comparing to other materials. For this reason, it has been used extensively in many laser systems over the years. However, no octave spanning spectrum is generated from Ti:sapphire so far. For a broader spectrum, new approaches had to be developed.

The Kerr comb is a major type that relies on mode-locking based on Kerr-effects in special laser media, which are also known as Kerr media. The first nonlinear susceptibility that contributes to the Kerr effect is the third order susceptibility $\chi^{(3)}$ because a Kerr medium has an inversion symmetry, which drops the even terms out [279]. A schematic is given in Figure 30 below to show the nonlinear self-focusing of an intense laser pulse propagating through a Kerr medium. In such a medium, the refractive index is intensity-dependent and is given by:

$$n = n_o + n_{Kerr}\,I$$

This effect is also called "self-phase modulation" because the refractive index changes temporally as the short pulse propagates in this medium [279]. In many cases, this is external to the laser cavity by means of using an optical fiber. However, this effect in optical fibers is limited by the group-velocity dispersion (GVD), which reduces the peak intensity.
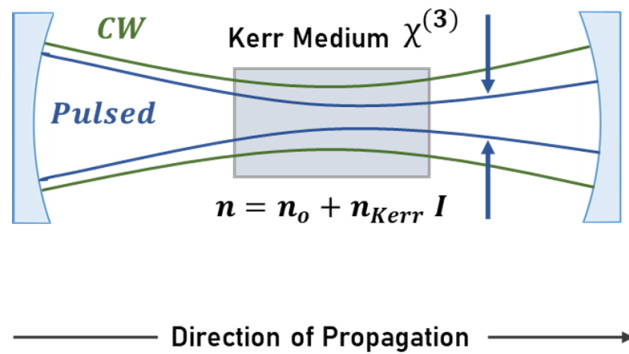
Figure 30 A schematic of mode-locking using a Kerr medium. The dependence of the refractive index in the medium on the intensity of light imposes a focusing effect on the laser pulse while causing high losses for the low-energy CW wave.

Because of its broad gain bandwidth, the Ti:sapphire material has been extensively used as a laser medium in frequency comb systems. Ranka *et al* found that this broad spectrum can be extended even further by using a microstructure fiber [280]. In general, the group velocity dispersion in a typical optical fiber limits the spectral broadening because short pulses spread temporally which results in a lower peak power, as we explained earlier. However, a microstructure fiber allows for a zero dispersion in the group velocity, which preserves the peak intensity. The photonic crystal fiber was a key element in a Noble prize [275, 281]. In addition, the small silica core surrounded by air holes in the microstructure fiber supports spectral phase matching and enhances the nonlinearity [219]. Utilizing both the zero-dispersion fibers and the wide gain spectrum of a Ti:sapphire laser medium can provide an octave spanning spectrum. This was one of the major breakthroughs that led to the proceeding advances in femtosecond frequency comb technology [276].

Over the last couple of decades, decent progress has been made in the field of material sciences, material engineering, and fabrication methods. This has contributed to the development of several materials suitable as gain media for IR lasers. For example, doping chalcogenide glasses with chromium ($Cr$) or iron ($Fe$) provides laser gain materials with large bandwidths in the mid-IR. This comes as a result of homogeneous broadening by coupling electronic transitions in active metals to the lattice phonons of the crystal [44], as illustrated in Figure 31. The low phonon energies of $ZnSe$ and $ZnS$ put them among the most common host material used in mid-IR lasers [144, 186, 282]. Mode-locking is achieved in such lasers by adding a Kerr lens or a saturable absorber in the laser cavity [44].

**(a)**

Laser Oscillator

Pump

Gain Medium    SA

Mid-IR
Pulses

Output Coupler

**(b)**

Non-Radiative Transition

Pump

Laser Transition
in Mid-IR

Non-Radiative Transition
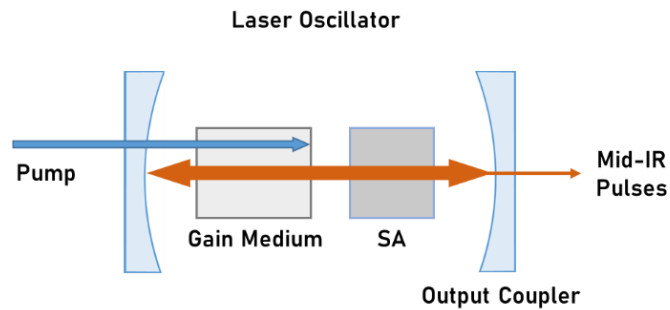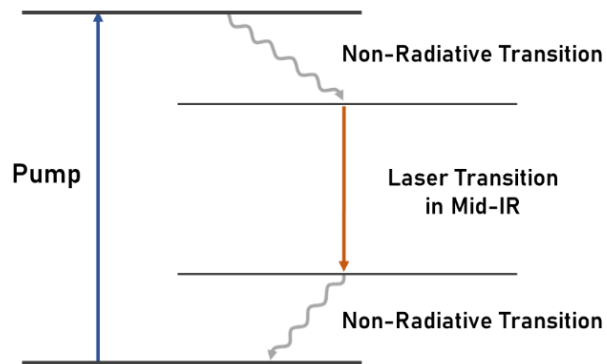
Figure 31 (a) A schematic of a mode-locked femtosecond laser based on $Fe^{2+}:ZnSe$ gain medium and a saturable absorber. (b) A simplified energy diagram showing the mid-IR laser transition.

Nonlinear optical processes in certain materials enable the extension of IR emission to the mid-IR region [232, 244, 257, 270]. This is another approach for providing laser emission at mid-IR wavelengths. Molecular fingerprinting applications are a large market for mid-IR frequency combs of broad tunability in the IR region [28, 31, 46, 48, 54], which was a major driving force behind the development and the progress in the DFG- and OPO-comb technology [44, 227].

A variety of nonlinear crystals are used for mid-IR comb generation. Output powers obtained from DFG-based frequency combs can reach hundreds of $mW$ in average [283, 284]. However, OPO-based combs are capable of producing higher powers at the expense of more complicated system designs [112]. Examples of both systems are included in the table at the end of this section. Another approach is based on doubly resonant OPOs, which have an alternative design that allows for lower threshold levels and therefore promises field applicability [285].

Fiber frequency combs exploit the features of available ultrafast fiber lasers [113, 125, 143, 146, 218]. Therefore, fiber-based combs offer compactness and excellent optical characteristics that are demanded in a variety of applications such as precision measurements, control systems, manufacturing, medical systems, and the search for exoplanets [156, 286]. Mode-locking is essential in fiber frequency combs and several techniques have been demonstrated to meet this requirement [277, 286, 287]. In our laboratory, we use frequency combs based on erbium-doped fiber lasers to conduct experiments for environmental and medical purposes [12, 13, 288].

Most of the initial techniques that were used to generate stable frequency combs are based on mode-locked fiber lasers and depend on the broadening effects in nonlinear fibers [289, 290]. In fiber-comb systems, the quality of the phase is determined by the feedback bandwidth [291], which itself is limited by the laser response (typically in the kHz range) [292, 293]. The stabilization of the repetition rate $f_r$ is realized by using a feedback loop that adjusts the cavity length [290, 292]. Whereas, controlling the power of

the pump source by another feedback loop is the conventional way to stabilize $f_o$ [292, 294].

Frequency combs based on fiber lasers doped with different rare-earth ions; e.g. $Er^{3+}, Ho^{3+}$, and $Tm^{3+}$, have been demonstrated and used in frequency comb applications [295, 296]. Examples of different glass materials doped with rare earth ions were given in Section 2.2.4. As can be seen in that section, some of the available host materials have large transparency windows in the IR, which allow for light emission over thousands of nanometers [116, 177-183].

Applications of frequency combs involve different levels of stability. Some frequency comb applications utilize free-running combs, but most comb-based applications require phase-locking. The phase-locking can be achieved by only controlling two degrees of freedom; $f_o$ as we explained earlier, and another frequency. Locking the phase of $f_o$ to a reference radio frequency means that $f_o$ is stabilized [219]. On the other hand, different techniques can be employed to control the second degree of freedom. One approach is by comparing one of the comb modes to an optical standard, while another method involves $f_r$ stabilization using direct comparison to a radio frequency standard [276, 297]. The second approach is more common and has shown to be sufficient for most applications even with the presence of mechanical and acoustic noise that can impact $f_r$ [298].

Stabilizing $f_r$ of a femtosecond frequency comb generated from a mode-locked laser by a radio-frequency source involves frequency division. Consequently, there is no phase noise in this process because the phases of all comb components are locked, which

is considered an advantage of this stabilization approach [276]. When it comes to $f_o$, it is enough to stabilize it to a few millihertz (mHz) because this contributes to the optical carrier a frequency noise of less than $10^{-17}$ [219]. At this point, let us discuss a fiber frequency comb system as an example and explain its stabilization explicitly.

Three compact comb sources based on polarization-maintaining fiber were designed and examined by Sinclair and co-workers towards a field-deployable comb design [298]. In this design, they used the first stabilization method that we mentioned earlier. The concept of this method is illustrated in Figure 32. Let us consider $f_{cw}$ to be the reference optical frequency, which is typically the frequency of a CW laser, $f_m$ to be the frequency of the comb line close to the optical reference, and $f_{opt}$ to be the frequency difference between the two of them, as shown in Figure 32,

$$f_{opt} = f_{cw} - f_m$$

Then, the frequency of any comb line $n$ of the generated comb can be found from the following equation [298]:

$$f_n = f_m + \left(\frac{n-m}{m}\right)(f_m - f_o)$$

where $m$ is the mode number of the comb line locked to the CW reference, $f_m$ is the frequency of the specified comb line, and $f_o$ is the carrier-envelop offset frequency. In this case, the repetition frequency $f_r$ of the comb is related to $f_o$ by the following relation [298]:

$$f_r = \left(\frac{1}{m}\right)(f_m - f_o)$$

The system operation has showed a high level of stability (with uncertainties of less than $1\ mHz$ in $1\ s$ for the optical frequency) suitable for out-of-laboratory applications. This stabilization technique is called "full self-referencing" because both $f_o$ and $f_{opt}$ are stabilized by phase-locking to standard radio frequencies determined based on $f_r$ of the comb [299, 300]. Locking the phase of $f_o$ was achieved by a feedback to the pump current, and locking that of the heterodyne frequency $f_{opt}$ was realized through feedback to the PZT fiber stretchers that control the cavity length.
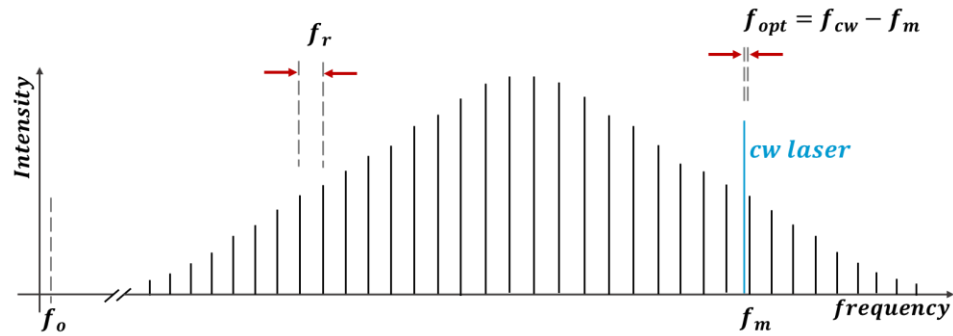


Figure 32 Comb stabilization by phase-locking the radio frequency $f_{opt}$ instead of the typical locking of $f_r$, where $f_{cw}$ here is the frequency of the CW reference laser which is very close to the frequency of the $mth$ comb mode $f_m$.

One the primary types of mid-IR frequency combs is based on the DFG process explained in Section 2.2.5.2. A mid-IR comb can be generated by mixing a near IR comb with a suitable CW laser in a nonlinear crystal. In this case, the difference-frequency conversion process produces a down-shifted frequency comb with comb modes equal to:

$$(f_n)_{DFG} = |f_n - f_{cw}|$$

where $f_n$ are the frequencies of the modes of the original comb and $f_{cw}$ is the frequency of the CW laser [44]. The two main challenges with this technique are finding a material with a sufficiently large second-order susceptibility $\chi^{(2)}$ and matching the phases of light-waves generated in the crystal at different depths. A detailed explanation is given in Section 2.2.5 of mid-IR DFG laser sources, but let us recall the phase-matching requirement in DFG processes. To acquire phase-matching, it is required to use special materials such as periodically-poled materials. This type of materials is fabricated with a specific poling period, and this period is optimized so that a quasi-phase-matching is achieved for a specific set of wavelengths. In other words, the phase-matching is imperfect and is applied only to a portion of the comb spectrum, which imposes a limitation on the width of the generated comb [44]. Frequency combs based on this technique have been reported, and their demonstrations show that the spectral span does not exceed a certain limit and the mode power is relatively low [276, 301]. DFG-comb sources based on pulsed lasers, however, are tunable over broad ranges in the mid-IR with output powers sufficient for molecular spectroscopy [283, 284].

Another approach for DFG combs is to use two frequency combs, but this approach is considerably expensive. Therefore, researchers have tried to obtain a DFG comb from a single optical comb by mixing different comb teeth in a nonlinear crystal. The modes of the new comb can be found using [44]:

$$\left(f_{n,m}\right)_{DFG} = |n - m|\, f_r$$

where $f_r$ is the repetition frequency of the original comb and $n$ and $m$ are integers.

A cavity is not required in a DFG comb source, which makes it simpler than an OPO-based frequency comb and free of alignment difficulties. Recently, fiber-based DFG comb systems with sufficient optical efficiencies have been reported, and some of those systems are commercially available [44, 283, 296, 302]. Lee *et al* demonstrated a frequency comb source emitting at mid-IR wavelengths between $6\ \mu m$ and $11\ \mu m$ using Er- and Tm-fiber lasers to obtain DFG in $OP-GaP$ material [303]. In our fiber laboratory, we use MenloSystems combs, which have a high coherence degree, in collaboration with the company [218]. A block diagram and a photograph of one of our mid-IR frequency comb sources, which operates between $2.9-3.5\ \mu m$, is presented in Section 4.2.3 as a part of my experimental work. We performed dual frequency comb spectroscopy based on two frequency combs of the mentioned type [12].

Sotor and co-workers have demonstrated an all-fiber frequency comb source for even longer wavelengths based on DFG in an orientation-patterned $GaP$ medium of a thickness of $3\ mm$ [304]. Using different periods of quasi-phase matching, they mixed the output from a highly nonlinear fiber with the output from an Er-doped fiber laser, emitting at $1.9\ \mu m$ and $1.55\ \mu m$ respectively, and obtained an idler beam tunable over the spectral range from $6$ to $9\ \mu m$.

Let us take their system as an example of an all-fiberized comb-source based on DFG processes in a nonlinear crystal and describe the system with larger detail. In their comb design, shown in Figure 33 [304], the pulse emitted from a mode-locked Er-doped fiber oscillator splits evenly. At one arm, an Er-doped fiber amplifier (EDFA-1) is used to amplify the power to $120\ mW$. After that, a HNLF is used to shift the wavelength to

longer IR regions (by about a 2 $\mu m$ shift). Then, another amplifier based on thulium-doped fiber increases the power to higher levels between 50 and 235 $mW$. A variable delay line (VDL) at the second arm acts to shift the wavelength and impose an optical delay. The two beams are then combined by a wavelength division multiplexer (WDM) and focused on the $OP - GaP$ crystal by a reflective collimator (COL). A barium fluoride lens collimates the resulting idler beam, and a long pass filter (F) blocks undesired light transmitted from the pump and the signal beams. An average output power of 7.4 $mW$ was measured for this system at the central wavelength 7.5 $\mu m$. This is a recent example of an efficient fully-fiberized mid-IR DFG comb system that can open the door for field applications based on mid-IR frequency combs.

EDFA-1  HNLF  DCF-1  TDFA

OSC

48 MHz
1560 nm

50/50

DCF-2  EDFA-2

VDL

WDM  COL  OP-GaP  F

BaF$_2$  MIR
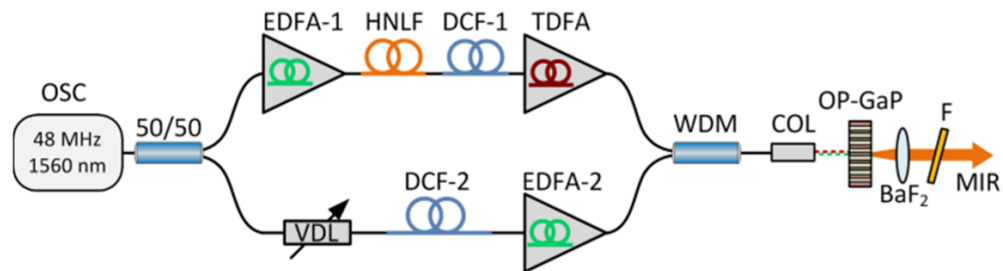
Figure 33 The experimental setup of the mid-IR DFG comb centered at 7.5 $\mu m$ that was designed and tested by Sotor and co-workers for the detection of methane in a gas-filled cell (Reprinted with permission from [304] copyright 2018 The Optical Society)

To validate the performance of their frequency comb system, Sotor and his co-workers used this comb source in an absorption spectroscopy experiment to investigate

methane [304]. Since the comb source is tunable between the mid-IR wavelengths $6\ \mu m$ and $9\ \mu m$, the concentration of methane was measured in the region between 7.5 and 8.3 $\mu m$, which is within that range. Their measurement of the concentration of methane in a $10\ cm$-long gas cell revealed a good agreement with the results calculated from HITRAN database. Overall, a substantial advantage they reported for this all-fiber DFG-comb is that it only requires the $f_r$ to be stabilized since $f_o$ is canceled passively [304].

Another example is for a frequency comb based on a single laser, in which active phase-locking was achieved from a CW-QCL source by exploiting the large gain it provides and using a four-wave mixing process [97, 305]. In this work, Hugi *et al* demonstrate a solid-state mid-IR frequency comb that emits at $7\ \mu m$ and covers $308\ nm$. Their QCL is a hetrostructure based on InGaAs/InAlAs materials grown on InP material. This material combination allowed for a multimode operation close to zero-GVD. The inter-subband transitions in this material exhibit large third-order susceptibilities $\chi^{(3)}$. As a result, equidistant modes were obtained based on parametric nonlinear processes and four-wave mixing.

Both the low GVD and the high nonlinearity are considered key characteristics of materials used for QCL-combs [305, 306]. Remarkable advantages of QCL-combs are the compactness, robustness, and design-flexibility of the system, which make them ideal for all-solid-state spectrometers in the mid-IR. Furthermore, the ongoing progress in bandgap engineering and fabrication technologies can lead to designs with broader spectral coverage and deeper mid-IR emission [306-308].

A new area that has been rapidly developing in the last few years is the generation of frequency combs from on-chip integrated microresonators [309, 310]; in particular the generation of microresonator Kerr frequency combs [311, 312]. Comparing to other techniques of comb generation, Kerr combs depends on a mechanism that combines third-order nonlinear effects and four-wave mixing, as we briefly discussed earlier [312, 313]. Illustrated in Figure 34 is a dielectric material of third-order nonlinearity $\chi^{(3)}$ placed in a resonator. As two pump photons from a powerful CW source penetrates through the dielectric material, a nonlinear process takes place and two new photons are generated; a signal and an idler [44, 311], such that:

$$2\hbar\omega_p = \hbar\omega_s + \hbar\omega_{id}$$

Another pair of photons from the same pump source result in signal and idler photons of different frequencies, and so on. A four-wave mixing process requires that:

$$\hbar\omega_s + \hbar\omega_{id} = \hbar\omega'_s + \hbar\omega'_{id}$$

Thus, the result will be a cascade of sidebands that cover a broad range of frequencies. Using a strong near-IR source for pumping will extend the generated Kerr comb to the mid-IR region. Besides, the power of the modes can be improved if large mode spacing (in the gigahertz range) is used along with a strong pump source [44, 312]. This simple yet novel concept of microresonator Kerr comb generation promises compact frequency comb systems for a number of spectroscopic and metrology applications [38, 42, 314, 315]. A detailed description of the operation, the different types, and the several generating techniques of micro-combs have been reported [309, 312, 316].

(a)
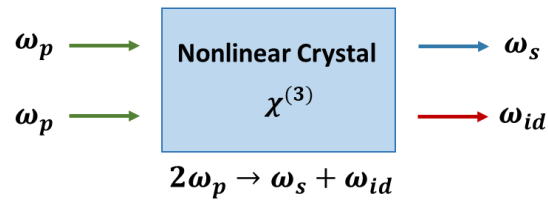


(b)
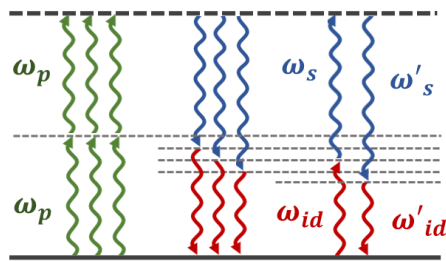
Figure 34 An illustration of the processes in a Kerr frequency comb. (a) A third-order nonlinear process where two pump photons results in a signal and idler pair of new frequencies, and (b) a four-wave mixing process where signal and idler photons result in new pairs at different frequencies.

A comb-assisted application is an application that takes advantage of the properties of a frequency comb and deploys the comb as an assistance optical element to improve the performance or the characteristics of the overall system [317]. Some of these applications utilize the features of an optical comb by using it as a transfer oscillator in comb-assisted experiments [318, 319]. They use a master laser and a slave laser and, with the use of an optical comb, transfers the coherence properties of the master to the slave. Then, the spectral measurement is obtained at the wavelength of interest using the slave laser.

103

Locking the phase of one of the comb lines to a CW reference of a narrow-linewidth allows for transferring its coherence properties to all the lines of the frequency comb [112]. This has proven to decrease the phase noise, improve the relative linewidths [320], and allow for stability of the long-term phase [321]. Phase-coherent mapping between the radio-wave and optical spectra is also a special feature made possible by self-referenced combs [112].

The unique characteristics of optical frequency combs make them extremely accurate tools for high precision measurement applications [43, 322-324]. Diverse research avenues have been opening since the invention of the optical frequency comb [2, 8, 27, 41-43, 286, 312, 315, 317]. Broadband spectroscopy with frequency combs utilizes all of the comb lines, which allows for obtaining absorption measurements for multiple gas species in a single shot [3, 9, 19, 27, 41, 296]. Shown in Figure 35 is the general concept of frequency comb absorption spectroscopy, which we apply in our laboratory to measure the concentration of molecules [12, 13, 218, 288]. Experimental details are covered in Chapter 4 as well as several examples of frequency comb spectroscopy techniques and applications.
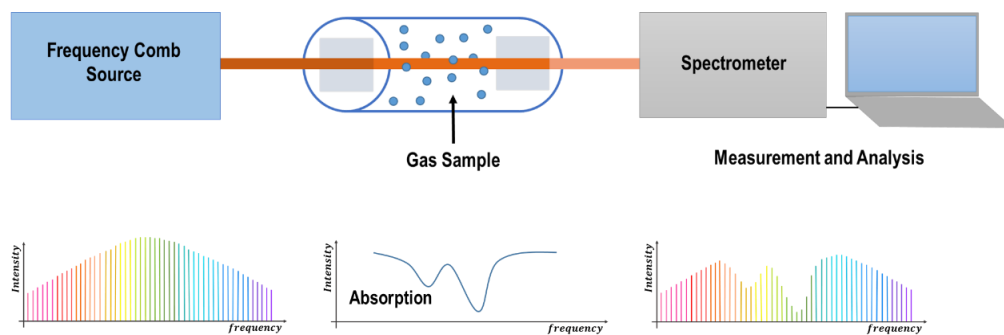
Figure 35 Direct absorption spectroscopy based on frequency comb sources.

Comparing to other spectral regions, the mid-IR region experiences multiple challenges in terms of instrumentation and detection methods. However, the progress in frequency comb generation in the last decade is remarkable and has led to the development of optical frequency combs emitting at longer mid-IR wavelengths with broad spectral coverage. Table 9 presents many examples of different sources of frequency combs with a variety of repetition rates and spectral coverage.

Table 9 Characteristics of Recent Examples of IR Optical Frequency Combs. Each Comb Source is characterized by the Approach used to Generate the Comb, the Repetition Rate of the Comb, the Spectral Span, and the Average Output Power.

| Approach | Repetition Rate (*MHz*) | Spectral Span (*µm*) | $P_{avg}$ (*mW*) | Ref. |
|---|---|---|---|---|
| *DFG* | 100 | $2.8 - 3.5$ | 500 | [283] |
| *DFG* | 125 | $2.7 - 4.2$ | 237 | [284] |
| *DFG* | 151 | $3 - 10$ | 1.5 | [302] |
| | | $3 - 4.6$ | 55 | |
| *DFG* | 48 | $6 - 9$ | $152 - 235$ | [304] |
| *DFG* | 184 | $3.1 - 5.2$ | 1.64 | [325] |
| *OPO* | 250 | $2.9 - 3.4$ | 70 | [326] |
| *OPO* | 136 | $2.8 - 4.8$ | $1.5 \times 10^3$ | [327] |
| *Kerr* | $500 \times 10^3$ | $3.7 - 5.5$ | 50 | [328] |

To conclude the whole section of IR sources, let us present a brief summary. The field of mid-IR spectroscopy employs different types of IR sources, and the choice of the

suitable source depends on many aspects ranging from the output intensity to the spectral

coverage to the capabilities and limiting factors. In a study conducted on 2016 by Haas

and Mizaikoff, they highlighted different aspects of the field of mid-IR spectroscopy for

sensing, and provided a summary of recent and relevant IR sources, materials, and

detectors [104, 329]. Their summary is shown in Figure 36 below [329]. In addition, a

very recent review by Picqué and Hänsch discusses frequency comb spectroscopy in detail

[281, 315, 330].
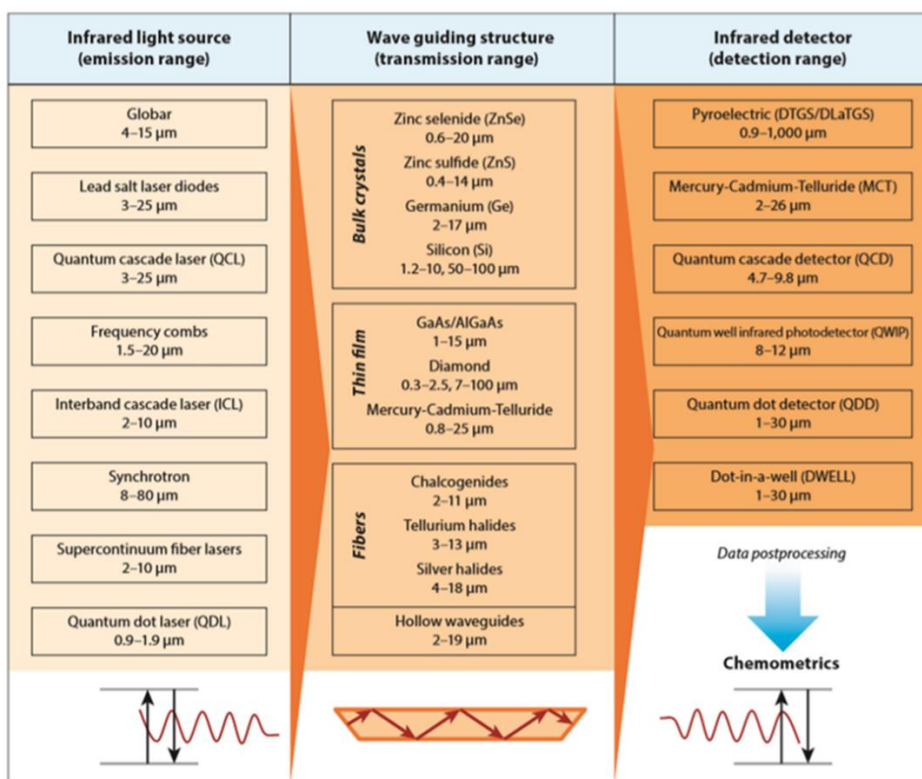


Figure 36 A summary of IR detectors, recent sources of IR radiation, and materials used for transmission or guiding. Emission, transmission, and detection ranges are specified, respectively (Reprinted with permission from [329] copyright 2016 Annual Reviews).

## 2.3 Detection of Electromagnetic Radiation

### 2.3.1  Basic Concepts

Sources of electromagnetic radiation have various characteristics and capabilities, which are considered for each scientific or industrial application. Some of these characteristics include wavelength coverage, stability, coherence length, beam shape, the area of emission, and lifetime. Accordingly, the selection of the photodetector suitable for an application depends on the light source used in that application.

In general, the detection of electromagnetic radiation means that radiation energy is absorbed and converted into an electrical signal. When light is incident on the detector, the optical field excites the electrons in the initial bound state $|a>$ resulting in a transition to a higher state $|b>$, as illustrated in Figure 37, which is equivalent to Figure 1 in Section 1.1. Electrons in higher states are free to move, which contribute to the flow of electric current [331].

$$|b>$$

$$hv$$

$$|a>$$
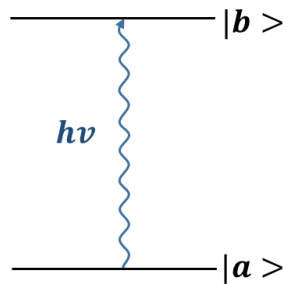
Figure 37 Transition from an initial state to a higher state after absorption of a photon of energy $hv$.

Different detection techniques can be used to measure and display the intensity of the optical field. In the following subsections, we present a general overview of different types of detectors that were developed over the years, and discuss some of their features. First, the well-known vacuum photocathode is reviewed briefly and the definition of quantum efficiency is introduced. Second and third, photomultipliers and photoconductive detectors are discussed, respectively. Then, photodiodes based on the p-n junction and the p-i-n junction are covered. Avalanche photodiodes, in which a single electron results in multi-photon-emission, are explained next, and the section concludes with examples of the most popular materials for infrared detectors.

### 2.3.2  *The Vacuum Photocathode*

Detection based on a photocathode depends on emission of free electrons, by the photoelectric effect, from surfaces made of special materials. Electrons are collected by an anode which has a high voltage. To avoid electrons collision with gas molecules, this detection system is enclosed in a vacuum envelope.

Current will flow only when the photon energy is larger than the photoelectric work function $\phi$ of the cathode, which makes $h\nu = \phi$ the low-frequency detection limit. When the photon energy is smaller than $\phi$, no current. Therefore, materials with low work functions are used for the photocathode. The first compound used in photocathode materials is *Ag-O-Cs*, which was developed in 1929 [39, 332-334]. To extend the performance of photocathodes to longer wavelength regions, many compounds have been developed and manufactured, such as *Na-K-Sb-Cs*, *GaAs*, and *InGaAs* [305]. The latter is

so popular nowadays in infrared applications due to its high sensitivity comparing to other compounds.

The quantum efficiency (QE) is one of the main characteristics to be considered for any detector. From the discussion of the photocathode, it is noticeable that the electric signal is proportional to the rate of electrons excitation. This is described by the quantum efficiency as follows:

$$\eta = \frac{Number\ of\ charge\ carriers\ generated\ per\ second}{Number\ of\ photons\ absorbed\ per\ second}$$

It can also be interpreted as the number of electrons released for each photon absorbed [331]. The higher the quantum efficiency, the more efficient the detection process. For this reason, a detector with a large quantum efficiency is preferred by experimentalists.

The QE of cesium iodide (*CsI*) photocathodes was investigated by Rabus and coworkers in the 120-220 nm range [335]. They calibrated a *GaAsP* Schottky photodiode as a transfer detector standard, and were able to prove a quantum efficiency $\sim 42\%$ with improved accuracy, due to the sufficient stability of *GaAsP* Schottky photodiode in the VUV region. More recent results indicate that a QE up to 60% can be measured for *CsI* photocathodes, with a total relative uncertainty controllable within 5.4% [336]. In this experiment, Xie *et al* used a measurement system with a synchrotron radiation light source to establish the QE of different samples of *CsI* photocathodes. They used a photodiode as a transfer detector standard to ensure reliability of QE measurements. Uchiyama *et al* reported an exteremly high quantum efficiency for a *GaN*-based photocathode [337]. He

and coworkers have used *Mg*-doped *GaN* films in fabricated phototubes to investigate the quantum efficiency. With an *Mg*-doping concertation of $3 \times 10^{19} \, cm^{-3}$ and a photon energy of $5.4 \, eV$, they obtained a QE = 71.9% as the maximum calibrated quantum efficiency of the photocathode. In addition, they found that the spectral response of QE strongly depends of the *Mg*-doping concertation [337]. Generally, applications using photocathodes are limited nowadays, since solid state detectors are faster, uses less power, and provides higher sensitivity.

### 2.3.3   The Photomultiplier

A photomultipliers combines the technology of a vacuum photocathode with a series of dynodes made of materials that enhances the number of emitted electrons $(\delta)$. The dynodes are electrodes with a typical potential difference of $100 - 200 \, V$ between each two, and the last dynode is the anode which collects the electrons [331]. They are kept at high potential with respect to the cathode. Figure 38 shows a schematic of a traditional photomultiplier [332].
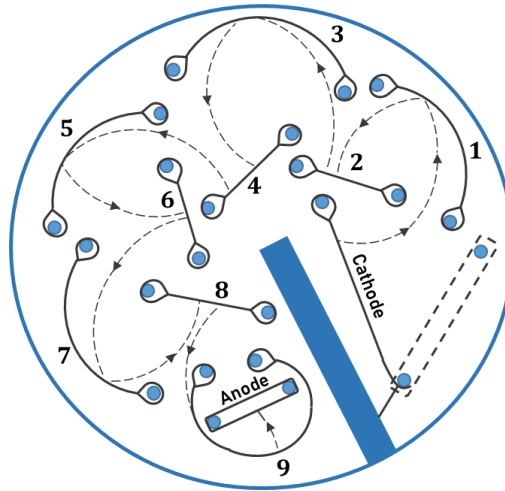
Figure 38 The configuration of a photomultiplier where secondary emission occurs at each of the 9 dynodes (Reproduced with permission from [332] copyright 1968 John Wiley & Sons).

In photomultipliers, voltages should be chosen correctly so that the kinetic energy of the electron striking the material is large enough (typically between $100\ V$ and $200\ V$). This results in $\delta > 1$ and current amplification is achieved. If a photomultiplier has N dynodes and the emission ratio for each dynode is $\delta$, then the current gain is

$g = \frac{i_{out}}{i_{in}} = \delta^N$ which is very large and noise-free [331-333]. For example, if $\delta = 5$ and

N $= 11$ , the gain is huge, $g \approx 4.9 \times 10^7$.

Having low noise and high current amplification, the photomultiplier is considered an extremely sensitive instrument under optimal operation. However, photomultipliers have similar disadvantages of vacuum-photocathodes; they are large, require high voltages, and can get easily damaged if not handled with care.

### 2.3.4 Photoconductive Detectors

There are two types of semiconductors that are used in photoconductive detectors; n-type and p-type semiconductors. For an n-type semiconductor, an incident optical field will ionize a donor resulting in excess number of electrons in the conduction band. Whereas for a p-type semiconductor, an incident optical field will ionize a donor resulting in excess number of holes in the valence band. In both cases, the increase in the number of free carriers will contribute to flow of signal current, until electron-hole recombination.

Basic circuitry inside a photoconductive detector involves a semiconductor crystal, a load resistance, and a power supply of voltage V. Figure 39 illustrates the operation of a typical photoconductive detector [331]. Let's assume we have an n-type semiconductor crystal. The light incident on the crystal will excite electrons from the valence band to the conduction band resulting in positively ionized donors and negatively ionized acceptors. The resistance of the semiconductor $R_d$ is chosen such that it is much larger than the load resistance $R_{load}$ of the circuit. This ensures that most of the bias voltage contribute to the detection signal $V_{signal}$. As the carriers move under the influence of the internal field inside the semiconductor crystal, this flow of free carriers lowers the resistance of the semiconductor. Consequently, more voltage appears across $R_{load}$ and this voltage $V_{signal}$ is proportional to the intensity of incident light. If we refer to the average carrier lifetime as $\tau_o$ and to the time the carrier takes to cross the gap of width $d$ between the valence and the conduction bands as $\tau_d$, then the photoconductive gain can be obtained as $g = \frac{\tau_o}{\tau_d}$.
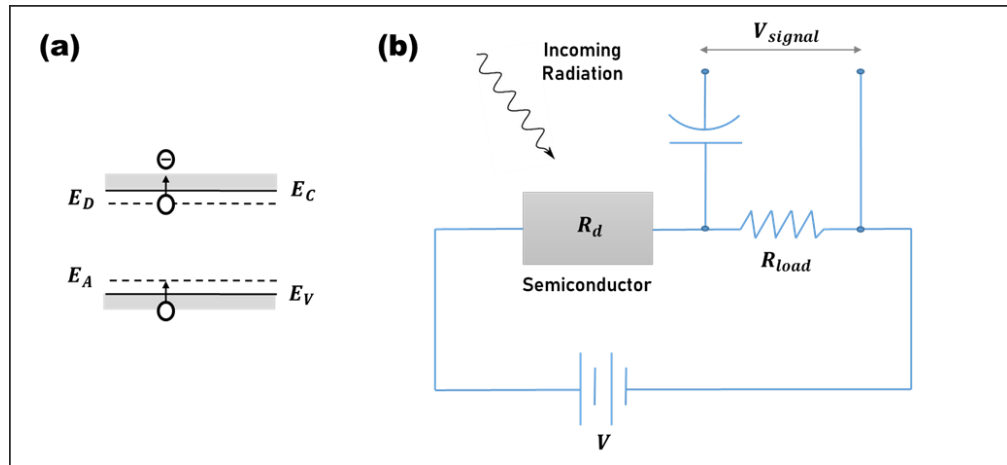
Figure 39 (a) A schematic of the valence and conduction bands in a semiconductor. (b) Biasing circuit of detectors based on photoconductors.

Comparing to photomultipliers, photoconductors do not involve a current amplification process. However, they have the advantage of extending the detection range to long-wavelength radiation. This is achieved by doping with impurities which have sufficiently low ionization energies. A detector based on germanium doped with mercury, ($Ge{:}Hg$, $28^o$K) for example, requires a photon energy of at least 0.09 eV to lift an electron from the valence band and therefore ionize an acceptor atom. Whereas in detectors based on copper-doped germanium ($Ge{:}Cu$, $4.2^oK$), the ionization energy is 0.04 eV which allows for longer wavelength detection up to 32 µm [338]. In this example, the characteristics of impurity atoms added to $Ge$ crystals define the properties of the photoconductor in terms of sensitivity and wavelength coverage. The sensitivity of detectors that depend on this mechanism is called "extrinsic sensitivity". On the other hand, sensitivities of detectors which inherit their properties form the host crystal are

called "intrinsic". Extrinsic germanium photodetectors, specifically, provide high sensitivities in the 2-200 µm spectral region [338]. The band structure of the photoconductive material determines the possible electronic transitions and the generation process of free charge carriers. Thus, different materials are used for different spectral regions [339].

A general description of the carrier generation rate $(G)$ in a photoconductive detector is in terms of the power of the incident beam $P$, the frequency $v$, and the quantum efficiency $\eta$ of the detector: $G = \frac{P\eta}{hv}$. The carriers recombine after an average lifetime $\tau_o$ in a recombination rate $R_{rec} = \frac{N_{avg}}{\tau_o}$, where $N_{avg}$ is the average number of generated carriers. Since the generation rate $G$ and the recombination rate $R_{rec}$ are equal, the average number of carriers can be found from $\frac{N_{avg}}{\tau_o} = G$ as follows:

$$N_{avg} = G\tau_o = \eta \left(\frac{P}{hv}\right)\tau_o$$

The total current is a product of $N_{avg}$ and the external current $I_{ext} = \frac{qv}{d}$, where v is the drift velocity under the influence of the field, and $d$ is the width of the band gap of the semiconductor. The drift velocity is a product of the mobility and the electric field. The drift time $\tau_d$ in terms of the drift velocity across the band gap is $\tau_d = \frac{d}{v}$. So the total current [331] can be written in the form:

$$I_{tot} = N_{avg} I_{ext} = \frac{\eta P \tau_o}{hv}\frac{q}{\tau_d} = \frac{\eta q}{hv}\left(\frac{\tau_o}{\tau_d}\right)P$$

One of the major difficulties associated with detectors based on photoconductors is the high probability of thermal ionization at room temperature. In order to extend their

115

performance to longer wavelengths, semiconductors with small band gaps are required [339, 340]. This will help to detect photons with small energies, but it has the drawback of thermal excitation of carriers at room temperature [331, 341]. As a result, most of the available semiconductor detectors are cooled to liquid nitrogen ( $77^o\,K$ ) or liquid helium ($4.2^o\,K$ ) temperatures [339]. In Section 4.2.5 of the experimental part, a liquid-nitrogen-cooled photodetector is used to eliminate the unwanted effects of room temperature detection.

In cooled photoconductor-based detectors, shot noise is still present due to the randomness of generating individual carriers by the incident optical flux. However, another main source of noise in photoconductors is the randomness in carriers' lifetimes [342, 343]. To clarify, it can be seen from the equation of total current $I_{tot}$ that the carriers contribute with the term $q\,\dfrac{\tau}{\tau_d}$ where $\tau$ here is the lifetime of the carrier, which is not a constant value.

### 2.3.5   The P-N Junction Photodiode

The operation of a junction photodiode can be understood by the interpretation of the semiconductor p-n junction. It consists of two different semiconductor materials, doped to be a p-type and an n-type. As mentioned in the previous section, the p-type semiconductor has an acceptor-doped region which is rich in holes, and the n-type semiconductor has a donor-doped region which is rich in electrons. The acceptor density is constant and is denoted by $N_A$ , and the donor density is constant and is denoted by $N_D$.

When the two materials are joined to form a junction, electrons flow from the n-type region to the p-type, and holes flow from the p-type region to the n-type. This creates donor ions and negatively charged acceptors resulting in an internal field that prevents more carriers from leaving. A charge carrier wondering into this space-charge region will get accelerated by the field and will drift to the opposite side. This is responsible for the drift current across the junction. This current is balanced by a current flowing opposite to it due to diffusion of carriers [344].

Applying a reverse bias voltage across the junction lowers the number of crossing charge carriers, but normally this process continues depending on how often these minority carriers wonder into the space-charge region [344]. Figure 40 illustrates the operation of a reverse biased p-n junction [345].
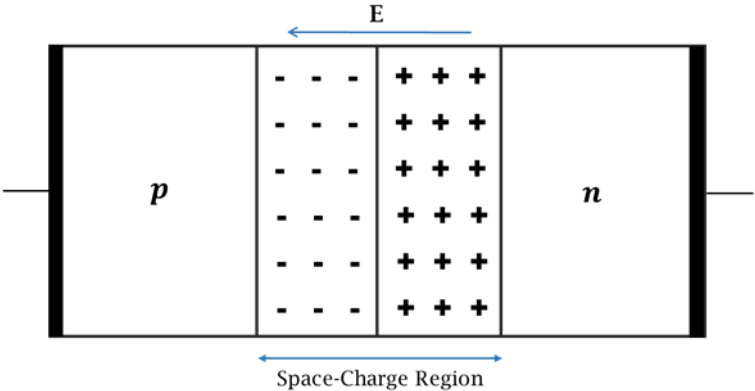


Figure 40 The space-charge region and the internal field in a p-n junction.

*2.3.6    Semiconductor Photodiodes and the P-I-N Junction*

A p-i-n junction has an intrinsic layer between the n and p layers of a p-n junction. When the incident light passes through the detector and gets absorbed in the neutral regions of n and p, most of the created electron-hole pairs recombine before they reach the junction. These pairs do not get influenced by the field in the space-charge region, and therefore do not contribute to the current. The electron-hole pairs created within a diffusion length of the space-charge region have larger probability of reaching the space-charge region and drifting under the influence of the field.

In indirect semiconductors, *Si* for example, the majority of carriers that contribute to the current are created within the neutral p and n regions, since the diffusion lengths exceeds the width of the space-charge region [346]. Based on this, the photocurrent is not exactly proportional to the number of incident photons, and it depends on two main elements. First, it depends on absorption of incident radiation in the space-charge region which excites the carriers and induces a current in the external circuit. Second, it depends on absorption of radiation and production of electron-hole pairs within a diffusion length from the space-charge region.

The diffusion process is relatively slow. However, the contribution of these carriers in the current is significant and must be considered. For the reasons mentioned above, photodiodes based on simple p-n junctions suffer from slow time response. The p-i-n junction comes as an alternative for p-n junctions in areas where the time response factor plays an important role. Adding an intrinsic layer of a proper thickness, between the n and p layers of the junction where the field is large, increases the number of charge-

118

carriers generated in this area. In this case, the current depends on the fast drift of carriers within the large field region rather than the slow process of diffusion.

In general, the photodetection process in a p-i-n junction can be summarized as follows. Electrons in the valence band are excited by the incident optical signal. The excited electrons move to the conduction band and leaves holes in the valence band. Then, the electrons and holes move under the influence of the internal electric field of the device, which generates an electric current that can be measured. A proper thickness of the intrinsic layer (i) compared to the optical absorption length ensures that most of the carriers are generated in this layer [331, 346]. The large field in this layer collects the charge carriers at the appropriate contacts with a fast drift, thus enhancing the induced electric current in the circuit. This also lowers the capacitance, which is another advantage of using the p-i-n junction.

To determine the electric current of p-i-n photodetectors in general [347], consider an intensity modulated optical signal:

$$P(\omega) = P_O \left[ 1 + \cos(\omega t) \right]$$

where $\omega$ is the modulation frequency, $m$ is the modulation index, $P_o$ and is the average optical power of the incoming signal. As a function of the wavelength $\lambda$ and the modulation frequency $\omega$, the rms current of the signal can be written in terms of the rms optical power $P_{rms} = \frac{m\,P_o}{\sqrt{2}}$ as:

$$i_P(\lambda, \omega) = \frac{q\,m\,P_o}{h\upsilon\,\sqrt{2}}\,\eta(\lambda, \omega)$$

119

Here, $hv$ is the photon energy corresponding to the wavelength of radiation $\lambda$, $q$ is the electron charge, and $\eta(\lambda, \omega)$ is the quantum efficiency of the detector. The quantum efficiency of p-i-n based photodiodes also depends on the geometry of the detector and the properties of the materials which the p-i-n junction is made of. The efficiency $\eta(\lambda, \omega)$ can approach unity and be independent of $\lambda$ and $\omega$ for well-constructed photodiodes [347].

Different current sources contribute to the shot-noise in the output signal [342]. The incident optical radiation results in an average current $I_P$ given by:

$$I_P = \frac{q\,P_o}{hv}\,\eta(\lambda, 0)$$

Background radiation produces a current $I_{BG}$, which is expressed in terms of the background power $P_{BG}(\lambda)$ as:

$$I_{BG} = q\int \frac{\eta(\lambda', 0)\,P_{BG}(\lambda')}{hv}\,d\lambda'$$

Another source of current in p-i-n junctions, which exists regardless of an incident optical signal or a non-equilibrium background radiation, is thermal excitations of charge carriers in the depletion region [331, 342]. These thermal excitations, in addition to possible surface leakage currents, result in a dark current $I_D$. The randomness in the generation of charge-carriers that contribute to the total current introduces shot-noise fluctuations [343]. Therefore, for a detector of bandwidth $B$, the mean square shot-noise current is expressed in terms of the signal and shot-noise currents as follows:

$$\langle i_s{}^2 \rangle = 2\,q\,(I_P + I_{BG} + I_D)\,B$$

The output voltage of the detector is produced from the original signal and the associated noise currents through an interaction circuit that includes, in the simplest case,

a load resistance $R_L$. Figure 41 shows schematically the different sources of current and the thermal noise contribution to the output signal [347, 348]. As can be seen, the interaction circuit is another source of thermal noise.

**(a)**



**(b)**
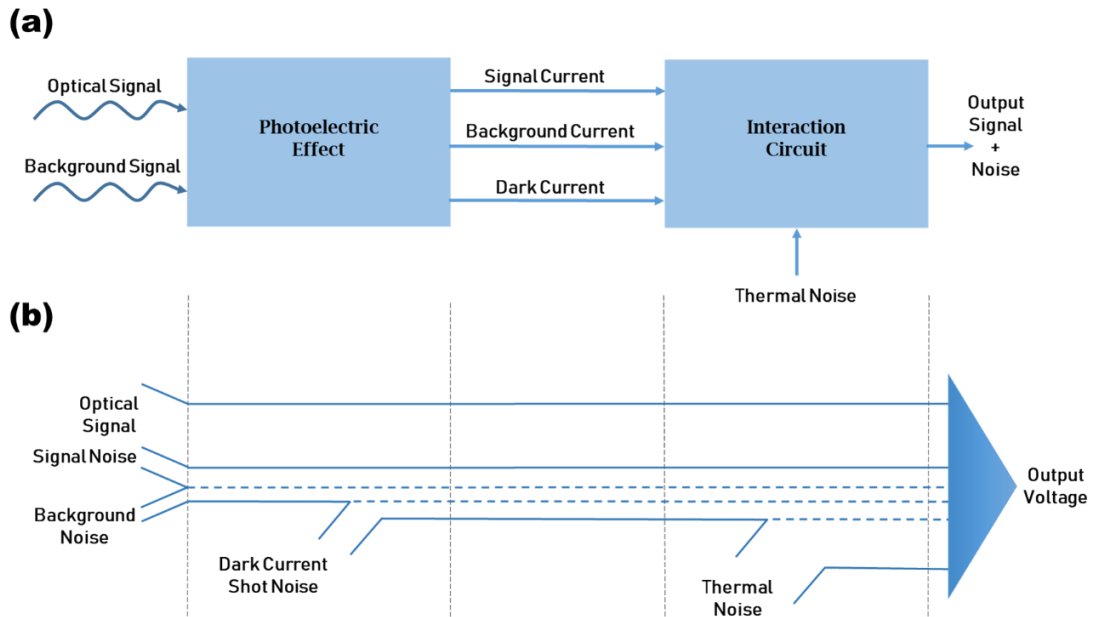
Figure 41 (a) A block diagram for a general detection process in a p-i-n junction photodiode. (b) Different sources of current at different stages of the process (Reproduced with permission from [347] copyright 1977 Academic Press, and [348] copyright 1966 IEEE).

Following the path along the detection process, described in the figure, indicates that the signal-to-noise ratio (SNR) is decreasing as more noise currents are added to the total current. The electrical elements involved in the circuitry of a p-i-n junction diode are shown in Figure 42 [348]. The external load resistance is $R_L$ , the input resistance of the

amplifier following the circuit is $R_i$ , and the other elements resemble the p-i-n detector [347].
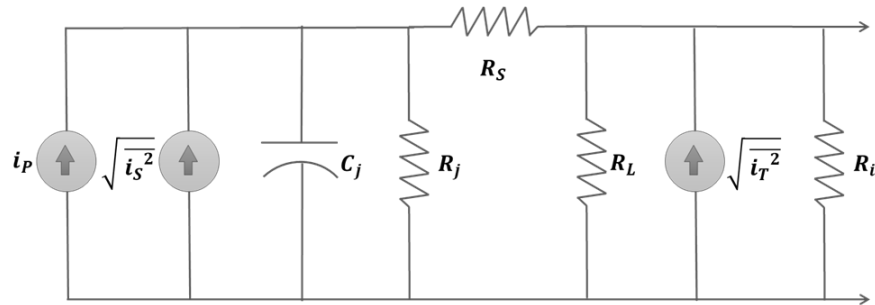


Figure 42 An equivalent circuit of a p-i-n detector (Reproduced with permission [347, 348]).

The thermal noise contribution from all the resistors in the circuit is added to the total noise of the detector. $R_S$ is the series resistance, which is very small compared to $R_L$ , $R_j$ , and $R_i$ , and therefore its contribution can be neglected. For the currents across those resistors, the mean square thermal noise can be expressed in terms of temperature $T$, Boltzmann constant $k$, and the detector's bandwidth $B$ as follows:

$$\langle i_j{}^2 \rangle = 4kB \frac{T_D}{R_j}$$

$$\langle i_L{}^2 \rangle = 4kB \frac{T_L}{R_L}$$

$$\langle i_A{}^2 \rangle = 4kB \frac{T_A}{R_A}$$

where $R_j$ is the shunt resistance of the detector, $T_D$ is the temperature of the detector, $R_L$ is the load resistance at a temperature $T_L$, and $R_A$ is the resistance of the amplifier at an effective temperature $T_A$. This temperature is associated with a source resistance $\frac{1}{R_A} = \frac{1}{R_j} + \frac{1}{R_L}$ [347]. Considering an equivalent resistance $\frac{1}{R_{eq}} = \frac{1}{R_j} + \frac{1}{R_L} + \frac{1}{R_i}$ and combining all thermal noise contributions in one expression yields:

$$\langle i_T{}^2 \rangle = 4kB \frac{T_{eff}}{R_{eq}}$$

For an optical signal with an average power $P_o$ and a 100% modulation incident at a p-i-n photodetector, the signal-to-noise power ratio can be written as:

$$\frac{S}{N} = \frac{i_P{}^2 R_{eq}}{\langle i_N{}^2 \rangle R_{eq}} = \frac{\left(\frac{q P_o}{h\nu \sqrt{2}} \eta\right)^2}{\langle i_s{}^2 \rangle + \langle i_T{}^2 \rangle} = \frac{\frac{1}{2}\left(\frac{q\eta P_o}{h\nu}\right)^2}{2q(I_P + I_{BG} + I_D)B + 4kB \frac{T_{eff}}{R_{eq}}}$$

From this result and the expression for $I_P$, the minimum average power of a 100% modulated optical signal to acquire a signal-to-noise ratio $\frac{S}{N}$ is:

$$P_o = \frac{2h\nu B}{\eta} \left(\frac{S}{N}\right) \left\{ 1 + \left[ 1 + \frac{I_{eq}}{qB\left(\frac{S}{N}\right)} \right]^{\frac{1}{2}} \right\}$$

and the expression of the equivalent $I_{eq}$ is given by:

$$I_{eq} = I_{BG} + I_D + \left( 2k \frac{T_{eff}}{qR_{eq}} \right)$$

If we consider the limit $\frac{I_{eq}}{qB\left(\frac{S}{N}\right)} \ll 1$, the minimum optical power will only be limited by the quantum noise resulting from the incident radiation. For example, to get a

value of $\left(\frac{S}{N}\right)$ around $40-50\ dB$ for a detector with a bandwidth $50\ MHz$, this limit should apply. But in practice, this cannot be realized for large bandwidths since the amplifier noise increases.

To characterize the system or device performance, a quantity or expression called "figure-of-merit" is often used [349]. In engineering, figures of merit are commonly used to decide if a material or a device is convenient for a particular application. Scientists in many fields employ them in analytical calibrations to compare different methods. In spectroscopy, we can refer to figures of merit to determine the capabilities of a detector in the spectral region of interest.

The limit $\frac{I_{eq}}{qB\left(\frac{S}{N}\right)} \gg 1$ is applicable when the contribution of background radiation is large, or the thermal noise resulted from the load resistor is large. This corresponds to a figure-of-merit for a detector where the output current, resulted from the rms power of the optical signal, and the rms noise current are equal. The required rms optical power to produce $\left(\frac{S}{N}\right) = 1$ in a $B = 1$ Hz is defined as the "noise equivalent power," or NEP. In this case, when the modulation frequency and the wavelength of incident radiation are normalized to a 1 Hz bandwidth, the NEP refers to the figure-of-merit of the detector. Inserting $\left(\frac{S}{N}\right) = 1$ and $B = 1$ in the result we obtained previously for a p-i-n photodetector, we arrive at the following expression for the NEP of the detector:

$$\text{NEP} = \sqrt{2}\ \frac{h\nu}{\eta}\left(\frac{I_{eq}}{q}\right)^{\frac{1}{2}}$$

For a small background radiation and a sufficiently large equivalent resistance, the contribution of $I_{BG}$ and $\left(2k\frac{T_{eff}}{qR_{eq}}\right)$ to $I_{eq}$ can be neglected. This leaves us with $I_{eq} \cong I_D$ , which can be used in the equation of NEP to arrive at the ultimate sensitivity of the detector in terms of dark current and quantum efficiency [346, 347].

From the expressions of NEP and $I_{eq}$ , it can be seen that a large $R_{eq}$ is necessary to have NEP limited only by $I_D$ or $I_{BG}$ . At the same time, the upper cutoff frequency and the base-bandwidth are mostly governed by $R_{eq}$ and $C_j$ in parallel. In practice, to have a balance between all the limiting factors, and to meet the requirements of a background-limited and a dark current-limited NEP, the bandwidth of the detector will not exceed a maximum value determined by the material of the device. Therefore, typical p-i-n photodiodes have the utility for applications that involve low bandwidths with a relatively large background contribution. With a current gain mechanism, lower values of NEP are achievable. The current multiplication process is discussed in the following section.

Advances in p-i-n photodiodes followed with attempts to improve the saturation output and the frequency response [350]. InGaAr p-i-n detectors provide large spectral response in the near-infrared region with quantum efficiencies between 50% and 70% [351, 352]. A new design for a wide bandwidth p-i-n detector was proposed back in 2001 by Chang and co-workers [353]. This new design is based on the idea of adding an un-doped buffer layer between the intrinsic layer (i) and the n-type layer (n). They used indium-gallium-arsenide (InGaAr) of a thickness between 1-6 µm for the layer I and indium-phosphide (InP) of thickness ~ 0.5 µm for the buffer layer. They found that adding

a relatively thick buffer layer lowers the capacitance of the photodetector, and thus provides a wide bandwidth. Chang's design of p-i-n junctions contributed to the development of sensitive detection devices characterized by a single potential barrier. Lately, the wavelength coverage of InGaAr p-i-n photodiodes has been extended to 2.6 µm. An example is the IG26-Series by Laser Components.

### 2.3.7    *The Avalanche Photodiode*

An avalanche photodiode consists of a p-n junction, or a p-i-n junction, and a depletion region.  The depletion region, between the n-type and the p-type doped-semiconductors of the junction, is neutral. Although the designs of the avalanche photodiode and the p-i-n junction diode are so similar, the depletion layer is relatively thin in avalanche photodiodes. The primary difference lies in the internal gain mechanism which is the main feature of avalanche photodetectors.

Avalanche photodetectors inherent this name from the multiplication process that occurs in the junction and results in a substantial increase in the current. It starts with free carriers with high enough kinetic energy and ends up with a large number of carriers that contribute to the current. The sequence of excitations and the dramatic increase in the current give this process the characteristics of an avalanche.

Producing carriers with large kinetic energy in the junction is achieved by increasing the field across the junction by means of increasing the reverse bias voltage (up to $\sim 2500 \; V$). However, increasing the voltage over the limit specified for the detector,

known as the maximum rated value, may result in a breakdown or a degradation of its performance.

Let us review the avalanche process in more depth. At first, an incident photon enters the depletion region and excites an electron or a hole. As Yariv explains [331], when the first excited electron has enough kinetic energy, it can "kick new electrons from the valence to the conduction band, while still traversing the layer," referring to the depletion layer. This creates a new electron-hole pair, and the energetic electron and hole can also excite new carriers. This continues and the number of charge carriers multiplies. The avalanche of carriers contribute to the dramatic increase in the current, which is similar to the current multiplication process that happens at the dynodes in a photomultiplier tube. Figure 43 is an example of the gain profiles of two different structures of avalanche photodiodes (APDs) by Excelitas Technologies [354].
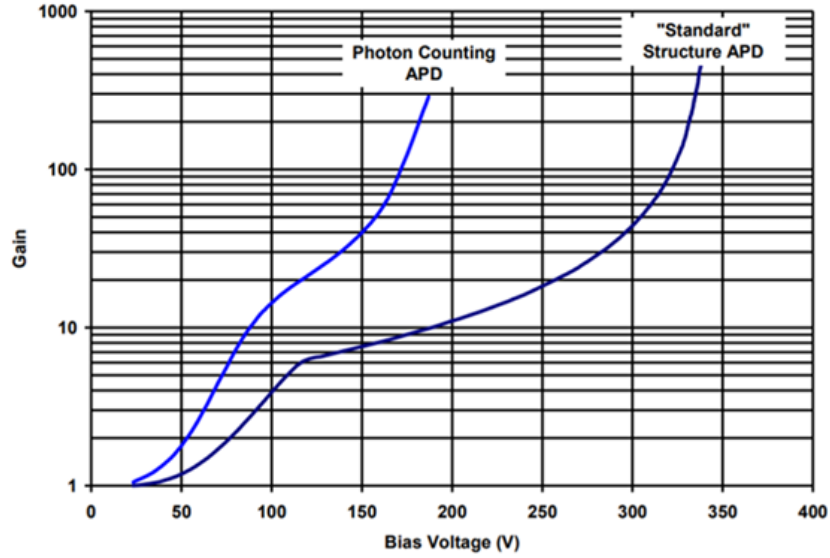
Figure 43 Gain for different APD structures as a function of the bias voltage (Reprinted with permission from [354] copyright 2011 Excelitas Technologies).

Following the same approach we used for p-i-n junction diodes, we start with the rms photocurrent:

$$i_P(\lambda, \omega) = \frac{q\, m\, P_o}{h\nu\, \sqrt{2}}\, M(\lambda, \omega)\, \eta(\lambda, \omega)$$

where $M(\lambda, \omega)$ here is the "avalanche gain," which is equal to the average multiplication and depends on the modulation frequency $\omega$ and the wavelength $\lambda$ [347]. The circuit elements of an avalanche photodiode detector are similar to that of a p-i-n detector. An equivalent APD circuit is presented in Figure 44. As mentioned before, the sources of current noise in a junction-based photodiode are average signal current $I_P$, background current $I_{BG}$, and dark current $I_D$. Since there is noise in the current before current multiplication takes place, it will also multiply and contribute excess-noise to the avalanche current gain.

128
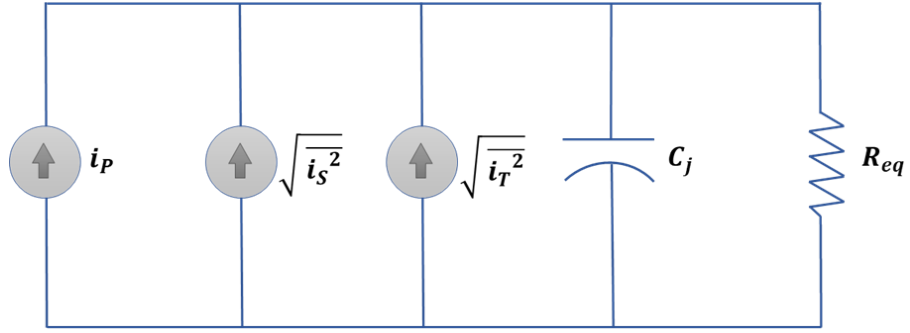
Figure 44 An equivalent circuit of an avalanche detector (Reproduced with permission [347, 348]).

After current multiplication, the mean square shot-noise current is:

$$\langle i_S{}^2 \rangle = 2q\left[ I_P\ M_P{}^2\ F_P +\ I_{BG}\ M_{BG}{}^2\ F_{BG} + (I_D)_{Surf} + (I_D)_{Bulk}\ M_D{}^2\ F_D \right] B$$

where $F_P$, $F_{BG}$, and $F_D$ are the excess-noise factors, and $M_P$, $M_{BG}$, and $M_D$ represent the avalanche gain associated with each source of current [331, 347]. Because of the dependence of the average multiplication $M$ on wavelength and frequency, the values of $M_P$, $M_{BG}$, and $M_D$ are not necessarily equal. $(I_D)_{Surf}$ and $(I_D)_{Bulk}$ are the surface leakage dark current and the bulk dark current, respectively. Since $(I_D)_{Surf}$ does not multiply, the shot-noise expression can be rewritten as:

$$\langle i_S{}^2 \rangle = 2q\left\{ [ I_P\ F_P +\ I_{BG}\ F_{BG} + (I_D)_{Bulk}\ F_D]M^2(\lambda, \omega) + (I_D)_{Surf} \right\} B$$

where the multiplication factors are considered to be equal to $M(\lambda, \omega)$ for convenience.

Considering the excess noise from the amplifier, which follows the circuit, we arrive at the same expression for the equivalent mean square thermal-noise current:

$$\langle i_T{}^2 \rangle = 4kB\frac{T_{eff}}{R_{eq}}$$

Note that it is similar to the result obtained for a p-i-n photodiode in the previous section. Using all the results and assuming a 100% modulated optical signal of average incident power $P_o$ , the signal-to-noise power ratio can be written as:

$$\frac{S}{N} = \frac{i_P{}^2 R_{eq}}{\langle i_N{}^2 \rangle R_{eq}} = \frac{\left(\frac{q\,P_o}{hv\,\sqrt{2}}\,M\,\eta\right)^2}{\langle i_S{}^2 \rangle + \langle i_T{}^2 \rangle}$$

$$= \frac{\frac{1}{2}\left(\frac{q\eta P_o}{hv}\right)^2}{2qB[\,I_P F_P + I_{BG} F_{BG} + (I_D)_{Bulk} F_D\,] + \frac{2qB(I_D)_{Surf}}{M^2(\lambda, \omega)} + 4kB\dfrac{T_{eff}}{R_{eq} M^2(\lambda, \omega)}}$$

In this equation, we can see that the avalanche gain $M(\lambda, \omega)$ increases the SNR only by reducing the contribution of the last two terms in the denominator. In general, the excess-noise factors are $F_P \geq 1$, $F_{BG} \geq 1$, and $F_D \geq 1$ and can increase during the avalanche process. Hence, for an incident optical power $P_o$ there is an optimal value of $M(\lambda, \omega)$ that will produce the maximum SNR [347]. In other words, this optimal value of avalanche gain means that two conditions are met. First, the maximum possible signal-to-noise ratio is achieved, which is crucial for sensitive experimental measurements. And second, the current resulted from the different sources of noise prior to multiplication does not override the current resulted from the optical signal. For example, if one decides to build an avalanche detector with a very large multiplication factor $M$ and without considering other limitations, the noise will multiply tremendously and the photocurrent will be buried by the excess noise in the circuit producing a meaningless very noisy output signal [355-358]. The condition of optimum gain $M_{Opt}(\lambda, \omega)$ is met when the following terms from the denominator of SNR are approximately equal:

$$2qB[\, I_P F_P + I_{BG} F_{BG} + (I_D)_{Bulk} F_D\,] \; \cong \; \frac{2qB(I_D)_{Surf}}{M^2(\lambda,\omega)} + 4kB\,\frac{T_{eff}}{R_{eq}M^2(\lambda,\omega)}$$

Arriving at:

$$M_{Opt} \cong \left\{ \frac{2qB\,R_{eq}(I_D)_{Surf} \,+\, 4kB\,T_{eff}}{2qBR_{eq}[\, I_P F_P + I_{BG} F_{BG} + (I_D)_{Bulk} F_D\,]} \right\}^{\frac{1}{2}}$$

The minimum average optical power of a 100% modulated signal in terms of the SNR and

other elements is obtained by rearranging $\left(\frac{S}{N}\right)$ equation to get [347]:

$$P_o = \frac{2h\nu BF_P}{\eta} \left(\frac{S}{N}\right) \left\{ 1 + \left[ 1 + \frac{I_{eq}}{qBF_P{}^2 \left(\frac{S}{N}\right)} \right]^{\frac{1}{2}} \right\}$$

Where:

$$I_{eq} = I_{BG} F_{BG} + (I_D)_{BG} F_D + \frac{(I_D)_S}{M^2(\lambda,\omega)} + \left( 2k\,\frac{T_{eff}}{qR_{eq}M^2(\lambda,\omega)} \right)$$

The general detection and current multiplication process for avalanche photodetectors is shown in a schematic in part (a) of Figure 45. The dark current due to surface leakage is referred to in the figure as the un-multiplied dark current. Part (b) of Figure 45 is parallel to part (a). It shows the flow of current in the detector, the sources of noise, and the effect of the avalanche current gain on the signal and noise currents [347, 348].

**(a)**

Excess Noise

Optical Signal

Background Signal

Photoelectric Effect

Signal Current
Background
Dark Current

Avalanche Current Gain

Interaction Circuit

Output Signal + Noise

Unmultiplied Dark Current

Thermal Noise

**(b)**

Optical Signal
Signal Noise
Background Noise
Dark Current Shot Noise

Excess Noise

Thermal Noise
and Unmaltiplied Dark Current Noise

Output Voltage

Figure 45 (a) A block diagram for a general detection process in an APD. (b) Different sources of current at different stages of the process (Reproduced with permission from [347] copyright 1977 Academic Press, and [348] copyright 1966 IEEE).

### 2.3.8    Advances in Infrared Detection Techniques

Several materials were developed over the years allowing for designs of IR detectors with enhanced capabilities, improved performance, and higher system flexibility. Infrared detectors based on InGaAs are very popular nowadays, and have been used widely in different applications. A schematic of a typical detection setup using an InGaAs detector is given in Figure 46. However, the most popular semiconductor for mid wavelength infrared and long wavelength infrared $(3 - 30 \ \mu m)$ has been the mercury-cadmium-telluride (HgCdTe) for over four decades [52]. This comes from the fundamental advantages of this semiconductor material, flexibility of structuring, and

broad spectral coverage. Elliott regards the HgCdTe material as essential to the industry of IR systems as silicon is to the industry of electronics [359].
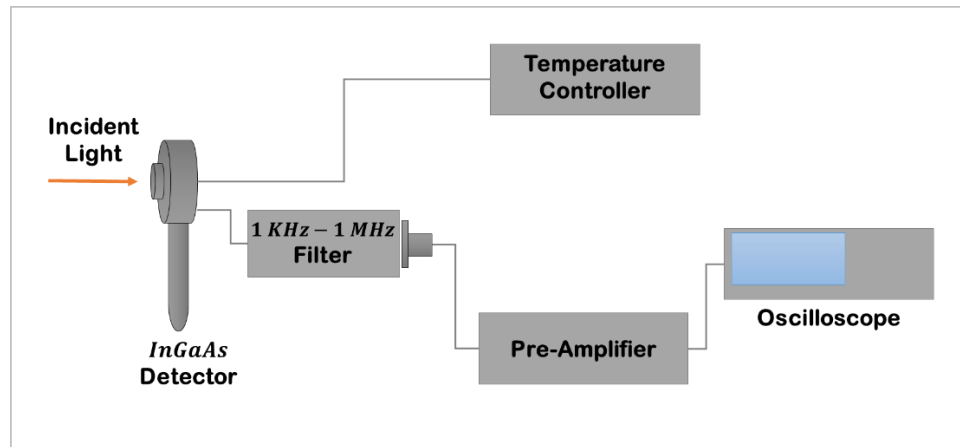
Figure 46 An example showing one part of an experiment in our laboratory where an InGaAs detector is used for detecting methane in the near-infrared.

The first investigation of the HgCdTe material was conducted by Lawson and his colleagues in 1959 to study the properties of mixed crystals of HgTe and CdTe [73]. This is the first time the photovoltaic effects in HgCdTe were reported. Since then, improvements in the design and fabrication techniques of this material have been emerging [51, 360].

A primary advantage of the HgCdTe material is its strong absorption of infrared radiation, which makes it nearly ideal for infrared detection and sensing [360]. This is because large optical absorption coefficients enable high quantum efficiencies. Moreover, a low thermal generation rate is a fundamental property of this material. For example, the

quantum efficiency of a device based on this material with a thickness around $10\ \mu m$ can be close to 100% [361].

The bandgap of HgCdTe is tunable over the $1-30\ \mu m$ range, corresponding to a bandgap energy-tunability between zero and $1.6\ eV$. Thus, it offers ultimate coverage of the whole IR spectral range. HgCdTe material has two compounds; HgTe and CdTe. The mole fraction of CdTe determines the composition, which is referred to as $x$ in $Hg_{1-x}Cd_xTe$. The two compounds have almost the same lattice parameter, so the lattice parameter of the material does not have a strong dependence on the composition $x$ [341]. This is an advantage that allows engineers to grow the bandgap structure with minimal strain [362]. In addition, for values of $x$ less than 0.5, doping the material to be p-type or n-type are both possible [361].

Another key feature is that it can perform in high operating temperatures [53]. This is based on the relatively long carrier lifetimes, which either results in low dark currents or allow the device to operate at higher temperatures, and both are advantageous [341]. High mobility of carriers is also a characteristic of this material [51].

Mercury-cadmium-telluride material is also called MCT referring to the first letters of the names of the three elements. The fundamental properties of this material can be described by the following most frequently used formulas. Using the mole fraction of the CdTe compound $x$ and the operating temperature $T$ , the energy of the bandgap $E_g$ can be written as [363]:

$$E_g = -0.302 + 1.93x - 0.81x^2 + 0.832x^3 + 5.35 \times 10^{-4}(1-2x)T$$

The cutoff wavelength of the material is sensitive to the composition $x$, especially in the long-wavelength infrared LWIR range. Therefore, specifying a value for $x$ in the process of growing HgCdTe layers for device fabrication must consider both the operating temperature and the cutoff wavelength [361]. For HgCdTe layers thicker than 5 $\mu m$, the spectrum of infrared transmission has a sharp cutoff wavelength given by:

$$\lambda = \frac{hc}{E_g} = \frac{1.2398 \text{ eV}\mu\text{m}}{E_g}$$

where $c$ is the speed of light and $h$ is Plank's constant. The intrinsic carrier concentration in this material can be found using the following well-known formula [364]:

$$n_{in} = (5.585 - 3.82x + 0.001753T - 0.001364xT) \times 10^{14} \, E_g^{\frac{3}{4}} \, T^{\frac{3}{2}} \, e^{-\frac{E_g}{2k_BT}}$$

where $k_B$ is Boltzmann constant and $n_{in}$ is in units of $cm^{-3}$. One of the parameters often used to characterize MCT detectors is the electron mass ratio:

$$\frac{m_o}{m_e^*} = 1 + 2F + \frac{E_p}{3}\left(\frac{2}{E_g} + \frac{1}{E_g + \Delta}\right)$$

where $m_o$ is the free electron mass, $m_e^*$ is the electron effective mass, $F = -0.8$, $\Delta = 1$ eV, and $E_p = 19$ eV [365].

Detection in MCT detectors is based on transitions between the valence and conduction bands of the semiconductor, as generally shown in Figure 47. In the valence band there are light and heavy holes, but the density of states of the heavy holes is much greater and therefore they dominate. The effective mass ratio of the heavy holes $\frac{m_{hh}^*}{m_o}$ is almost independent of $x$ [359, 361]. An effective mass ratio 0.443 is used by Hansen *et al* for the heavy hole [364]. Another commonly used value for this ratio, in modelling of IR

detectors, is 0.55 [51]. Advances in technology resulted in well-established practical approaches for device fabrication and manufacturing. However, developing MCT detectors to operate in the LWIR is still facing challenges because of the narrow gap [361].
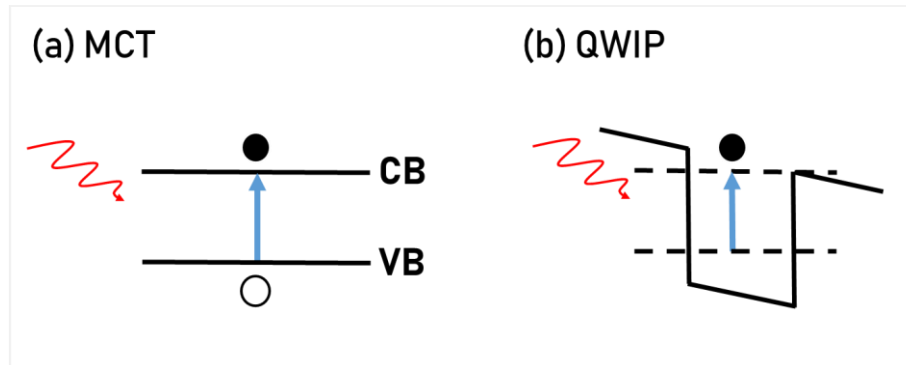


Figure 47 The energy band diagrams of (a) MCT showing an interband electronic transition compared to (b) a quantum well infrared photodetector (QWIP) showing an inter-subband electronic transition.

The outstanding advantages of HgCdTe in the IR region allows to optimize the detector for operation at temperatures ranging from liquid-nitrogen temperature to room temperature. For example, photovoltaic HgCdTe detectors are used in 2D arrays in advanced thermal imaging systems, which require large detection sensitivity and high image resolution [366]. The infrared focal plane arrays (IR-FPAs) are two-dimensional arrays of IR detectors on a focal plane. Despite the fact that HgCdTe can operate at different modes, photodiodes are preferred over photoconductors for 2D focal plane arrays [341]. This is because of the very low power dissipation in photodiodes, which makes

them suitable for large arrays that operate at room temperature. Photodiodes can also operate at a reverse bias or at zero.

The fundamental limits of HgCdTe semiconductor material meet the demand in almost all IR detection systems. However, technological issues related mainly to uniformity and cost of production impose a major limitation. Large area array detectors were developed in consequence to the advances in two major fields. First, new narrow bandgap semiconductor materials were discovered and used in detectors, with significant improvements in device fabrication over the years. And the second contribution comes from the progress in the integrated circuit technology and nanoelectronics [367].

A variety of IR detectors with various operating temperatures are available today. Experimentalists select the suitable detector by looking at the characteristics and limitation factors of the available detectors at the spectral range of interest. IR detectors of high performance capabilities were reviewed recently by Tan and Mohseni [55]. In their review, they provide examples of a large number of materials for detectors at different temperatures based on the normalized detectivity, which is defined as follows [51]:

$$D^* = \frac{\sqrt{A_d\,\mathcal{B}}}{NEP}$$

where $A_d$ is the detector area, $\mathcal{B}$ is the electrical bandwidth, and $NEP$ is the noise-equivalent power. These examples can be seen in Figure 48 [55].
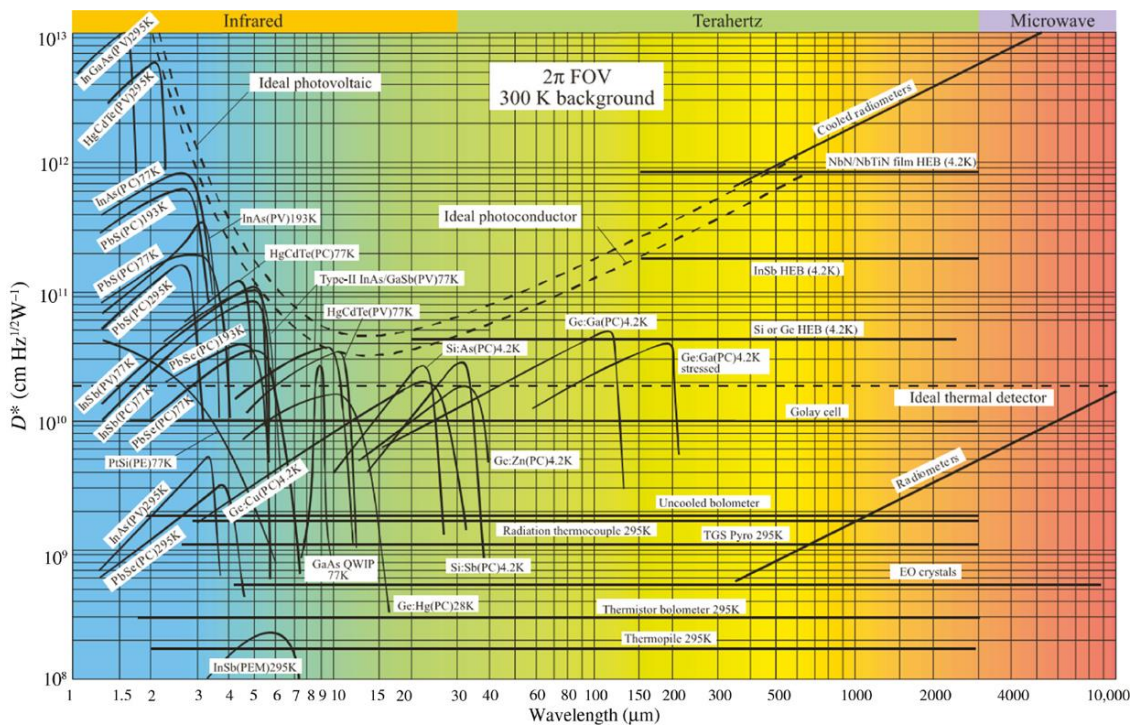
Figure 48 Comparison of the detectivity of various available detectors operating at the indicated temperatures and wavelengths (Reprinted with permission from [55] copyright 2017 Hooman Mohseni et al, De Gruyter).

## 2.4 Optical Ray Tracing

To provide an overall picture of the concepts of laser spectroscopy, it is beneficial to review some general theory related to the propagation of electromagnetic radiation through optical elements [346, 368]. Maxwell's equations and the wave equation are briefly reviewed in Appendix B. In this section, we present some basics of ray tracing since it is essential for understanding and determining the performance of optical systems.

When the dimensions of the light beam and the size of the objects with which it interacts are much larger than the wavelength of light, then we can describe it as rays obeying some geometrical rules [368]. In other words, a ray propagates parallel to the path

138

at the center of a very slowly diverging electromagnetic wave. The general form of the ABCD matrix [346] that relates the input ray ( $r_{in}$ , $r'_{in}$ ) and the output ray ( $r_{out}$ , $r'_{out}$ ) at the input and output planes of an optical system is given by:

$$\begin{bmatrix} r_{out} \\ r'_{out} \end{bmatrix} = \begin{bmatrix} A & B \\ C & D \end{bmatrix} \begin{bmatrix} r_{in} \\ r'_{in} \end{bmatrix}$$

This general description is illustrated in Figure 49.
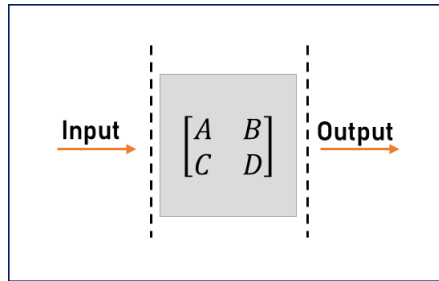


Figure 49 Propagation through a paraxial system described by an ABCD matrix.

For a beam propagating through free space or homogenous medium of length $d$, the ABCD matrix reduces to $\begin{bmatrix} 1 & d \\ 0 & 1 \end{bmatrix}$. Whereas, for propagation through a thin lens of focal length $f$, it reduces to $\begin{bmatrix} 1 & 0 \\ -\frac{1}{f} & 1 \end{bmatrix}$. This matrix, for example, can be deduced from the general expression mentioned above [331]. Let us consider a thin lens of a focal length $f$ and take the axis of symmetry along $z$. Let ( $r_{in}$ , $r'_{in}$ ) represent the input ray and ( $r_{out}$ , $r'_{out}$ ) represent the output ray, where $r$ is the distance from the ray to the $z$ axis, and $r'$ is the slope $r' = \frac{dr}{dz}$. From the definition of a thin lens, we find that $r_{out} =$

$r_{in}$ . The slope for an undeflected central ray in terms of the input slope $r'_{in}$ is given

by $r'_{out} = r'_{in} - \frac{r_{out}}{f}$ . Using a column matrix $\begin{bmatrix} r(z) \\ r'(z) \end{bmatrix}$ to represent a ray at position z, the

two results $r_{out}$ and $r'_{out}$ can be written in a form of matrix multiplication:

$$\begin{bmatrix} r_{out} \\ r'_{out} \end{bmatrix} = \begin{bmatrix} 1 & 0 \\ -\frac{1}{f} & 1 \end{bmatrix} \begin{bmatrix} r_{in} \\ r'_{in} \end{bmatrix}$$

which shows the same result for paraxial ray propagation through a thin lens as we

mentioned. The focal length is greater than zero for a converging lens, and less than zero

for a diverging one.

For the case shown in Figure 50, the matrix algebra of ray propagation through a

free space followed by a thin lens gives $\begin{bmatrix} 1 & 0 \\ -\frac{1}{f} & 1 \end{bmatrix} \begin{bmatrix} 1 & d \\ 0 & 1 \end{bmatrix} = \begin{bmatrix} 1 & d \\ -\frac{1}{f} & 1 - \frac{d}{f} \end{bmatrix}$ . Notice that

the free space matrix is to the right since the beam propagates in free space first. The

arrangement of matrices in the correct order is important for obtaining a correct final result

for the optical system.
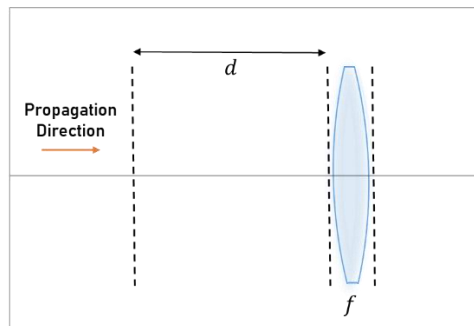


Figure 50 Propagation through free space followed by a thin lens.

A ray directed to a spherical mirror, as shown in Figure 51, experiences the same effect of a thin lens with the focal length being half of the radius of curvature of the mirror $f = \frac{R}{2}$. This gives an ABCD matrix as follows $\begin{bmatrix} 1 & 0 \\ -\frac{1}{f} & 1 \end{bmatrix} = \begin{bmatrix} 1 & 0 \\ -\frac{2}{R} & 1 \end{bmatrix}$.
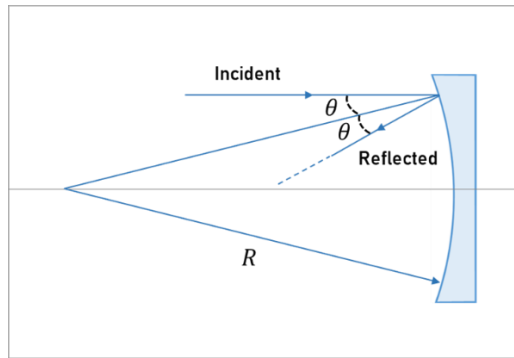


Figure 51 An optical ray enters and exits on the same side of a spherical mirror.

For a ray propagating through a dielectric interface, Snell's law $n_1 \sin \theta_1 = n_2 \sin \theta_2$ is used with the approximation $\sin \theta \approx \theta$ for a paraxial ray, resulting in an ABCD matrix of the form $\begin{bmatrix} 1 & 0 \\ 0 & \frac{n_1}{n_2} \end{bmatrix}$ .An illustration is given in Figure 52, where $n_1$ and $n_2$ are the refractive indices of the two media.
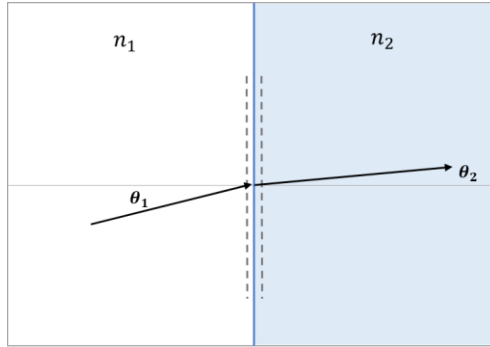
Figure 52 Ray propagation through a plane dielectric interface.

A similar ray matrix as the one mentioned previously for free space can be used to obtain the ABCD matrix for a system where a ray propagates through a dielectric of thickness $d$, which is shown in Figure 53. The matrices are applied in cascade and matrix multiplication takes place in several steps. At first, a paraxial ray propagating from a medium of refractive index $n_1$ to a medium of a dielectric of refractive index $n_2$ results in an ABCD matrix of the form $\begin{bmatrix} 1 & 0 \\ 0 & \frac{n_1}{n_2} \end{bmatrix}$, as obtained earlier. At second, the paraxial ray propagates along a distance equal to the thickness $d$ of the dielectric material, which is described by the matrix $\begin{bmatrix} 1 & d \\ 0 & 1 \end{bmatrix}$. Third, a matrix of the form $\begin{bmatrix} 1 & 0 \\ 0 & \frac{n_2}{n_1} \end{bmatrix}$ represents ray propagation from the dielectric of refractive index $n_2$ to a medium of refractive index $n_1$, such that:

$$\begin{bmatrix} r_{out} \\ r'_{out} \end{bmatrix} = \begin{bmatrix} 1 & 0 \\ 0 & \frac{n_2}{n_1} \end{bmatrix} \begin{bmatrix} 1 & d \\ 0 & 1 \end{bmatrix} \begin{bmatrix} 1 & 0 \\ 0 & \frac{n_1}{n_2} \end{bmatrix} \begin{bmatrix} r_{in} \\ r'_{in} \end{bmatrix} = \begin{bmatrix} 1 & 0 \\ 0 & \frac{n_2}{n_1} \end{bmatrix} \begin{bmatrix} 1 & \frac{n_1}{n_2}d \\ 0 & \frac{n_1}{n_2} \end{bmatrix} \begin{bmatrix} r_{in} \\ r'_{in} \end{bmatrix} = \begin{bmatrix} 1 & \frac{n_1}{n_2}d \\ 0 & 1 \end{bmatrix} \begin{bmatrix} r_{in} \\ r'_{in} \end{bmatrix}$$
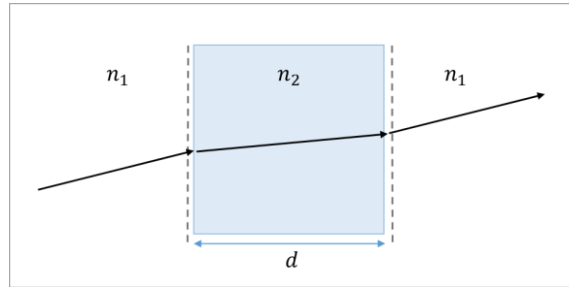
Figure 53 Ray propagation through a dielectric medium of thickness $d$.

## 2.5 Enhancement Cavities and Optical Cells

### 2.5.1  High Finesse Cavities

A major step towards improving the sensitivity of measurements in absorption spectroscopy experiments is to increase the length of interaction between the light beam and the molecular species in the gas sample [9, 18, 23, 26, 47]. Techniques that rely on this concept are commonly referred to as cavity-enhanced absorption spectroscopy (CE-AS) techniques [2, 5, 8, 10]. Using an enhancement cavity permits for higher measurement sensitivities and promising system compactness.

The Beer-Lambert law, discussed in Section 2.1.3, relates the ratio of transmitted and incident light intensity to the amount of absorption of electromagnetic radiation by the gaseous molecules [68-70]. This law concludes that absorption is proportional to the concentration of molecules and the interaction length between the molecules and the light beam. For this reason, increasing the length of interaction has been a leading approach in absorption spectroscopy experiments.

Considering the desire for compact system designs, it is important to enhance light-matter interaction without using a large area on the optical table. This can be achieved

with highly reflective (HR) mirrors, which allow for a large number of optical passes with minimum reflection losses and therefore increase the interaction length. Recent work show mirror reflectivity of 99% or even higher around wavelengths of interest in the near and mid-IR regions [9, 12, 15].

When light bounces between cavity-mirrors, it suffers from optical losses due to diffraction, absorption, and scattering of light. The cavity finesse ($\mathcal{F}$) is a parameter that has an inverse proportionality with the total losses inside the cavity. It is commonly used in spectroscopic experiments to determine the quality of the passive optical cavity. Using high finesse cavities can reduce the losses significantly and improve measurement sensitivity. For an optical cavity of two HR mirrors, the finesse can be determined using the following equation [369]:

$$\mathcal{F} = \frac{\pi \, (R_1 \, R_2)^{\frac{1}{4}}}{1 - (R_1 \, R_2)^{\frac{1}{2}}}$$

Here, $R_1$ is the reflectivity of the first mirror and $R_2$ is the reflectivity of the second mirror. In this expression, scattering losses are neglected. In the limit of low losses and using mirrors of the same reflectivity $R$, this expression can be reduced to:

$$\mathcal{F} \cong \frac{\pi}{1 - R}$$

To give an example, a finesse in the order of tens of thousands can be achieved by using mirrors of high reflectivity in the range $R \geq 0.9999$ [370]. We obtained a value of $31{,}000$ for our high-finesse ringdown cavity, as discussed later in Section 4.1. Hindle *et al* applied terahertz spectroscopy using a Fabry-Pérot cavity of finesse $\mathcal{F} \sim 3200$ [371].

In a very recent work by Zaborowski and coworkers, $\mathcal{F} = 637000$ was achieved in a cavity ringdown spectrometer towards studying molecular electrodynamics [372]. An illustration of a simple system with a high finesse cavity is shown in Figure 54.
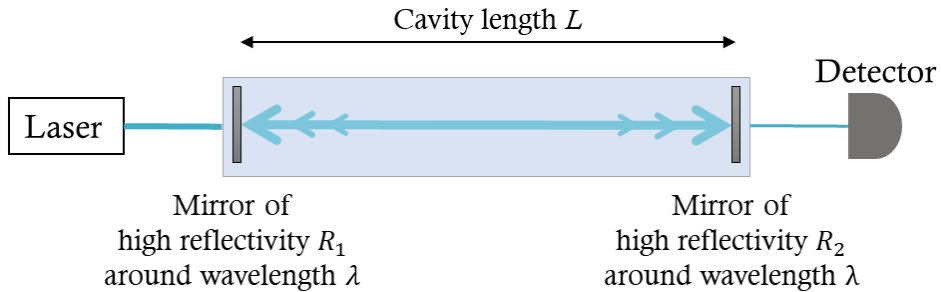


Figure 54 An illustration of a high finesse cavity which uses mirrors of high reflectivity at wavelengths of interest to increase the effective interaction with the sample.

Coupling the light effectively into the high finesse cavity requires mode-matching between the light source and the cavity. Section 4.1.4 covers the mode-matching step with more details, but let us explain it briefly in this section. In frequency domain, two resonant cavity modes have a spacing between them known as the free spectral range ($FSR$) of the cavity, which can be written as [370]:

$$FSR = \frac{c}{2L + c \left( \frac{\partial \phi}{\partial \omega} \right) \Big|_{\omega}}$$

Here, $c$ is the speed of light, $L$ is the cavity length, and $c \left( \frac{\partial \phi}{\partial \omega} \right) \Big|_{\omega}$ is the frequency-dependent term responsible for the intracavity dispersion. A low dispersion is desirable as it allows

for a more effective overlapping of resonant modes, especially when the light source has a broad bandwidth. Since the cavity finesse and the $FSR$ are related, the finesse can be expressed in terms of the $FSR$ as follows:

$$\mathcal{F} = \frac{FSR}{\Delta v}$$

where $\Delta v$ is the linewidth. This expression is commonly used in cavity-enhanced techniques [10].

When setting up a mode-locked optical cavity, an important element to consider is the cavity length. The suitable cavity length depends on many factors including the properties of the radiation source used for the experiment. Given that efficient mode-matching is obtained, the intensity of the resonant mode builds up inside the cavity, as further discussed in Section 4.1.4 of the experimental part. Figure 55 shows the intensity build-up after bouncing multiple times between cavity mirrors. As time goes by, the optical power confined inside the cavity increases. This increase allows for improved sensitivity, which is also explained in Section 4.1.
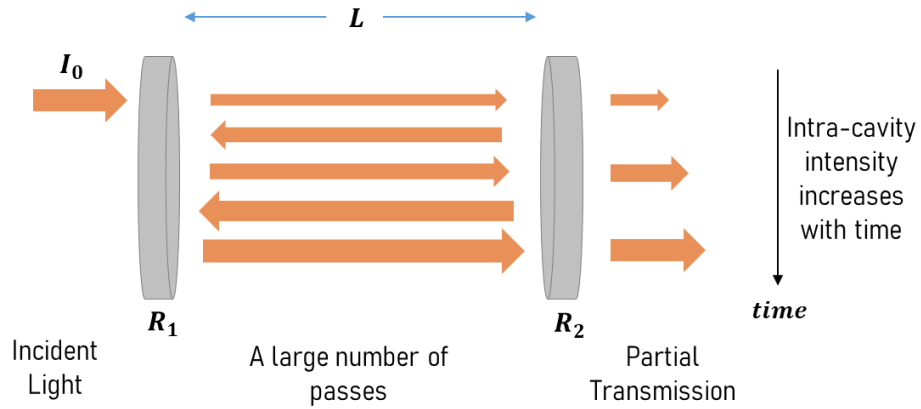
Figure 55 A simplified schematic of the intensity build-up after several passes between highly reflective cavity mirrors of a high-finesse optical cavity.

To describe the transmitted field mathematically, we can start with adding all fields inside the cavity:

$$E_0 = T \, E_0 \, e^{i\omega t}$$

$$E_1 = T \, R^2 \, E_0 \, e^{i(\omega t - 2L|\vec{k}|)}$$

$$E_2 = T \, R^4 \, E_0 \, e^{i(\omega t - 4L|\vec{k}|)}$$

$$E_n = T \, R^{2n} \, E_0 \, e^{i(\omega t - 2nL|\vec{k}|)}$$

$$E_{cavity} = \sum_{n=0}^{\infty} E_n = E_0 \, e^{i\omega t} \left( \frac{T}{1 - R^2 e^{-i\delta}} \right)$$

This expression describes the field at the coupling mirror, where $\delta = 2L|\vec{k}|$. The field at the transmitting mirror after incorporating the transmission coefficient is:

$$E_T = E_0 \, e^{i\omega t} \left( \frac{T^2 e^{-i\delta}}{1 - R^2 e^{-i\delta}} \right)$$

The transmitted intensity can be written in terms of the cavity finesse as:

147

$$I_T = \frac{1}{1 + F \ sin^2(\frac{\delta}{2})} I_0$$

where $F$ is the finesse coefficient given by $F = \left(\frac{2R}{1-R^2}\right)^2$ and is related to the cavity finesses

by:

$$\mathcal{F} = \frac{2\pi}{\Delta\delta} = \frac{\pi\sqrt{F}}{2}$$

This expression defines the finesses in terms of the full-width at half-maximum phase

width ($\Delta\delta$) and the cavity mode spacing ($2\pi$).

Long optical path-lengths can be achieved when a high finesse cavity is used in

the experiment. This length is also known as the effective path-length ($L_{eff}$). Lengths that

range between hundreds of meters to several kilometers are reported based on different

experimental techniques [9, 23, 26, 47]. For example, we obtained an effective path-length

of $12 \ Km$ in our experiment using a cavity with a high finesse equal to $31,000$. This

experiment is described in Section 4.1. Hindle and colleagues achieved a length of

interaction of $1 \ Km$ for their terahertz spectrometer [371]. The effective path-length inside

the cavity, during which light-matter interaction occurs, can be calculated using this

equation:

$$L_{eff} = \frac{2\mathcal{F}}{\pi} L$$

where $\mathcal{F}$ is the cavity finesse and $L$ is the cavity length, which is equal to the distance

between the two mirrors as illustrated in Figure 54. Another approach to increase the

interaction length depends on increasing the number of reflections on the HR mirrors

without turning the incident light off, as described in the following section.

*2.5.2   Multipass Optical Cells*

Different types of multipass cells have been used to enhance light-matter interaction by allowing for a large number of passes before the light beam exits the cell [18, 373]. Herriott cells and White cells are common types of multipass cells [374-376]. In many research groups, several unique designs were developed for absorption spectroscopy applications using different cell-configurations [12, 19, 377-379]. Comparing to high finesse cavities, absorption of radiation inside a multipass cell depends on the number of passes, and the power of the output beam is measured without blocking the incident beam or turning it off. Moreover, the beam enters and exits the cell through a hole, or two different holes, while there are no holes on the mirrors of a high finesse cavity. An advantage of multipass cells over high finesse cavity is that mode-matching is not required. However, beam-adjustment lenses can be used to reduce beam-divergence inside the multipass cell [12].

In general, a multipass optical cell is composed of highly reflective mirrors at the two ends of the cell. A hole on one of the mirrors allows the beam to enter and exit the optical cell. Most configurations use the same hole as beam entrance and exit, while in other configurations two holes are used; one as beam entrance and the other as beam exit. A simplified version of a multipass system is schematically shown in Figure 56.

In some configurations, the mirrors at the two ends are divided into smaller mirrors or sectors towards an easier alignment of the optical path inside the cell. A good example is the multipass cell used in one of our experiments, which consists of three mirrors at each side of the cell [12]. With a distance $d = 1\ m$ between the two sides of the cell and

149

a total number of passes equal to 580, we obtained an interaction length of 580 $m$, as explained explicitly in Section 4.2.2. An algorithm is used to calculate the reflection pattern on the mirrors, which helps to achieve a long interaction length and allows for proper beam propagation until the beam exits the cell.
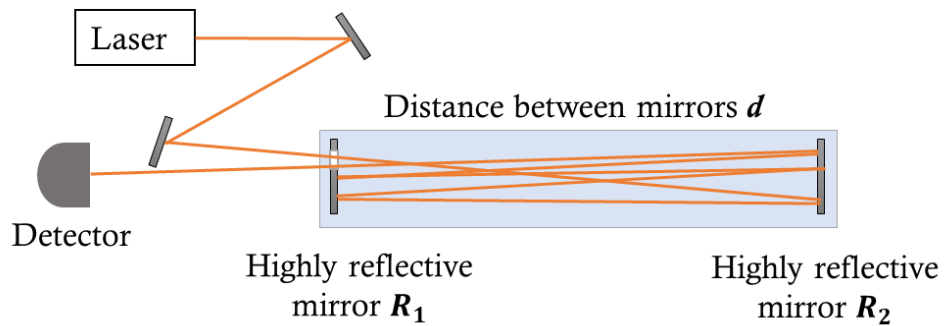


Figure 56 A schematic of a simple system with a multipass optical cell that employs two highly reflective mirrors. Two mirrors are also used outside of the cell to align the path of the laser beam. The beam follows a certain path inside the cell until the output beam is detected.

# 3. EXPERIMENTAL TOOLS AND INSTRUMENTATION

## 3.1 Diffraction-Grating-Based Spectrometers

Diffraction effects have been known for over two centuries. The first reported study of diffraction of light by a periodic structure on a surface was in 1786 by the astronomer David Rittenhouse. The effect was observed by his friend Francis Hopkinson, who later shared it with Rittenhouse. Hopkinson viewed light emitted by a distant source through a handkerchief made from fine French silk. He noticed light patterns that did not change as he moved the handkerchief. To investigate the effects, Rittenhouse used fine screws made by a watchmaker and fixed parallel hairs across the screws on a small half-inch square. Then in a dark room, he used his tool of 53 apertures to observe the light coming from a small opening in the window shutter. What he saw was three images of almost equal brightness, and other images on both sides but fainter, colored, and hardly noticeable. He also noticed that red light was bent more than blue light, and he assigned the effects to diffraction [380].

A scientific study published in 1803 by Thomas Young described the behavior of light after passing through a transmission grating [381]. The grating he used is a glass stage micrometer with a ruling of 500 lines per inch. He investigated light from four different directions and used the sine of the angles to find the wavelength of the colors he observed [382]. Table 10 records his findings.

Table 10 Results of Young's Experiment

| Start at | Red | Yellow | Green | Blue | Violet | Stop at |
|----------|-----|--------|-------|------|--------|---------|
| 675 nm | 650 | 576 | 536 | 498 | 442 | 424 nm |

In 1822, a patent by Sir John Batron described decomposition of light using crossed gratings on steel, which were cut by a ruling engine that uses diamond. The purpose of his ruling engine was to make decorative buttons with rainbow colors to be used for men waistcoats at that time [383]. Later, his idea of using a ruling engine contributed the development of grating-based products that are available today.

The first scientist to study the optical behavior of gratings seriously was Fraunhofer. His thorough investigation of gratings, which involved higher orders, polarization effects, diffraction efficiencies, and instrumental operating in collimated light, is the reason behind calling him "the father of grating technology" [382]. He had an optical company in Germany, where he was the manager of the optical shop. Therefore, the accuracy of the refractive index measurements of glass was a great concern to him [384-386]. His work on diffraction gratings was elevated after he repeated in 1821 the experiment by Rittenhouse, which uses fine wire gratings [387]. Further improvements in design and manufacturing of diffraction gratings continued, and these days it is considered as a well-developed field. Commercial fast recording IR spectrometers were available around 1946, many of which employed diffraction gratings [388].

A mathematical description of the diffraction of light by gratings is beneficial towards understanding how gratings work and how to use them in experiments and instruments. Let us consider that the wave field is along y-direction and represent it in an exponential form using the base of the natural logarithms $e$ and the complex number $i = \sqrt{-1}$ as follows:

$$y = a\, e^{i2\pi\left(vt - \frac{x}{\lambda}\right)} = a\, e^{i2\pi vt} e^{-i2\pi \frac{x}{\lambda}}$$

where $v$ is the frequency of oscillation, $\lambda$ is the wavelength, $x$ is the distance of any given point from the origin, and $t$ is the time. We can also represent $y$ as a function of the angular frequency $\omega = 2\pi v$ and the wave number $k = \frac{2\pi}{\lambda}$ in the form $y = a\, e^{i(\omega t - kx)}$.

For waves of the same frequency $v$, the time-varying factor $e^{i2\pi vt}$ stays the same and therefore we can ignore it. The factor $a\, e^{-i2\pi \frac{x}{\lambda}}$ is the complex amplitude of the wave. Adding two or more waves can be done by adding their complex amplitudes:

$$Ae^{i\varphi} = A[\cos(\varphi) + i\sin(\varphi)] = a_1\cos(\varphi_1) + a_2\cos(\varphi_2) + i[a_1\sin(\varphi_1) + a_2\sin(\varphi_2)]$$

$$= a_1 e^{i\varphi_1} + a_2 e^{i\varphi_2}$$

where we used Euler's theorem:

$$e^{i\varphi} = \cos(\varphi) + i\sin(\varphi)$$

The intensity is obtained from the real amplitude by multiplying the complex amplitude with its complex conjugate:

$$I = |A|^2 = Ae^{i\varphi} \times Ae^{-i\varphi} = A^2 e^{i(\varphi - \varphi)} = A^2$$

Here we used the complex conjugate of the function, which by definition has the same real part as the function but the complex part is equal in magnitude and opposite in sign.

153

Consider a diffraction grating in the form of a series of equally spaced slits [387]. With amplitude $a$ and a phase difference $\delta$, between each adjacent slits, the complex amplitude corresponding to the nth slit can be written as $ae^{in\delta}$. Adding all contributions from the $N$ slits gives the result for the grating as:

$$Ae^{i\varphi} = a(1 + e^{i\delta} + e^{i2\delta} + \cdots + e^{i(N-1)\delta}) = a\frac{1 - e^{iN\delta}}{1 - e^{i\delta}}$$

Then we multiply this result by its complex conjugate to arrive at the following expression for the intensity:

$$A^2 = a^2\frac{(1 - e^{iN\delta})(1 - e^{-iN\delta})}{(1 - e^{i\delta})(1 - e^{-i\delta})} = a^2\frac{1 - \cos(N\delta)}{1 - \cos(\delta)} = a^2\frac{\sin^2(N\gamma)}{\sin^2(\gamma)}$$

where

$$\gamma = \frac{\delta}{2} = \frac{\pi\, d\, \sin(\theta)}{\lambda}$$

We used the expression of the phase $\delta$ from the result of a single slit case, as shown in Figure 57. For a single slit, the amplitude after the aperture is the same, but the phase depends on the distance traveled. If point (A) in the figure is our reference, then from point (C) we get a phase difference $\frac{2\pi\,(CS-AS)}{\lambda}$. A series of $N$ slits resembles a diffraction grating with $d$ being the period of the grating and $\theta$ being the blaze angle.
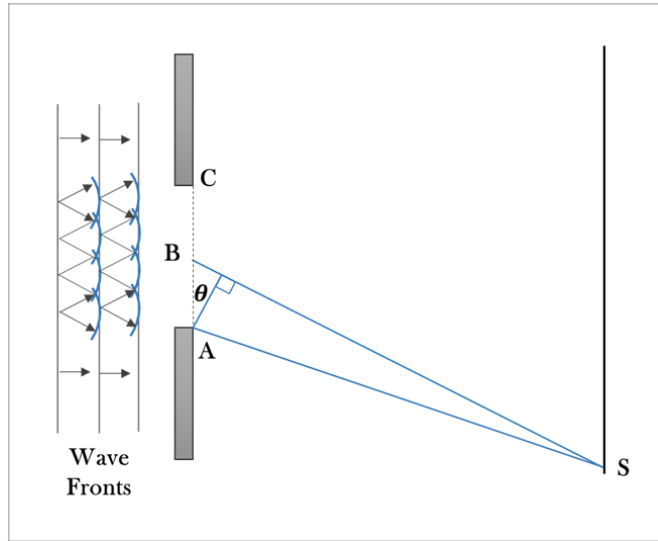
Figure 57 Diffraction of waves by an aperture (Reproduced with permission from [387] copyright 1982 Academic Press).

Assume the phase difference between wave contribution from the beam center and the edges is $\beta$ , then the amplitude at point (S) for the beam is $\sum a \; \frac{\sin(\beta)}{\beta}$ . Substituting it to the intensity of $N$ slits yields:

$$I = A^2 = \frac{\sin^2(\beta)}{\beta^2} \cdot \frac{\sin^2(N\gamma)}{\sin^2(\gamma)}$$

To visualize the diffraction pattern resulted from this, we consider the term $\frac{\sin^2(N\gamma)}{\sin^2(\gamma)}$. The numerator $\sin^2(N\gamma)$ is equal to zero whenever $\gamma = \frac{p\pi}{N}$, where $p = 0,1,2,3,...$ is an integer. However, at $p = 0$ and $p = l\pi$, where $l$ is an integer, the term $\frac{\sin^2(N\gamma)}{\sin^2(\gamma)}$ is indeterminate. If we take the limit $\gamma \to l\pi$, we will get:

$$\lim_{\gamma \to l\pi} \left( \frac{\sin(N\gamma)}{\sin(\gamma)} \right) = \lim_{\gamma \to l\pi} \left( N \frac{\cos(N\gamma)}{\cos(\gamma)} \right) = \pm N$$

155

This means that the function $\frac{sin(N\gamma)}{sin(\gamma)}$ has maximum values at $\gamma = l\pi$, with an intensity equal to that diffracted by a single slit times $N^2$. Recalling the expression we obtained for $\gamma$, we find that this diffraction condition is equivalent to the condition $d\ sin(\theta) = l\pi$. At $\gamma = \frac{p\pi}{N} + \frac{\pi}{2}$, subsidiary maxima appear with an intensity that decreases the further they are from a main maximum. Shown in Figure 58 is an example of the resulting intensity distribution for the case of wave propagation through $N$ slits [387]. Between two main maxima, there are $N - 2$ secondary maxima.
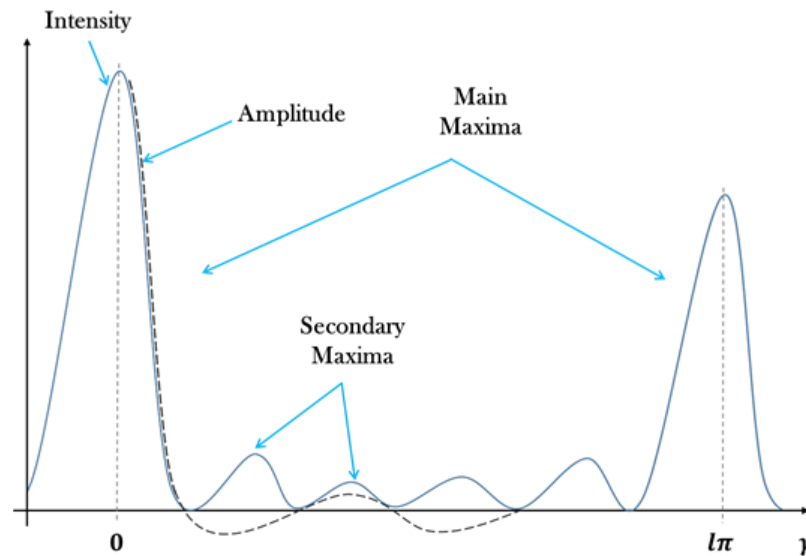


Figure 58 The form of the diffraction pattern produced by a series of narrow slits.

So far, we considered the case of a plane wave with a normal incidence on a grating, and we arrived at the required condition for light diffraction. The more general case is when we have an arbitrary angle of incidence $\alpha$. Let $\beta$ be the angle of transmission,

or reflection, then the path difference between the source and the image must be equal to a whole number of wavelengths $m\lambda$ so that a diffraction order is formed [389]. This can be summarized in a fundamental equation for gratings as follows, where $m$ is an integer that indicates the order of diffraction:

$$d \sin(\alpha) + d \sin(\beta) = m\lambda$$

The order number is equal to zero for the reflected beam $\beta = \alpha$, which is not deviated, and we call that beam the "0-order". Whereas, the order number takes a positive or a negative sign depending on the location of the diffracted beam from the zero-order. Figure 59 demonstrate the difference between a reflected diffraction order and a transmitted one. In practice, reflective diffraction gratings are more commonly used in experiments and applications of spectral analysis [387].
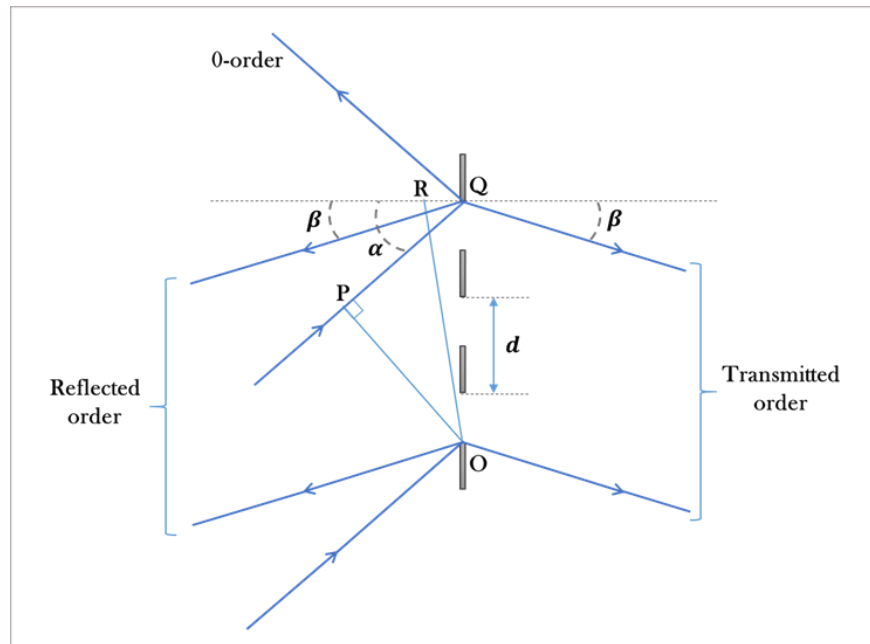
Figure 59 The Sign convention for orders of diffraction. The difference between reflected and transmitted orders is illustrated (Reproduced with permission from [387] copyright 1982 Academic Press).

The grating equation is of fundamental importance in determining the properties of diffraction gratings. It not only refers to the orders of diffraction, but also explains how the spectrum is formed. Let us consider a set of grooves blazed at different angles. Figure 60 illustrates this concept. By controlling the optical path across each groove, the grating will support a chosen order. In other words, a grating can be blazed for a specific order by controlling the shape of its grooves.
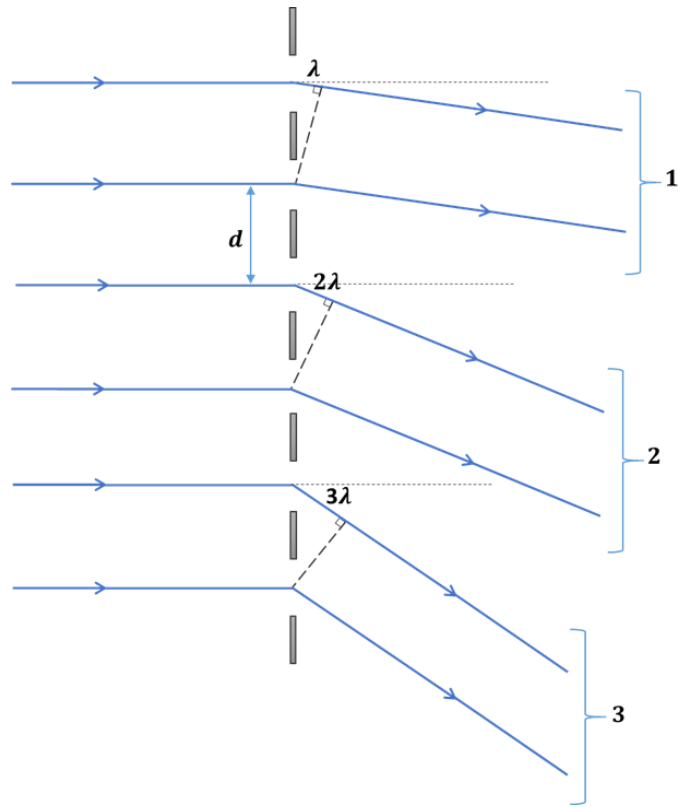
Figure 60 Generation of diffracted orders by considering different grove shapes.

The spectrum produced by a diffraction grating depends on the wavelength of the incident radiation, as the grating equation shows. To find the dependence of the variation of angle $\beta$ on the wavelength $\lambda$, we differentiate the equation with respect to $\lambda$:

$$\frac{\partial}{\partial \beta}\{d\left[sin(\alpha) + sin(\beta)\right]=m\,\lambda\}$$

$$d\,cos(\alpha)\frac{\partial \alpha}{\partial \beta} + d\,cos(\beta) = m\frac{\partial \lambda}{\partial \beta}$$

Consider a spectrograph with a fixed angle of incidence, then we have $\frac{\partial \alpha}{\partial \beta} = 0$ , which yields:

$$\frac{\partial \beta}{\partial \lambda} = \frac{m}{d \cos(\beta)}$$

This result is known as the angular dispersion of a grating. It is a function of the order number $m$, the period of the grating $d$, and the cosine of the diffraction angle $\beta$. For a grating of a given period $d$, the angular dispersion increases for higher diffraction orders. Whereas, $\frac{\partial \beta}{\partial \lambda}$ for a chosen order increases if we use a grating with a smaller period $d$. The angular dispersion also increases for large angles of diffraction. In the limit $\beta \rightarrow 90^o$ we have $\frac{\partial \beta}{\partial \lambda} \rightarrow \infty$. Recall that $\beta$ can be determined from the grating equation as a function of $m$, $d$, and $\alpha$.

A linear spectrum is more practical in spectroscopic experiments. The linear dispersion is found from the angular dispersion and the focal length $f$ of the lens, or curved mirror, used with the spectrograph:

$$\frac{\partial x}{\partial \lambda} = f \frac{\partial \beta}{\partial \lambda}$$

given that the focal plane and the diffracted beam are perpendicular to each other. If the focal plane is inclined at an angle $\emptyset$, a plate factor $F = \frac{1}{\cos(\emptyset)}$ should be included so that:

$$\frac{\partial x}{\partial \lambda} = F f \frac{\partial \beta}{\partial \lambda}$$

Up to this point, the expressions of dispersion are applicable to the case when the light in incident on the grating at a fixed angle [387]. This is found in spectrographs, which record the spectrum on a photographic plate. However, this dispersion does not fully describe a monochromator because a monochromator involves rotation of the diffraction grating.

160

In general, a monochromator is an optical instrument used to select a portion of the incident radiation. The optical elements and their arrangement inside a Czerny–Turner monochromator are shown schematically in Figure 61. It consists of a grating, two fixed slits; one as an entrance and one as an exit, and two curved mirrors. This first mirror collimates the light beam and the second mirror focuses the diffracted beam at the exit slit. The width of this slit can be adjusted to allow a narrow band of wavelengths to exit the instrument and get measured by a detector. This instrument enables mechanical rotation of the diffraction grating, which allows for scanning and recording the whole spectrum. In this case, both angles $\alpha$ and $\beta$ are changing with respect to $\lambda$, but the difference between them remains the same; $\alpha - \beta = constant$.
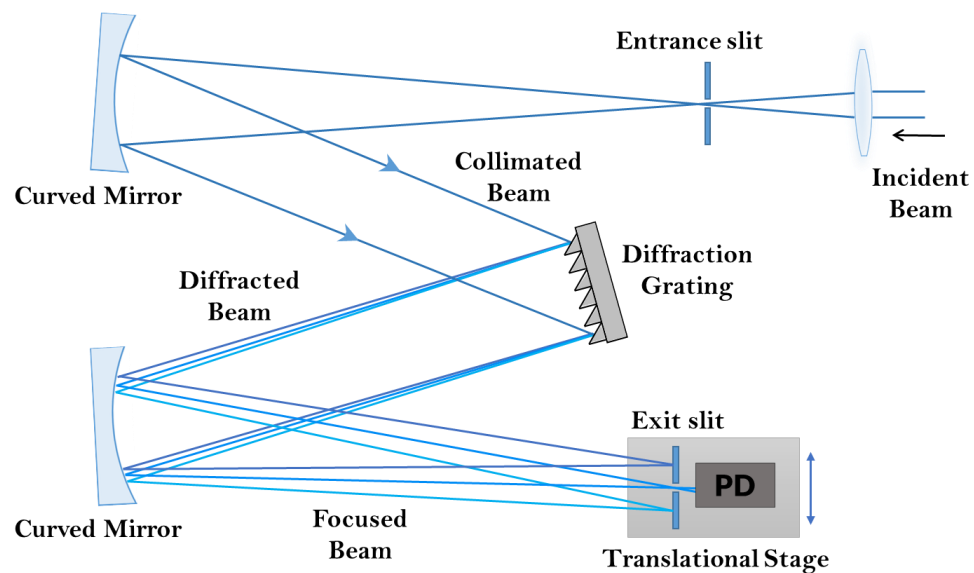


Figure 61 A schematic of a Czerny–Turner monochromator.

Let us consider the case of "Littrow mounting" for simplicity. In this case, the beam is incident along the normal of the grating and the diffracted beam takes the same path of the incident beam, as illustrated in Figure 62. The angles of incidence and diffraction are equal, hence the grating equation becomes:

$$2d \sin(\theta) = m\lambda$$

From this, we can find the relation between the change in the angle of rotation and the shift in the wavelength passing through the instrument:

$$2d \cos(\theta)\, \partial\theta = m\, \partial\lambda$$

$$\frac{\partial\theta}{\partial\lambda} = \frac{m}{2\, d \cos(\theta)} = \frac{\tan(\theta)}{\lambda}$$
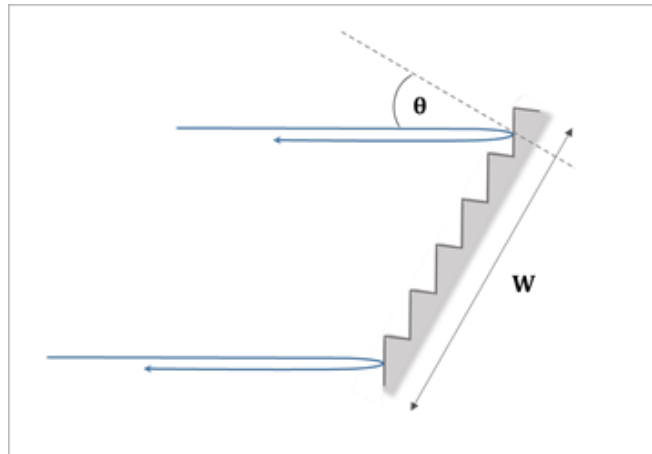


Figure 62 An illustration of a Littrow mounting of diffraction gratings.

Comparing the result $\frac{\partial\theta}{\partial\lambda}$ for a Littrow case with the one we obtained before for

angular dispersion $\frac{\partial\beta}{\partial\lambda}$, we find that $\frac{\partial\theta}{\partial\lambda} = \frac{1}{2}\frac{\partial\beta}{\partial\lambda}$. This is reasonable, since we know that by

rotating a mirror with an angle, the beam reflected on it will rotate by twice that angle.

However, using a monochromator requires us to consider the dependence of the angular

spread of the spectrum on the rotation of the grating.

The resolution of a spectroscopic experiment is a measure of its capability to detect

a small change in the wavelength. The smaller the change, the higher the resolution. In

general, the resolution is a function of all elements, used in the instrument, that adjust or

redirect the light beam. The resolution of a monochromator is not only determined by the

grating, but is also limited by other factors such as the size of the entrance slit.

From the result of the diffraction pattern of an aperture, we consider the diffraction

in the focal plane of a spectrometer using a transmission grating, as Figure 63 shows. The

intensity at a point $x$ can be written as:

$$I_x = I_o \frac{sin^2(\gamma)}{\gamma^2}$$

where $\gamma$ is the phase difference between contributions from the edge and the center of the

aperture, as explained earlier.

For an aperture, the first minimum occurs at $\gamma = \pm\frac{\pi}{N}$. Based on the result we have derived

previously $\gamma = \frac{\pi\, d\, \sin(\theta)}{\lambda}$ , a generalized expression of $\gamma$ for a grating of width $W$ can be

written as:

$$\gamma = \frac{W'}{N}\frac{\pi \sin(\partial\beta)}{\lambda}$$

163

and the angle $\partial\beta$ in Figure 63 can be written in terms of $x$ and $f$ so that the first minimum arises at:

$$W' \frac{\pi}{\lambda} \sin(\partial\beta) = W' \frac{\pi}{\lambda} \frac{x_o}{f} = \pi$$

Thus we get:

$$x_o = \frac{f\lambda}{W'}$$
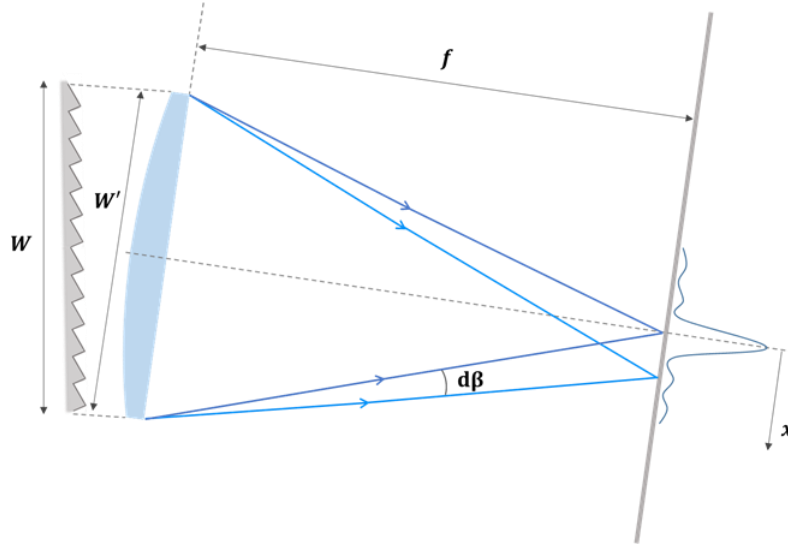


Figure 63 Resolving different wavelengths by a grating (Reproduced with permission from [387] copyright 1982 Academic Press).

To interpret this result, assume we have two wavelengths in our beam and the difference between them is $\Delta\lambda$. Then, the displacement along $x$ direction of one wavelength with respect to the other is:

$$\Delta x = \frac{mf}{d \cos(\beta)} \Delta\lambda$$

164

where we used the expression of the linear dispersion $\frac{\partial x}{\partial \lambda}$ that we derived previously.

An instrument with a high resolution is capable of resolving the power of each component. In making such instrument or setting up an experiment, it is essential to determine how close the patterns can be without emerging to one another. According to Rayleigh criterion, this requirement is met when the maximum of a pattern coincides with the minimum of the next pattern, as shown in Figure 64. This refers to the condition $\Delta x = x_o$, which gives:

$$\frac{mf}{d \cos(\beta)} \Delta\lambda = \frac{f}{W'} \lambda$$
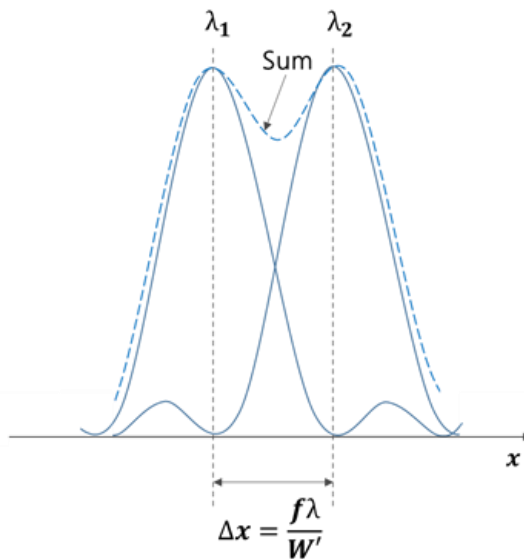


Figure 64 Rayleigh criterion for overlapping wavelengths.

From Figure 63, we have $W' = W \cos(\beta)$, so the equation reduces to:

$$\frac{\lambda}{\Delta\lambda} = \frac{mW}{d} = mN$$

where $N$ is the total number of grooves and $m$ is the order of diffraction. All the grooves have to be illuminated for the best results. Recall the grating equation $d[\sin(\alpha) + \sin(\beta)] = m\lambda$, we can substitute for $\frac{m}{d}$ to get:

$$\frac{\lambda}{\Delta\lambda} = \frac{W}{\lambda}[\sin(\alpha) + \sin(\beta)]$$

which in Littrow mounting is written:

$$\frac{\lambda}{\Delta\lambda} = \frac{2W}{\lambda}\sin(\theta)$$

The resolution of a grating is a dimensionless quantity that describes the ability of the grating to resolve the power of the incident light beam. It characterizes the grating and is independent of other mechanical and optical components of the system. Therefore, in most occasions it is preferable to use the term "resolving power" to describe gratings. Whereas, the resolution of a spectrometer is expressed in spectral units and it depends on many factors. In addition to the resolving power of the grating, it also depends on slit size, focal length, system alignment, and quality of optical components.

The expressions we obtained for the resolving power of a grating are used universally even though they are based on Rayleigh criterion which is quiet arbitrary. First, it assumes that images corresponding to different wavelengths have the same intensity, but in practice this is not the case. Second, it considers that a detectable pattern should at least have its maximum at the minimum of the next pattern. However, by applying

advanced image processing techniques we can improve the image resolution and resolve overlapping patterns.

Hence, the resolution is not only a function of the spectrometer, but is also affected by the lower limit of detection and image enhancement limits. Moreover, the uniformity of the intensity distribution at the aperture and the shape of the aperture are other factors that contribute to the resolution. However, the Rayleigh criterion preserves its significance and applicability for most purposes.

The three expressions of $\frac{\lambda}{\Delta\lambda}$ are of high importance and it is beneficial to discuss the physical meaning behind them. For a given $d$ and $m$, the resolving power increases with the use of a grating of larger width $W$. Also, we can achieve the same resolving power if we use a grating of larger $m$ but with smaller $d$. For example, a grating of period $d$ used in the first order $m = 1$ gives the same result as that of a period $2d$ used in second order $m = 2$. The simplest result to remember is the product of grooves total number $N$ and the diffraction order $m$. The third expression relates the resolving power of a grating to the angles of incidence and diffraction, $\alpha$ and $\beta$ respectively. From Figure 65, we find that the resolving power is equal to the number of wavelengths contained in the difference of the light paths traveled from the two edges of the grating. Referring to the figure, we get the same result [387]:

$$RP = \frac{AP + PB}{\lambda} = \frac{W[\sin(\alpha) + \sin(\beta)]}{\lambda}$$
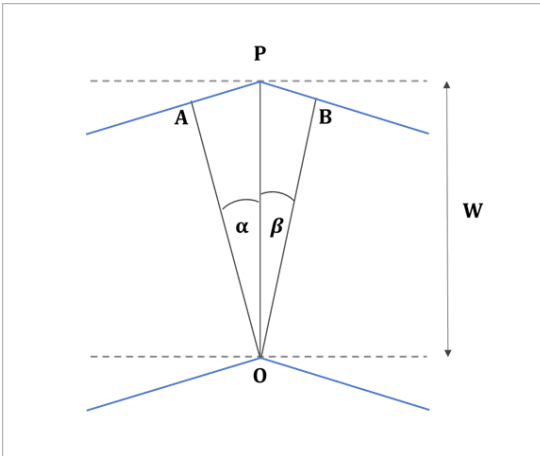
Figure 65 An illustration of the difference in path lengths introduced by the two edges of a grating (Reproduced with permission from [387] copyright 1982 Academic Press).

Note that when we compare this result with the resolving power of a multiple beam interferometer $\frac{\lambda}{\Delta\lambda} = \frac{2L}{\lambda}\left(\frac{\pi R}{1-R^2}\right)$, we find an equivalence. The first part $\frac{2L}{\lambda}$ is the number of wavelengths in one round trip path, where $L$ is the length between the mirrors. The second part $\frac{\pi R}{1-R^2}$ is a measure of the finesse of the etalon, which denotes the effective number of inter-reflections between the two mirrors until the contribution of the beam is neglected. As a result, the resolving power of the interferometer can be interpreted as the number of wavelengths in the path difference between the extreme rays [387].

The grating equation sets an upper limit for the wavelength that can be diffracted by a grating. We know that the sine of an angle does not exceed one, and that a diffracted order can have a minimum value $|m| = 1$. Thus, the upper limit of wavelength corresponds to a Littrow mounting $\sin(\alpha) = 0$. In this case, the grating equation gives the

result $\lambda_{max} = d$. In other words, the maximum efficiency of a grating is obtained at the blaze wavelength.

Comparing to a prism, a grating generates more than one spectrum because of the various diffraction orders. The disadvantage of this feature lies in the complication of spectral measurements. This complication rises from the overlapping of orders, which causes confusion in distinguishing between them especially if we are using a source of a wide range of wavelengths. For example, based on the grating equation we can see that a light of wavelength λ in first order can overlap with light of wavelength 2λ in second order and with light of wavelength 3λ in third order, and so on. Figure 66 presents an illustration of this feature.
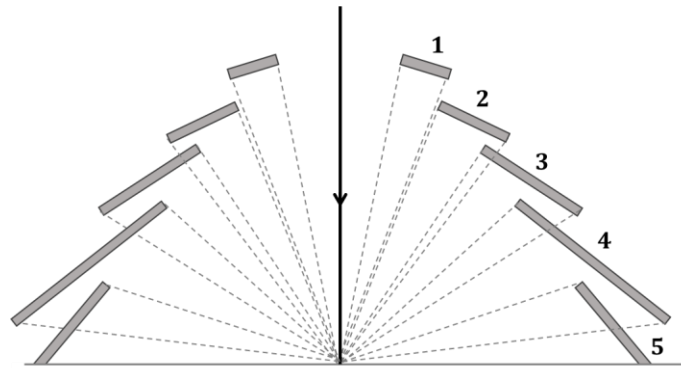


Figure 66 Overlapping of different orders of diffraction (Reproduced with permission from [387] copyright 1982 Academic Press).

The overlapping of orders is not a major concern if the detector can respond only to the wavelength range of interest. Otherwise, spectral filtering or blocking techniques must be considered. Experiments based on synchrotron radiation are a good example of

this situation, in which entangled spectra are a serious issue. The reason is that this radiation source covers a broad range which extends from X-ray region up to the IR [76, 78-81].

For a grating, the largest bandwidth in a given diffracted order $m$ which does not overlap with that of the adjacent order $m + 1$ is known as the "free spectral range" of the grating [387]. Assume that the lower and upper limits of the band are $\lambda_1$ and $\lambda_2$ respectively. Let $\lambda_2$ be the long-wave end of the band in the specified order $m$, and $\lambda_1$ be the wavelength diffracted at the same angle but in order $m + 1$. In this case, the condition of overlapping at the long-wave end of the band is given by:

$$\lambda_2 m = \lambda_1 (m + 1)$$

which indicates that overlapping can be avoided at the long-wave end of the band if:

$$\lambda_2 - \lambda_1 \geq \frac{\lambda_1}{m}$$

Whereas, overlapping at the short-wave end of the band occurs if $\lambda_1$ in order $m$ interfere with $\lambda_2$ in order $m - 1$:

$$\lambda_1 m = \lambda_2 (m - 1)$$

Similarly, overlapping can be avoided at the short-wave end of the band if:

$$\lambda_2 - \lambda_1 \geq \frac{\lambda_2}{m}$$

However, since we made the assumption that $\lambda_2$ is the longer wavelength, we only keep the first expression of the free spectral range $\lambda_2 - \lambda_1 \geq \frac{\lambda_1}{m}$, where $\lambda_1$ is the shorter wavelength. It is evident from the equation that the free spectral range decreases for higher orders. It can also be expressed in terms of the longer wavelength as follows:

170

$$\lambda_2 - \lambda_1 = \frac{\lambda_2}{m+1}$$

Blazed gratings redirects the light into the direction of the desired diffracted order. In reflective blazed gratings, each groove resembles a mirror inclined at an angle, and reflects the portion of light incident on it independently. While in the case of transmission gratings, each groove constitutes a prism.

Recall Figure 59 at the beginning of this section, which compares reflected and transmitted orders. Light incident on a reflective grating at an angle $\alpha$ is diffracted at an angle $\beta$ measured from the grating normal. The facet normal in a blazed grating is the normal to the surface of the groove, which makes an angle $\phi$ with the grating normal as shown in Figure 67. To satisfy the blaze condition, the angle of incidence and the angle of reflection both measured with respect to the facet, must be equal:

$$\alpha - \phi = \beta + \phi$$

As a result, the facet angle in terms of $\alpha$ and $\beta$ is found from $\phi = \frac{\alpha - \beta}{2}$, which indicates its dependence on the mounting of the grating [387]. For example, the facet angle in the Littrow mount situation, where $\alpha = -\beta$ so $\phi = \beta$, can be found from the grating equation $2d \sin(\phi) = m\lambda$ so that:

$$\phi = sin^{-1} \left( \frac{m\lambda}{2d} \right)$$
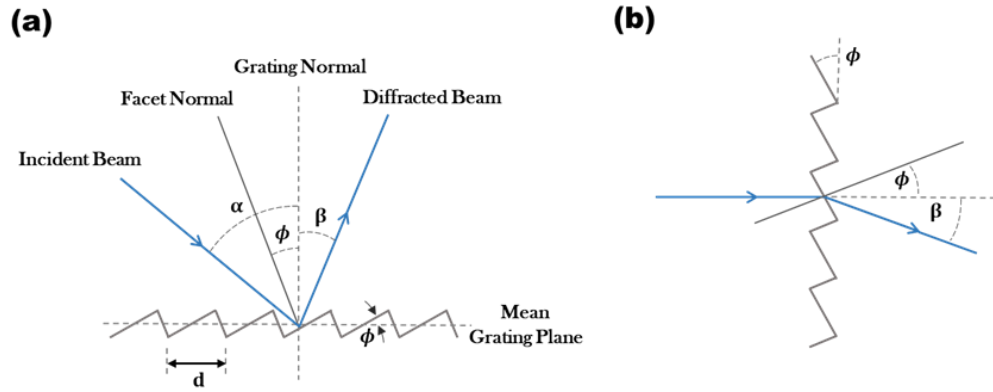
Figure 67 Determination of the facet angle (a) for a reflective blazed grating, and (b) for a blazed grating used in transmission.

For normal incidence however, where $\alpha = 0$ so $\phi = \frac{-\beta}{2}$, the grating equation gives $\beta = \sin^{-1}\left(\frac{-m\lambda}{d}\right)$ which results in:

$$\phi = \frac{1}{2}\sin^{-1}\left(\frac{m\lambda}{d}\right)$$

These results point out that the facet angle changes in response to a change in the angle of incidence. In other words, it implies that when a given grating is used at different angles of incidence, it will be blazed for different wavelengths.

Let us look for a general expression for the blaze wavelength $\lambda_b$ and investigate its dependence on the facet angle $\phi$. From $\phi = \frac{\alpha - \beta}{2}$ we can write $\beta = \alpha - 2\phi$, so the grating equation becomes:

$$d \sin(\alpha) - d \sin(\alpha - 2\phi) = m\lambda_b$$

$$2\,d \sin(\alpha)\,\cos(\alpha - \phi) = m\lambda_b$$

172

The first order $m = 1$ in Littrow mounting has a blaze wavelength $(\lambda_b)_{Litt} = 2\,d\,\sin(\alpha)$. It can be substituted into the grating equation to get an expression for the blaze wavelength:

$$m\lambda_b = (\lambda_b)_{Litt}\,\cos(\alpha - \phi)$$

which suggest that the blaze wavelength decreases as the angle of incidence increases.

Transmission gratings involve refraction at the back surface, so for simplicity let us consider normal incidence only. Let $n$ be the refractive index of the grating material, then Snell' slaw can be written as:

$$n\,\sin(\phi) = \sin(\phi + \beta)$$

which, according to Figure 67, gives:

$$\tan(\phi) = \frac{\sin(\beta)}{n - \cos(\beta)}$$

From the grating equation of the transmission grating in our case $d\,\sin(\beta) = m\lambda$, we can write:

$$\tan(\phi) = \frac{m\lambda}{dn - (d^2 - m^2\lambda^2)^{\frac{1}{2}}}$$

Total internal reflection at the facet sets an upper limit for the facet angle $\phi$. In this particular situation, the angle of refraction is $\phi + \beta = 90^o$. As a result, $n\,\sin(\phi_{max}) = 1$ so $\phi_{max} = \sin^{-1}\left(\frac{1}{n}\right)$, which indicates that the exact value of $\phi_{max}$ depends on the material. Usually, a reasonable value is $\sim40^o$.

Let us take an example where we want to make a grating with 1200 grooves per millimeter blazed at a wavelength $\lambda = 500\,nm$. In this case, it is not practical to use a

material with $n = 1.5$. Consider the same assumption but with a grating of 600 grooves/mm. In the small angle approximation, where $\cos(\beta) = \beta$ and $\sin(\beta) = \tan(\beta) = \beta$, we get:

$$\phi_{refl} = \frac{m\lambda}{2d}$$

$$\phi_{trans} = \sin(\beta)\left(\frac{1}{n - \cos(\beta)}\right) = \frac{m\lambda}{d}\left(\frac{1}{n - 1}\right) = \frac{m\lambda}{d}\left(\frac{1}{1.5 - 1}\right) = \frac{2m\lambda}{d} = 4\phi_{refl}$$

Defects and random irregularities on the reflective surfaces of a grating due to mechanical errors may result in stray light. Furthermore, if groove spacing or shape suffer from periodic errors, it can produce false spectral lines, which are known as "ghosts" [390, 391]. In general, accurate analysis of stray light is a requirement to verify the operation of an optical instrument [392, 393].

Recombination ghosts in spectrographs of a Littrow configuration, based on Volume Phase Holographic (VPH) gratings, were studied by Burgh and co-workers [394]. They used a camera and observed ghosts reflected off the surface of the detector, recombined by the grating, and then recollected by the camera onto the detector. For this reason, these are called "recombination ghosts". In their work, they reported two different ways of recombination. Though, the phenomenon of ghosts has been observed in different systems based on conventional gratings both in Littrow and non-Littrow configurations. Finkelstein *et al* used an interferometric error recorder to determine the errors caused by the ruling engine. He reported a relative ghost intensity less than 0.025 in the first order of a 600 groove/mm grating at wavelength 5461 $A^o$ [395].

Sensitivity is a crucial element in spectroscopic measurements. This has stimulated various developments in material science, design, and testing. With modern ruling engines, higher diffraction efficiencies are achievable by modern blazed gratings. Lerner *et al* reported efficiencies larger than 97% and improved flatness for higher orders [396]. Moreover, gratings with grooves densities that exceed 6000 groves/mm are available, enabling scanning spectrometers and flat field spectrographs to operate up to the IR region.

Higher spectral resolution can be realized by considering a special configuration of the spectrometer. Zhou *et al* used a new design for the setup of their spectrometer to improve the resolution. The setup is based on a conventional flat-field concave-grating spectrometer with the addition of a small mirror placed close to the detector. The mirror divides the wide spectral band into two adjacent narrower bands. The results show good agreement between simulated and experimental measurements, with a resolution of $1.6 \, nm$ across a $700 \, nm$ spectral band [397].

A complete description of a grating not only depends on the groove profile of the grating, but also relies on the efficiency. An absolute efficiency of a diffraction grating is a measure of the percentage of the incident radiation that feeds the desired diffracted order. This is the definition of grating efficiency usually used in spectroscopy. The shape of the grooves and the reflectivity of the coating material determine the absolute efficiency. The larger the absolute efficiency, the higher the SNR of spectroscopic measurements [387].

On the other hand, a grating can be characterized by a relative efficiency, which is a measure of the energy diffracted into the order of interest in comparison with the energy reflected by a plane mirror of the same coating material. This efficiency is also known as

175

the groove efficiency since it depends on the groove profile. In general, relative efficiencies are larger than absolute efficiencies because the latter is a function of material reflectivity, which is less than unity.

In summary, reflective diffraction gratings are characterized by the number of lines per centimeter, size, blaze angle, angular dispersion, material used for coating the surfaces, free spectral range, resolving power, and efficiency. Figure 68 illustrates the parameters of a reflective blazed grating.
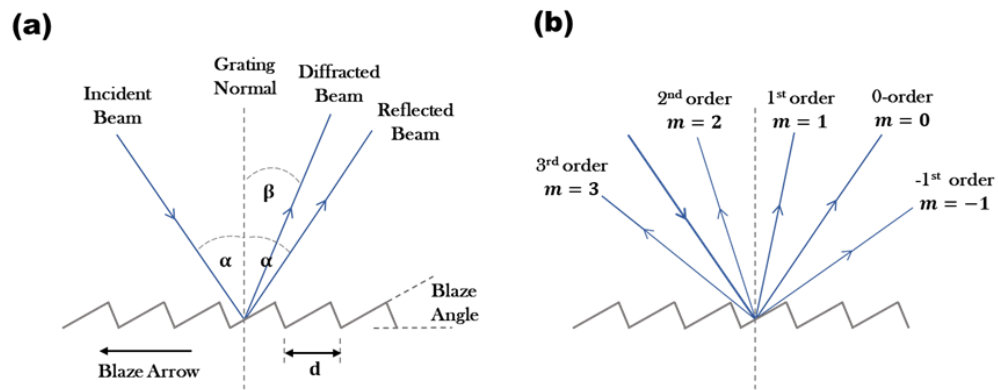


Figure 68 (a) Parameters of a blazed diffraction grating. (b) Diffracted orders.

To find the resolution of a grating spectrometer based on the width of the entrance and exit slits; $w_1$ and $w_2$ respectively, consider that the angle of rotation is $\gamma$. Then:

$$w_{total} = w_1 + w_2$$

Let us use the negative sign notation for the grating equation,

$$d \sin(\alpha) - d \sin(\beta) = m\lambda$$

then the angles can be expressed in terms of the rotation angle as:

$$\alpha = \theta - \gamma$$

$$\beta = \theta + \gamma$$

And accordingly we get:

$$d\sin(\theta - \gamma) - d\sin(\theta + \gamma) = -2d\cos(\theta)\sin(\gamma) = m\lambda$$

So the resolution can be found from:

$$2d\cos(\theta)\sin(\Delta\gamma) = m\,\Delta\lambda$$

If the mirrors of the spectrometer have a focal length $f$, then by tracing the path that the beam follows between the two mirrors and the grating we obtain:

$$\Delta\gamma = arctan\left(\frac{w_1 + w_2}{f}\right)$$

Therefore, the resolution $\Delta\lambda$ can be determined from the width of the spectrometer slits and the focal length of the collimating and focusing mirrors.

Diffraction gratings are key elements in a variety of applications. In material sciences, the laser diffraction spectrometry is the most applied technique for particle sizing, given that the material particles are relatively large comparing to the wavelength of light [386, 398]. In astronomical and astrophysical instruments, high efficiency diffraction gratings are major components of the system [399, 400].

A clear description of resonant effects in dielectric gratings became available in the early 1990s [401], which promised for optical sensing and filtering applications in free space [402-404]. Recently, sub-wavelength dielectric gratings (SWGs) have emerged providing new functionalities in the area of broadband, high-reflectivity filtering. In

177

SWGs, the first order diffracted mode is a guided wave trapped in the dielectric layer, so it does not propagate freely. In addition to allowing for near-field amplification, SWGs also enable polarization control [405].

## 3.2 Piezoelectric Transducers

The term piezo comes from Greek and means pressure. The phenomenon of piezoelectricity was first observed by the brothers Curie. They found that under some stress, the material is polarized and an electric field is generated. Vice versa, when a voltage is applied on a piezoelectric material, a mechanical deformation takes place in the material [406].

The mechanical stress on the piezoelectric material can take the form of a force, a shock, or a sound wave. When force is applied, the distribution of electric charge in the material will change, resulting in a positive charge at one end and a negative charge at the other [407], as illustrated in Figure 69. If the material is connected to electrodes, the potential difference across its sides will result in a flow of an alternating current. The voltage across the material can be measured, and as expected, it will be proportional to the applied mechanical stress [408]. Part (a) of Figure 70 shows this concept schematically.
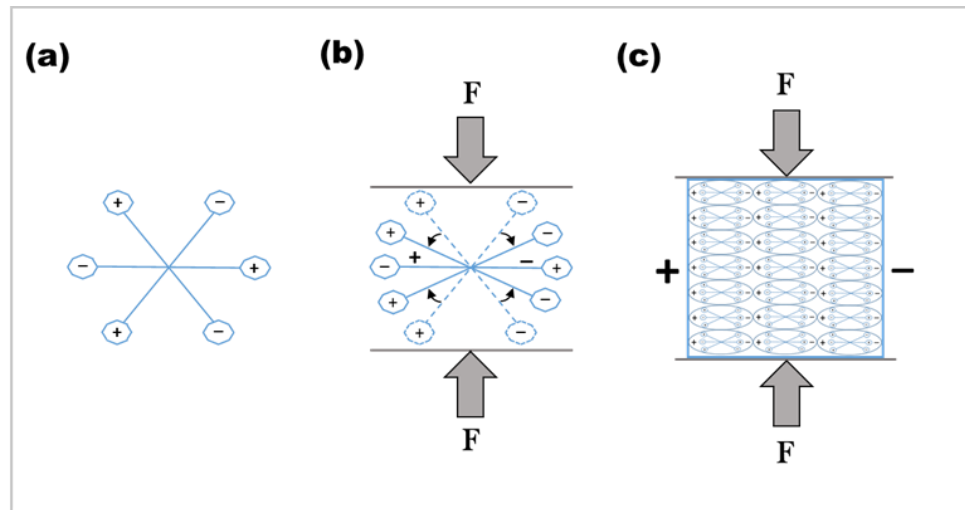
Figure 69 The Piezoelectric effect. (a) A simple model of an unperturbed molecule. (b) An external force applied on the molecule. (c) A potential difference appears across the piezoelectric material (Reproduced with permission from [407] copyright 2008 Springer Nature).

The piezoelectric transducer (PZT) relies on the reverse case, in which an applied voltage produces a displacement, or a deformation, in the piezoelectric material. This effect is displayed in part (b) of Figure 70. In experiments, function generators are often used to provide the desirable voltage. This varying voltage generates vibrations in the material, and those vibrations play an essential role in many applications. A thorough explanation of the piezoelectric effect is provided in Appendix C [406-423].
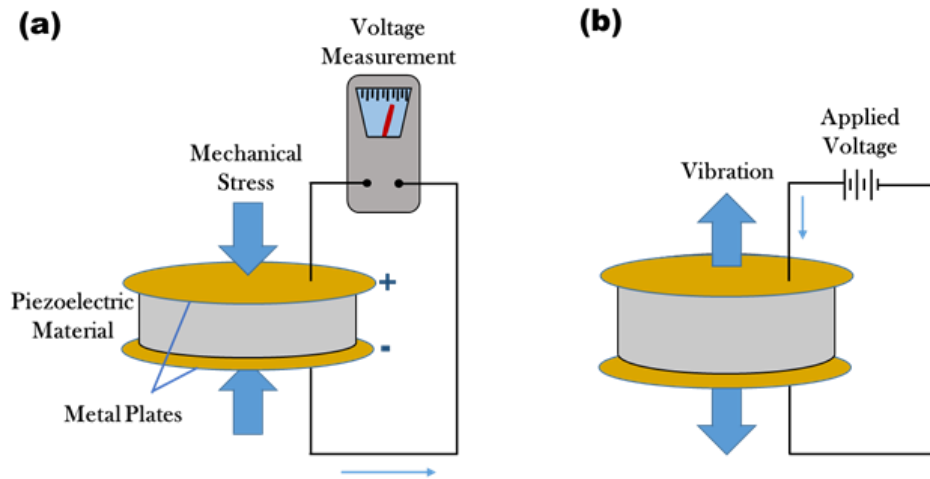
Figure 70 An illustration of the reversible piezoelectric effect. (a) Pressure causes charge displacement and a potential difference is generated as a result. (b) A change in the material dimensions in response to a varying applied voltage.

## 3.3 Acousto-Optical Modulators

Acousto-optic modulators (AOMs) are based on the interaction of an optical wave with an acoustic wave. With a periodic change in the refractive index of the material, the acoustic wave acts as an optical grating and modulates the phase of the optical wave. The light scatters such that:

$$2 \lambda_a \sin \theta' = m \lambda_i$$

where $\theta'$ is the angle between the incident and scattered light, $\lambda_a$ is the wavelength of the acoustic wave, $\lambda_i$ is the wavelength of the incident wave, and $m$ is an integer describing the order of scattering [18, 424].

The acousto-optic modulation process in an AOM is illustrated in Figure 71, where $\theta'$ in this case is equal to $2\theta$. An AOM driver provides a radio frequency (RF) signal to the piezoelectric transducer, which generates an acoustic wave in the crystal, or the

transparent AOM material. Rarefactions and compressions of the acoustic waves cause periodic spatial variations in the density of the material. This creates a moving refractive-index grating that the incident light experiences as it propagates through the material. The diffraction of light by the travelling acoustic waves in this medium is similar to Bragg scattering of X-rays from atomic planes in a crystal [424]. AOMs allow for the modulation of intensity, frequency, or direction of the laser beam and are key devices in many experiments.
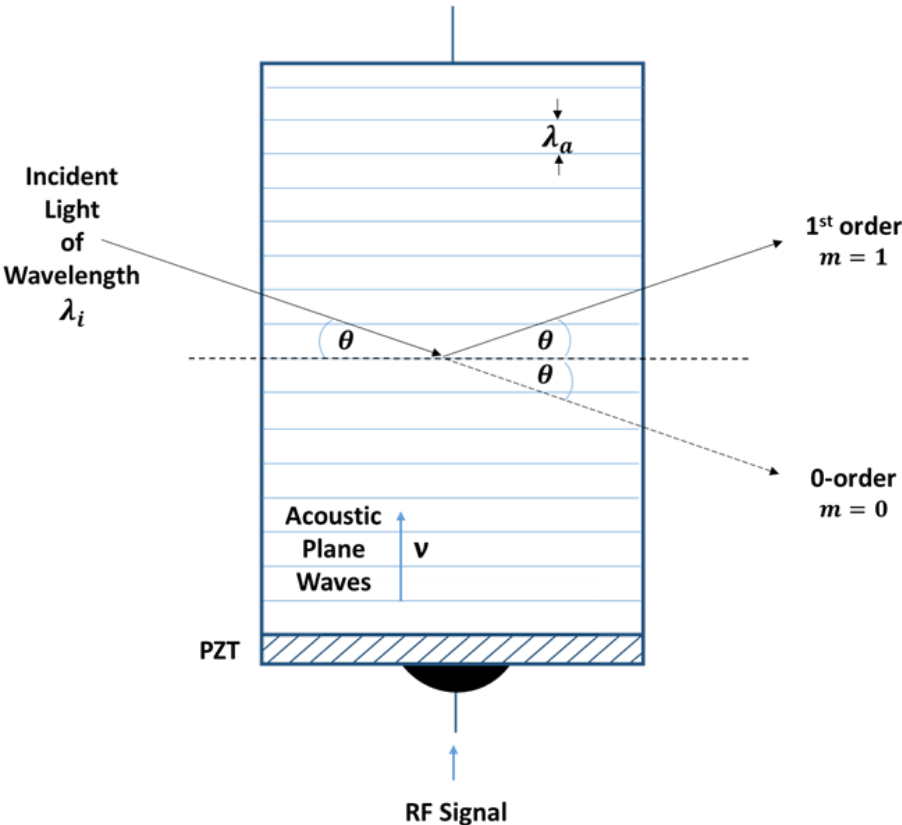


Figure 71 Diffraction of light by the acoustic waves in an acousto-optical modulator. The refraction of light at the boundaries is not shown here.

## 3.4 Optical Choppers

Optical modulators are used widely in different applications to manipulate the properties of light. Experiments that involve detection of weak or very small optical signals require a lock-in technique. In spectroscopic experiments, one of the major parts needed to apply a lock-in detection technique is an optical chopper system.

Optical chopper systems consist of an optical chopper and a controller. The controller allows for setting and adjusting the chopping frequency and other operating parameters. The chopping frequency is determined using the internal frequency synthesizer or from an external reference signal connected to the controller. Advanced controllers have different options for the chopping mode. For example, fundamental, harmonic, and sub-harmonic are mode options offered by Newport Optical Chopper System Model 75160NF. In general, an optical chopper is a rotating sector blade. In other words, it is a wheel with holes in it to chop the optical power periodically. An illustration of interrupting light with an optical chopper is given in Figure 72.
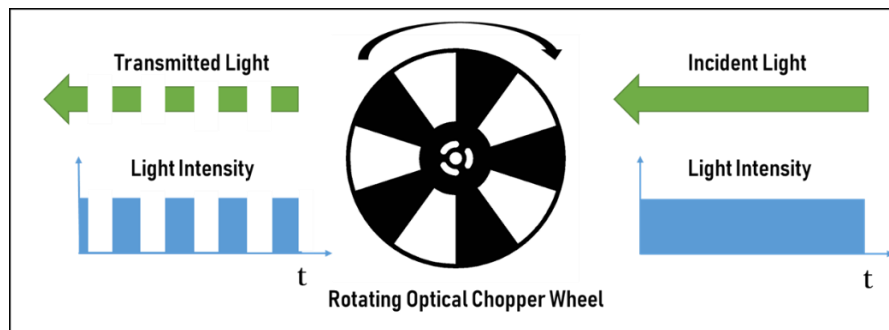


Figure 72 A basic illustration of light chopping using a rotating sector blade.

Optical choppers are often used with lock-in amplifiers for phase modulation. They are available in different sizes and shapes [425]. Some optical choppers, available from ThorLabs, are shown in Figure 73 as an example [426]. Choosing an optical chopper for an experiment depends on the purpose and availability. For instance, some experiments use a beam splitter and two different chopper wheels, one for the signal and one for the reference, to improve the configuration of the spectrometer.

Another example is modulation at two different frequencies, which can be of interest in some applications. Let us consider that the chopping frequency of the signal is $f$; then it is possible to use a multiple of it $mf$ or a different chopping frequency $f'$ for modulation of the reference [427]. In this case, a proper experimental configuration is required, and two lock-in amplifiers might be needed.
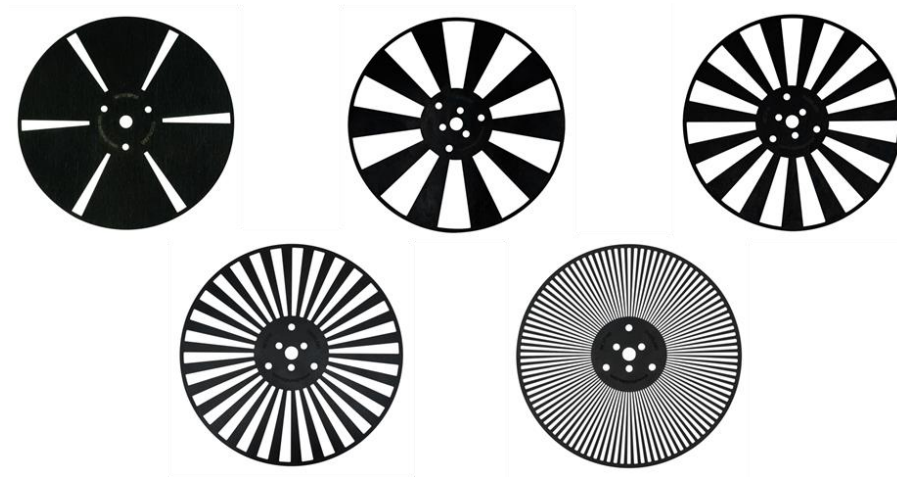


Figure 73 Examples of rotated sector blades available from ThorLabs for optical chopping [426].

Optical choppers with a twofold division are also available. Some available divisions can be seen in Figure 74 below. This type of optical chopper wheels is divided into an inner sector blade and an outer sector blade. If an experimental setup has limited space, one optical chopper with a twofold division is a good option to modulate the signal and reference at different frequencies. Usually, these choppers have more divisions in the outer sector than in the inner sector of the wheel. This means that the light passing through the outer sector will be chopped with a higher chopping rate than the light passing through the inner sector. Using an optical chopper with a twofold division in spectrometers is often combined with the use of a rotating sectioned mirror. This mirror reflects light in a sequence to each assigned arm, allowing for a more compact experimental arrangement [427].



Figure 74 Examples of rotated sector blades with twofold divisions available from ThorLabs [426].

Osawa and co-workers have developed two different types of optical choppers. They obtained promising results with high resolution and improved SNR, comparing to

other techniques that rely on conventional detectors in their research field [428]. Their experiment is based on synchrotron radiation (SR), which has a large tunability relevant to spectroscopic applications. However, they used pulsed light and pump-and-probe technique to achieve time-resolved measurements. Figure 75 gives an example of pulsed light interruption by a rotating sector blade. Some pump-and-probe spectroscopic experiments use one pulsed laser source and split the laser beam into two arms, a pump to excite the sample and a probe to monitor the changes in the optical constant of the sample after the light passes through it, e.g., absorption, transmission, or reflectivity. In the pump-and-probe experiment by Osawa and co-workers, the repetition rate of the probe pulses highly exceeds the repetition rate of the pump pulses. For this reason, they use an optical chopper to select bunches of individual pulses from the probe laser beam [428].
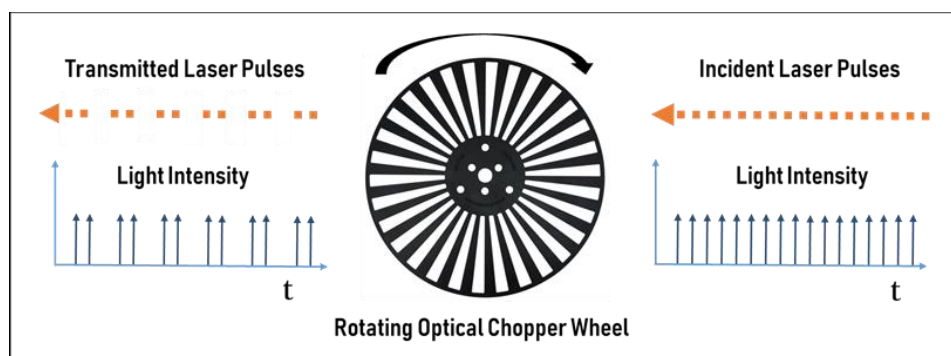


Figure 75 A simplified picture that illustrates optical chopping of a pulsed laser beam.

Let us take the optical chopper developed by Osawa *et al* as an example [428, 429]. Their rotating disc has 108 grooves and can rotate with a speed of 28,997 rounds per

minute (rpm) in synchronization with the required frequency. This chopper disc allows for the incident radiation to pass through it with an opening time of $1.17\ \mu s$. The design of the disc has another set of grooves, which consists of a two-step depth structure. The opening time offered by the second set of grooves with the same rotation speed is $0.52\ \mu s$. Their system is capable of selecting a single pulse every few periods of the bunch structure, which is determined by the pulse frequency of the light source [429].

## 3.5 Lock-in Amplifiers

Lock-in amplifiers are widely used in different scientific and industrial applications to extract a signal with a known frequency from a background signal of multiple frequencies. This feature is essential in many experiments and applications that involve light modulation at certain frequencies, which allows improving the SNR of the measurement.

In general, the primary purpose of lock-in amplifiers is to extract a weak signal from a very noisy measurement. A general schematic of its operation is displayed in part (a) of Figure 76. This electronic device is highly selective, which makes it equivalent to a bandpass filter with a central frequency set by the reference signal [427]. An example of a typical experiment based on a lock-in amplifier is given in part (b) of Figure 76. For more explanation of the performance of these systems, refer to Appendix D [331, 427, 430].
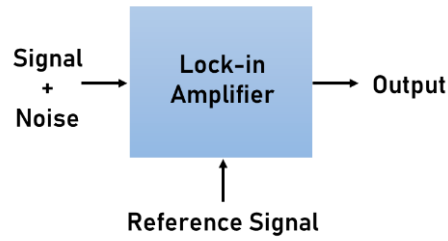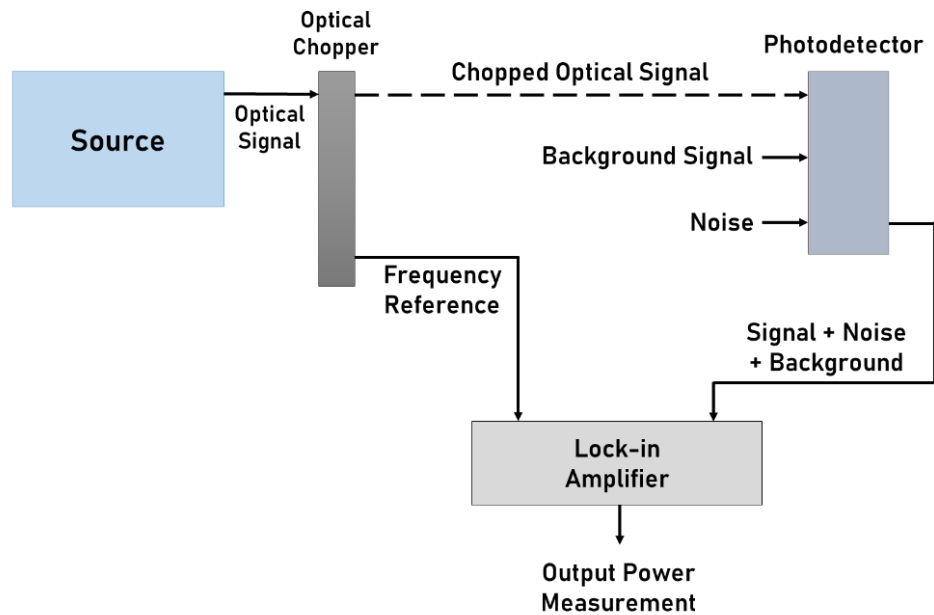
Figure 76 (a) Basic operation of a lock-in amplifier. (b) An example to illustrate the use of lock-in amplifiers in experimental setups.

## 3.6 The LabVIEW Program

LabVIEW is a software developed by National Instruments to serve for measurement systems, testing, and control purposes. It is a platform-based approach that

has libraries for built-in analysis, capability of hardware interface, and scalability across different operating systems. A brief description of the software environment is given in Appendix E based on National Instruments User Guide [431].

# 4. INFRARED SPECTROSCOPY WITH FREQUENCY COMBS

## 4.1 Cavity Ringdown Spectroscopy in the Near Infrared

### *4.1.1    Introduction*

Cavity ringdown spectroscopy (CRDS) systems based on pulsed, CW, and quasi-CW lasers have been used for years to measure concentrations of trace molecules in gases [58, 432-435]. In a CRDS technique with a CW laser, decay rates of exponential decay signals carry the molecular absorption information at certain detuning frequencies [434]. Absorption measurements obtained with CRDS systems are highly sensitive and can provide accurate information about the molecules present in the air [14, 434], or in a gas sample [9, 15]. Systems based on the CRDS technique can also be designed in a compact, stable, and easy-to-operate form, which benefits applications in various areas. Those advantages influenced many research studies and industrial applications at different levels [435-438].

In the semiconductor industry, it is crucial to examine the purity of gases used in manufacturing processes because the purity level has a major impact on the quality of products. CRDS comes into play as one of the most powerful and sensitive spectroscopic techniques for those industrial applications [439]. However, each CRDS system based on a CW laser can only be used to identify one or two molecular species at a time because of the minimal frequency coverage of the laser. In contrast to CRDS systems, FT-IR systems provide detection over a broad bandwidth, but the system requires a relatively long time to provide high-resolution spectral data.

The potential of the CRDS technique for different applications has demanded improvement of performance to cover a broad spectral range and enhance sensitivity and measurement time even further. Using a high-power broadband coherent laser source is a significant step towards this goal. The novel optical frequency comb, which was born shortly before the beginning of this century, is the perfect candidate for the category of broadband spectroscopy [276, 278, 292, 323, 440].

Early applications of frequency combs in spectroscopy have proven their unique characteristics and capabilities [10, 13, 43, 440]. However, to fully utilize this recently-developed broadband highly-coherent light source, it is necessary also to improve the stability of the system and the resolvability of the detection technique [219]. Coupling frequency combs into enhancement cavities, and matching the modes of the comb source to the cavity modes with high efficiency have proven to be advantageous for sensitive spectroscopic measurements.

In general, a CRDS system consists of a high power laser, a cavity with HR mirrors, a signal-triggering mechanism, and a detection method [9, 58]. Using enhancement-cavities allow for a longer length of interaction between the light beam and the gaseous molecules in a sample. With efficient mode-matching, which is described further in Section 4.1.4, the resonance condition is met and the highest possible intensity can be coupled out of the cavity and measured at the detector. Moreover, the long interaction length reduces the noise in the signal and allows for a considerable increase in the $SNR$.

## 4.1.2 Basic Concepts

The cavity ringdown technique depends on measuring the intensity of light that leaks out of a high finesse optical cavity after turning the incoming light off. High finesse optical cavities used in ringdown experiments are often passive Fabry-Pérot cavities formed by two HR mirrors to reduce the losses. In most cases, the cavity consists of a curved mirror and a flat mirror bonded to a piezoelectric transducer. The behavior of the ring-down cavity can be described by the cavity finesse $\mathcal{F}$ and the free spectral range $FSR$. The first parameter ($\mathcal{F}$), which is defined in Section 2.5, describes the resonance quality of the cavity, so it is often used to characterize optical cavities [370]. The higher the cavity finesse, the larger the enhancement of spectroscopic measurements.

By matching the modes of the light source and the optical cavity, one of the modes builds up inside the cavity until reaching a threshold level. After that, the oscilloscope is set up to send a signal to the acousto-optical modulator (AOM) to switch the incident light off, and the decaying signal from the ringdown cavity is recorded to extract the decay time at a certain wavelength. The decay constants at different wavelengths are then used to reveal the absorption spectra of trace gas molecules present in the gas sample inside the cavity.

In terms of the cavity $FSR$, the decay time of the cavity can be written as:

$$\tau_c = \frac{1}{(FSR)\,(Loss)} = \frac{1}{(FSR)} \frac{1}{(1 - R_1 R_2\, e^{-2\alpha L})}$$

where $FSR$ is the free spectral range of the cavity, $R_1$ is the reflectivity of the first mirror, $R_2$ is the reflectivity of the second mirror, $\alpha$ is the absorption coefficient, and $L$ is

the length [8, 9]. Typical values of $\tau_c$ are in the $ns - ms$ time domain, depending on the values of $R_1, R_2$, and $L$. In the high reflectivity limit ($R > 0.999$), the change in $\tau_c$ as a result of absorption is:

$$\frac{\delta \tau_c}{\tau_c} \cong \frac{\mathcal{F} \, \alpha \, L}{\pi}$$

The CRDS technique gives an indirect measurement of the gas concentration based on cavity decay times with and without absorption; $\tau$ and $\tau_0$ respectively [18]. Assuming two HR mirrors with the same reflectivity $R$ such that $1 - R \leq 10^{-4}$, the decay constants can be written as:

$$\tau_0 = \frac{L}{(1 - R) \, c}$$

$$\tau = \frac{L}{(1 - R + \alpha L) \, c}$$

where $\alpha = n\sigma$ is the frequency-dependent absorption coefficient, $L$ is the interaction length, and $c$ is the speed of light. Then, the concentration can be retrieved based on the ringdown times using the following equation:

$$n = \frac{1}{c \, \sigma(\lambda)} \left( \frac{1}{\tau} - \frac{1}{\tau_0} \right)$$

Let us recall the Beer-Lambert law from Section 2.1.3. As molecules absorb the radiation in resonance with a molecular transition, absorption losses contribute to the exponential decay of the transmitted intensity, in addition to mirror losses. The decay in the exponential signal increases with the interaction length. This is because the longer the length of interaction, the higher the rate of absorption. To illustrate the concept of the

CRDS technique, an example of two decay signals one when absorbing molecules are present and the other without absorption, is shown in Figure 77.
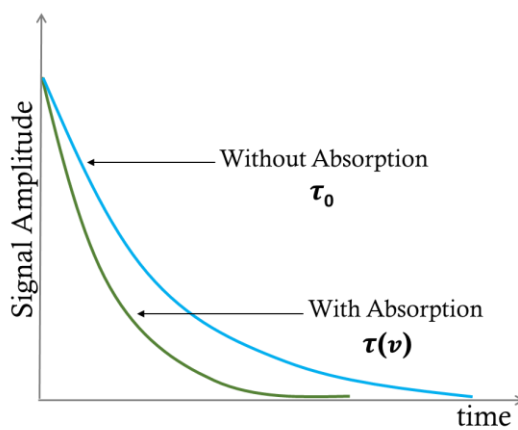


Figure 77 An example of the difference in the cavity decay-times with and without absorption.

Applying this technique with a pulsed laser results in a decay trace formed by the decaying intensity of optical pulses. The same ringdown concept applies but in this case a decrease in the intensity of individual transmitted pulses can be observed [58]. A simplified picture is shown in Figure 78 to compare the decay of the intensity of laser pulses with and without absorption.

Short laser pulse       High finesse cavity       Exponential decay signal
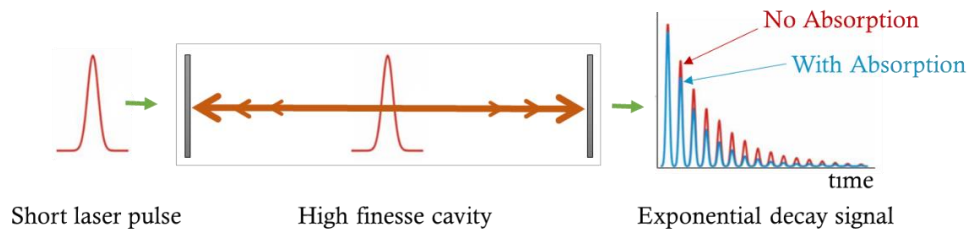
Figure 78 A ringdown decay trace with a pulsed laser source. Different colors are used for the decay signals with and without absorption.

After coupling the resonant cavity modes with comb components efficiently, the field builds up inside the cavity with time, as illustrated in part (a) of Figure 79. A long cavity lifetime permits sufficient light-matter interaction and therefore enhances the sensitivity proportionally to cavity finesse. When the AOM is switched off, it turns off the incoming light, so the intensity inside the cavity starts to decay. Part (b) of Figure 79 shows the decaying intensity after switching off the light. With time, the intracavity intensity decreases because of the losses on the mirrors and possibly the absorption of radiation by molecules.

The rate of this intracavity optical power decay depends on the ratio between total losses and the round-trip time inside the cavity. Therefore, the cavity finesse can be expressed in terms of the cavity decay time $\tau_c$ and the free spectral range as follows [10]:

$$\mathcal{F} = 2\pi\, \tau_c\, FSR$$

This equation can be used for cavities with mirrors of $R > 0.999$ to determine cavity finesses based on the decay time $\tau_c$ [370].
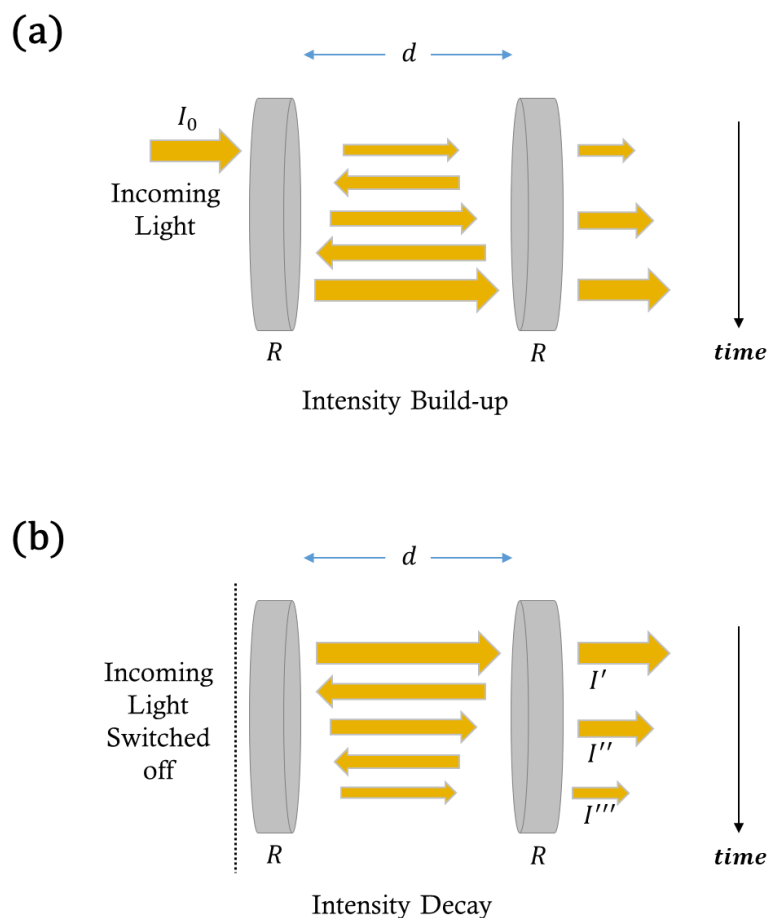
Figure 79 The basic concept behind CRD spectroscopy. (a) The laser beam is coupled into a high finesse cavity, and intensity builds up until reaching a certain threshold level. (b) The AOM is turned off, and no more light is entering the cavity. Light continues to bounce between the cavity mirrors, and the intensity of light decays exponentially. The decay trace is then used to reveal the absorption constant. Note that only the concept is illustrated here, and in practice the build-up is faster than the decay.

CRDS experiments with CW lasers depend on fast sweeping of the laser frequency across the resonant mode of the cavity such that the resonance condition is met for a period of time shorter than the lifetime of the cavity [433]. An electro-optic modulator (EOM) or an AOM can be used to switch off the incoming light [15]. Light from a CW laser can also

195

be turned off directly by fast switching of the source. Applying the CRDS technique with frequency combs requires that the mode spacing of the comb and the cavity are almost matched [9]. This case is explained schematically in Figure 80 below, and further discussions can be found in Section 4.1.4.

As moving away from the central frequency, which we can denote as $\omega_o$, cavity modes are shifted with respect to comb modes because of intracavity dispersion. This effect imposes a limit on the bandwidth that can be coupled into the cavity [370]. A crucial step towards minimizing this effect is to optimize the mode-matching.
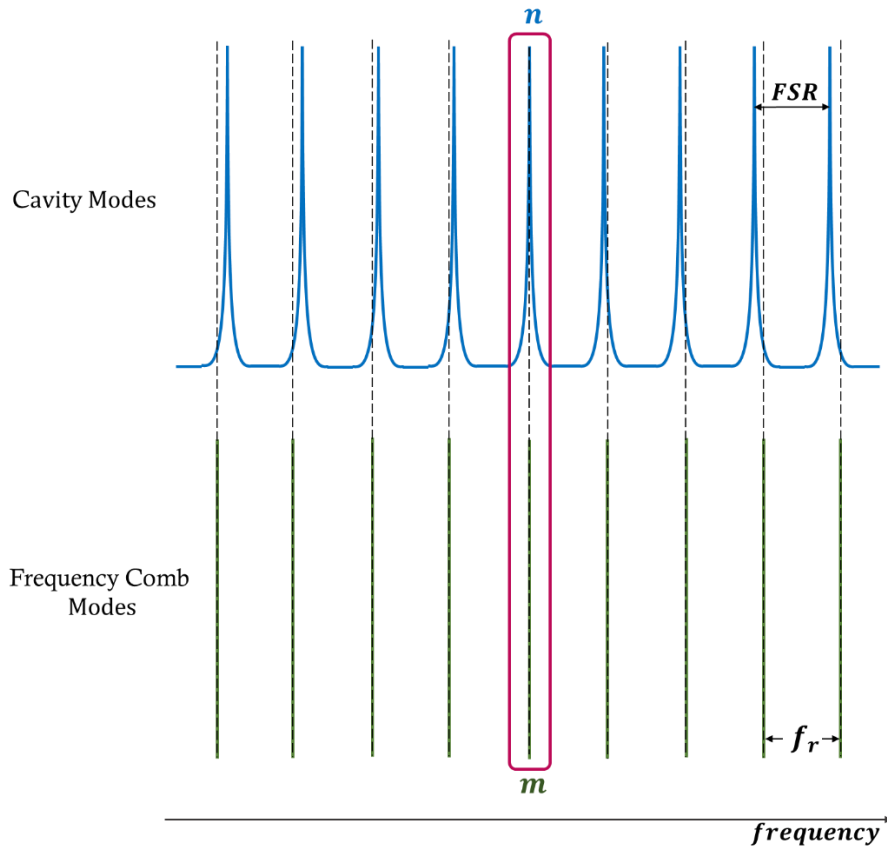
Figure 80 A schematic to show the perfect match of the repetition rate of the comb and the free spectral range of the cavity when the $nth$ cavity mode overlaps with the corresponding comb line.

Optimum coupling is obtained when $f_o$ is selected properly and the condition $f_r = FSR$ is met. Let mode $m$ be the reference comb mode that exactly matches the $nth$ mode of the cavity. In this case, the highest transmission is achieved as in Figure 81.

Both of the characteristic frequencies of the frequency comb, $f_o$ and $f_r$, have to be adjusted to get maximum transmission. When proper values are selected, the largest signal, which corresponds to mode $m$, can be observed. Equidistant signals form the maximum peak can be seen at the two sides, corresponding to modes $m + 1$ and $m - 1$,

197

with equal signal amplitudes. Experimentally, getting an approximately symmetrical

signal similar to the one in Figure 81 indicates that $f_o$ is adjusted to the correct value.
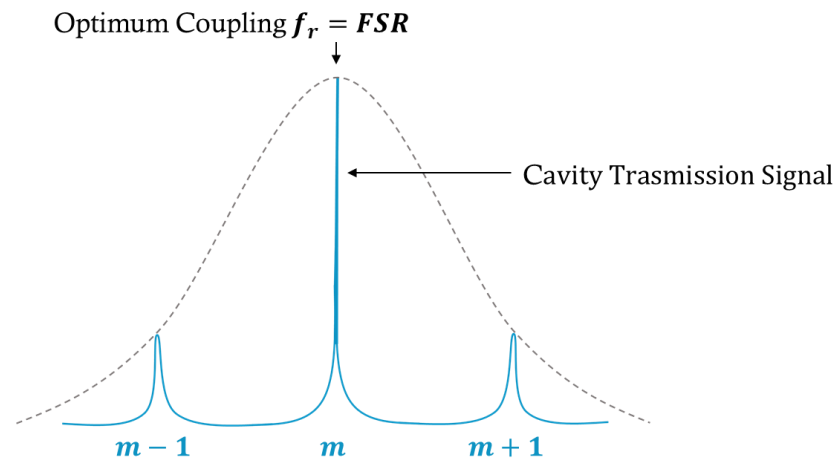


Figure 81 A schematic of the desired transmission signal from the cavity of a CRD spectroscopy experiment with a frequency comb. The central peak indicates optimum matching between free spectral range and comb repetition rate.

Using a frequency sweep between cavity modes and the comb utilizes the spectral

bandwidth of interest and reduces the suffering from dispersion inside the cavity [9]. In

this frequency-sweeping method of cavity-comb coupling, an exact overlapping of modes

at the same time is not a requirement because the resonance condition between different

modes is met at different times. Furthermore, signal transmission does not suffer from

intensity noise in this case, which is another feature of resonance sweeping. Whereas,

mechanical noise largely contributes to the transmitted signal when the cavity-comb

locking approach is selected. This is because fluctuations in cavity length can produce an

intensity noise, which lowers the SNR. In that case, the noise can be suppressed by

sweeping at higher frequencies to avoid the dominant frequencies of mechanical vibrations. The optimum cavity transmission signal in CRDS experiments can be seen in Figure 82. Having the resonance signal at the same position with respect to the sweep function is a sign of efficient mode-matching.
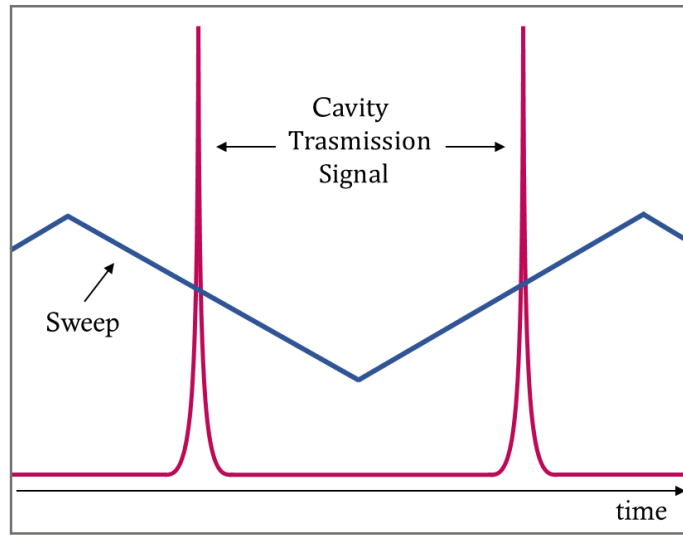


Figure 82 An example of a sharp signal transmitted by the cavity when a high-finesse cavity is used and efficient mode-matching is achieved. The sharpness of the signal shows a high-resonance situation, and its occurrence at the same point in time with respect to the frequency sweep function indicates efficient coupling of the comb spectrum into the cavity.

For the transmission of a single comb line through an enhancement cavity that contains absorbing molecules, the general expression for the electric field is given by [441]:

$$E_T = E_o \frac{T\, e^{-\frac{i\varphi}{2}-\delta L-i\phi L}}{1 - R\, e^{-i\varphi-2\delta L-2i\phi L}}$$

where $E_o$ is the incoming electric field, $\varphi$ is the phase shift after one round trip, $R$ is the mirror reflectivity, $T$ is the mirror transmission coefficient, $\delta$ is the attenuation shift, and $\phi$ is the phase shift of the electric field per unit length caused by the molecules present in the cavity. The three parameters in the exponential term are given by:

$$\varphi = \frac{4\pi v n L}{c}$$

$$\delta = \frac{1}{2} S \, n_\alpha \, \mathrm{Re}(\chi)$$

$$\phi = \frac{1}{2} S \, n_\alpha \, \mathrm{Im}(\chi)$$

In these relations, $v$ is the frequency, $n$ is the refractive index, $L$ is the cavity length, $S$ is the molecular line strength, $n_\alpha$ is the concentration of molecules per unit volume, and $\chi$ is the complex line shape function [2].

Based on this result, the frequency-dependent intensity of transmitted light can be found using $E_T(v) \, E_T^*(v)$, and with normalization it yields [441]:

$$\frac{I_T}{I_o} = \frac{T^2 \, e^{-2\delta L}}{1 - R^2 \, e^{-4\delta L} - 2R \; e^{-2\delta L} \cos(2\phi L + \varphi)}$$

If the attenuation $\delta$ is small comparing to cavity losses, this result for $\frac{I_T}{I_o}$ can be expanded in a series to give the well-known result:

$$\frac{\Delta I}{I_o} = \frac{2 \, \mathcal{F} \, \alpha \, L}{\pi} = \alpha \, L_{eff}$$

Here, $\Delta I = I_T - I_o$ is the difference in the intensity, $\alpha = 2\delta$ is the absorption per unit length for one path inside the cavity, $\mathcal{F}$ is the finesses of the cavity, and $L_{eff} = \frac{2 \, \mathcal{F} \, L}{\pi}$ is the effective interaction length defined previously in Section 2.5.

### 4.1.3  *Gaussian Beams and the Knife-Edge Method*

The beam shape is a crucial feature of the laser beam used in spectroscopy. When the experiment includes an optical cavity other than the laser cavity, and its performance relies on matching the modes of the laser to the modes of the optical cavity, it becomes important to characterize the beam size and shape. Different modes, each of which has a different frequency, can oscillate inside the cavity. Therefore, efficient mode-matching in a CRDS system is required so that the fundamental mode $TEM_{00}$ is stable and its intensity can build up inside the high finesse cavity [9, 442].

The shape of the light beam used in our experiment is a Gaussian, as illustrated in Figure 83. To characterize the beam, we use the well-known equations of a Gaussian beam profile:

$$w(z) = w_0 \sqrt{1 + \left(\frac{z}{z_R}\right)^2}$$

$$R(z) = z \left(1 + \left(\frac{z}{z_R}\right)^2\right)$$

Here, $w_0 = w(0)$ is the beam waist, $w(z)$ is the beam size at a distance $z$ from the waist, $z_R = \frac{\pi \, w_0^2}{\lambda}$ is the Rayleigh range at which $w(z_R) = w_0 \sqrt{2}$. The second equation gives the radius of curvature $R(z)$ at a distance $z$ from the beam waist.
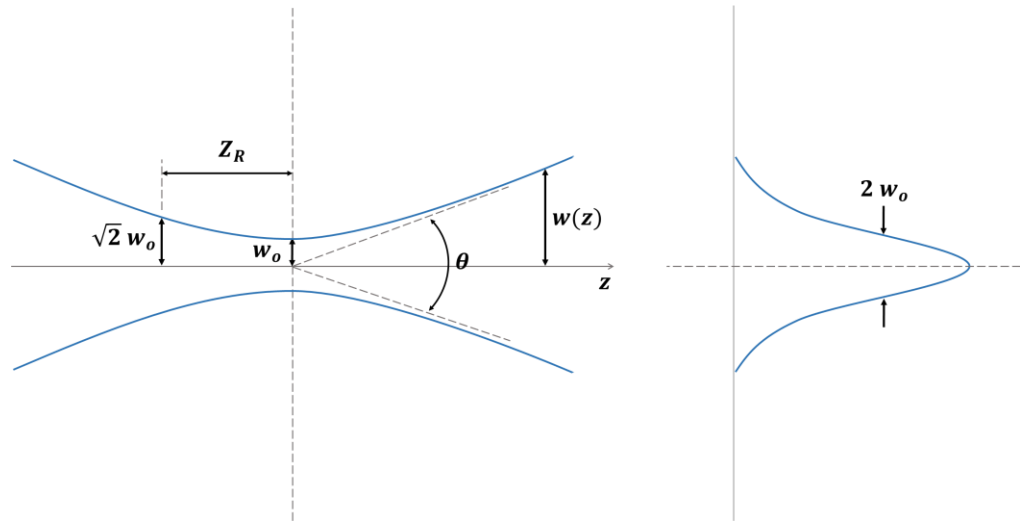
Figure 83 The Gaussian beam profile and its defining parameters. The smallest beam waist is $w_o$ at $z = 0$, and $z_R$ is the Rayleigh range at $w = \sqrt{2}\, w_0$.

A knife-edge method is implemented to determine the beam size. In this method, we use a sharp metallic blade fixed on a translational stage, and we measure the diameter of the beam at three different points along the path of the beam. The sharp edge of the blade blocks part of the beam as we change the position of the stage with small increments. At each position, we measure the power using a powermeter placed at a fixed distance from the blade. This method is shown schematically in Figure 84.
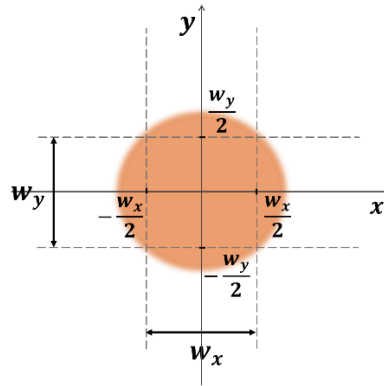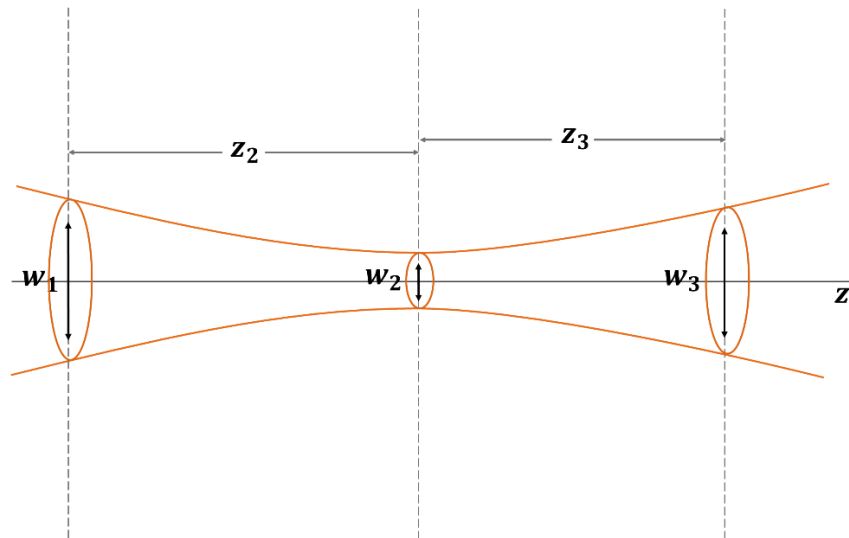
Figure 84 An illustration to explain the knife-edge method used to determine the size of the beam experimentally. (a) A cross-section of a Gaussian beam where the intensity is larger in the middle and lower at the edges, and (b) a schematic of the side view of the beam as it propagates which shows the beam-size measurement at three different points in space.

For the intensity of the Gaussian beam distribution, as shown in part (a) of Figure 84, it is found that:

$$\frac{1}{C} \int_{-\infty}^{-\frac{w}{2}} e^{\frac{-2x^2}{w^2}} \, dx = 0.84$$

$$\frac{1}{C} \int_{-\infty}^{+\frac{w}{2}} e^{\frac{-2x^2}{w^2}} \, dx = 0.16$$

where $C$ is a normalization constant given by $C = \int_{-\infty}^{+\infty} e^{\frac{-2x^2}{w^2}} \, dx$. Before moving the knife-edge, the total power $P_T$ is measured. Then, we adjust the translational stage with increments of few millimeters each time and we measure the power. When we get power values of 16% and 84% of $P_T$, we record the position in $mm$. At the end of each measurement, we find the difference between the two positions, which gives us the beam diameter at that spatial location. This procedure is repeated at different spatial points along the propagation direction until the position of the beam waist is determined.

Let us consider that we have the beam size at two different points; $w_1$ and $w_2$, and let us denote a reference point from the beam waist $x$, then we have two equations that we can solve for the values of $w_o$ and $z_R$:

$$w(z_1) = w_0 \sqrt{1 + \left(\frac{x + z_1}{z_R}\right)^2}$$

$$w(z_2) = w_0 \sqrt{1 + \left(\frac{x + z_2}{z_R}\right)^2}$$

At any given $z$, the beam waist can be also determined based on the full width at half maximum ($FWHM$) using the following relation:

$$w(z) = \frac{FWHM(z)}{\sqrt{2\,ln2}}$$

### 4.1.4 *Mode-Matching the Light Source to the High Finesse Cavity*

Coupling the frequency comb to the cavity efficiently demands resonance between all comb lines with corresponding cavity modes, or at least the largest possible number of lines. Only when the comb mode overlaps with the cavity mode, a transmission peak is obtained from the cavity, as explained earlier in Figure 80 and Figure 81.

Depending on the repetition rate of the mode-locked laser used to generate the frequency comb, the corresponding $FSR$ of the enhancement cavity is determined. The dependence of the $FSR$ on the frequency, as a result of dispersion, causes a variation in the $FSR$. This variation indicates that we can maintain the mode-matching condition within a limited range only [370].

For mode-matching, we use two lenses and we fixe one of them on a one-dimensional translational stage to allow for adjustments when necessary. Characterizing the beam profile earlier, as explained in the previous section, helps to select the most convenient set of mode-matching lenses depending on where we want to set up our high finesses cavity. The concept of mode-matching is shown schematically in Figure 85.
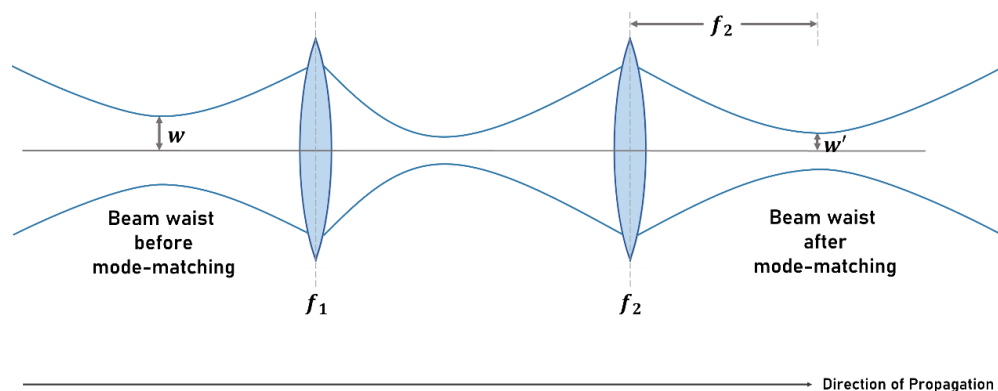
Figure 85 The mode-matching scheme with two lenses. This step is completed before placing the cavity mirrors so that the new beam waste is at the center of the high finesses cavity. The dimensions in this schematic are arbitrary.

### 4.1.5 A Schematic of the 30 cm Grating-Based Spectrometer

In CRDS experiments, there are different detection schemes. A charge-coupled device (CCD) or an array of photodiodes are often used for parallel detection of spectral components [9, 443]. Even though these methods are convenient, it comes with a compromise on the expenses of the system. In our experiment, we use a grating-based spectrometer and a single avalanche photodetector (APD) on a two-dimensional translational stage to detect the transmission signal, as can be seen in Figure 86.

A spectrometer of high resolvability allows to detect the leaking intensity from a CRDS system with a sufficient resolution. Let us recall the equation we obtained in Section 3.1 for the spatial separation between different wavelengths in a diffraction grating spectrometer, which states:

$$\Delta x = \frac{mf}{d \cos(\beta)} \Delta \lambda$$

206

We can differentiate $\lambda = \frac{2\pi c}{\omega}$ to get this relation $\Delta\lambda = -\frac{\lambda^2}{2\pi c}\Delta\omega$, and then substitute it in

the equation of $\Delta x$ to arrive at the spatial separation of the resolved frequency channels:

$$\Delta x = \frac{m\,\lambda^2\,f}{2\pi c\,d\,\cos(\beta)}\Delta\omega$$

Here, $m$ is the diffraction order, $\lambda$ is the wavelength of light, $f$ is the focal length of the

focusing optical element, $d$ is the line-spacing of the diffraction grating, $\beta$ is the angle of

diffraction, and $c$ is the speed of light. For the largest diffraction efficiency to be achieved,

the first order of diffraction $m = 1$ is used. These two expressions can be used to assign a

certain measurement to the corresponding wavelength or frequency. Part (b) of Figure 86

shows the experimental setup of the $30\ cm$ spectrometer used in our CRDS experiment.

A schematic of this setup is illustrated in part (a) of Figure 86.
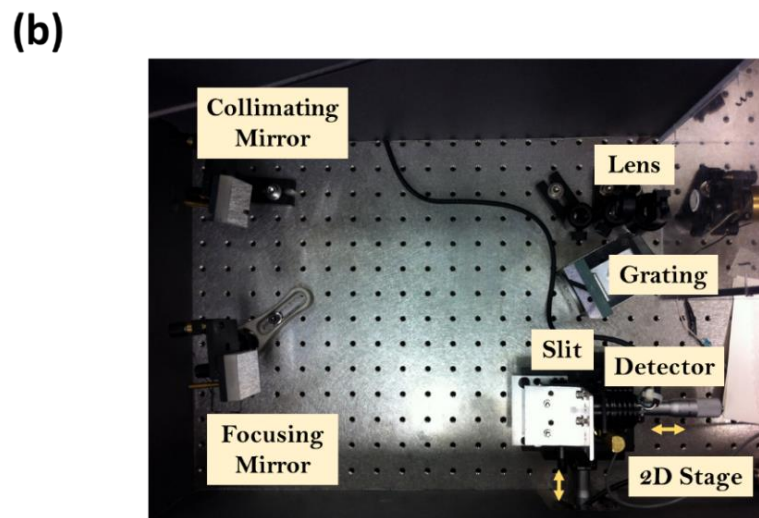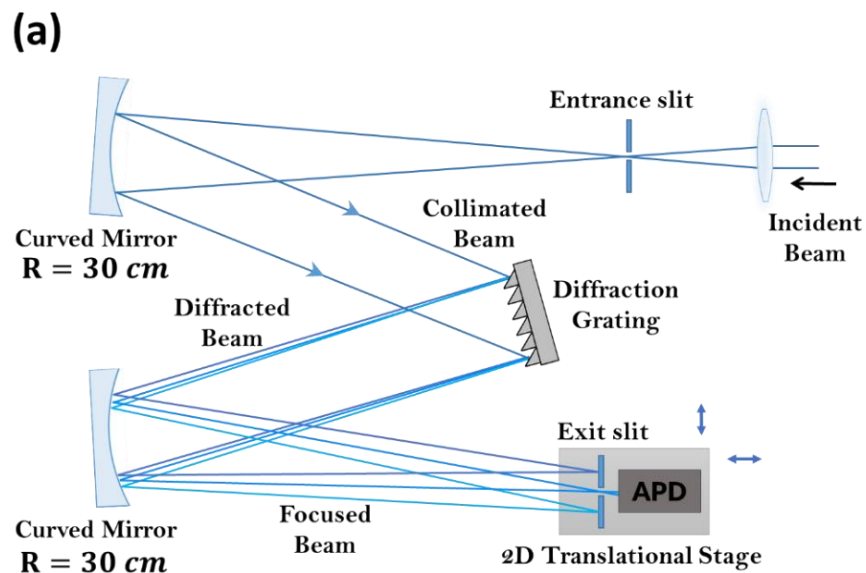
Figure 86 The 30 cm home-built diffraction-based spectrometer used in our CRDS experiment for spectral measurements. (a) A schematic of the setup, and (b) the experimental setup as can be seen on the optical table.

### 4.1.6 The Experimental Setup of the CRDS System

Before applying any locking scheme or running the experiment, it is essential to adjust the three main parameters of a CRDS experiment with a frequency comb source. These parameters are $f_r$ and $f_o$ of the comb and $FSR$ of the cavity, which are also known as the degrees of freedom for comb-based CRDS systems [370].

The repetition rate of the near-IR frequency comb used in our CRDS experiment is 250 $MHz$. In time domain, the pulse train consists of ultrashort pulses of duration less than 100 $fs$. The pulses are separated by 4 $ns$, which is equal to the round-trip time inside the laser cavity. Based on $f_r = 250\ MHz$ of our near IR frequency comb, the length of the high finesse cavity is $L = 60\ cm$.

The sweeping can be applied either to the cavity length ($L$) or the repetition rate ($f_r$). In our experiment, we use a sweep function to scan the cavity length. The two cavity mirrors have HR coating with a reflectivity $R = 99.99\%$ for both mirrors in the near IR. The first one is a plain mirror fixed on a one-dimensional translational stage, and the second is a concave mirror with a 2 $m$ radius of curvature ($R_c$). As illustrated in Figure 87, this mirror is glued on a PZT to scan the cavity length. The voltage applied to the PZT for generating the frequency sweep is provided by a function generator. Changing the voltage allows for changing the sweep frequency. A comprehensive description of the PZT effect can be found in Section 3.2 and Appendix C.
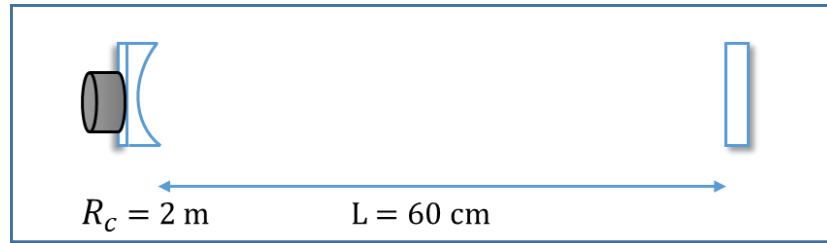
Figure 87 A schematic of the 0.6 m high-finesse cavity used in our experiment. The high reflectivity of the mirrors is close to 99.99% in the near IR. One is a plain mirror and the other is a curved mirror glued on a piezoelectric material. Cavity length is scanned by applying voltage to the piezoelectric transducer.

The finesse of our ringdown cavity, based on the finesse equation found in Section 2.5.1, is around $\mathcal{F} = 31{,}000$. The effective path length $(L_{eff})$ is calculated using the equation from Section 2.5 o be around $12$ kilometers. As we can see, the high finesse results in a long $L_{eff}$ which promises highly sensitive absorption measurements. Other methods for enhancing the sensitivity are available, such as optimized optical switching [444].

Our frequency comb is centered at $1.6 \, \mu m$, which allows for the detection of $CO_2$ gaseous molecules in this near IR region $1.5 - 1.7 \, \mu m$. To check the comb spectrum before running the experiment, a flipping mirror is used to direct the beam to a fiber coupler. The beam is focused by a lens of a short focal length to couple it into the fiber, and the fiber is connected to an optical spectrum analyzer (OSA). This analyzer, shown in Figure 88, has a display screen where we can see the shape of the spectrum and check on the other parameters.
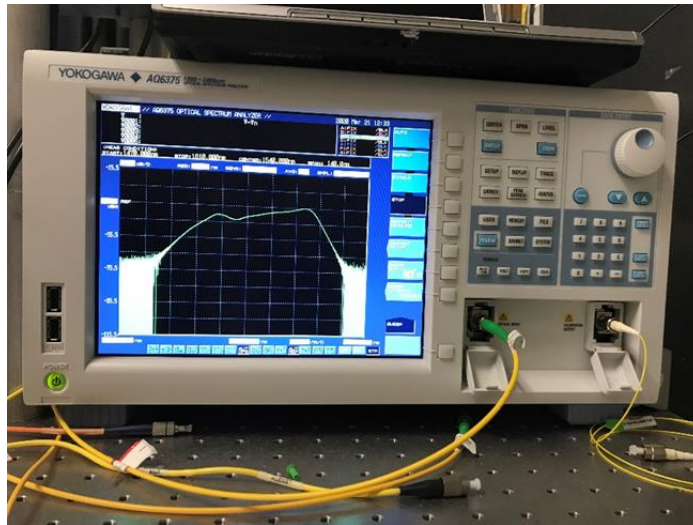
Figure 88 The Yokogawa optical spectrum analyzer used in our laboratory to display the spectrum of the IR frequency comb.

A schematic of the experimental setup of our CRD experiment is illustrated in Figure 89 below. An acousto-optical modulator (AOM) is used in our experiment to turn the incident light off when the build-up of intracavity intensity is sufficiently large. This is done using a trigger signal on the oscilloscope which is connected to the AOM drive. Two mode-matching lenses and two alignment mirrors are used to adjust the beam and control beam propagation. A red alignment laser and a detector are used to align the direction of the beam in parallel to the optical table before placing the cavity mirrors. Then, we remove the alignment detector and let the transmitted signal enter the $30\ cm$ spectrometer through a pin hole. For detection, an exit slit and an $InGaAs$ APD are fixed on a translational stage that can move in two directions.
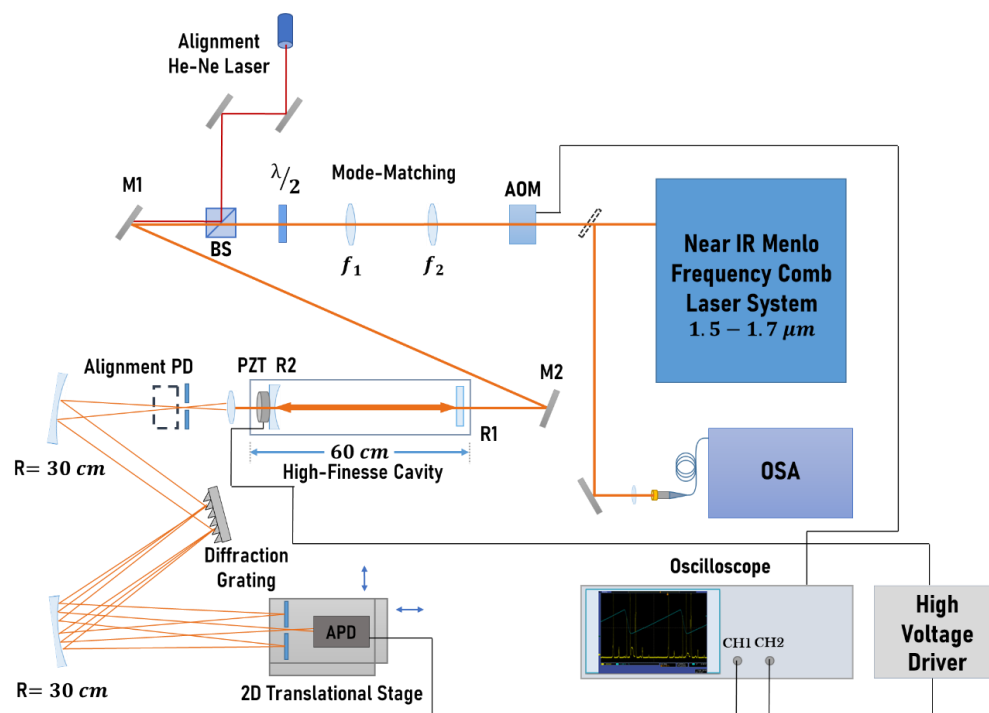
Figure 89 A schematic of the CRDS experimental setup. The output beam is first sent to an optical spectrum analyzer (OSA) to check the spectrum. An acousto-optical modulator (AOM) switches the light off after threshold is reached. Intracavity intensity decays exponentially giving a ringdown measurement. The transmission signal is resolved by a home-built spectrometer and measured by an avalanche photodetector (APD) fixed on a two-dimentional stage.

It seems from the viewpoint of experimentalists that the most challenging part in CRDS experiments based on frequency combs is the sampling scheme. Optical combs are broadband sources and this results in thousands of detection channels simultaneously. Therefore, fast sampling is required to get the absorption spectrum of the gaseous molecule. For highly accurate measurements, a sampling rate of $1\ MHz$, at least, has to be used [10, 445].

*4.1.7   Discussion of the Performance of CRDS Systems*

Spectroscopic techniques based on resonance cavities have been a leading approach in trace gas sensing and analysis for scientific research [9, 445, 446], environmental monitoring [2, 432, 435, 437], industrial quality assessments [439], and most recently breath analysis [8, 15, 31, 32, 438, 447] and isotopic analysis in outer space [448]. Using a high finesses resonance cavity results in a long length of interaction between the laser beam and the gaseous molecules. With a close-to-optimal mode-matching and a high system stability, the expected improvement in measurement sensitivity can be on the order of the finesse [10].

The spectral bandwidth of the HR mirrors is limited by the properties of materials used for mirror coating. The mirrors used in our experiment have multilayer dielectric coating. Combining materials of a larger difference between refractive indices can increase the width of the reflectivity band, which can open the door for a better utilization of the broad spectrum of frequency combs [370].

The intensity of the fundamental transverse mode, $TEM_{00}$, builds up inside the high finesse cavity, as can be seen in Figure 90. However, higher order modes can also be seen. When higher order modes are present, one can consider checking on the efficiency of mode-matching, or improving beam alignment. Suppressing the higher modes results in more intensity being fed to the fundamental mode, which has a positive impact on the $SNR$.
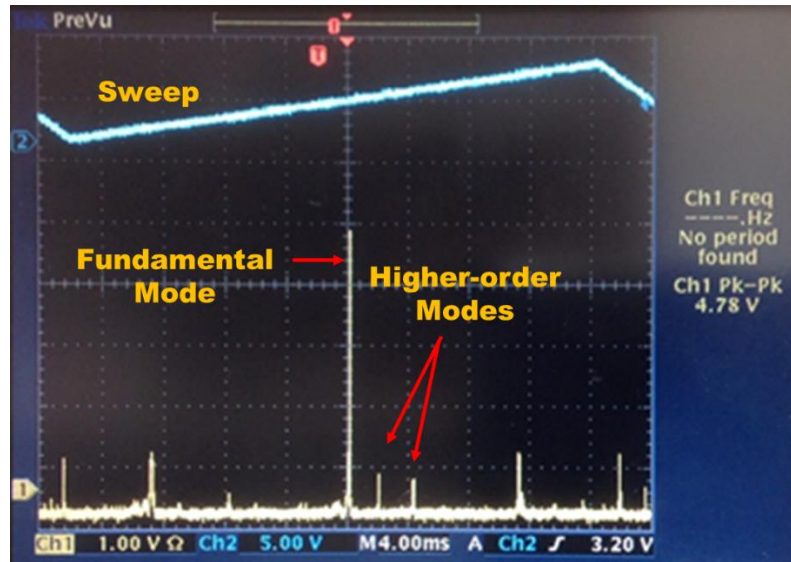
Figure 90 A screenshot of the experimental results showing the transmission signal obtained by mode-matching the frequency comb to the cavity. Higher order modes can be seen which means the intensity of the transmission signal can be further improved by adjusting alignment mirrors or mode-matching lenses.

The spectral bandwidth of overlapping between cavity modes and the comb is a crucial issue when we use a frequency comb source in an experiment for spectroscopy [315, 330]. As described in Section 2.2.6, the lines of a frequency comb have equal spacing between them in the frequency domain. However, the modes of a resonant cavity have a dependence on the frequency because of the intracavity dispersion term $c \left( \frac{\partial \phi}{\partial \omega} \right) \big|_{\omega}$, as can be seen in the $FSR$ equation found in Section 2.5.1. Low dispersion is required so that overlapping of the largest number of comb lines and their corresponding cavity modes is obtained.

Locking the defining frequencies of a broadband frequency comb; $f_r$ and $f_o$, to the cavity is necessary to achieve efficient coupling, which will improve the spectral

214

bandwidth [10]. When a broadband optical frequency comb is used as the light source, servo loops have proven to provide efficient locking [449]. The idea of using servo loops depends on generating an error signal based on the initial results, and then feeding that error signal back to the system to control the frequencies of the comb. If this option is selected for the locking scheme, each of $f_r$ and $f_o$ will have its own servo loop [276].

As we have seen experimentally, mirror losses result in the decay of the intensity when no absorption occurs. Whereas, the intensity decays at a faster rate when absorbing molecules are present. This can be seen in Figure 91, which shows a cavity decay signal recorded in our laboratory using an APD fixed on a translational stage. The position of the detector is changed slightly over a linear path to record the decay traces at different spatial positions. The expressions that relate the recorded measurement to the corresponding wavelength, or frequency, can be found in Section 4.1.5.
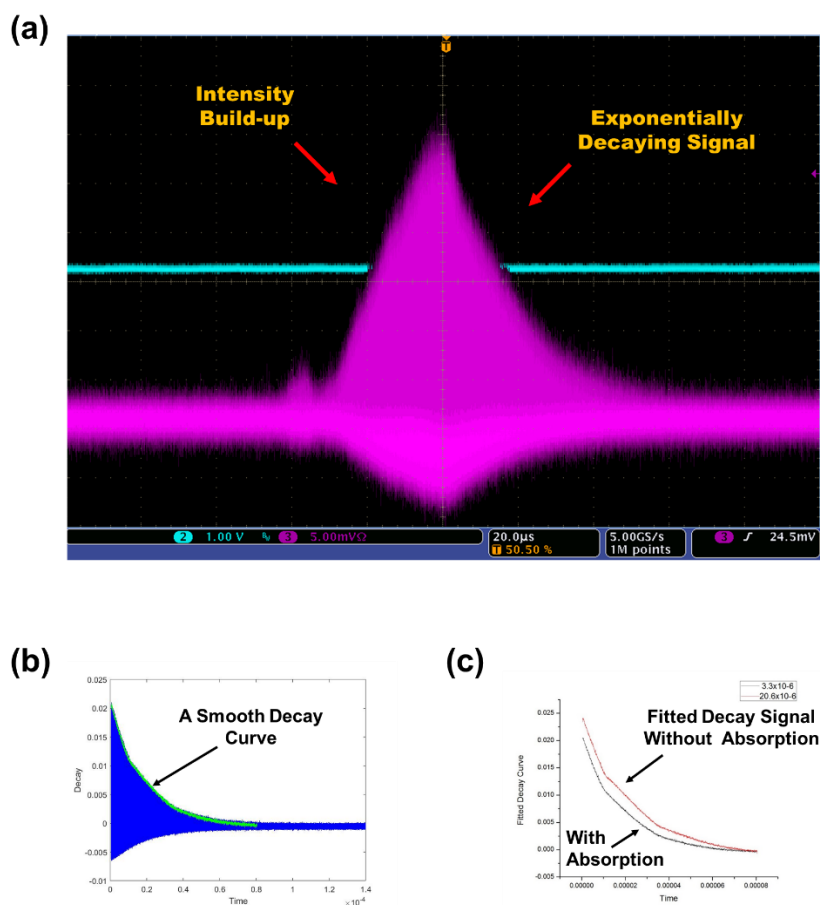
Figure 91 (a) The decay of the intensity recorded on our scope after shutting the AOM off. An APD detector is used for the detection. (b) A smooth ring-down curve obtained using a MATLAB code. (c) A comparison between two fitted decay traces, one with absorption and one without absorption. A faster decay trace indicates molecular absorption at that particular wavelength.

Using a broadband frequency comb for a CRDS experiment increases the complexity of the system, which is a drawback of this powerful technique. However, several research groups showed very successful implementations of the technique based on broadband sources [9, 370, 445]. Thorpe *et al* demonstrated a frequency comb-based breath analysis system capable of detecting ammonia ($NH_3$) molecules in breath samples

collected from patients with an estimate of $8 \times 10^{-10} \ cm^{-1}$ for the minimum detectable absorption [8, 10]. The high sensitivity was realized with a cavity-enhanced technique using mirrors of high reflectivity, which is equal to 99.989%, based on a near IR frequency comb at $1.6 \ \mu m$. New designs of optical combs with high power and compact sizes are available these days and many other are under development, which is a remarkable advantage for the diverse *in-situ* applications of frequency comb spectroscopy [27, 312, 330, 439, 450, 451].

Moreover, the stability and the design of the system contribute to the performance efficiency. Pressure fluctuations alter the ringdown time, which changes the FSR of the cavity by values that can reach 1.5 MHz [2, 445]. Therefore, a well-isolated system from vibrations in the surrounding environment is desired for a stable and robust performance.

A fast PZT can be used in the cavity to scan the cavity length so that the comb is dithered around cavity modes at a fast rate. Hoghooghi *et al* used $12 \ mm$ cavity mirrors with a thickness of $3 \ mm$ in their enhancement cavity [452]. One mirror is glued on a $6 \ mm$ PZT, which provides a bandwidth of about $10 \ kHz$ thus enabling cavity locking with a high SNR.

In addition to the high accuracy of spectral data collected by CRDS systems, there are many other positive features. For instance, absorption measurements based on CRDS do not suffer from laser intensity fluctuations. Being free from intensity fluctuation noise is an advantage of this technique over other cavity-enhancement techniques. Moreover, no calibration time is needed to adjust the cavity finesse in CRDS experiments before

217

making each measurement. This is because the finesse is a stable quantity determined by mirror reflectivity.

The ultimate goal in new and developing CRDS systems is to reach detection limits where very low concentrations of trace molecules can be monitored and quantified accurately. Further improvements in system design, stabilization, and noise-isolation can be applied to our CRDS experiment towards reliable absorption measurements that exceed the performance of available systems and provide high-sensitivity data. In a recent work by McHale and colleagues, a near IR sensor based on an open-path CRDS technique was implemented using mirrors of high reflectivity ~ 99.996% to investigate methane [14, 453]. They used this sensor for a field application to monitor the emission of natural gases [453]. A similar methane sensor with $10 - 30\ ppb$ precision was developed by the same group and attached to a small unmanned aerial system (sUAS) for applications in the natural gas industry [454]. Jin *et al* applied the CRDS technique based on a frequency comb centered at a mid-IR wavelength of 4.5 $\mu m$ [325, 455]. As the demand on sensitive trace gas analysis increases, advances in the field of IR cavity-enhanced absorption spectroscopy will continue and new approaches will follow [372, 455, 456].

**4.2 Mid-Infrared Dual Frequency Comb Spectroscopy***

*4.2.1   Principles of Dual Frequency Comb Spectroscopy*

The dual frequency comb technique is one of the new techniques for frequency comb spectroscopy that emerged about a decade ago and proved to be an attractive spectroscopic tool [11, 13, 457-459]. The technique relies on interfering the beams emitted from two frequency comb sources to get an interferogram [452, 458]. A difference $\Delta f_r$ in the repetition rates of the two frequency combs is required, in general, for the dual comb technique. The interferogram is then converted to the frequency domain through Fourier transformation (FT) to get the absorption spectra of gaseous molecules. This method is simple, yet very powerful in terms of precision and data acquisition time. It utilizes the broad bandwidth, high coherence, and frequency accuracy of frequency combs and provides highly sensitive results [12, 47, 452, 460-464].

The concept of this technique in time and frequency domains is simplified and presented in Figure 92. As the train of femtosecond pulses emitted from the first frequency comb samples the pulse train of the second comb, an interferogram is obtained similar to that of conventional FT-IR spectroscopy [458, 460]. In the time domain presentation, illustrated in part (a) of Figure 92, the delay between each pair of pulses increases linearly with time. As time goes by, a new pair overlaps and the same picture is repeated. The distance between an interferogram and the next one is equal to $\frac{1}{\Delta f_r}$. The frequency domain

picture of dual comb spectroscopy shows the modes of the two combs and the difference $\Delta f_r$ between them, as can be seen in part (b) of Figure 92.
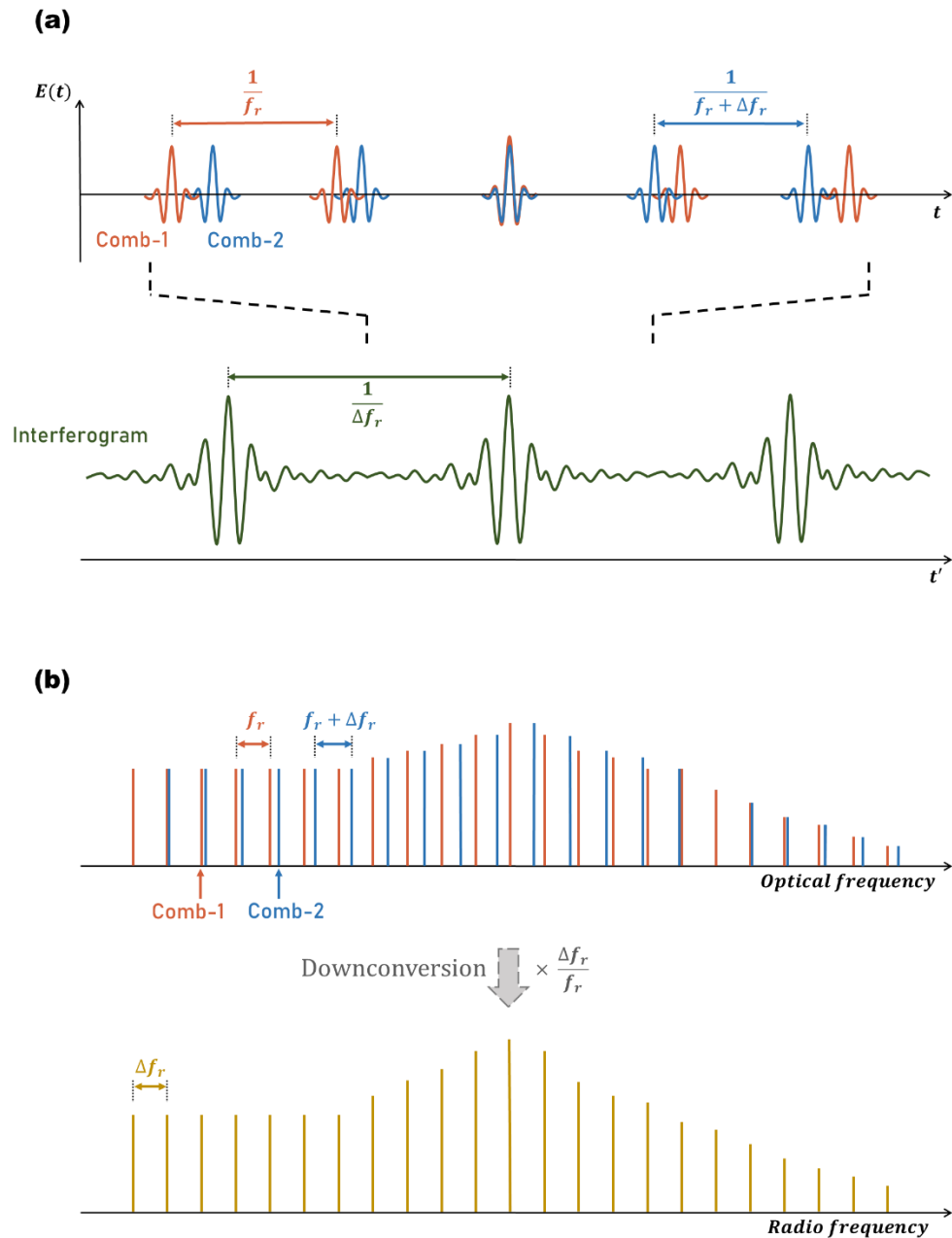
Figure 92 A schematic of the concept of dual frequency comb spectroscopy technique. (a) The time domain picture showing the overlap of the pulses emitted by the two sources and the corresponding center burst when the two pulses completely overlap. Each center burst is separated from the previous one by $1/\Delta f_r$. (b) The frequency domain picture of dual comb and the down-conversion from optical frequency to radio frequency.

To present a mathematical treatment, the two combs can be described in terms of their defining frequencies:

$$(f_n)_1 = (n\,f_r)_1 + (f_o)_1$$

$$(f_n)_2 = (n\,f_r)_2 + (f_o)_2$$

$$(f_r)_1 = (f_r)_2 + \Delta f_r$$

where $(f_n)_1$ is the frequency of the nth mode of comb-1 and $(f_n)_2$ is the frequency of the nth mode of comb-2, as defined in Section 2.2.6 for a frequency comb, $\Delta f_r$ is the difference in the repetition rates of the two frequency combs, $(f_r)_1$ is the repetition rate of comb-1, and $(f_r)_2$ is the repetition rate of comb-2. When a beat signal is obtained for the same mode, let us say mode $n$, then the result can be written as:

$$(f_n)_{Beat} = (f_n)_1 - (f_n)_2 = \left[ (f_o)_1 - (f_o)_2 \right] + n\,\Delta f_r = \Delta f_o + n\,\Delta f_r$$

An advantage of this technique is that mapping the spectrum to the radio frequency (RF) domain allows for detection with RF electronics. The RF spectrum can be obtained from a series of interferograms by an FT analysis. There is a heterodyne beat signal in the RF domain for each pair of lines from the two frequency combs. The beating of comb lines from the two sources results in a down-conversion factor given by:

$$m = \frac{f_{optical}}{f_{RF}} = \frac{nf_r}{n\Delta f_r} = \frac{f_r}{\Delta f_r}$$

Let us denote the width of the optical spectrum by $\Delta v$, then we have an RF spectrum of width $\frac{\Delta v}{m}$, where $m$ is the compression factor equal to $\frac{f_r}{\Delta f_r}$ [457, 465]. For a clear mapping to the RF domain, the repetition rates $(f_r)_1$ and $(f_r)_2$ should be very close such that [466]:

$$\Delta f_r \leq \frac{(f_r)^2}{2 \, \Delta v}$$

Having a small difference allows the large number of comb lines $(10^5 - 10^6)$ to be observed simultaneously [11, 47, 452].

In general, the time required for a single spectrum is at least $\frac{1}{\Delta f_r}$. However, some experiments rely on using multiple spectra and co-adding them to achieve a desired SNR [460]. In that case, the desired SNR level determines the minimum acquisition time. Other experiments apply an alternative method to increase the sensitivity and relax the requirement of a large SNR, which includes using multipass cells [12, 19], resonant cavities [370, 452], or a long open-path approach [3, 47, 462]. We use a multipass cell in our experiment, which is discussed in the next section, to increase the light-matter interaction length and investigate the concentration of methane $(CH_4)$ molecules in the surrounding air inside our laboratory.

### 4.2.2   Enhancement of Interaction Length Using a Multipass Cell

To enhance the absorption signal, a $100 \, cm$ multipass cell is used at one of the beam paths. The multiple passes inside the cell increase the light-matter interaction length to $580 \, m$. The molecules along the beam path absorb light at wavelengths that correspond to certain molecular transitions. The absorption signal, after hundreds of passes, becomes sufficiently large and can be used to identify the absorbing molecules, as described in Section 2.1.3.

The alignment of the multipass optical cell in our laboratory is based on a computer algorithm that provides a pattern of spots [12]. This pattern allows for a large number of reflections on the confocal mirrors at the two sides of the optical cell. The size of the mirrors is $5 \times 5 \; cm^2$ and the radii of curvature are $100 \; cm$. Each mirror has three parts, two on the top and one on the bottom, that are visually divided into smaller reflection areas as illustrated in Figure 93. There is only one hole $5 \; mm$ in size to allow the beam to enter and exit the cell. The pattern we followed was generated using a software algorithm to provide an optical path length of $580 \; m$, as shown schematically in part (a) of Figure 93. The theoretical discussion of the interaction length was covered in Section 2.5.
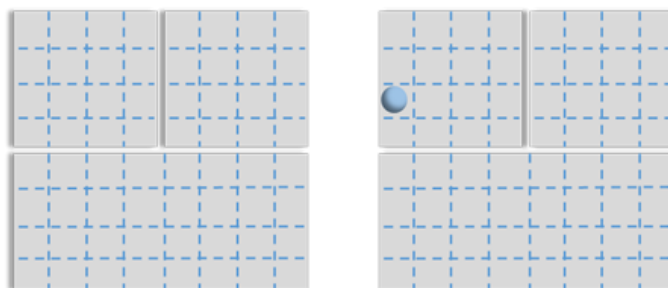


Figure 93 A schematic of mirror mapping for the multipass cell used in the dual frequency comb spectroscopy experiment in our laboratory. A single hole on one of the mirrors allows the beam to enter and exit the cell.

Frequency comb spectroscopy requires HR mirrors with special coating materials because frequency combs have broad bandwidths. The mirrors used in this experiment are manufactured with a coating material that provides a high reflectivity $R \approx 0.9985$ in the mid-IR wavelength region $3.1 - 3.6 \; \mu m$ and a high reflectivity $R \approx 0.999$ also in the red-

224

color region $670 - 680\ nm$. An experimental determination of mirror reflectivity is provided in Appendix F. The reflectivity is determined to be around $0.9955$ based on measurements of the input power before the beam enters the multipass cell and the output power after the beam completes 580 passes inside the cell. A schematic of the multiple reflections inside the cell is given in part (a) of Figure 94, and the mulipass cell we used in this experiment is shown in part (b) of Figure 94.

**(a)**
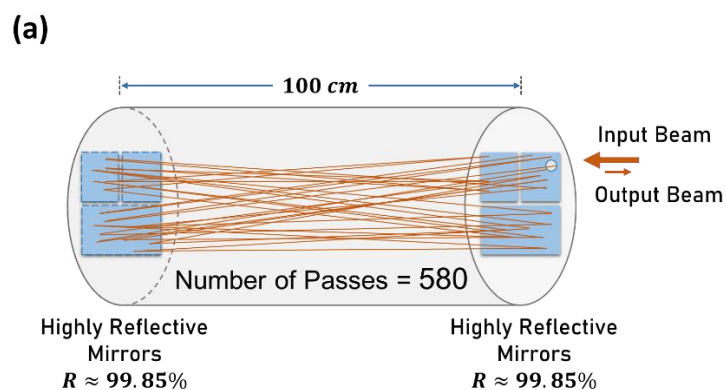


**(b)**
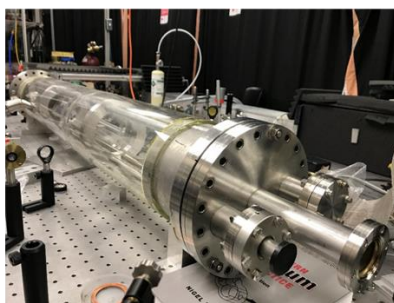


Figure 94 The multipass optical cell used for increasing the light-matter interaction length. (a) A schematic to show multiple reflections on the mirrors inside the cell before the beam exits through the same hole. (b) The 100 cm multipass cell used for the dual comb spectroscopy experiment in our laboratory.

The pattern of red spots, which can be seen in Figure 95, is achieved using a red diode laser. Mirror mounts are adjusted sequentially and repeatedly until the pattern is complete and the maximum output power is obtained. Even though this alignment step requires sufficient time and effort, it is very crucial because a well-aligned multipass cell improves the performance of the system and provides the desired sensitivity of measurements. The pattern observed experimentally on the mirrors of the multipass cell, which can be seen in Figure 95, also indicates the level of efficiency of the alignment step.
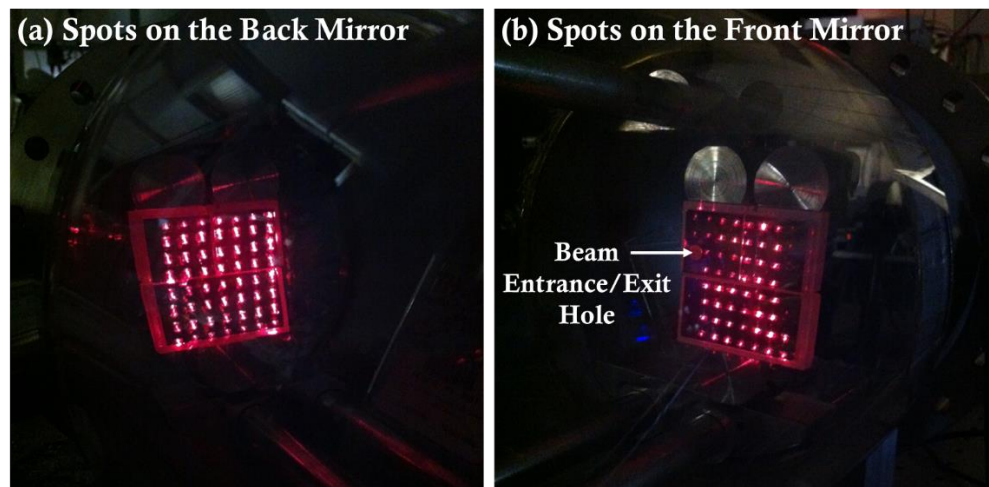


Figure 95 The pattern of spots on the mirrors inside the multipass cell obtained using a red diode laser. The mirrors are carefully adjusted without disturbing the pattern until the maximum output power is measured. (a) The spots on the back mirror, and (b) the spots on the front mirror with one entrance and exit hole on the side.

### 4.2.3 The Two Mid-Infrared Frequency Comb Sources

Frequency combs based on femtosecond lasers are now available in the mid-IR [156, 266]. These optical sources, which are also known as femtosecond frequency combs [219], have proven to be very efficient for molecular spectroscopy [220, 315, 276]. Many applications deploy femtosecond combs for molecular fingerprinting to investigate concentrations of trace gases such as iodine vapour [48], methane [12, 462], ammonia [9], acetone [47], ethane [452], and acetylene [9, 467].

The two mid-IR frequency comb sources used in our experiment are based on femtosecond erbium-doped fiber oscillators [218, 291]. Both combs are stabilized at a repetition rate $f_r = 250\ MHz$ with a small difference between them equal to $\Delta f_r = 1.489\ KHz$. The frequency comb source used to interact with the air sample inside the mutlipass cell is shown in Figure 96. The blue box in part (a) of the figure contains all of the elements of the comb source that are shown schematically in part (b). Erbium-doped fiber amplifiers are used to increase the power. The two combs are based on DFG processes which involve a nonlinear conversion to lower frequencies, as explained previously in Section 2.2.5. Combining the pump and signal beams at the nonlinear crystal results in an output beam emitted at a mid-IR wavelength of $3.25\ \mu m$. The properties of our frequency combs have been demonstrated explicitly by Zhu and other colleagues in our research group [218].

**(a)**
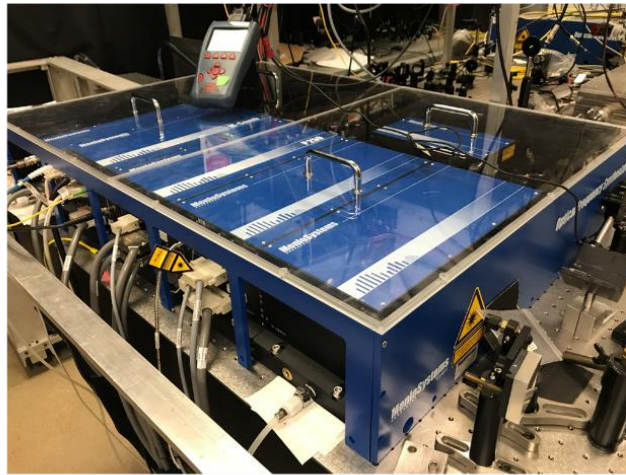
**(b)**
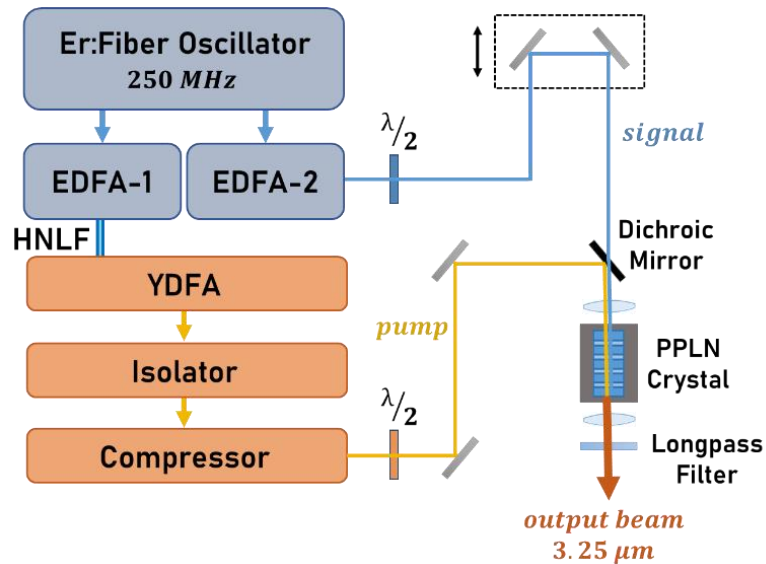
Figure 96 The mid-IR frequency comb used to carry the absorption information of methane in the multipass cell. (a) The actual comb source on the optical table in the laboratory. (b) A schematic of the comb source which mainly shows an erbium fiber oscillator of 250 MHz repetition rate, two erbium-doped fiber amplifiers (EDFA), a highly nonlinear fiber (HNLF), a ytterbium-doped fiber amplifier (YDFA), the periodically-poled lithium niobate crystal used for nonlinear DFG effects, and the emitted mid-IR output beam.

A rubidium ($Rb$) frequency standard is used as a reference in each frequency comb to lock the repetition rate. The carrier-envelop offset frequencies of the two DFG combs; $(f_o)_1$ and $(f_o)_2$, are stabilized passively because both the pump and the signal beams are produced by the same source, which eliminates any phase slip in the output beam.

### 4.2.4   Characterization of the Pulses by Autocorrelation Traces

Before proceeding with the experiment, we characterize the two frequency combs based on their spectra and interferometric autocorrelation traces. A commercial McPherson monochromator, shown in Figure 97, is used to scan the spectrum of each comb along the mid-IR region $2.8 - 3.8\ \mu m$. We can choose either to scan from shorter to longer wavelengths or in the opposite direction, and we can select the scanning range through the controllers on the side of the monochromator, which can be seen in part (b) of Figure 97. A lens is used to focus the beam at the entrance slit of the monochromator, and a detector is placed right at the exit slit to record the spectrum. A scanning speed of $500\ A^o/min$ was selected for the recording. The same steps are followed for both of our mid-IR frequency combs, and the measured spectra are displayed in Section 4.2.6 as part of the experimental results.
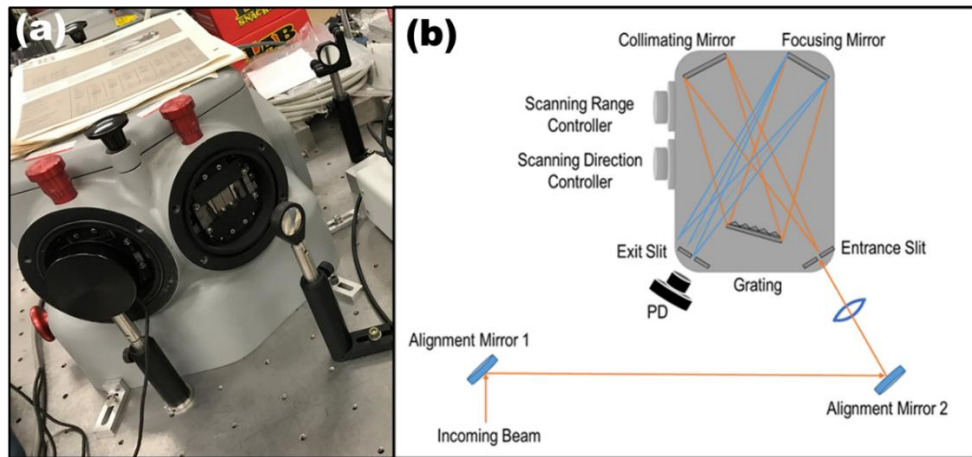
Figure 97 (a) The 30 cm commercial McPherson scanning monochromator used for recording the spectra of the two mid-IR frequency combs. The focusing lens and the detector are shown. (b) A schematic showing the top view of the monochromator and the beam path inside it. The main parts include an entrance slit, a collimating mirror, a diffraction grating, a focusing mirror, and an exit slit. The controllers are on the side.

The autocorrelator used to obtain the interferometric autocorrelations of the short pulses emitted by the frequency comb sources is illustrated in Figure 98. A simplified version of the setup is shown schematically in part (a), and the experimental setup in our laboratory is displayed in part (b) of Figure 98. Using a nonlinear crystal at the output allows for a second harmonic generation. The results, which can be found in Section 4.2.6, show the characteristic ratio of 8: 1 for the autocorrelations, and reveal the pulse duration.
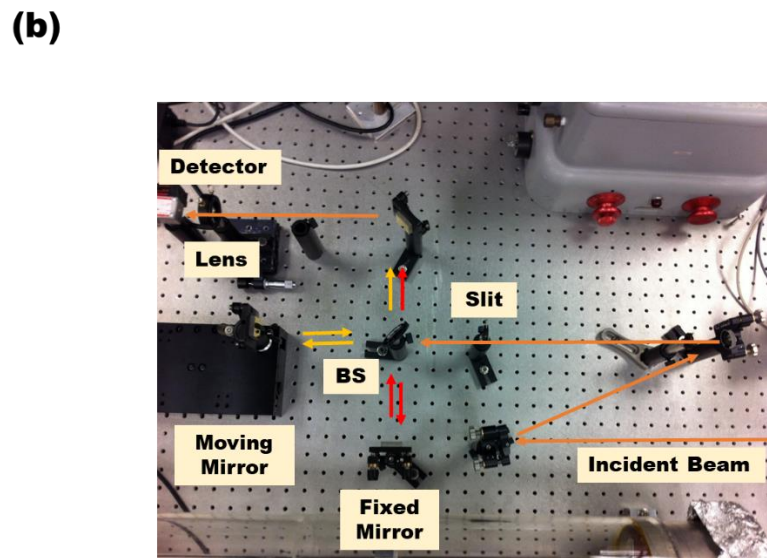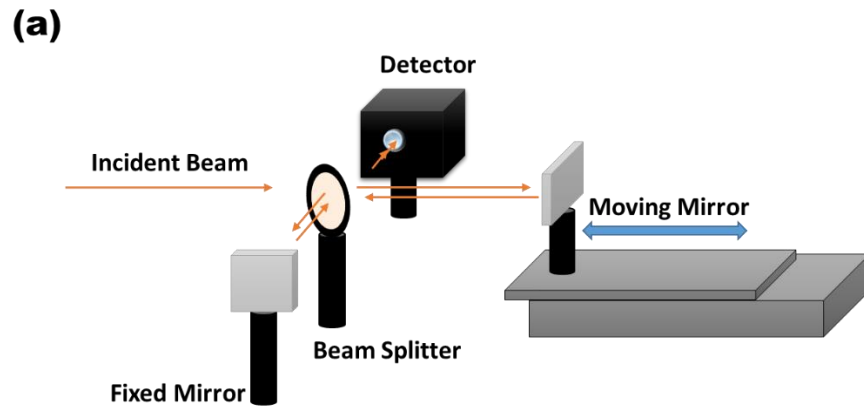
Figure 98 (a) A simple schematic of an interferometric autocorrelator showing a moving arm, a fixed arm, a beam splitter, and the detector box which contains some other elements. (b) The experimental setup of the interferometric autocorrelator used for characterizing the temporal properties of the pulses emitted from our frequency comb sources. The autocorrelation trace obtained from this setup reveals the pulse duration.

*4.2.5    The Experimental Setup*

Our experimental setup includes the two mid-IR frequency combs, beam-adjustment lenses, alignment mirrors, two beam splitters, a $100\ cm$ multipass optical cell, a liquid-nitrogen-cooled detector, signal filters, and an oscilloscope. The laser beam from one of the frequency comb sources enters the multipass cell, interacts with the sample, and carries the absorption information about the gaseous molecules. We denote this source as comb-1. The second comb, referred to as comb-2, is used as a reference in the dual frequency comb technique. We use the second frequency comb in our experiment for overlapping with the output beam from the multipass cell and providing the desired interferogram.

The repetition rate of mid-IR frequency comb-1 is $249.998633\ MHz$ and that of mid-IR comb-2 is $250.000122\ MHz$. A repetition rate difference of $\Delta f_r = 1489\ Hz$ is selected such that beating of comb modes at frequencies larger than $\frac{f_r}{2}$ is avoided, but fast recording is still achievable [13].

In our experimental setup, we use three lenses to control the propagation and the size of the beam, which we call the beam-adjusting lenses. The purpose of using these lenses, as illustrated in Figure 99, is to prevent the beam from diverging out of the cell and therefore maintain its optical power. After we finished this step with the lenses, we placed the multipass cell on its current position on the optical table.
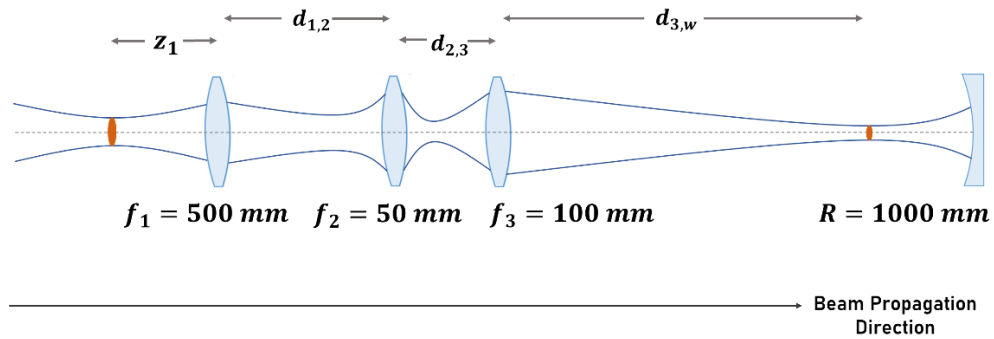
Figure 99 A schematic of the beam-adjustment step based on three lenses. This scheme is used to control the propagation of the beam and reduce beam divergence inside the multipass cell. Here, $z_1$ is the distance between the beam waist and the first lens, $d_{1,2}$ is the distance between the first and second lenses, $d_{2,3}$ is the distance between the second and the third lenses, and $d_{3,w}$ is the distance between the third lens and the new beam waist. All these values are used in calculations for beam characterization.

Before using the mid-IR laser beam, which is invisible to our eyes, we align the $100\ cm$ multipass cell using a red diode laser. As mentioned in Section 4.2.2, the mirrors of the multipass cell are highly reflective at both red-color wavelengths and mid-IR wavelengths. Having the spot pattern, shown previously in Figure 95, and recording the highest possible output power from the multipass cell indicates that the cell is well-aligned and ready for the experiment.

Alignment mirrors are used to control the propagation of the beam towards the entrance hole of the multipass cell. When the beam from comb-1 is directed to enter the multipass cell, it passes first through a $50:50$ beam splitter that splits the beam into two parts, one of them serves as a reference. Having only one of the combs transmitted through the gas sample makes this dual comb approach an asymmetric approach [11]. Figure 100 shows the experimental procedure we followed for aligning the beam.

233
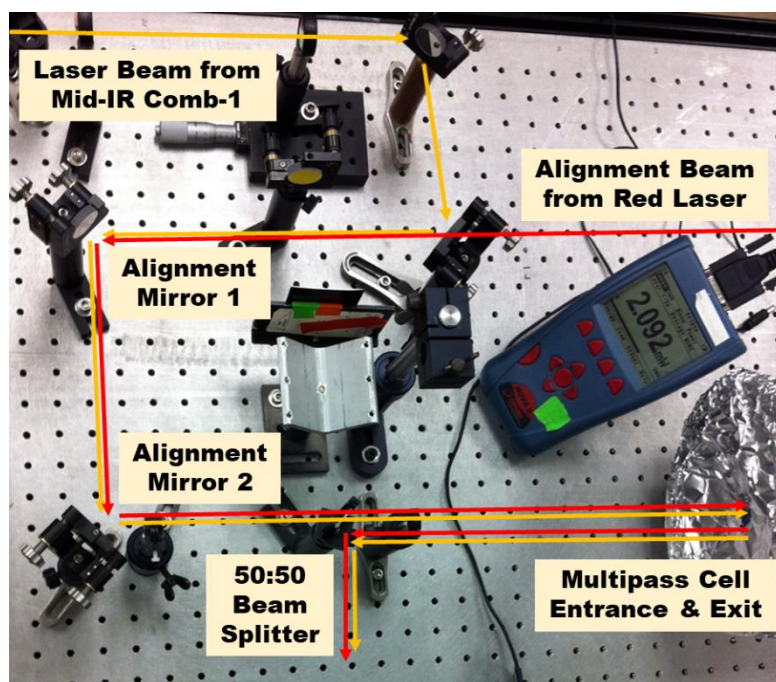
Figure 100 The alignment of the multipass cell using a red diode laser. This red laser is used first to align the mirrors of the cell until the maximum output power is measured. The red arrows represent the direction of the red laser and the yellow arrows denote the beam from mid-IR comb-1. The sides of the multipass cell are covered while not in use to avoid dust accumulation on the mirrors.

The setup of our mid-IR dual comb spectroscopy experiment is illustrated in Figure 101, which shows the two mid-IR comb sources, the $1\,m$ multipass cell, the detection scheme, and the optical elements such as lenses, mirrors, and beam splitters. Two slits and two alignment mirrors are used to direct the mid-IR beam into the multipass cell so that it almost follows the same path as the red alignment laser. Furthermore, there are two beam splitters in this setup. The first beam splitter allows the input beam from mid-IR comb-1 to be transmitted and then the output beam from the mutlipass cell to be reflected, while the second beam splitter combines the output beam from comb-1, which carries the

absorption information, with the incident beam from comb-2 for dual comb measurements.
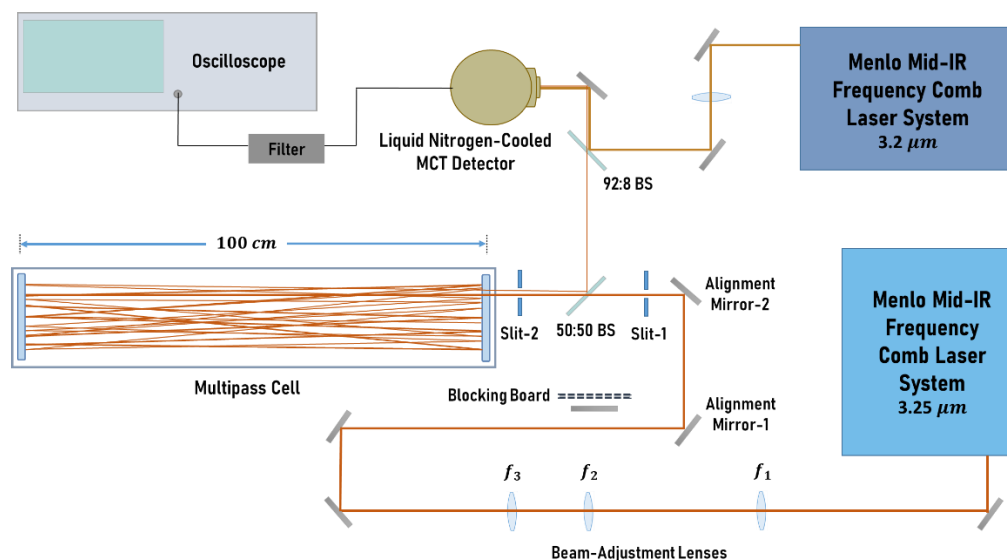


Figure 101 A schematic of the experimental setup of dual comb spectroscopy experiment based on two mid-infrared frequency combs. Two mirrors and two slits are used for beam alignment. One laser beam interacts with the molecules inside a 100 cm multipass cell. The two beams interfere and the resultant signal is detected by a cooled MCT detector.

Among all types of IR detectors, mercury-cadmium-tellurite (MCT) is one of the most capable and commonly used detectors [329]. In this dual comb experiment, we use a liquid nitrogen-cooled MCT detector to detect the signal after the two beams overlap, as shown in Figure 102. The low operating temperature of the detector is essential for reducing measurement noise. A $92\!:\!8$ beam splitter is used to combine the laser beams

from the two sources, and a focusing mirror to focus them at the detector. This is illustrated in Figure 101 schematically, and the experimental version can be seen in Figure 102.
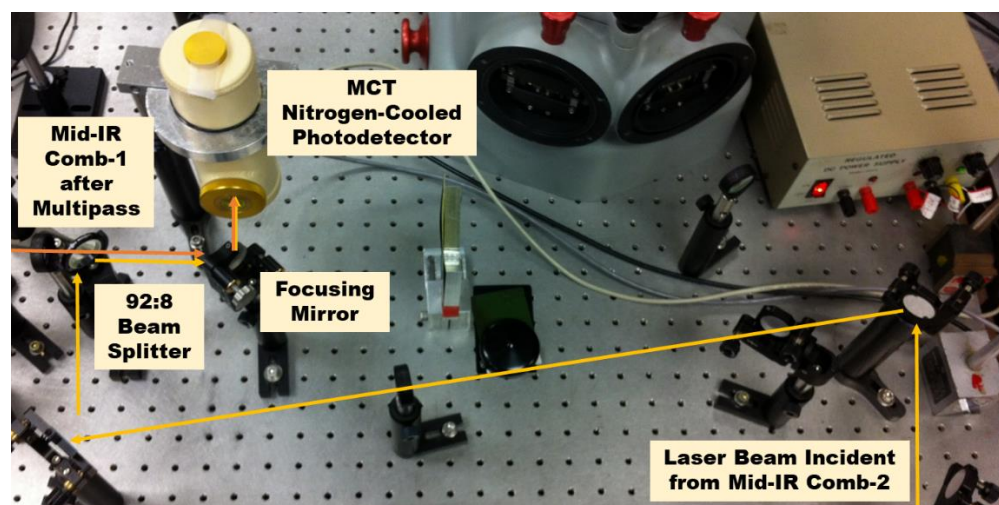


Figure 102 The experimental setup of the detection part showing the beam splitter and the focusing mirror used to combine and focus the two beams, and showing the MCT cooled detector used to record the dual comb results.

### 4.2.6   Results and Data Analysis

The output power from frequency comb-1 and frequency comb-2 sources were measured to be around 375 $mW$ and 120 $mW$, respectively. In the design of comb-1, a $Yb$-doped fiber amplifier was used to increase the power to the 300 $mW$ level. The spectra of the two mid-IR frequency combs were recorded using a 30 $cm$ commercial McPherson scanning monochromator. The two combs have similar spectra that span the region between 2.8 µ$m$ and 3.6 µ$m$, and are centered on the vicinity of 3.2 µ$m$. Furthermore, an interferometric autocorrelation trace was obtained for each frequency comb to verify the

temporal characteristics of the emitted short pulses. The results for the interferometric autocorrelation traces and the spectra of the two combs are presented in Figure 103. These results show a pulse duration of about $80\,fs$ for both sources and a ratio of $8:1$ for the peak as compared to the wings of the trace, as expected when measuring ultrashort laser pulses [468, 469].

**(a)**
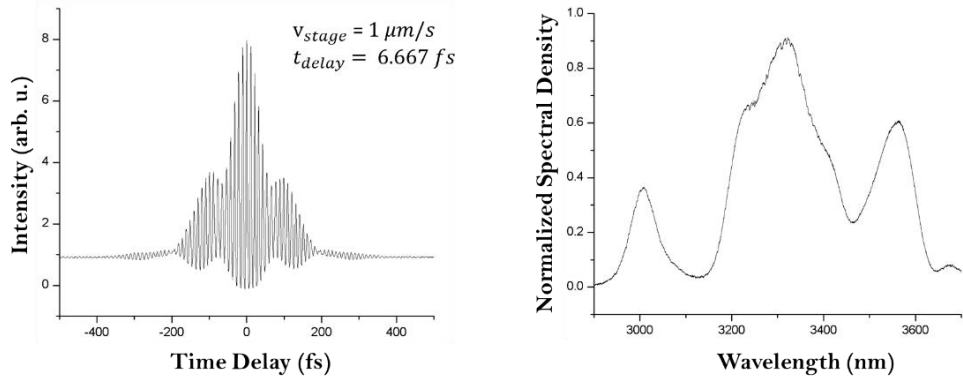


**(b)**
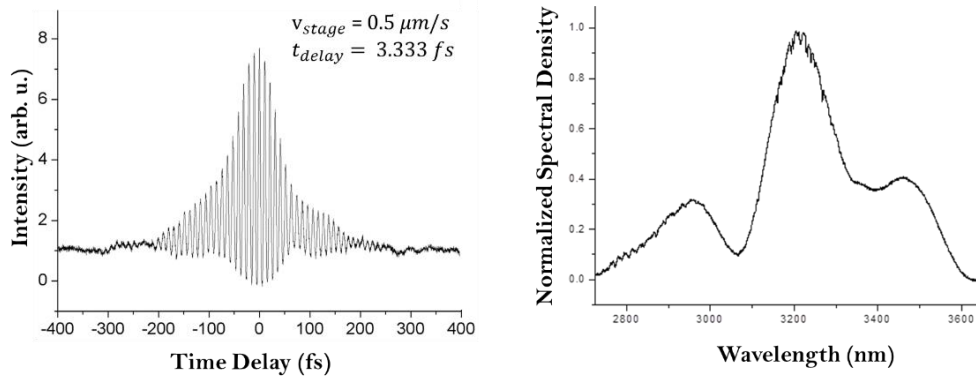


Figure 103 The experimentally recorded autocorrelation traces and spectra of the combs used in the dual comb experiment. (a) The results for frequency comb-1. (b) The results for frequency comb-2. The stage-speeds used for the moving arm of the autocorrelator are indicated for both parts.

A long interaction path-length of $L = 580\ m$ is achieved using a $1\ m$ multipass cell with HR mirrors. Using a beam-adjustment technique have reduced the losses significantly, as we observed experimentally. However, the beam power has largely decreased after the multiple reflections due to absorption, scattering, and reflection losses

in each pass. As a result, the power of the beam exiting the multipass cell after completing 579 reflections is between 1 and $2\ mW$. When we run the experiment on a relatively humid day, we get lower output powers because of the large absorption of optical power by water vapor molecules. The red lines in Figure 104 show one set of experimental data obtained for methane in air based on an interaction length of $580\ m$.
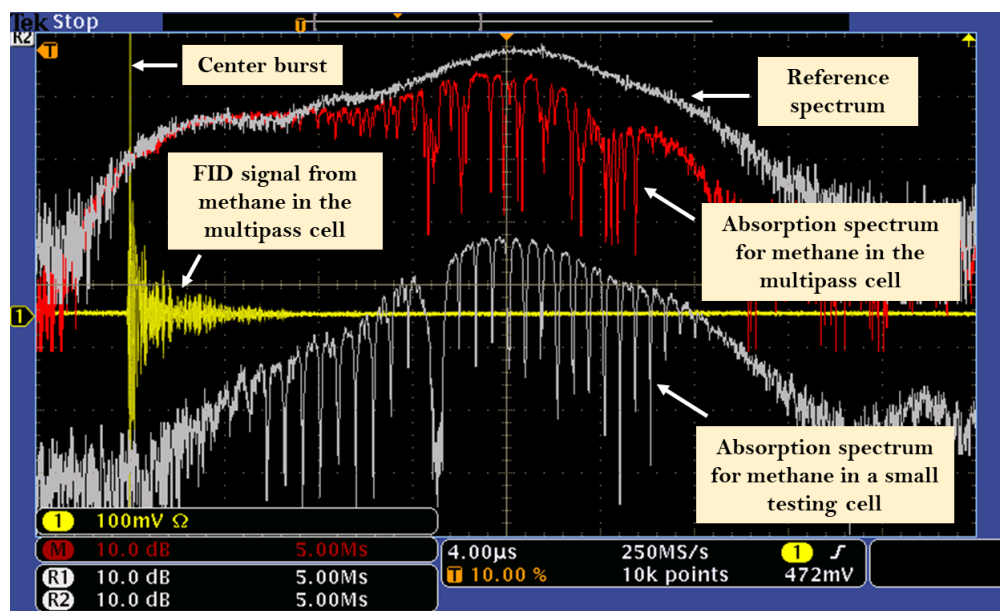


Figure 104 A screenshot of the experimental results obtained for methane detection using mid-IR dual comb spectroscopy and a multipass cell with a total interaction length of 580 m. The center burst can be seen with the FID signal from molecules present in the multipass cell. Shown here are a reference spectrum, a spectrum for methane-in-the-air, and a methane spectrum from a small testing cell recorded on the screen of a fast oscilloscope.

The largest peak seen in Figure 104, also known as the "center burst," occurs when the short pulses from the two comb sources arrive at the detector at the same time. The

week signal at the tail of the interferogram, which can also be seen in part (b) of Figure 105, is known as the free induction decay (FID) signal. It carries the information about the absorbing molecules in the beam path. As can be seen from Figure 104 and Figure 105, this FID signal appears at one side of the central peak because the interaction with the molecular sample in the cell involves only one of the two laser beams.

When a new pair of pulses overlap, a new interferogram is generated. Each interferogram is far from the previous one by a time duration equal to $\frac{1}{\Delta f_r} \sim 0.67 \ ms$. The interferograms are recorded with an oscilloscope at $250 \ MHz$ sampling rate and a 10-bit resolution. A total number of 118 interferograms are recorded, and the longest length of recording is $80 \ ms$, or 20 Mega points. In Figure 105, three experimental interferograms are displayed to show the difference between three cases. The first one is a reference interferogram, the second is a result of our experiment with the multipass cell, and the third one has a larger signal since we used a small cell with a high concentration of $CH_4$ for testing.
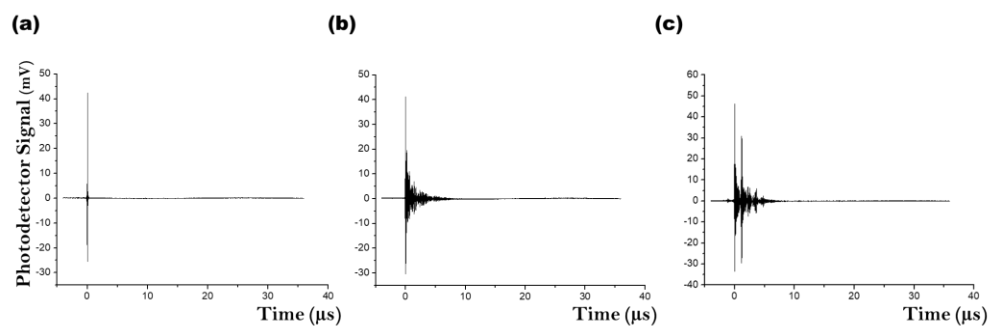
Figure 105 The experimental results. (a) The reference interferogram. (b) The interferogram with the FID signal from the gaseous molecules in the multipass cell. (c) The interferogram with a large FID signal from a small testing cell filled with methane gas.

The average interferogram is analyzed by FT to reveal the magnitude and phase in RF domain, and the spectra are converted to mid-IR. Figure 106 shows the experimental results of mid-IR dual comb spectroscopy with a $580\ m$ length of interaction. The upper part is the normalized absorbance $(\alpha L)$, which contains the absorption lines of methane and water molecules based on a simulation from the HITRAN-2012 database for molecular species [36]. The inverted part shows the experimental absorption lines for both methane and water vapor molecules present in the multipass cell. The results in both parts are based on $580\ m$ interaction length.
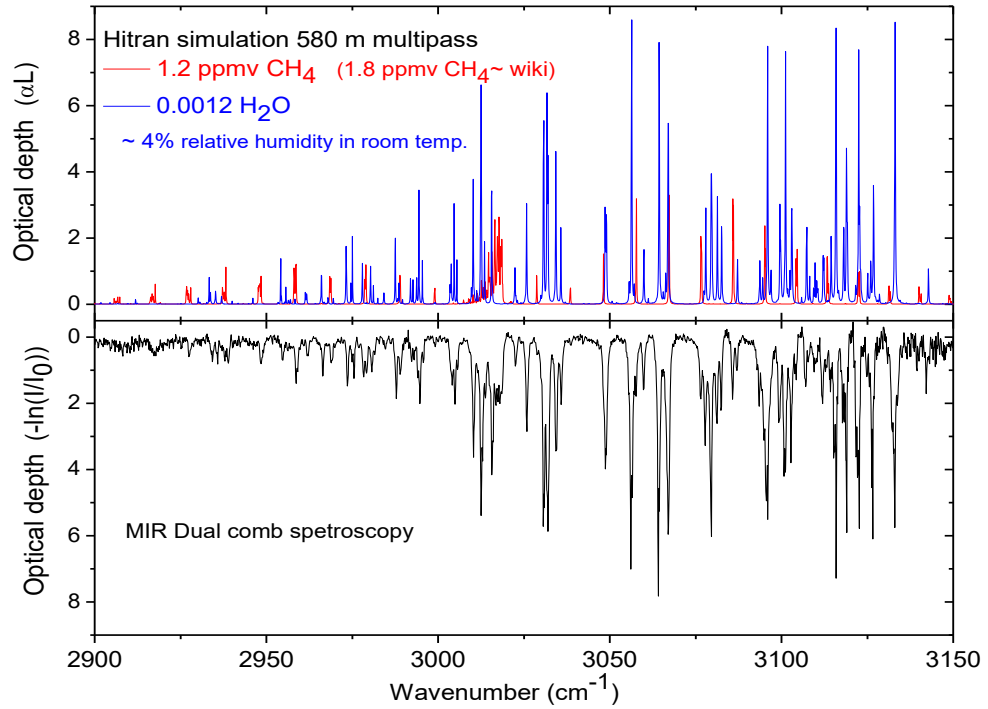
Figure 106 The normalized absorption spectrum of methane and water vapor in the mid-infrared region 2900-3150 cm$^{-1}$. The inverted part is obtained experimentally using a multipass cell with a total interaction length of 580 m, and the upper part using HITRAN database calculation for the two molecules under experimental conditions: room temperature, atmospheric pressure, 580 m path length, 1.5 ppmv of methane, and 1300 ppmv of water. Methane lines are in red, and in blue is the water vapor absorption in this region around 2.3 µm.

In obtaining the absorption spectrum, we used the following expression for the complex spectrum:

$$S = S_o e^{-\frac{\alpha L}{2} - i\varphi}$$

where $\alpha$ is the absorption coefficient, $L$ is the path length, $\varphi$ is the phase shift, $S$ is the signal complex spectrum and $S_o$ is the reference one, and all are functions of the optical frequency [12, 36]. At the center of the spectrum, the SNR for methane is estimated to be 75 and for water is 150. These values are lower at the edges of the comb spectrum.

242

To evaluate the sensitivity of our absorption measurements, we choose the central region, where the optical power is maximum and no absorption lines are present, to get the root mean square noise ($\sigma$). Then, this parameter is used to determine the sensitivity based on the following relation:

$$\alpha_{min} = \frac{\sigma}{L}$$

In our case, the measurement sensitivity is found to be around $7.6 \times 10^{-7} \ cm^{-1}$.

Comparing the experimental data with HITRAN calculations, we found that the concentration of methane in the surrounding air is in the level of 1.5 ppmv with $\pm 0.1$ ppmv to compensate for experimental errors. The concentration of water vapor molecules is estimated to be $1300 \pm 100$ ppmv, equivalent to a relative humidity of 4%. For our system, the minimum limit of methane detection in the surrounding air is 60 ppbv.

Early demonstrations of the dual frequency comb spectroscopy technique identify a quality factor and use it to assess the system performance [11, 458]. This factor is found from multiplying the number of resolved elements and the SNR after normalization by acquisition time-square root. We found the quality factor of our experimental setup, with an acquisition time of $80 \ ms$, SNR around 100, and a total number of spectral elements equal to $\frac{250 \ cm^{-1}}{0.07 \ cm^{-1}} = 3600$, to be around $1.3 \times 10^6 \ Hz^{\frac{1}{2}}$ [12, 460]. A more accurate characterization of the current system can be achieved by evacuating the cell and using a mixture of gases.

The Dual frequency comb technique has been applied based on mode-locked $Cr^{2+}:ZnSe$ lasers [282], DFG combs [470], and OPO sources, which are convenient for

broadband coverage [461, 471]. Mid-IR and far-IR applications based on QCL frequency combs are also available today not only with high repetition rates [305, 464] but also on the chip scale [88, 328]. Very recently, a $60\,nm$ bandwidth spectroscopy system based on the dual comb technique was demonstrated with an enhancement factor of $12,000$ [452]. The large enhancement results from a long path length $\sim 930\,m$ and a high finesse in the order of $39,000$ in a $7.5\,cm$ cavity. As technology advances and new materials become available, the progress in research areas and applications of the dual frequency comb spectroscopy technique continues [472-475].

# 5. CONCLUSIONS

Proceeding advances in laser sources, detectors, and experimental techniques have opened new doors for various research topics and applications in different fields. This work mainly focuses on mid-IR spectroscopy and presents an overview of principles, properties, and capabilities of the most recent and commonly used IR sources with a primary focus on optical frequency combs. Many of the topics covered in this work are connected to the IR and THz regions in general. Furthermore, two powerful techniques of IR laser spectroscopy are demonstrated based on near and mid-IR fiber frequency combs.

Infrared spectroscopy based on frequency combs is ideal for broadband absorption spectroscopy applications, as they allow for simultaneous detection of different molecules with high accuracy. The importance of the mid-IR region of the spectrum relies on the abundance of molecular fingerprint lines with sharp absorption features. Nonlinear processes, such as difference frequency generation and optical parametric oscillations, allow for pushing the emission range of different IR sources towards longer mid-IR wavelengths. This advantage facilitates the detection of gaseous molecules in regions that were inaccessible before. Combining this advantage with the unique characteristics of stabilized optical frequency combs makes it possible to obtain absorption measurements with ultra-high sensitivity in extremely short recording times.

A cavity ringdown spectroscopy technique is implemented based on a near IR frequency comb source centered at $1.6 \, \mu m$. In this system, we used low-dispersion HR mirrors for the ringdown cavity, which profoundly reduced the intra-cavity reflection

245

losses. The cavity finesse is 31000, which provides an effective length of 12 $Km$. The length of the cavity is chosen such that the free spectral range matches the repetition rate of the frequency comb. The cavity used in this experiment is 60 $cm$ long, yielding an FSR of 250 $MHz$.

To couple the modes of the frequency comb laser to the resonant modes of the high finesse cavity and achieve stable transmission, both the repetition rate $f_r$ and the carrier-envelop offset frequency $f_o$ were adjusted and stabilized. The fundamental mode builds up inside the high finesse cavity until a certain intensity level is reached. After switching off the incident light by an AOM, the intensity of pulses transmitted through the output mirror decays exponentially due to intra-cavity absorption, scattering, and reflection.

In this technique, molecular absorption can be retrieved from the decay rate, making this technique free of intensity fluctuation noise. Measuring ringdown times at different wavelengths can be achieved either by scanning the grating or fixing the grating and adjusting the position of the detector. In our ringdown experiment, we used a 30 $cm$ home-built spectrometer with a fixed diffraction grating and an indium-gallium-arsenide avalanche photodetector on a moving translational stage.

The performance of ringdown spectroscopic systems based on frequency combs can be improved through several avenues. Using a gas calibration design instead of a direct concentration measurement in the air is a positive step towards designing high-reliability systems for many applications. Parallel acquisition using CCD cameras, for example, allows for higher sensitivities and broadband spectral recording. On the other hand, it is limited by the availability of CCD cameras in different IR regions. Virtually imaged

phased array (VIPA) spectrometers can also be used for parallel detection [48], but it requires focal plane array detectors with fast recording speeds to read out the ringdown signals in parallel [445]. Furthermore, careful cavity designs are required for field-deployable spectroscopy applications to improve the stability of the ringdown system. Highly stable CRDS systems with very high cavity finesse can also be used to study molecular electrodynamics [372].

The Mid-IR dual frequency comb spectroscopy technique utilizes the high coherence and the broad spectral coverage of frequency combs. This technique also provides high-accuracy measurements with a single photodetector in extremely short acquisition times, making it very convenient to be used as a measurement tool in numerous applications. In this work, we apply the dual frequency comb technique in our laboratory and demonstrate sensitive detection of methane in the surrounding air between 3.1 $\mu m$ and 3.4 $\mu m$ based on two Mid-IR frequency combs and a multipass cell.

A multipass cell is typically a cell with high-reflectivity mirrors on both sides and a hole or two holes for beam entrance and exit. Processing a software algorithm for modeling the beam path inside the cell can provide a large number of passes, which is desired in absorption spectroscopy applications. In our experiment, the enhancement of light-matter interaction is achieved by implementing a $100\ cm$ multipass cell and following a spot pattern generated by a software algorithm. A total path length of $580\ m$ is achieved, which provided a high SNR for our measurement.

The spectra and interferometric autocorrelations of the two mid-IR frequency combs used in the dual frequency comb experiment are measured. The spectra of the two

combs cover between $2900 - 3150 \, cm^{-1}$ of the mid-IR region with $0.07 \, cm^{-1}$ resolution, which is equivalent to $2.1 \, GHz$. The two frequency combs are centered on $3.25 \, \mu m$. The autocorrelation traces characterize the temporal features of emitted short pulses and reveal $80 \, fs$ pulse duration.

Methane ($CH_4$) and carbon dioxide ($CO_2$) are considered the top two trace gas molecules that contribute to the greenhouse effect. As a result, numerous studies have been conducted in various fields over the years to identify their sources, study their isotopes, and monitor their concentrations. In this experiment, we measure the concentration of $CH_4$ molecules in the air towards trace gas monitoring applications and air quality assessment.

Measuring the concentration of methane in the surrounding air demonstrates the capability of our dual comb experimental setup. The concentration of methane returned by fitting the experimental results to the calculated spectra from the HITRAN database is 1.5 ppmv, and 1300 ppmv is the concentration of water vapor molecules. A minimum detectable methane concentration of 60 ppbv was obtained based on an interaction length of $580 \, m$.

Our experimental results agree with the calculated ones despite some challenges that we faced because our experiment investigates molecular concentrations in the surrounding air directly. Some of those challenges are spectral overlapping and scattering from particles in the air. The sensitivity of measurement based on our results is $7.6 \times 10^{-7} \, cm^{-1}$.

The performance level of our mid-IR dual frequency comb system is estimated to be around $1.3 \times 10^6 \ Hz^{\frac{1}{2}}$ with an acquisition time of $80 \ ms$. A single spectrum can be obtained with this technique in $\frac{1}{\Delta f_r} \sim 0.67 \ ms$. No moving parts or tuning are required in this technique, which is a primary advantage over conventional FT-IR spectroscopy methods.

Applications of broadband absorption spectroscopy to trace gas analysis are found in different and diverse areas such as detection of molecular biomarkers for breath analysis [8, 15, 31, 32, 447], detection of impurities or trace molecules in industrial processes [37, 38, 475], monitoring of greenhouse gases in the atmosphere [4, 18, 24, 28, 236, 473], searching for natural gas and oil reservoirs [453], and many other fields [66]. In addition to broadband spectroscopy, IR spectroscopy has applications in determining the structure of chemical substances [329, 388], studying the outer space [41, 399, 448], understanding molecular electrodynamics [372], imaging of biological systems [78, 84, 86, 102, 417, 476], determining fundamental constants [446], and controlling food quality [477].

Applications of optical frequency combs are found in various areas. Some of the leading applications and techniques of frequency combs are shown in Figure 107. The application areas include, but not limited to, metrology [43, 289, 478], radio-frequency signal processing [479, 480], optical ranging [314], astronomy and exoplanet research [41, 42, 481], industry [370, 439, 482], trace gas sensing [2, 3, 10, 12, 40, 48, 288, 315, 326, 452, 461, 482], biology [483, 484], quantum information processing [485], high-precision transmission [486], and scientific research [286, 312, 322, 324, 370, 487].
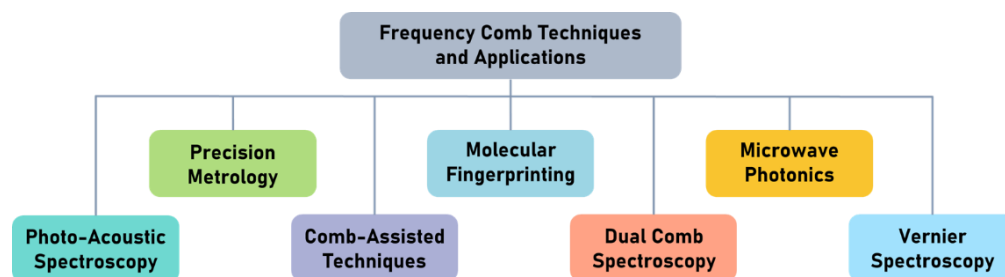
Figure 107 Examples of different applications of frequency combs and leading techniques of frequency comb spectroscopy.

Advances in mid-IR frequency combs and their capabilities continue to expand, promising improved sources with broader bandwidths, higher repetition rates, and a further extension to longer IR wavelengths [295, 315, 451, 488]. These advances can permit measuring absorption spectra of larger numbers of molecules and over new spectral regions [27, 282, 296, 488, 489]. In the last couple of years, several research groups have reported parallel molecular sensing and isotope ratio analysis in the mid-IR region based on optical frequency combs [330, 452, 490, 491], which indicates that the field of frequency comb spectroscopy is progressing rapidly. Accordingly, higher levels of accuracy, stability, compatibility, control, and SNR are expected to follow.

To summarize, a perspective on experimental instrumentation and IR absorption spectroscopy techniques are provided in this work. Major types of IR sources are discussed, including sum- and difference-frequency generation, optical parametric sources, semiconductor and quantum cascade lasers, synchrotron sources, and fiber lasers. In particular, a detailed discussion of IR frequency combs and generation techniques is given, and applications of frequency comb spectroscopy to trace gas detection in the IR

are demonstrated. Enhancement cavities and optical cells are used to increase light-matter interaction length and improve the sensitivity of absorption measurements. The concepts of other useful elements for spectroscopic experiments are explained briefly, and several illustrations and examples of different systems are also discussed. Moreover, descriptions of the performance of some commonly-used detectors and materials are included. Overall, this material is prepared to form a basis for a graduate course on IR absorption spectroscopy. The course is intended for teaching graduate and senior undergraduate students at Kuwait University.

REFERENCES

[1] J. Hansen, R. Ruedy, M. Sato, and K. Lo, "Global surface temperature change," Rev. Geophys. 48, RG4004 (2010).

[2] A. Foltynowicz, P. Masłowski, A. J. Fliesher, B. J. Bjork, and J. Ye, "Cavity-enhanced optical frequency comb spectroscopy in the mid-infrared application to trace detection of hydrogen peroxide," Appl. Phys. B 110, 163–175 (2013).

[3] L. Nugent-Glandorf, F. R. Giorgetta, and S. A. Diddams, "Open-air, broad-bandwidth trace gas sensing with a mid-infrared optical frequency comb," Appl. Phys. B 119, 327–338 (2015).

[4] C. Schütze , S. Lau, N. Reiche, U. Sauer, H. Borsdorf, and P. Dietrich, "Ground-based remote sensing with open-path fourier-transform infrared (OP-FTIR) spectroscopy for large scale monitoring of greenhouse gases," Energy Procedia 37, 4276–4282 (2013).

[5] O. J. Kennedy, B. Ouyang, J. M. Langridge, M. J. S. Daniels, S. Bauguitte, R. Freshwater, M. W. McLeod, C. Ironmonger, J. Sendall, O. Norris, R. Nightingale, S. M. Ball, and R. L. Jones, "An aircraft based three channel broadband cavity enhanced absorption spectrometer for simultaneous measurements of $NO_3$, $N_2O_5$ and $NO_2$," Atmos. Meas. Tech. 4, 1759–1776 (2011).

[6] V. Kapishon, G. K Koyanagi, V. Blagojevic, and D. K Bohme, "Atmospheric pressure chemical ionization mass spectrometry of pyridine and isoprene: Potential breath exposure and disease biomarkers," J. Breath Res. 7, 026005 (2013).

[7] N. M. Pak, O. Rempillo, A. -L. Norman, and D. B. Layzell, "Early atmospheric detection of carbon dioxide from carbon capture and storage sites," J. Air Waste Manag. Assoc. 66(8), 739–747 (2016).

[8] M. Thorpe, D. Balslev-Clausen, M. Kirchner, and J. Ye, "Cavity-enhanced optical frequency comb spectroscopy: application to human breath analysis," Opt. Exp. 16(4), 2387–2397 (2008).

[9] M. Thorpe, K. Moll, R. Jones, B. Safdi, and J. Ye, "Broadband cavity ringdown spectroscopy for sensitive and rapid molecular detection," Science 311, 1595–1599 (2006).

[10] M. Thorpe and J. Ye, "Cavity-enhanced direct frequency comb spectroscopy," Appl. Phys. B 91, 397–414 (2008).

[11] N. R. Newbury, I. Coddington, and W. Swann, "Sensitivity of coherent dual-comb spectroscopy," Opt. Express 18, 7929–7945 (2010).

[12] F. Zhu, A. Bicer, R. Askar, J. Bounds, A. A. Kolomenskii, V. Kelessides, M. Amani and H. A. Schuessler, "Mid-infrared dual frequency comb spectroscopy based on fiber lasers for the detection of methane in ambient air," Laser Phys. Lett. 12, 095701 (2015).

[13] F. Zhu, T. Mohamed, J. Strohaber, A. A. Kolomenskii, Th. Udem, and H. A. Schuessler, "Real-time dual frequency comb spectroscopy in the near infrared," Appl. Phys. Lett. 102, 121116 (2013).

[14] L. E. McHale, A. Hecobian, and A. P. Yalin, "Open-path cavity ring-down spectroscopy for trace gas measurements in ambient air," Opt. Express 24, 5523–5535 (2016).

[15] A. Bicer, J. Bounds, F. Zhu, A. A. Kolomenskii, N. Kaya, E. Aluauee, M. Amani, and H. A. Schuessler, "Sensitive spectroscopic analysis of biomarkers in exhaled breath," Int. J. Thermophys. 39(6), 69 (2018).

[16] K. H. Michaelian, *Photoacoustic IR Spectroscopy* (WILEY-VCH Verlag GmbH & Co., 2010).

[17] I. Sadiek, T. Mikkonen, M. Vainio, J. Toivonen, and A. Foltynowicz, "Optical frequency comb photoacoustic spectroscopy," in CLEO, OSA Technical Digest (online) (Optical Society of America, 2019), paper SW3L.5.

[18] X. Cui, C. Lengignon, T. Wu, W. Zhao, G. Wysocki, E. Fertein, C. Coeur, A. Cassez, L. Croize, W. Chen, Y. Wang, W. Zhang, X. Gao, W. Liu, Y. Zhang, and F. Dong,

"Photonic sensing of the atmosphere by absorption spectroscopy," J. Quant. Spectrosc. Radiat. Transf. 113, 1300–1316 (2012).

[19] T. Mohamed, F. Zhu, S. Chen, J. Strohaber, A. A. Kolomenskii, A. A. Bengali, and H. A. Schuessler, "Multipass cell based on confocal mirrors for sensitive broadband laser spectroscopy in the near infrared," Appl. Opt. 52, 7145–7151 (2013).

[20] W. W. Kellogg and R. Schware, *Climate change and society: consequences of increasing atmospheric carbon dioxide* (Taylor & Francis, 2018).

[21] J. O. Kaplan and M. New, "Arctic climate change with a 2 ℃ global warming: Timing, climate patterns and vegetation change," Clim. Change 79, 213–241 (2006).

[22] P. Werle, R. Miicke, and F. Slemr, "The limits of signal averaging in atmospheric trace-gas monitoring by tunable diode-laser absorption spectroscopy (TDLAS)," Appl. Phys. B 57, 131–139 (1993).

[23] R. M. Varma, D. S. Venables, A. A. Ruth, U. Heitmann, E. Schlosser, and S. Dixneuf, "Long optical cavities for open-path monitoring of atmospheric trace gases and aerosol extinction," Appl. Opt. 48, B159–B171 (2009).

[24] M. N. Fiddler, I. Begashaw, M. A. Mickens, M. S. Collingwood, Z. Assefa, and S. Bililign, "Laser spectroscopy for atmospheric and environmental sensing," Sensors 9, 10447–10512 (2009).

[25] J. Xia, F. Zhu, S. Zhang, A. Kolomenskii, and H. Schuessler, "A ppb level sensitive sensor for atmospheric methane detection," Inf. Phys. Tech. 86, 194–201 (2017).

[26] J. Xia, F. Zhu, S. Zhang, A. Kolomenskii, J. Dong, K. Okada, J. Strohaber, and H. A. Schuessler, "Probing greenhouse gases in turbulent atmosphere by long-range open-path wavelength modulation spectroscopy," Opt. Laser Eng. 117, 21–28 (2019).

[27] K. C. Cossel, E. M. Waxman, I. A. Finneran, G. A. Blake, J. Ye, and N. R. Newbury, "Gas-phase broadband spectroscopy using active sources: progress, status, and applications," J. Opt. Soc. Am. B 34, 104–129 (2017).

[28] Z. Du, S. Zhang, J. Li, N. Gao, and K. Tong, "Mid-infrared tunable laser-based broadband fingerprint absorption spectroscopy for trace gas sensing: a review," Appl. Sci. 9(2), 338 (2019).


[29] A. P. Siegel, A. Daneshkhah, D. S. Hardin, S. Shrestha, K. Varahramyan, and M. Agarwal, "Analyzing breath samples of hypoglycemic events in type 1 diabetes patients: Towards developing an alternative to diabetes alert dogs," J. Breath Res. 11, 026007 (2017).


[30] W. J. Wood, D. J. Mangino, T. D. Wood, R. J. Karalus, M. Gooldy, S. Glogowski, R. Fitzpatrick, and D. J. Higbee, "Analysis of volatile bacterial metabolites by gas chromatography-mass spectrometry," Spectroscopy 21, 20–25 (2006).


[31] C. Wang and P. Sahay, "Breath analysis using laser spectroscopic techniques: Breath biomarkers, spectral fingerprints, and detection limits," Sensors 9(10), 8230–8262 (2009).


[32] M. R. McCurdy, Y. Bakhirkin, G. Wysocki, R. Lewicki, and F. K. Tittel, "Recent advances of laser spectroscopy techniques for applications in breath analysis," J. Breath Res. 1(1), 014001 (2007).


[33] J. C. Anderson, W. J. E. Lamm, and M. P. Hlastala, " Measuring airway exchange of endogenous acetone using a single-exhalation breathing maneuver," J. Appl. Physiol. 100, 880–889 (2006).


[34] M. P. Engelen, R. Jonker, E. A. Veley, R. Harrykissoon, J. J. Thaden, and N. E. Deutz, "Exhaled concentration of nitric oxide (Feno) does not reflect the Upregulated whole body nitric oxide synthesis in patients with chronic obstructive pulmonary disease," Clin. Nutr. 34, S232 (2015).


[35] M. Fang, J. Ivanisevic, H. P. Benton, C. H. Johnson, G. J. Patti, L. T. Hoang, W. Uritboonthai, M. E. Kurczy, and G. Siuzdak, "Thermal degradation of small molecules: A global metabolomic investigation," Anal. Chem. 87, 10935–10941 (2015).


[36] I. Gordon, L. Rothman, C. Hill, R. Kochanov, Y. Tan, P. Bernath, M. Birk, V. Boudon, A. Campargue, K. Chance, B. Drouin, J.-M. Flaud, R. Gamache, J. Hodges, D. Jacquemart, V. Perevalov, A. Perrin, K. Shine, M. -A. Smith, J. Tennyson, G. Toon, H.

Tran, V. Tyuterev, A. Barbe, A. Császár, V. Devi, T. Furtenbacher, J. Harrison, J. -M. Hartman, A. Jolly, T. Johnson, T. Karman, I. Kleiner, A. Kyuberis, J. Loos, O. Lyulin, S. Massie, S. Mikhailenko, N. Moazzen-Ahmadi, H. Müller, O. Naumenko, A. Nikitin, O. Polyansky, M. Rey, M. Rotger, S. Sharpe, K. Sung, E. Starikova, S. Tashkun, J. Vander Auwera, G. Wagner, J. Wilzewski, P. Wcisło, S. Yu, and E. Zak, "The HITRAN2016 molecular spectroscopic database," J. Quant. Spectrosc. Radiat. Transf. 203, 3–69 (2017).

[37] I. Linnerud, P. Kaspersen, and T. Jæger, "Gas monitoring in the process industry using diode laser spectroscopy," Appl. Phys. B 67, 297–305 (1998).

[38] N. Lang, U. Macherius , S. Glitsch, H. Zimmermann, J. Röpcke, and J. H. van Helden, "*In situ* monitoring capabilities of quantum cascade laser absorption spectroscopy in industrial plasma processes," Contrib. Plasma Phys. 55(10), 758–773  (2015).

[39] S. Svanberg, "Laser-spectroscopic applications," in *Atomic and Molecular Spectroscopy* (Springer, 2004), Chap. 10.

[40] R. Grilli, G. Méjean, S. Kassi, I. Ventrillard, C. Abd-Alrahman, and D. Romanini, "Frequency comb based spectrometer for *in situ* and real time measurements of IO, BrO, $NO_2$, and $H_2CO$ at pptv and ppqv levels," Environ. Sci. Technol. 46, 10704−10710 (2012).

[41] E. Obrzud, M. Rainer, A. Harutyunyan, B. Chazelas, M. Cecconi, A. Ghedina, E. Molinari, S. Kundermann, S. Lecomte, F. Pepe, F. Wildi, F. Bouchy, and T. Herr, "Broadband near-infrared astronomical spectrometer calibration and on-sky validation with an electro-optic laser frequency comb," Opt. Express 26(26), 34830−34841 (2018).

[42] M. -G. Suh, X. Yi, Y. -H. Lai, S. Leifer, I. S. Grudinin, G. Vasisht, E. C. Martin, M. P. Fitzgerald, G. Doppmann, J. Wang, D. Mawet, S. B. Papp, S. A. Diddams, C. Beichman, and K. Vahala, "Searching for exoplanets using a microresonator astrocomb," Nat. Photonics 13, 25–30 (2019).

[43] Th. Udem, R. Holzwarth, and T. W. Hänsch, "Optical frequency metrology," Nature 416, 233–237 (2002).

[44] A. Schliesser, N. Picqué, and T. W. Hänsch, "Mid-infrared frequency combs," Nat. Photonics 6, 440–449 (2012).

[45] F. K. Tittel, D. Richter, and A. Fried, "Mid-infrared laser applications in spectroscopy," in *Solid State Mid-Infrared Laser Sources*, I. T. Sorokina and K. L. Vodopanov, eds., in Topics in Applied Physics 89, C. E. Ascheron, H. J. Koelsch, and W. Skolaut, eds. (Springer-Verlag, 2003), pp. 445–511.

[46] L. Maidment, P. G. Schunemann, and D. Reid, "Molecular fingerprint-region spectroscopy from 5 to 12 μm using an orientation-patterned gallium phosphide optical parametric oscillator," Opt. Lett. 41(18), 4261–4264 (2016).

[47] G. Ycas, F. R. Giorgetta, K. C. Cossel, E. M. Waxman, E. Baumann, N. R. Newbury, and I. Coddington, "Mid-infrared dual-comb spectroscopy of volatile organic compounds across long open-air paths," Optica 6(2), 165–168 (2019).

[48] S. A. Diddams, L. Hollberg, and V. Mbele, "Molecular fingerprinting with the resolved modes of a femtosecond laser frequency comb," Nature 445, 627–630 (2007).

[49] W. Herschel, "Experiments on the refrangibility of the invisible rays of the sun," Philos. Trans. MDCCC, 284 (1800).

[50] W. Herschel, *The Scientific Papers of Sir William Herschel*, J. L. E. Dreyer, ed. (Cambridge University Press, 2013).

[51] A. Rogalski, *Infrared Detectors* (CRC Press, 2011).

[52] A. Rogalski, "History of infrared detectors," Opto-Electron. Rev. 20(3), 279–308 (2012).

[53] A. Rogalski, "Infrared detectors: an overview," Infrared Phys. Technol. 43, 187–210 (2002).

[54] C. R. Petersen, U. Møller, I. Kubat, B. Zhou, S. Dupont, J. Ramsay, T. Benson, S. Sujecki, N. Abdel-Moneim, Z. Tang, D. Furniss, A. Seddon, and O. Bang, "Mid-infrared supercontinuum covering the 1.4–13.3 μm molecular fingerprint region using ultra-high NA chalcogenide step-index fibre," Nat. Photonics 8, 830–834 (2014).

[55] C. Tan and H. Mohseni, "Emerging technologies for high performance infrared detectors,"Nanophotonics 7(1), 169–197 (2018).

[56] W. S. Baird, H. M. O'Bryan, G. Ogden, and D. Lee, "An automatic recording infrared spectrophotometer," J. Opt. Soc. Am. 37, 754–761 (1947).

[57] P. Giacomo, "The Michelson Interferometer," Mikrochim. Acta 93, 19–31 (1987).

[58] A. O'Keefe and D. A. G. Deacon, "Cavity ring-down optical spectrometer for absorption measurements using pulsed laser sources," Rev. Sci. Instrum. 59(12), 2544–2551 (1988).

[59] M. A. Belkin and F. Capasso, "New frontiers in quantum cascade lasers: high performance room temperature terahertz sources," Phys. Scr. 90, 118002 (2015).

[60] M. Ebrahimzadeh, "Mid-IR ultrafast and continuous-wave optical parametric oscillators," in *Solid State Mid-Infrared Laser Sources*, I. T. Sorokina and K. L. Vodopanov, eds., in Topics in Applied Physics 89, C. E. Ascheron, H. J. Koelsch, and W. Skolaut, eds. (Springer-Verlag, 2003), pp. 179–218.

[61] ] K. Vodopyanov, "Pulsed Mid-IR Optical Parametric Oscillators," in *Solid State Mid-Infrared Laser Sources*, I. T. Sorokina and K. L. Vodopanov, eds., in Topics in Applied Physics 89, C. E. Ascheron, H. J. Koelsch, and W. Skolaut, eds. (Springer-Verlag, 2003), pp. 141–178.

[62] V. Petrov, "Frequency down-conversion of solid-state laser sources to the mid-infrared spectral range using non-oxide nonlinear crystals," Prog. Quantum Electron. 42, 1–106 (2015).

[63] S. C. Kumar, P. G. Schunemann, K. T. Zawilski, and M. Ebrahim-Zadeh, "Advances in ultrafast optical parametric sources for the mid-infrared based on $CdSiP_2$," J. Opt. Soc. Am. B 33(11), D44–D56 (2016).

[64] M. Pollnau and S. D. Jackson, "Mid-infrared fiber lasers," in *Solid State Mid-Infrared Laser Sources*, I. T. Sorokina and K. L. Vodopanov, eds., in Topics in Applied Physics

89, C. E. Ascheron, H. J. Koelsch, and W. Skolaut, eds. (Springer-Verlag, 2003), pp. 141–178.

[65] W. Demtröder, *Molecular Physics* (WILEY-VCH Verlag GmbH & Co., 2005).

[66] H. Günzler and H. -U. Gremlich, *IR Spectroscopy: An Introduction* (WILEY-VCH Verlag GmbH, 2002).

[67] P. Bouguer, "Optics essay on the attenuation of light," ("Essai d'optique sur la gradation de la lumière " in French), Claude Jombert, Paris, France 16–22 (1729).

[68] J. H. Lambert, *Photometry, or, On the measure and gradations of light, colors, and shade*, ("Photometria sive de mensura et gradibus luminis, colorum et umbrae" in German), Eberhardt Klett. Augsburg, Germany (1760).

[69] A. Beer, "Determination of the absorption of red light in colored liquids," ("Bestimmung der Absorption des rothen Lichts in farbigen Flüssigkeiten" in German), Annalen der Physik und Chemie. 86, 78–88 (1852).

[70] T. G. Mayerhçfer, H. Mutschke, and J. Popp, "Employing theories far beyond their limits— The case of the (Boguer-) Beer–Lambert law," ChemPhysChem. 17, 1948–1955 (2016).

[71] W. Fred McClure, "204 years of near infrared technology: 1800–2003," J. Near Infrared Spectrosc. 11, 487–518 (2003).

[72] E. Scott Barr, "Historical survey of the early development of the infrared spectral region," Am. J. Phys. 28, 42–54 (1960).

[73] W. D. Lawson, S. Nielsen, E. H. Putley, and A. S. Young, "Preparation and properties of HgTe and mixed crystals of HgTe-CdTe," J. Phys. Chem. Solids 9, 325–329 (1959).

[74] R. A. Soref, "Extrinsic IR Photoconductivity of Si Doped with B, Al, Ga, P, As, or Sb," J. Appl. Phys. 38, 5201–5209 (1967).

[75] W. S. Boyle, G. E. Smith, "Charge coupled semiconductor devices," The Bell Sys. Tech. J. 49, 587–593 (1970).

[76] A. Nucara, S. Lupi, and P. Calvani, "The infrared synchrotron radiation beamline at the third generation light source ELETTRA," Rev. Sci. Instrum. 74(9), 3934–3942 (2003).

[77] K. -D. Liss and K. Chen, "Frontiers of synchrotron research in materials science," MRS Bulletin, 41(6), 435–441 (2016).

[78] L. M. Miller and P. Dumas, "Infrared spectroscopy using synchrotron radiation," in *Encyclopedia of Biophysics*, G. C. K Roberts, ed. (Springer, 2013), pp. 1106–1112.

[79] G. P. Williams, "Infrared synchrotron radiation instrumentation and applications," Rev. Sci. Instrum. 63(1), 1535–1538 (1992).

[80] M. Watanabe, S. Sato, I. Munro, and G. S. Lodha, *A Guide to Synchrotron Radiation* (Narosa Publishing House, 2016).

[81] A. Piednoir, F. Creuzet, C. Licoppe, and J. M. Ortkga, "Locally resolved infrared spectroscopy," Ultramicroscopy 57, 282–286 (1995).

[82] L. M. Miller and R. J. Smith, "Synchrotrons versus globars, point-detectors versus focal plane arrays: Selecting the best source and detector for specific infrared microspectroscopy and imaging applications," Vib. Spectrosc. 38, 237–240 (2005).

[83] G. L. Carr, M. Hanfland, and G. P. Williams, "Performance of an infrared microspectrometer at the NSLS," Rev. Sci. Instrum. 66(2), 1643–1645 (1995).

[84] L. M. Miller and P. Dumas, "Chemical imaging of biological tissue with synchrotron infrared light," Biochim. Biophys. Acta Biomembr. 1758(7), 846–857 (2006).

[85] L. Vaccari, G. Birarda, G. Grenci, S. Pacor, and L. Businaro, "Synchrotron radiation infrared microspectroscopy of single living cells in microfluidic devices: advantages, disadvantages and future perspectives," J. Phys. Conf. Ser. 359, 012007 (2012).

[86] A. Marcelli, A. Cricenti, W. M. Kwiatek, and C. Petibois, "Biological applications of synchrotron radiation infrared spectromicroscopy," Biotech. Adv. 30(6), 1390–1404 (2012).

[87] J. Faist, F. Capasso, D. L. Sivco, C. Sirtori, A. L. Hutchinson, and A. Y. Cho, "Quantum cascade laser," Science 264, 553–556 (1994).

[88] L. Bush, "Quantum cascade lasers for infrared spectroscopy: theory, state of the art, and applications," Spectroscopy 28(4), 1–6 (2013).

[89] C. Gmachl, F. Capasso, D. L. Sivco, and A. Y. Cho, "Recent progress in quantum cascade lasers and applications," Rep. Prog. Phys. 64(11), 1533–1601 (2001).

[90] Y. Wang, M. G. Soskind, W. Wang, and G. Wysocki, "High-resolution multi-heterodyne spectroscopy based on Fabry-Perot quantum cascade lasers," Appl. Phys. Lett. 104, 031114 (2014).

[91] J. Westberg, L. A. Sterczewski, and G. Wysocki, "Mid-infrared multiheterodyne spectroscopy with phase-locked quantum cascade lasers," Appl. Phys. Lett. 110, 141108 (2017).

[92] J. Faist, C. Gmachl, F. Capasso, C. Sirtori, D. L. Sivco, J. N. Baillargeon, and A. Y. Cho, "Distributed feedback quantum cascade lasers," Appl. Phys. Lett. 70, 2670–2672 (1997).

[93] R. F. Curl, F. Capasso, C. Gmachl, A. A. Kosterev, B. McManus, R. Lewicki, M. Pusharsky, G. Wysockic, and F. K. Tittel, "Quantum cascade lasers in chemical physics," Chem. Phys. Lett. 487, 1–18 (2010).

[94] J. S. Yu, S. Slivken, S. R. Darvish, A. Evans, B. Gokden, and M. Razeghi, "High-power, room-temperature, and continuous-wave operation of distributed-feedback quantum-cascade lasers at $\lambda \sim 4.8$ μm," Appl. Phys. Lett. 87, 041104 (2005).

[95] Q. Y. Lu, Y. Bai, N. Bandyopadhyay, S. Slivken, and M. Razeghi, "2.4 W room temperature continuous wave operation of distributed feedback quantum cascade lasers," Appl. Phys. Lett. 98, 181106 (2011).

[96] B. G. Lee, M. A. Belkin, R. Audet, J. MacArthur, L. Diehl, C. Pflügl, and F. Capasso, "Widely tunable single-mode quantum cascade laser source for mid-infrared spectroscopy," Appl. Phys. Lett. 91, 231101 (2007).

[97] A. Hugi, R. Terazzi, Y. Bonetti, A. Wittmann, M. Fischer, M. Beck, J. Faist, and E. Gini, "External cavity quantum cascade laser tunable from 7.6 to 11.4 µm," Appl. Phys. Lett. 95, 061103 (2009).

[98] Y. Yao, A. J. Hoffman, and C. F. Gmachl, "Mid-infrared quantum cascade lasers," Nat. Photonics 6, 432–439 (2012).

[99] J. R. Meyer, I. Vurgaftman, R. Q. Yang, and L. R. Ram-Mohan, "Type-II and type-I interband cascade lasers," Electron. Lett. 32(1), 45–46 (1996).

[100] I. Vurgaftman, W. W. Bewley, C. L. Canedy, C. S. Kim, M. Kim, J. R. Lindle, C. D. Merritt, J. Abell, and J. R. Meyer, "Mid-IR type-II interband cascade lasers," IEEE J. Sel. Top. Quantum Electron. 17(5), 1435–1444 (2011).

[101] C. L. Canedy, J. Abell, C. D. Merritt, W. W. Bewley, C. S. Kim, M. Kim, I. Vurgaftman, and J. R. Meyer, "Pulsed and CW performance of 7-stage interband cascade lasers," Opt. Express 22(7), 7702–7710 (2014).

[102] A. Schwaighofer, M. Brandstetter, and B. Lendl, "Quantum cascade lasers (QCLs) in biomedical spectroscopy," Chem. Soc. Rev. 46, 5903–5924 (2017).

[103] R. Köhler, A. Tredicucci, F. Beltram, H. E. Beere, E. H. Linfield, A. G. Davies, D. A. Ritchie, R. C. Iotti, and F. Rossi, "Terahertz semiconductor-heterostructure laser," Nature 417, 156–159 (2002).

[104] L. Hozdara, N. Pennington, M. Kraft, M. Karlowatz, and B. Mizaikoff, "Quantum cascade lasers for mid-infrared spectroscopy," Vib. Spectrosc. 30(1), 53–58 (2002).

[105] A. Kosterev, G. Wysocki, Y. Bakhirkin, S. So, R. Lewicki, M. Fraser, F. Tittel, and R. F. Curl, "Application of quantum cascade lasers to trace gas analysis," Appl. Phys. B 90(2), 165–176 (2008).

[106] J. S. Li, W. Chen, and H. Fischer, "Quantum cascade laser spectrometry techniques: A new trend in atmospheric chemistry," Appl. Spectrosc. Rev. 48, 523–559 (2013).

[107] J. Röpcke, P. B. Davies, N. Lang, A. Rousseau, and S. Welzel, "Applications of quantum cascade lasers in plasma diagnostics: a review," J. Phys. D: Appl. Phys. 45(42), 423001 (2012).

[108] A. Schwaighofer, M. R. Alcaráz, C. Araman, H. Goicoechea, and B. Lendl, "External cavity-quantum cascade laser infrared spectroscopy for secondary structure analysis of proteins at low concentrations," Sci. Rep. 6, 33556 (2016).

[109] M. Tonouchi, "Cutting-edge terahertz technology," Nat. Photonics 1, 97–105 (2007).

[110] P. Kotidis, E. Deutsch, H. Ye, A. Mazurenko, A. K. Goyal, and J. S. Socha, "Quantum cascade laser based gas sensing system and method," U. S. Patent 9,983,126 (May 29, 2018).

[111] E. Snitzer, "Optical maser action of Nd$^{+3}$ in a barium crown glass," Phys. Rev. Lett. 7(12), 444–446 (1961).

[112] M. E. Fermann and I. Hartl, "Ultrafast fiber lasers," Nat. Photonics 7, 868–874 (2013).

[113] W. Shi, Q. Fang, X. Zhu, R. A. Norwood, and N. Peyghambaria, "Fiber lasers and their applications," Appl. Opt. 53(28), 6554–6568 (2014).

[114] T. M. Shay and F. J. Duarte, "Tunable fiber lasers," in *Tunable Laser Applications*, F. J. Duarte, ed. (CRC Press, Taylor & Francis Group, 2016), pp. 243–361.

[115] Fiberlabs, "Fiber Laser," (Fiberlabs Inc., 2020). https://www.fiberlabs.com/glossary/fiber-laser/

[116] J. Lucas, "Infrared glasses," Curr. Opin. Solid State Mater. Sci. 4, 181–187 (1999).

[117] M. E. Fermann, "Single-mode excitation of multimode fibers with ultrashort pulses," Opt. Lett. 23(1), 52–54 (1998).

[118] G. Gu, F. Kong, T. W. Hawkins, P. Foy, K. Wei, B. Samson, and L. Dong, "Impact of fiber outer boundaries on leaky mode losses in leakage channel fibers," Opt. Express 21(20), 24039–24048 (2013).

[119] F. Stutzki, F. Jansen, T. Eidam, A. Steinmetz, C. Jauregui, J. Limpert, and A. Tünnermann, "High average power large-pitch fiber amplifier with robust single-mode operation," Opt. Lett. 36(5), 689–691 (2011).

[120] J. Limpert, F. Stutzki, F. Jansen, H. -J. Otto, T. Eidam, C. Jauregui, and A. Tünnermann, "Yb-doped large-pitch fibres: effective single-mode operation based on higher-order mode delocalization," Light-Sci. Appl. 1, e8 (2012).

[121] T. T. Alkeskjold, M. Laurila, L. Scolari, and J. Broeng, "Single-mode ytterbium-doped large-mode-area photonic bandgap rod fiber amplifier," Opt. Express 19(8), 7398–7409 (2011).

[122] E. Coscelli, F. Poli, T. T. Alkeskjold, M. M. Jørgensen, L. Leick, J. Broeng, A. Cucinotta, and S. Selleri, "Thermal effects on the single-mode regime of distributed modal filtering rod fiber," J. Lightwave Technol. 30(22), 3494–3499 (2012).

[123] D. Yelin, B. E. Bouma, S. H. Yun, and G. J. Tearney, "Double-clad fiber for endoscopy," Opt. Lett. 29(20), 2408–2410 (2004).

[124] S. Tokita, M. Murakami, S. Shimizu, M. Hashida, and S. Sakabe, "Liquid-cooled 24 W mid-infrared Er:ZBLAN fiber laser," Opt. Lett. 34(20), 3062–3064 (2009).

[125] L. Dong and B. Samson, *Fiber Lasers: Basics, Technology, and Applications* (CRC Press, Taylor & Francis Group, 2017).

[126] Y. Tang and J. Xu, "High-power pulsed 2-µm $Tm^{3+}$-doped fiber laser," in *Semiconductor Laser Diode: Technology and Applications*, D. S. Patil, ed. (InTech, 2012), pp. 287–320.

[127] S. T. Jackson, "Towards high-power mid-infrared emission from a fiber laser," Nat. Photonics 6, 423–31 (2012).

[128] X. Zhu and R. Jain, "Compact 2 W wavelength-tunable Er:ZBLAN mid-infrared fiber laser," Opt. Lett. 32(16), 2381–2383 (2007).

[129] A. T. Gursel, "Fiber lasers and their medical applications," in *Optical Amplifiers: A Few Different Dimensions*, P. K. Choudhury, ed. (InTechOpen, 2018).

[130] M. Hinkelmann, D. Wandt, U. Morgner, J. Neumann, and D. Kracht, "Mode-locked Ho-doped laser with subsequent diode-pumped amplifier in an all-fiber design operating at 2052 nm," Opt. Express 25(17), 20522–20529 (2017).

[131] T. C. Newell, P. Peterson, A. Gavrielides, and M. P. Sharma, "Temperature effects on the emission properties of Yb-doped optical fibers," Opt. Communic. 273(1), 256–259 (2007).

[132] V. Sypin, N. Voronkov, and O. Ryabushkin, "Longitudinal temperature distribution inside active optical fiber in lasing condition," in Advanced Photonics 2018, OSA Technical Digest (online) (Optical Society of America, 2018), paper SeM2J.3.

[133] M. Yan, S. Li, Z. Han, H. Shen, and R. Zhu, "Theoretical and experimental study on the thermally dependent transient response of the high power continuous wave Yb-doped fiber laser," Appl. Opt. 58(20), 5525–5532 (2019).

[134] J. Yang, Y. Wang, Y. Tang, and J. Xu, "Influences of pump transitions on thermal effects of multi-kilowatt thulium-doped fiber lasers," Phys. Opts. arXiv: 1503.07256, 1–9 (2015).

[135] M. Karimi, "Theoretical study of the thermal distribution in Yb-doped double-clad fiber laser by considering different heat sources," Prog. Electromagn. Res. C 88, 59–76 (2018).

[136] H. Kawase and R. Yasuhara, "A watt-level efficient continuous wave Er:YAP laser at 2.92 µm," in Laser Congress 2018 (ASSL), OSA Technical Digest (online) (Optical Society of America, 2018), paper AM6A.31.

[137] M. Gorjan, R. Petkovšek, M. Marinček, and M. Čopič, "High-power pulsed diode-pumped Er:ZBLAN fiber laser," Opt. Lett. 36(10), 1923–1925 (2011).

[138] W. Wang, X. Yang, Y. Shen, L. Li, L. Zhou, Y. Yang, Y. Bai, W. Xie, G. Ye, and X. Yu, "High beam quality of a Q-switched 2-µm Tm,Ho:LuVO$_4$ laser," Appl. Phys. B 124:82, 1–5 (2018).

[139] X. Zhu, G. Zhu, C. Wei, L. Vasilyevich Kotov, J. Wang, M. Tong, R. A. Norwood, and N. Peyghambarian, "Pulsed fluoride fiber lasers at 3 µm," J. Opt. Soc. Am. B 34(3), A15–A28 (2017).

[140] M. C. Falconi, D. Laneve, M. Bozzetti, T. T. Fernandez, G. Galzerano, and F. Prudenzano, "Design of an efficient pulsed Dy$^{3+}$: ZBLAN fiber laser operating in gain switching regime," J. Lightwave Technol. 36(23), 5327–5333 (2018).

[141] S. Crawford, D. D. Hudson, and S. D. Jackson, "High-power broadly tunable 3-µm fiber laser for the measurement of optical fiber loss," IEEE Photonics J. 7, 1–9 (2015).

[142] L. Shen, M. Cai, Y. Lu, N. Wang, F. Huang, S. Xu, and J. Zhang, "Preparation and investigation of Tm$^{3+}$/Ho$^{3+}$ co-doped germanate-tellurite glass as promising materials for ultrashort pulse laser," Opt. Mater. 67, 125–131 (2017).

[143] I. T. Sorokina, V. V. Dvoyrin, N. Tolstik, and E. Sorokin, "Mid-IR ultrashort pulsed fiber-based lasers," IEEE J. Sel. Top. Quantum Electron. 20(5), 0903412 (2014).

[144] H. Luo, J. Yang, J. Li, and Y. Liu, "Widely tunable passively Q-switched $Er^{3+}$-doped $ZrF_4$ fiber laser in the range of 3.4–3.7 µm based on a $Fe^{2+}$:ZnSe crystal," Photon. Res. 7(9), 1106–1111 (2019).

[145] X. Zhang, B. Bureau, P. Lucas, C. Boussard-Pledel, and J. Lucas, "Glasses for seeing beyond visible," Chem. Eur. J. 14(2), 432–442 (2008).

[146] M. C. Falconi, D. Laneve and F. Prudenzano, "Advances in mid-IR fiber lasers: tellurite, fluoride and chalcogenide," Fibers 5, 23 (2017).

[147] J. Dong, Y. Q. Wei, A. Wonfor, R. V. Penty, I. H. White, J. Lousteau, G. Jose, and A. Jha, "Dual-pumped tellurite fiber amplifier and tunable laser using $Er^{3+}$/$Ce^{3+}$ codoping Scheme," IEEE Photonics Technol. Lett. 23(11), 736–738 (2011).

[148] C. Wei, H. Shi, H. Luo, H. Zhang, Y. Lyu, and Y. Liu, "34 nm-wavelength-tunable picosecond $Ho^{3+}$/$Pr^{3+}$-codoped ZBLAN fiber laser," Opt. Express 25(16), 19170–19178 (2017).

[149] Ł. Sójka, Z. Tang, D. Jayasuriya, M. Shen, D. Furniss, E. Barney, T. M. Benson, A. B. Seddon, and S. Sujecki, "Ultra-broadband mid-infrared emission from a $Pr^{3+}$/$Dy^{3+}$ co-doped selenide-chalcogenide glass fiber spectrally shaped by varying the pumping arrangement," Opt. Mater. Express 9(5), 2291–2306 (2019).

[150] M. Robinson and D. P. Devor, "Thermal switching of laser emission of $Er^{3+}$ at 2.69 µ and $Tm^{3+}$ at 1.86 µ in mixed crystals of $CaF_2$:$ErF_3$:$TmF_3$," Appl. Phys. Lett. 10, 167–170 (1967).

[151] M. C. Brierley and P. W. France, "Continuous wave lasing at 2.71 µm in an erbium doped fluorozirconate fibre," Electron. Lett. 24(15), 935-937 (1988).

[152] O. P. Kulkarni, V. V. Alexander, M. Kumar, M. J. Freeman, M. N. Islam, F. L. Terry, Jr., M. Neelakandan, and A. Chan, "Supercontinuum generation from ~1.9 to 4.5 µm in ZBLAN fiber with high average power generation beyond 3.8 µm using a thulium-doped fiber amplifier," J. Opt. Soc. Am. B 28(10), 2486–2498 (2011).

[153] Y. Baravets, F. Todorov, and P. Honzatko, "High-power thulium-doped fiber laser in an all-fiber configuration," Proc. SPIE 10142, 101420G (2016).

[154] Y. Tang, Y. Yang, J. Xu, and Y. Hang, "Passive Q-switching of short-length $Tm^{3+}$-doped silica fiber lasers by polycrystalline $Cr^{2+}$:ZnSe microchips," Opt. Commun. 281(22), 5588–5591 (2008).

[155] J. König, S. Nolte, and A. Tünnermann, "Plasma evolution during metal ablation with ultrashort laser pulses," Opt. Express 13(26), 10597–10607 (2005).

[156] S. Duval, M. Bernier, V. Fortin, J. Genest, M. Piché, and R. Vallée, "Femtosecond fiber lasers reach the mid-infrared," Optica 2(7), 623–626 (2015).

[157] X. Zhu and N. Peyghambarian, "High-power ZBLAN glass fiber lasers: Review and prospect," Adv. Optoelectron. 2010, 501956 (2010).

[158] O. Henderson-Sapir, S. D. Jackson, and D. J. Ottaway, "Versatile and widely tunable mid-infrared erbium doped ZBLAN fiber laser," Opt. Lett. 41(7), 1676–1679 (2016).

[159] P. Zhou, X. Wang, Y. Ma, H. Lü, and Z. Liu, "Review on recent progress on mid-infrared fiber lasers," Laser Phys. 22(11), 1744–1751 (2012).

[160] G. E. Snopatin, V. S. Shiryaev, V. G. Plotnichenko, E. M. Dianov, and M. F. Churbanov, "High-purity chalcogenide glasses for fiber optics," Inorg. Mater. 45(13), 1439–1459 (2009).

[161] Ł. Sójka, Z. Tang, H. Zhu, E. Bereś-Pawlik, D. Furniss, A. B. Seddon, T. M. Benson, and S. Sujecki, "Study of mid-infrared laser action in chalcogenide rare earth doped glass with $Dy^{3+}$, $Pr^{3+}$ and $Tb^{3+}$," Opt. Mater. Express 2(11), 1632–1640 (2012).

[162] J. S. Sanghera, L. B. Shaw, and I. D. Aggarwal, "Chalcogenide glass-fiber-based mid-IR sources and applications," IEEE J. Sel. Top. Quantum Electron. 15(1), 114–119 (2009).

[163] Ł. Sójka, Z. Tang, D. Furniss, H. Sakr, Y. Fang, E. Beres-Pawlik, T. M. Benson, A. B. Seddon, and S. Sujecki, "Mid-infrared emission in $Tb^{3+}$-doped selenide glass fiber," J. Opt. Soc. Am. B 34(3), A70–A79 (2017).

[164] S. Hocdé, C. Boussard-Plédel, G. Fonteneau, and J. Lucas, "Chalcogens based glasses for IR fiber chemical sensors," Solid State Sci. 3, 279–284 (2001).

[165] V. S. Shiryaev, J. -L. Adam, X. H. Zhang, C. Boussard-Plédel, J. Lucas, and M. F. Churbanov, "Infrared fibers based on Te–As–Se glass system with low optical losses," J. Non-Cryst. Solids 336(2), 113–119 (2004).

[166] D. Milanese, J. Lousteau, X. Zhu, A. Chavez-Pirson, D. Pugliese, N. G. Boetti, and N. Peyghambarian, "Nonsilica oxide glass fiber laser sources," in *Advances in Glass Science and Technology*, V. M. Sglavo, ed. (InTechOpen, 2018).

[167] X. Feng, P. Horak, and F. Poletti, "Tellurite glass fibers for mid-infrared nonlinear applications," in *Technological Advances in Tellurite Glasses*, V. Rivera and D. Manzani, eds., in Springer Series in Materials Science 254 (Springer, 2017).

[168] L. X. Li, W. C. Wang, C. F. Zhang, J. Yuan, B. Zhou, and Q. Y. Zhang, "2.0 μm $Nd^{3+}$/$Ho^{3+}$-doped tungsten tellurite fiber laser," Opt. Mater. Express 6(9), 2904–2914 (2016).

[169] H. P. T. Nguyen, K. Nagasaka, T. H. Tuan, T. S. Saini, X. Luo, T. Suzuki, and Y. Ohishi, "Highly coherent supercontinuum in the mid-infrared region with cascaded tellurite and chalcogenide fibers," Appl. Opt. 57(21), 6153–6163 (2018).

[170] B. N. Samson, L. R. Pinckney, J. Wang, G. H. Beall, and N. F. Borrelli, "Nickel-doped nano-crystalline glass-ceramic fiber," in Conference on Lasers and Electro-Optics (IEEE, 2002), paper CMD1.

[171] D. Kracht, M. Frede, R. Wilhelm, and C. Fallnich, "Comparison of crystalline and ceramic composite Nd:YAG for high power diode end-pumping," Opt. Express 13(16), 6212–6216 (2005).

[172] X. Mu, H. Meissner, H. -C. Lee, and M. Dubinskii, "True crystalline fibers: double-clad LMA design concept of Tm:YAG-core fiber and its mode simulation," Proc. SPIE 8237, 82373M (2012).

[173] J. Wang, D. Yin, P. Liu, J. Ma, Y. Wang, and D. Y. Tang, "Rare-earth doped sesquioxide ceramics for highly efficient mid-infrared lasers," in 2019 CLEO/Europe-EQEC (IEEE, 2019).

[174] S. Kang, H. Yu, T. Ouyang, Q. Chen, X. Huang, Z. Chen, J. Qiu, and G. Dong, "Novel $Er^{3+}/Ho^{3+}$-codoped glass-ceramic fibers for broadband tunable mid-infrared fiber lasers," J. Am. Ceram. Soc. 101(9), 3956–3967 (2018).

[175] L. Wang, H. T. Huang, D. Y. Shen, J. Zhang, H. Chen, and D. Y. Tang, "Diode-pumped high power 2.7 μm $Er:Y_2O_3$ ceramic laser at room temperature," Opt. Mater. 71, 70–73 (2017).

[176] L. Wang , H. Huang , X. Ren , J. Wang, D. Shen, Y. Zhao , W. Zhou , P. Liu, and D. Tang, "Nanosecond pulse generation at 2.7 μm from a passively Q-switched $Er:Y_2O_3$ ceramic laser," IEEE J. Sel. Top. Quantum Electron. 24(5), 1600906 (2018).

[177] K. Liu, J. Liu, H. Shi, F. Tan, and P. Wang, "High power mid-infrared supercontinuum generation in a single-mode ZBLAN fiber with up to 21.8 W average output power," Opt. Express 22(20), 24384–24391 (2014).

[178] M. R. Majewski, R. I. Woodward, and S. D. Jackson, "Dysprosium-doped ZBLAN fiber laser tunable from 2.8 μm to 3.4 μm, pumped at 1.7 μm," Opt. Lett. 43(5), 971–974 (2018).

[179] J. -C. Gauthier, V. Fortin, J. -Y. Carrée, S. Poulain, M. Poulain, R. Vallée, and M. Bernier, "Mid-IR supercontinuum from 2.4 to 5.4 μm in a low-loss fluoroindate fiber," Opt. Lett. 41(8), 1756–1759 (2016).

[180] L. Yang, B. Zhang, K. Yin, T. Wu, Y. Zhao, and J. Hou, "Spectrally flat supercontinuum generation in a holmium-doped ZBLAN fiber with record power ratio beyond 3 μm," Photon. Res. 6(5), 417–421 (2018).

[181] F. Maes, V. Fortin, S. Poulain, M. Poulain, J. -Y. Carrée, M. Bernier, and R. Vallée, "Room-temperature fiber laser at 3.92 µm," Optica 5, 761–764 (2018).

[182] J. Ari, F. Starecki, C. Boussard-Plédel, Y. Ledemi, Y. Messaddeq, J. -L. Doualan, A. Braud, B. Bureau, and V. Nazabal, "Co-doped $Dy^{3+}$ and $Pr^{3+}$ $Ga_5Ge_{20}Sb_{10}S_{65}$ fibers for mid-infrared broad emission," Opt. Lett. 43(12), 2893–2896 (2018).

[183] J. -P. Yehouessi, S. Vidal, J. -Y. Carrée, L. Bodin, S. Cozic, T. Berthelot, S. Poulain, L. Calvez, G. Huss, and J. Boullet, "3 W Mid-IR supercontinuum extended up to 4.6 µm based on an all-PM thulium doped fiber gain-switch laser seeding an $InF_3$ fiber", Proc. SPIE 10902, 1090207 (2019).

[184] C. Yao, Z. Jia, Z. Li, S. Jia, Z. Zhao, L. Zhang, Y. Feng, G. Qin, Y. Ohishi, and W. Qin, "High-power mid-infrared supercontinuum laser source using fluorotellurite fiber," Optica 5(10), 1264–1270 (2018).

[185] V. Fortin, F. Jobin, M. Larose, M. Bernier, and R. Vallée, "10-W-level monolithic dysprosium-doped fiber laser at 3.24 µm," Opt. Lett. 44(3), 491–494 (2019).

[186] A. V. Pushkin, E. A. Migal, H. Uehara, K. Goya, S. Tokita, M. P. Frolov, Yu. V. Korostelin, V. I. Kozlovsky, Ya. K. Skasyrsky, and F. V. Potemkin, "Compact, highly efficient, 2.1-W continuous-wave mid-infrared Fe:ZnSe coherent source, pumped by an Er:ZBLAN fiber laser," Opt. Lett. 43(24), 5941–944 (2018).

[187] G. Zhu, L. Geng, X. Zhu, L. Li, Q. Chen, R. A. Norwood, T. Manzur, and N. Peyghambarian, "Towards ten-watt-level 3-5 µm Raman lasers using tellurite fiber," Opt. Express 23(6), 7559–7573 (2015).

[188] V. Fortin, M. Bernier, and R. Vallée, "Mid-infrared Raman fiber lasers," in *Raman Fiber Lasers*, Y. Feng, ed., in Springer Series in Optical Sciences 207, W. T. Rhodes, ed. (Springer International Publishing, 2017), Chap. 3.

[189] V. R. Supradeepa, Y. Feng, and J. W. Nicholson, "Raman fiber lasers," J. Opt. 19, 023001 (2017).

[190] M. Bernier, V. Fortin, M. El-Amraoui, Y. Messaddeq, and R. Vallée, "3.77 µm fiber laser based on cascaded Raman gain in a chalcogenide glass fiber," Opt. Lett. 39(7), 2052–2055 (2014).

[191] X. Peng, P. Zhang, X. Wang, H. Guo, P. Wang, and S. Dai, "Modeling and simulation of a mid-IR 4.3 µm Raman laser in chalcogenide glass fibers," OSA Continuum 2(8), 2281–2292 (2019).

[192] A. V. Gladyshev, A. F. Kosolapov, M. M. Khudyakov, Y. P. Yatsenko, A. N. Kolyadin, A. A. Krylov, A. D. Pryamikov, A. S. Biriukov, M. E. Likhachev, I. A. Bufetov, and E. M. Dianov, "4.4 µm Raman laser based on hydrogen-filled hollow-core silica fiber," in 2017 Conference on Lasers and Electro-Optics, OSA Technical Digest (online) (Optical Society of America, 2017), paper JTh5A.7.

[193] A. V. Gladyshev, A. F. Kosolapov, M. M. Khudyakov, Y. P. Yatsenko, A. N. Kolyadin, A. A. Krylov, A. D. Pryamikov, A. S. Biriukov, M. E. Likhachev, I. A. Bufetov, and E. M. Dianov, "2.9, 3.3, and 3.5 µm Raman lasers based on revolver hollow-core silica fiber filled by $^1$H$_2$/D$_2$ gas mixture," IEEE J. Sel. Top. Quantum Electron. 24, 0903008 (2018).

[194] Y. Li, T. Du, B. Xu, H. Xu, Z. Cai, V. M. Mashinsky, and Z. Luo, "Compact all-fiber 2.1-2.7 µm tunable Raman soliton source based on germania-core fiber," Opt. Express 27(20), 28544–28550 (2019).

[195] L. Cao, S. -F. Gao, Z. -G. Peng, X. -C. Wang, Y. -Y. Wang, and P. Wang, "High peak power 2.8 µm Raman laser in a methane-filled negative-curvature fiber," Opt. Express 26(5), 5609–5615 (2018).

[196] P. Bourdon, L. Lombard, A. Durécu, J. Le Gouët, D. Goular, and C. Planchat, "Coherent combining of fiber lasers," Proc. SPIE 10254, 1025402 (2017).

[197] T. Y. Fan, "Laser beam combining for high power, high radiance sources," IEEE J. Sel. Top. Quantum Electron. 11, 567–577 (2005).

[198] Z. J. Liu, X. X. Jin, R. T. Su, P. Ma, and P. Zhou, "Development status of high power fiber lasers and their coherent beam combination," Sci. China Inf. Sci. 62(4), 041301 (2019).

[199] A. Klenke, M. Müller, H. Stark, F. Stutzki, C. Hupel, T. Schreiber, A. Tünnermann, and J. Limpert, "Coherently combined 16-channel multicore fiber laser system," Opt. Lett. 43, 1519–1522 (2018).

[200] C. Lei, Y. Gu, Z. Chen, Z. Wang, P. Zhou, Y. Ma, H. Xiao, J. Leng, X. Wang, J. Hou, X. Xu, J. Chen, and Z. Liu, "Incoherent beam combining of fiber lasers by an all-fiber $7 \times 1$ signal combiner at a power level of 14 kW," Opt. Express 26(8), 10421–10427 (2018).

[201] H. L. Yu, Z. X. Zhang, X. L. Wang, R. T. Su, H. W. Zhang, Y. X. Ma, P. Zhou, and J. B. Chen, "High average power coherent femtosecond pulse combining system based on an all fiber active control method," Laser Phys. Lett. 15, 075101 (2018).

[202] P. Zhao, Z. Dong, J. Zhang, and X. Lin, "Passive coherent beam combination of three Nd:YAG lasers using cascaded Michelson-type compound cavities," Opt. Express 26(14), 18019–18027 (2018).

[203] C. X. Yu, S. J. Augst, S. M. Redmond, K. C. Goldizen, D. V. Murphy, A. Sanchez, and T. Y. Fan, "Coherent combining of a 4 kW, eight-element fiber amplifier array," Opt. Lett. 36, 2686–2688 (2011).

[204] Z. Liu, P. Ma, R. Su, R. Tao, Y. Ma, X. Wang, and P. Zhou, "High-power coherent beam polarization combination of fiber lasers: progress and prospect," J. Opt. Soc. Am. B 34(3), A7–A14 (2017).

[205] M. Xu, F. Yu, M. R. Abu Hassan, and J. C. Knight, "Continuous-wave mid-infrared gas fiber lasers," IEEE J. Sel. Top. Quantum Electron. 24(3), 0902308 (2018).

[206] A. V. Vasudevan Nampoothiri, A. M. Jones, C. Fourcade-Dutin, C. Mao, N. Dadashzadeh, B. Baumgart, Y. Y. Wang, M. Alharbi, T. Bradley, N. Campbell, F. Benabid, B. R. Washburn, K. L. Corwin, and W. Rudolph, "Hollow-core optical fiber gas lasers (HOFGLAS): a review," Opt. Mater. Express 2(7), 948–961 (2012).

[207] A. V. Gladyshev, M. S. Astapovich, M. M. Khudyakov, A. F. Kosolapov, M. E. Likhachev, and I. A. Bufetov, "All-fiber high-average-power 4.42-μm Raman laser based on silica fiber," in 2019 CLEO/Europe-EQEC (IEEE, 2019), paper cj_3_3.

[208] A. M. Jones, A. V. Vasudevan Nampoothiri, A. Ratanavis, T. Fiedler, N. V. Wheeler, F. Couny, R. Kadel, F. Benabid, B. R. Washburn, K. L. Corwin, and W. Rudolph, "Mid-infrared gas filled photonic crystal fiber laser based on population inversion," Opt. Express 19(3), 2309–2316 (2011).

[209] Y. Cui, W. Huang, Z. Wang, M. Wang, Z. Zhou, Z. Li, S. Gao, Y. Wang, and P. Wang, "4.3 μm fiber laser in $CO_2$-filled hollow-core silica fibers," Optica 6(8), 951–954 (2019).

[210] M. Xu, F. Yu, and J. C. Knight, "Mid-infrared 1 Watt hollow-core fiber gas laser source," Opt. Lett. 42(20), 4055–4058 (2017).

[211] Z. Zhou, N. Tang, Z. Li, W. Huang, Z. Wang, W. Wu, and W. Hua, "High-power tunable mid-infrared fiber gas laser source by acetylene-filled hollow-core fibers," Opt. Express 26(15), 19144–19153 (2018).

[212] F. B. A. Aghbolagh, V. Nampoothiri, B. Debord, F. Gerome, L. Vincetti, F. Benabid, and W. Rudolph, "Mid IR hollow core fiber gas laser emitting at 4.6 μm," Opt. Lett. 44(2), 383–386 (2019).

[213] W. Huang, Y. Cui, Z. Zhou, Z. Li, Y. Chen, and Z. Wang, "Towards all-fiber structure pulsed mid-infrared laser by gas-filled hollow-core fibers," Chin. Opt. Lett. 17(9), 091402 (2019).

[214] M. Fermann, M. Hofer, F. Haberl, and S. P. Craig-Ryan, "Femtosecond fibre laser," Electron. Lett. 26, 1737–1738 (1990).

[215] A. S. Kurkov, E. M. Sholokhov, and Y. E. Sadovnikova, "All-fiber supercontinuum source in the range of 1550–2400 nm based on telecommunication multimode fiber," Laser Phys. Lett. 8(8), 598–600 (2011).

[216] D. Jain, R. Sidharthan, G. Woyessa, P. M. Moselund, P. Bowen, S. Yoo, and O. Bang, "Scaling power, bandwidth, and efficiency of mid-infrared supercontinuum source based on a $GeO_2$-doped silica fiber," J. Opt. Soc. Am. B 36(2), A86–A92 (2019).


[217] D. D. Hudson, S. Antipov, L. Li, I. Alamgir, T. Hu, M. El Amraoui, Y. Messaddeq, M. Rochette, S. D. Jackson, and A. Fuerbach, "Toward all-fiber supercontinuum spanning the mid-infrared," Optica 4(10), 1163–1166 (2017).


[218] F. Zhu, H. Hundertmark, A. A. Kolomenskii, J. Strohaber, R. Holzwarth, and H. A. Schuessler, "High-power mid-infrared frequency comb source based on a femtosecond Er:fiber oscillator," Opt. Lett. 38, 2360–2362 (2013).


[219] S. T. Cundiff and J. Ye, "Femtosecond optical frequency combs," Rev. Mod. Phys. 75, 325–342 (2003).


[220] Y. Zhang, S. Fan, L. Yan, L. Zhang, X. Zhang, W. Guo, S. Zhang, and H. Jiang, "Robust optical-frequency-comb based on the hybrid mode-locked Er:fiber femtosecond laser," Opt. Express 25(18), 21719–21725 (2017).


[221] J. Ari, F. Starecki, C. Boussard-Plédel, J. -L. Doualan, L. Quétel, K. Michel, A. Braud, P. Camy, R. Chahal, B. Bureau, Y. Ledemi, Y. Messaddeq, and V. Nazabal, "Rare-earth-doped chalcogenide glasses for mid-IR gas sensor applications," Proc. SPIE 10100, 101000Q (2017).


[222] B. T. Meggitt, "Fiber optics in sensor instrumentation," in *Instrumentation Reference Book*, W. Boyes, ed. (Elsevier, 2010), pp. 191–204.


[223] A. B. A. Seddon, "Prospective for new mid-infrared medical endoscopy using chalcogenide glasses," Int. J. Appl. Glass Sci. 2(3), 177–191 (2011).


[224] W. C. Wang, B. Zhou, S. H. Xu, Z. M. Yang, and Q. Y. Zhang, "Recent advances in soft optical glass fiber and fiber lasers," Prog. Mater. Sci.101, 90–171 (2019).

[225] S. Duval, Y. Wang, L. -R. Robichaud, M. Olivier, F. Jobin, J. C. Gauthier, P. Paradis, V. Fortin, P. Laporta, M. Bernier, M. Piché, G. Galzerano, and R. Vallée, "Ultrafast mid-infrared fiber lasers beyond 3 μm," in 2019 Conference on Lasers and Electro-Optics, OSA Technical Digest (online) (Optical Society of America, 2019), paper SF2L.1.

[226] P. Werle, F. Slemr, K. Maurer, R. Kormann, R. Mücke, and B. Jänker, "Near- and mid-infrared laser-optical sensors for gas analysis," Opt. Lasers Eng. 37, 101–114 (2002).

[227] C. Fischer and M. W. Sigrist, "Mid-IR difference frequency generation," in *Solid State Mid-Infrared Laser Sources*, I. T. Sorokina and K. L. Vodopanov, eds., in Topics in Applied Physics 89, C. E. Ascheron, H. J. Koelsch, and W. Skolaut, eds. (Springer-Verlag, 2003), pp. 97–140.

[228] M. S. Vitiello, G. Scalari, B. Williams, and P. De Natale, "Quantum cascade lasers: 20 years of challenges," Opt. Express 23(4), 5167–5182 (2015).

[229] M. Ebrahimzadeh, "Parametric light generation," Phil. Trans. R. Soc. Lond. A 361, 2731–2750 (2003).

[230] M. H. Dunn, M. Ebrahimzadeh, "Parametric generation of tunable light from continuous-wave to femtosecond pulses," Science 286, 1513–1517 (1999).

[231] P. A. Franken, A. E. Hill, C. W. Peters, and G. Weinreich, "Generation of optical harmonics," Phys. Rev. Lett. 7(4), 118–120 (1961).

[232] R. L. Byer and R. L. Herbst, "Parametric oscillation and mixing," in *Nonlinear Infrared Generation*, in Topics in Applied Physics 16, Y. -R. Shen, ed. (Springer, 1977), pp. 81–137.

[233] D. A. Kleinman, "Theory of optical parametric noise," Phys. Rev. 174(3), 1027–1041 (1968).

[234] J. D. Jackson, *Classical Electrodynamics* (Wiley, 1998).

[235] B. J. Orr, J. G. Haub, Y. He, and R. T. White, "Spectroscopic applications of tunable optical parametric oscillators," in *Tunable Laser Applications*, F. J. Duarte, ed. (CRC Press, Taylor & Francis Group, 2016), pp. 17–142.

[236] J. Peng, "Developments of mid-infrared optical parametric oscillators for spectroscopic sensing: a review," Opt. Eng. 53(6), 061613 (2014).

[237] D. N. Nikogosyan, *Nonlinear Optical Crystals: A Complete Survey* (Springer Science+Business Media, 2005).

[238] D. A. Roberts, "Simplified characterization of uniaxial and biaxial nonlinear optical crystals: a plea for standardization of nomenclature and conventions," IEEE J. Quantum Electron. 28(10), 2057–2074 (1992).

[239] M. D. Ewbank, M. J. Rosker, and G. L. Bennett, "Frequency tuning a mid-infrared optical parametric oscillator by the electro-optic effect," J. Opt. Soc. Am. B 14(3), 666–671 (1997).

[240] J. Y. Zhang, "Optical parametric generation and amplification in barium borate and lithium triborate crystals," J. Opt. Soc. Am. B 10(9), 1758–1764 (1993).

[241] D. A. Keszler, "Borates for optical frequency conversion," Solid State Mat. Sci. 1, 204–208 (1996).

[242] K. Zhong, J. Q. Yao, D. G. Xu, J. L. Wang, and J. S. Li, "High-pulse-energy high-efficiency mid-infrared generation based on KTA optical parametric oscillator," Appl. Phys. B 100(4), 749–753 (2010).

[243] F. Bai, Q. Wang, Z. Liu, X. Zhang, X. Wan, W. Lan, G. Jin, X. Tao, and Y. Sun "Theoretical and experimental studies on output characteristics of an intracavity KTA OPO," Opt. Express 20(2), 807–815 (2012).

[244] H. Huang, H. Wang, S. Wang, and D. Shen, "Designable cascaded nonlinear optical frequency conversion integrating multiple nonlinear interactions in two $KTiOAsO_4$ crystals," Opt. Express 26, 642–650 (2018).

[245] J. J. Zondy, D. Touahri, and O. Acef, "Absolute value of the $d_{36}$ nonlinear coefficient of AgGaS$_2$: prospect for a low-threshold doubly resonant oscillator-based 3:1 frequency divider," J. Opt. Soc. Am. B 14(10), 2481–2496 (1997).

[246] D. B. Kolker, N. Yu Kostyukova, A. A. Boyko, V. V. Badikov, D. V. Badikov, A. G. Shadrintseva, N. N. Tretyakova, K. G. Zenov, A. A. Karapuzikov, and J-. J. Zondy, "Widely tunable (2.6–10.4 μm) BaGa$_4$Se$_7$ optical parametric oscillator pumped by a Q-switched Nd:YLiF$_4$ laser," J. Phys. Commun. 2, 035039 (2018).

[247] V. Badikov, D. Badikov, G. Shevyrdyaeva, A. Tyazhev, G. Marchev, V. Panyutin, V. Petrov, and A. Kwasniewski, "Phase-matching properties of BaGa$_4$S$_7$ and BaGa$_4$Se$_7$: wide-bandgap nonlinear crystals for the mid-infrared," Phys. Status Solidi. RRL 5(1), 31–33 (2011).

[248] A. Hemming, J. Richards, A. Davidson, N. Carmody, S. Bennetts, N. Simakov, and J. Haub, "99 W mid-IR operation of a ZGP OPO at 25% duty cycle," Opt. Express 21(8), 10062–10069 (2013).

[249] A. F. Nieuwenhuis, C. J. Lee, P. J. M. van der Slot, P. Groß, and K. -J. Boller, "Mid-infrared ZGP optical parametric oscillator directly pumped by a lamp-pumped, Q-switched Cr, Tm, Ho: YAG laser," Proc. SPIE 6455, 645518 (2007).

[250] E. Pelletier, A. Sell, A. Leitenstorfer, and R. J. Dwayne Miller, "Mid-infrared optical parametric amplifier based on a LGSe crystal and pumped at 1.6 μm," Opt. Express 20(25), 27456–27464 (2012).

[251] V. Petrov, P. G. Schunemann, K. T. Zawilski, and T. M. Pollak, "Noncritical singly resonant optical parametric oscillator operation near 6.2 μm based on a CdSiP$_2$ crystal pumped at 1064 nm," Opt. Lett. 34(16), 2399–2401 (2009).

[252] P. S. Kuo, K. L. Vodopyanov, M. M. Fejer, D. M. Simanovskii, X. Yu, J. S. Harris, D. Bliss, and D. Weyburne, "Optical parametric generation of a mid-infrared continuum in orientation-patterned GaAs," Opt. Lett. 31(1), 71–73 (2006).

[253] P. G. Schunemann, L. A. Pomeranz, and D. J. Magarrell, "Optical parametric oscillation in quasi-phase-matched GaP," Proc. SPIE 9347, 93470J (2015).

[254] K. Liu, H. Liang, L. Wang, S. Qu, T. Lang, H. Li, Qi J. Wang, and Y. Zhang, "Multi-micro-joule GaSe-based midinfrared optical parametric amplifier with an ultrabroad idler spectrum covering 4.2–16 μm," Opt. Lett. 44(4), 1003–1006 (2019).

[255] J. Zhang, K. F. Mak, N. Nagl, M. Seidel, D. Bauer, D. Sutter, V. Pervak, F. Krausz, and O. Pronin, "Multi-mW, few-cycle mid-infrared continuum spanning from 500 to 2250 cm$^{-1}$," Light-Sci. Appl. 7, 17180 (2018).

[256] J. A. Armstrong, N. Bloembergen, J. Ducuing, and P. S. Pershan, "Interactions between light waves in a nonlinear dielectric," Phys. Rev. 127(6), 1918–1939 (1962).

[257] P. A. Franken and J. F. Ward, "Optical harmonics and nonlinear phenomena," Rev. Mod. Phys. 35(1), 23–39 (1963).

[258] M. Born and E. Wolf, *Principles of Optics: Electromagnetic Theory of Propagation, Interference and Diffraction of Light* (Cambridge University Press, 2010).

[259] R. Danielius, A. Piskarskas, A. Stabinis, G. P. Banfi, P. Di Trapani, and R. Righini, "Traveling-wave parametric generation of widely tunable, highly coherent femtosecond light pulses," J. Opt. Soc. Am. B 10(11), 2222–2232 (1993).

[260] K. A. Tillman and D. T. Reid, "Monolithic optical parametric oscillator using chirped quasi-phase matching," Opt. Lett. 32(11), 1548–1550 (2007).

[261] L. E. Myers, G. D. Miller, R. C. Eckardt, M. M. Fejer, R. L. Byer, and W. R. Bosenberg, "Quasi-phase-matched 1.064-μm-pumped optical parametric oscillator in bulk periodically poled LiNbO$_3$," Opt. Lett. 20(1), 52–54 (1995).

[262] W. R. Bosenberg, A. Drobschoff, and D. C. Gerstenberger, "Mid-infrared optical parametric oscillators based on quasi-phasematching," in Proceedings of IEEE Lasers and Electro-Optics Society 1995 Annual Meeting (IEEE, 1995), paper NLO1.1.

[263] D. S. Hum and M. M. Fejer, "Quasi-phase matching," C. R. Physique 8(2), 180–198 (2007).

[264] A. S. Pine, "Doppler-limited molecular spectroscopy by difference-frequency mixing," J. Opt. Soc. Am. 64, 1683–1690 (1974).

[265] G. Edwards, R. Logan, M. Copeland, L. Reinisch, J. Davidson, B. Johnson, R. Maciunas, M. Mendenhall, R. Ossoff, J. Tribble, J. Werkhaven, and D. O'Day, "Tissue ablation by a free-electron laser tuned to the amide II band," Nature 371, 416–419 (1994).

[266] C. R. Phillips, J. Jiang, C. Mohr, A. C. Lin, C. Langrock, M. Snure, D. Bliss, M. Zhu, I. Hartl, J. S. Harris, M. E. Fermann, and M. M. Fejer, "Widely tunable mid-infrared difference frequency generation in orientation-patterned GaAs pumped with a femtosecond Tm-fiber system," Opt. Lett. 37(14), 2928–2930 (2012).

[267] J. C. Casals, S. Parsa, S. C. Kumar, K. Devi, P. G. Schunemann, and M. Ebrahim-Zadeh, "Picosecond difference-frequency-generation in orientation-patterned gallium phosphide," Opt. Express 25(16), 19595–19602 (2017).

[268] Y. V. Aulin, A. Tuladhar, and E. Borguet, "Ultrabroadband mid-infrared noncollinear difference frequency generation in a silver thiogallate crystal," Opt. Lett. 43(18), 4402–4405 (2018).

[269] J. Wei, S. C. Kumar, H. Ye, K. Devi, P. G. Schunemann, and M. Ebrahim-Zadeh, "Nanosecond difference-frequency generation in orientation-patterned gallium phosphide," Opt. Lett. 42(11), 2193–2196 (2017).

[270] Y. He, Y. Guo, D. Xu, Y. Wang, X. Zhu, J. Yao, C. Yan, L. Tang, J. Li, K. Zhong, C. Liu, X. Fan, Y. Wu, and J. Yao, "High energy and tunable mid-infrared source based on $BaGa_4Se_7$ crystal by single-pass difference-frequency generation," Opt. Express 27(6), 9241–9249 (2019).

[271] F. Träger, ed., *Springer Handbook of Lasers and Optics* (Springer, 2012).

[272] C. C. Wang and G. W. Racette, "Measurement of parametric gain accompanying optical difference frequency generation," Appl. Phys. Lett. 6, 169–171 (1965).

[273] M. Yamada, N. Nada, M. Saitoh, and K. Watanabe, "First-order quasi-phase matched LiNbO$_3$ waveguide periodically poled by applying an external field for efficient blue second-harmonic generation," Appl. Phys. Lett. 62, 435–436 (1993).

[274] K. Devi, A. Padhye, Sukeert, and M. Ebrahim-zadeh, "Widely tunable room-temperature continuous-wave optical parametric oscillator based on periodically-poled KTiOPO$_4$," Opt. Express 27(17), 24093–24104 (2019).

[275] J. L. Hall, "Optical frequency measurement: 40 years of technology revolutions," IEEE J. Sel. Top. Quantum Electron. 6(6), 1136–1144 (2000).

[276] S. T. Cundiff and J. Ye, *Femtosecond Optical Frequency Comb Technology* (Springer, 2005).

[277] S. T. Cundiff, J. Ye, and J. L. Hall, "Optical frequency synthesis based on mode-locked lasers," Rev. Sci. Instrum. 72, 3749 (2001).

[278] S. T. Cundiff, J. Ye, and J. L. Hall, "Rulers of light," Sci. Am. 298(4), 74–81 (2008).

[279] G. P. Agrawal, "Self-phase modulation," in *Nonlinear Fiber Optics* (Elsevier, 2019), Chap. 4.

[280] J. K. Ranka, R. S. Windeler, and A. J. Stentz, "Visible continuum generation in air-silica microstructure optical fibers with anomalous dispersion at 800 nm," Opt. Lett. 25, 25 (2000).

[281] T. W. Hänsch, "Nobel lecture: Passion for precision," Rev. Mod. Phys. 78, 1297–1309 (2006).

[282] Q. Wang, J. Zhang, N. Nagl, V. Pervak, F. Krausz, O. Pronin, and K. F. Mak, "Highly efficient broadband mid-infrared generation (2.8–12.5 μm) based on a compact Cr:ZnS laser," in 2019 CLEO/Europe-EQEC (IEEE, 2019), pp. 1–1.

[283] F. C. Cruz, D. L. Maser, T. Johnson, G. Ycas, A. Klose, F. R.Giorgetta, I. Coddington, and S. A. Diddams, "Mid-infrared optical frequency combs based on difference frequency generation for molecular spectroscopy," Opt. Express 23(20), 26814–26824 (2015).

[284] G. Soboń, T. Martynkien, P. Mergo, L. Rutkowski, and A. Foltynowicz, "High-power frequency comb source tunable from 2.7 to 4.2 μm based on difference frequency generation pumped by an Yb-doped fiber laser," Opt. Lett. 42(9), 1748–1751 (2017).

[285] N. Leindecker, A. Marandi, R. L. Byer, and K. L. Vodopyanov, "Broadband degenerate OPO for mid-infrared frequency comb generation," Opt. Express 19(7), 6296–6302 (2011).

[286] W. Xia and X. Chen, "Recent developments in fiber-based optical frequency comb and its applications," Meas. Sci. Technol. 27, 041001 (2016).

[287] T. M. Fortier, D. J. Jones, S. A. Diddams, J. L. Hall, J. Ye, S. T. Cundiff, and R. S. Windeler, "Carrier-envelope phase stabilization of mode-locked lasers," Proc. SPIE 4271, 183–192 (2001).

[288] F. Zhu, J. Bounds, A. Bicer, J. Strohaber, A. A. Kolomenskii, C. Gohle, M. Amani, and H. A. Schuessler, "Near infrared frequency comb vernier spectrometer for broadband trace gas detection," Opt. Express 22(19), 23026–23033 (2014).

[289] T. R. Schibli, K. Minoshima, F. -L. Hong, H. Inaba, A. Onae, H. Matsumoto, I. Hartl, and M. N. Fermann, "Frequency metrology with a turnKey all-fiber system," Opt. Lett. 29(21), 2467–2469 (2004).

[290] B. R. Washburn, R. Fox, N. R. Newbury, J. W. Nicholson, K. Feder, P. S. Westbrook, and C. G. Jørgensen, "Fiber-laser-based frequency comb with a tunable repetition rate," Opt. Express 12(20), 4999–5004 (2004).

[291] N. R. Newbury and B. R. Washburn, "Theory of the frequency comb output from a femtosecond fiber laser," IEEE J. Quantum Electron. 41(11), 1388–1402 (2005).

[292] J. Rauschenberger, T. M. Fortier, D. J. Jones, J. Ye, and S. T. Cundiff, "Control of the frequency comb from a mode-locked Erbium-doped fiber laser," Opt. Express 10(24), 1404–1410 (2002).

[293] N. Haverkamp, H. Hundertmark, C. Fallnich, and H. R. Telle, "Frequency stabilization of mode-locked Erbium fiber lasers using pump power control," Appl. Phys. B 78, 321–324 (2004).

[294] B. R. Washburn, S. A. Diddams, N. R. Newbury, J. W. Nicholson, M. F. Yan, and C. G. Jørgensen, "Phase-locked Erbium-fiber-laser-based frequency comb in the near infrared," Opt. Lett. 29(3), 250–252 (2004).

[295] D. Sánchez, M. Hemmer, M. Baudisch, K. Zawilski, P. Schunemann, H. Hoogland, R. Holzwarth, and J. Biegert, "Broadband mid-IR frequency comb with $CdSiP_2$ and $AgGaS_2$ from an Er,Tm:Ho fiber laser," Opt. Lett. 39(24), 6883–6886 (2014).

[296] K. Krzempek, D. Tomaszewska, A. Gluszek, T. Martynkien, P. Mergo, J. Sotor, A. Foltynowicz, and G. Sobon, "Stabilized all-fiber source for generation of tunable broadband $f_{CEO}$-free mid-IR frequency comb in the 7 - 9 µm range," Opt. Express 27(26), 37435–37445 (2019).

[297] S. T. Cundiff, "Phase stabilization of ultrashort optical pulses," J. Phys. D: Appl. Phys. 35, R43–R59 (2002).

[298] L. C. Sinclair, J. -D. Deschênes, L. Sonderhouse, W. C. Swann, I. H. Khader, E. Baumann, N. R. Newbury, and I. Coddington, "A compact optically coherent fiber frequency comb," Rev. Sci. Instrum. 86, 081301 (2015).

[299] J. Ye, J. L. Hall, and S. A. Diddams, "Precision phase control of an ultrawide-bandwidth femtosecond laser: A network of ultrastable frequency marks across the visible spectrum," Opt. Lett. 25(22), 1675–1677 (2000).

[300] W. C. Swann, J. J. McFerran, I. Coddington, N. R. Newbury, I. Hartl, M. E. Fermann, P. S. Westbrook, J. W. Nicholson, K. S. Feder, C. Langrock, and M. M. Fejer, "Fiber-laser frequency combs with subhertz relative linewidths," Opt. Lett. 31(20), 3046–3048 (2006).

[301] J. -D. Deschênes and J. Genest, "Heterodyne beats between a continuous-wave laser and a frequency comb beyond the shot-noise limit of a single comb mode," Phys. Rev. A 87, 023802 (2013).

[302] A. Ruehl, A. Gambetta, I. Hartl, M. E. Fermann, K. S. E. Eikema, and M. Marangoni, "Widely-tunable mid-infrared frequency comb source based on difference frequency generation," Opt. Lett. 37(12), 2232–2234 (2012).

[303] K. F. Lee, C. J. Hensley, P. G. Schunemann, and M. E. Fermann, "Midinfrared frequency comb by difference frequency of erbium and thulium fiber lasers in orientation-patterned gallium phosphide," Opt. Express 25(15), 17411–17416 (2017).

[304] J. Sotor, T. Martynkien, P. G. Schunemann, P. Mergo, L. Rutkowski, and G. Soboń, "All-fiber mid-infrared source tunable from 6 to 9 μm based on difference frequency generation in OP-GaP crystal," Opt. Express 26(9), 11756–11763 (2018).

[305] A. Hugi, G. Villares, S. Blaser, H. C. Liu, and J. Faist, "Mid-infrared frequency comb based on a quantum cascade laser," Nature 492, 229–233 (2012).

[306] J. Faist, G. Villares, G. Scalari, M. Rösch, C. Bonzon, A. Hugi, and M. Beck, "Quantum cascade laser frequency combs," Nanophotonics 5(2), 272–291 (2016).

[307] J. Hillbrand, P. Jouy, M. Beck, and J. Faist, "Tunable dispersion compensation of quantum cascade laser frequency combs," Opt. Lett. 43(8), 1746–1749 (2018).

[308] Q. Y. Lu, M. Razeghi, S. Slivken, N. Bandyopadhyay, Y. Bai, W. J. Zhou, M. Chen, D. Heydari, A. Haddadi, R. McClintock, M. Amanti, and C. Sirtori, "High power frequency comb based on mid-infrared quantum cascade laser at $\lambda \sim 9$ μm," Appl. Phys. Lett. 106, 051105 (2015).

[309] T. J. Kippenberg, R. Holzwarth, and S. A. Diddams, "Microresonator-based optical frequency combs," Science 332, 555–559 (2011).

[310] P. Del'Haye, T. Herr, E. Gavartin, M. L. Gorodetsky, R. Holzwarth, and T. J. Kippenberg, "Octave spanning tunable frequency comb from a microresonator," Phys. Rev. Lett. 107, 063901 (2011).

[311] T. Herr, K. Hartinger, J. Riemensberger, C. Y. Wang, E. Gavartin, R. Holzwarth, M. L. Gorodetsky, and T. J. Kippenberg, "Universal formation dynamics and noise of Kerr-frequency combs in microresonators," Nat. Photonics 6, 480–487 (2012).

[312] Y. K. Chembo, "Kerr optical frequency combs: theory, applications and perspectives," Nanophotonics 5(2), 214–230 (2016).

[313] T. J. Kippenberg, A. L. Gaeta, M. Lipson, and M. L. Gorodetsky, "Dissipative Kerr solitons in optical microresonators," Science 361, 567 (2018).

[314] P. Trocha, M. Karpov, D. Ganin, M. H. P. Pfeiffer, A. Kordts, S. Wolf, J. Krockenberger, P. Marin-Palomo, C. Weimann, S. Randel, W. Freude, T. J. Kippenberg, and C. Koos, "Ultrafast optical ranging using microresonator soliton frequency combs," Science 359, 887–891 (2018).

[315] N. Picqué and T. W. Hänsch, "Frequency comb spectroscopy," Nat. Photonics 13, 146–157 (2019).

[316] A. Pasquazi, M. Peccianti, L. Razzari, D. J. Moss, S. Coen, M. Erkintalo, Y. K. Chembo, T. Hansson, S. Wabnitz, P. Del'Haye, X. Xue, A. M. Weiner, and R. Morandotti, "Micro-combs: A novel generation of optical sources," Phys. Rep. 729, 1–81 (2018).

[317] N. R. Newbury, "Searching for applications with a fine-tooth comb," Nat. Photonics 5, 186–188 (2011).

[318] J. Liu, V. Brasch, M. H. P. Pfeiffer, A. Kordts, A. N. Kamel, H. Guo, M. Geiselmann, and T. J. Kippenberg, "Frequency-comb-assisted broadband precision spectroscopy with cascaded diode lasers," Opt. Lett. 41(13), 3134–3137 (2016).

[319] J. Karhu, M. Vainio, M. Metsälä, and L. Halonen, "Frequency comb assisted two-photon vibrational spectroscopy," Opt. Express 25(5), 4688–4699 (2017).

[320] T. R. Schibli, I. Hartl, D. C. Yost, M. J. Martin, A. Marcinkevičius, M. E. Fermann, and J. Ye, "Optical frequency comb with submillihertz linewidth and more than 10 W average power," Nat. Photonics 2, 355–359 (2008).

[321] C.-C. Lee, C. Mohr, J. Bethge, S. Suzuki, M. E. Fermann, I. Hartl, and T. R. Schibli, "Frequency comb stabilization with bandwidth beyond the limit of gain lifetime by an intracavity graphene electro-optic modulator," Opt. Lett. 37(15), 3084–3086 (2012).

[322] Th. Udem, J. Reichert, R. Holzwarth, and T. W. Hänsch, "Absolute optical frequency measurement of the cesium D1 line with a mode-locked laser," Phys. Rev. Lett. 82(18), 3568–3571 (1999).

[323] Th. Udem, J. Reichert, R. Holzwarth, and T. W. Hänsch, "Accurate measurement of large optical frequency differences with a mode-locked laser," Opt. Lett. 24(13), 881–883 (1999).

[324] S. A. Diddams, Th. Udem, J. C. Bergquist, E. A. Curtis, R. E. Drullinger, L. Hollberg, W. M. Itano, W. D. Lee, C. W. Oates, K. R. Vogel, and D. J. Wineland," An optical clock based on a single trapped $^{199}$Hg$^+$ ion," Science 293, 825–828 (2001).

[325] L. Jin, V. Sonnenschein, M. Yamanaka, H. Tomita, T. Iguchi, A. Sato, K. Nozawa, K. Yoshida, S. -I. Ninomiya, and N. Nishizawa, "3.1–5.2 µm coherent MIR frequency comb based on Yb-doped fiber laser," IEEE J. Sel. Top. Quantum Electron. 24(3), 0900907 (2018).

[326] M. Vainio and J. Karhu, "Fully stabilized mid-infrared frequency comb for high-precision molecular spectroscopy," Opt. Express 25(4), 4190–4200 (2017).

[327] F. Adler, K. C. Cossel, M. J. Thorpe, I. Hartl, M. E. Fermann, and J. Ye, "Phase-stabilized, 1.5-W frequency comb at 2.8 to 4.8 µm," Opt. Lett. 34(9), 1330–1332 (2009).

[328] A. A. Savchenkov, V. S. Ilchenko, F. Di Teodoro, P. M. Belden, W. T. Lotshaw, A. B. Matsko, and L. Maleki, "Generation of Kerr combs centered at 4.5 µm in crystalline microresonators pumped with quantum-cascade lasers," Opt. Lett. 40(15), 3468–3471 (2015).

[329] J. Haas and B. Mizaikoff, "Advances in mid-infrared spectroscopy for chemical analysis," Annu. Rev. Anal. Chem. 9, 45–68 (2016).

[330] M. L. Weichman, P. B. Changala, J. Ye, Z. Chen, M. Yan, and N. Picqué, "Broadband molecular spectroscopy with optical frequency combs," J. Mol. Spectrosc. 355, 66–78 (2019).

[331] A. Yariv, *Introduction to Optical Electronics* (Holt, Rinehart and Winston, 1976).

[332] A. H. Sommer, *Photoemissive Materials: Preparation, Properties, and Uses* (Wiley, 1968).

[333] R. W. Engstrom, "Multiplier photo-tube characteristics: application to low light levels," J. Opt. Soc. Am. 37, 420–431 (1947).

[334] P. D. Townsend, "Photocathodes—past performance and future potential," Contemp. Phys. 44(1), 17–34 (2003).

[335] H. Rabus, U. Kroth, M. Richter, G. Ulm, J. Friese, R. GernhaKuser, A. KastenmuKller, P. Maier-Komor, and K. Zeitelhack, "Quantum efficiency of cesium iodide photocathodes in the 120-220 nm spectral range traceable to a primary detector standard," Nucl. Instrum. Methods Phys. Res. A 438(1), 94–103 (1999).

[336] Y. Xie, H. Liu, A. Zhang, Y. Liu, T. Hu, L. Zhou, Z. An, X. Cai, J. Fang, Y. Ge, Q. Lü, F. Shi, X. Sun, L. Sun, Z. Xue, B. Yu, Y. Zheng, and J. Lü, "Quantum efficiency measurement of CsI photocathodes using synchrotron radiation at BSRF," Nucl. Instrum. Methods Phys. Res. A 664(1), 310–316 (2012).

[337] S. Uchiyama, Y. Takagi, M. Niigaki, H. Kan, and H. Kondoh, "GaN-based photocathodes with extremely high quantum efficiency," Appl. Phys. Lett. 86, 103511 (2005).

[338] P. R. Bratt, "Impurity germanium and silicon infrared detectors," in *Semiconductors and Semimetals* 12, R. K. Willardson and A. C. Beer, eds. (Academic Press, 1977), pp. 39–142.

[339] I. M. Baker, "II-VI narrow bandgap semiconductors: optoelectronics," in *Springer Handbook of Electronic and Photonic Materials*, S. Kasap and P. Capper, eds. (Springer, 2017).

[340] C. Vérié, "Narrow bandgap semiconductors," in *Advances in Solid State Physics* 10, O. Madelung, ed. (Springer, 1970).

[341] J. F. Piotrowski and A. Rogalski, *High-Operating-Temperature Infrared Photodetectors* (SPIE Press, 2007).

[342] H. A. Haus, "Shot noise and thermal noise," in *Electromagnetic Noise and Quantum Optical Measurements* (Springer-Verlag, 2000), Chap. 4.

[343] P. Réfrégier, *Noise Theory and Application to Physics* (Springer, 2004).

[344] B. G. Streetman and S. Banerjee, *Solid State Electronic Devices* (Pearson, 2014).

[345] D. K. Bhattacharya and R. Sharma, *Solid State Electronic Devices* (Oxford University Press, 2013).

[346] J. T. Verdeyen, *Laser Electronics* (Prentice-Hall Inc., 1981).

[347] G. E. Stillman and C. M. Wolfe, "Avalanche Photodiodes," in *Semiconductors and Semimetals* 12, R. K. Willardson and A. C. Beer, eds. (Academic Press, 1977), pp. 291–393.

[348] L. K. Anderson and B. J. McMurtry, "High-speed photodetectors," Proc. IEEE 54(10), 1335–1349 (1966).

[349] A. C. Olivieri and G. M. Escandar, "Analytical Figures of Merit," in *Practical Three-Way Calibration* (Elsevier, 2014), pp. 93–107.

[350] T. Ishibashi, T. Furuta, N. Shimizu, K. Nagata, Y. Matsuoka, and M. Tomizawa, "PIN photodiode with improved frequency response and saturation output," U. S. Patent 5,818,096 (Oct 6, 1998).

[351] T. -P. Lee, C. A. Burrus, and A. G. Dentai, "InGaAs/InP pin photodiodes for lightwave communications at the 0.95-1.65 μm wavelength," IEEE J. Quantum Electron. 17(2), 232–238 (1981).

[352] K. Kato, A. Kozen, Y. Muramoto, Y. Itaya, T. Nagatsuma, and M. Yaita, "110-GHz, 50%-efficiency mushroom-mesa waveguide p-i-n photodiode for a 1.55-μm wavelength," IEEE Photon. Tech. Lett. 6(6), 719–721 (1994).

[353] C. C. Chang, R. E. Frahm, K. M. Lee, O. G. Lorimor, and D. R. Zolnowski, "Pin photodiode having a wide bandwidth," U. S. Patent 6,326,649 (Dec 4, 2001).

[354] Excelitas Technologies, "Understanding avalanche photodiodes for improving system performance," in *Avalanche photodiodes (APDs): A User Guide* (Excelitas Technologies Corp., 2011).

[355] R. J. McIntyre, "Multiplication noise in uniform avalanche diodes," IEEE Trans. Electron Devices 13(1), 164–168 (1966).

[356] R. J. McIntyre, "The distribution of gains in uniformly multiplying avalanche photodiodes: theory," IEEE Trans. Electron Devices 19(6), 703–713 (1972).

[357] H. Dautet, P. Deschamps, B. Dion, A. D. MacGregor, D. MacSween, R. J. McIntyre, C. Trottier, and P. P. Webb, "Photon counting techniques with silicon avalanche photodiodes," Appl. Opt. 32(21), 3894–3900 (1993).

[358] F. Zappa, S. Tisa, A. Tosi, and S. Cova, "Principles and features of single-photon avalanche diode arrays," Sens. Actuator A: Phys. 140(1), 103–112 (2007).

[359] P. Capper, ed., *Properties of narrow gap cadmium-based compounds*, in EMIS Datareviews Series 10 (IEE, 1994).

[360] R. E. Longshore, M. B. Reine, E. E. Krueger, P. O'Dette, C. L. Terzis, B. Denley, J. M. Hartley, J. H. Rutter, and D. E. Kleinmann, "Advances in 15-µm HgCdTe photovoltaic and photoconductive detector technology for remote sensing," Proc. SPIE 2816, 120–137 (1996).

[361] D. R. Rhiger, "HgCdTe Long-Wave Infrared Detectors," in *Advances in Infrared Photodetectors*, S. D. Gunapala, D. R. Rhiger, and C. Jagadish, eds., in Semiconductors and Semimetals 84, E .R. Weber and C. Jagadish, eds. (Elsevier, 2011), pp. 303–331.

[362] M. A. Kinch, "HgCdTe: Recent trends in the ultimate IR semiconductor," J. Electron. Mater. 39(7), 1043–1052 (2007).

[363] G. L. Hansen, J. L. Schmit, and T. N. Casselman, "Energy gap versus alloy composition and temperature in $Hg_{1-x}Cd_xTe$," J. Appl. Phys. 53(10), 7099–7101 (1982).

[364] G. L. Hansen and J. L. Schmit, "Calculation of intrinsic carrier concentration in $Hg_{1-x}Cd_xTe$," J. Appl. Phys. 54, 1639–1640 (1983).

[365] M. H. Weiler, "Magnetooptical Properties of $Hg_{1-x}Cd_xTe$ Alloys," in *Defects, (HgCd)Se, (HgCd)Te*, R. K. Willardson and A. C. Beer, eds., in Semiconductors and Semimetals 16 (Academic Press, 1981), pp. 119–191.

[366] E. N. Lewis, P. J. Treado, R. C. Reeder, G. M. Story, A. E. Dowrey, C. Marcott, and I. W. Levin, "Fourier transform spectroscopic imaging using an infrared focal-plane array detector," Anal. Chem. 67(19), 3377–3381 (1995).

[367] D. A. Scribner, M. R. Kruer, and J. M. Killiany, "Infrared focal plane array technology," Proc. IEEE 79(1), 66–85 (1991).

[368] B. E. A. Saleh and M. C. Teich, *Fundamentals of Photonics* (John Wiley & Sons, 2013).

[369] E. Hecht, *Optics* (Addison-Wesley, 1998), pp. 409–417.

[370] F. Adler, M. J. Thorpe, K. C. Cossel, and J. Ye, "Cavity-enhanced direct frequency comb spectroscopy: technology and applications," Annu. Rev. Anal. Chem. 3, 175–205 (2010).

[371] F. Hindle, R. Bocquet, A. Pienkina, A. Cuisset, and G. Mouret, "Terahertz gas phase spectroscopy using a high-finesse Fabry–Pérot cavity," Optica 6(12), 1449–1454 (2019).

[372] M. Zaborowski, M. Słowiński, K. Stankiewicz, F. Thibault, A. Cygan, H. Jóźwiak, G. Kowzan, P. Masłowski, A. Nishiyama, N. Stolarczyk, S. Wójtewicz, R. Ciuryło, D. Lisak, and P. Wcisło, "Ultra-high finesse cavity-enhanced spectroscopy for accurate tests of quantum electrodynamics for molecules," Opt. Lett. 45(7), 1603–1606 (2020).

[373] J. A. Silver, "Simple dense-pattern optical multipass cells," Appl. Opt. 44(31), 6545–6556 (2005).

[374] M. Dong, C. Zheng, D. Yao, G. Zhong, S. Miao, W. Ye, Y. Wang, and F. K. Tittel, "Double-range near-infrared acetylene detection using a dual spot-ring Herriott cell (DSR-HC)," Opt. Express 26(9), 12081–12091 (2018).

[375] T. A. Hu, E. L. Chappell, J. T. Munley, and S. W. Sharpe, "Improved multipass optics for diode laser spectroscopy," Rev. Sci. Instrum. 64(12), 3380–3383 (1993).

[376] B. Kühnreich, M. Höh, S. Wanger, and V. Ebert, "Direct single-mode fibre-coupled miniature White cell for laser absorption spectroscopy," Rev. Sci. Instrum. 87(2), 023111 (2016).

[377] K. Tanaka, K. Miyamura, K. Akishima, K. Tonokura, and M. Konno, "Sensitive measurements of trace gas of formaldehyde using a mid-infrared laser spectrometer with a compact multi-pass cell," Infrared Phys. Technol. 79, 1–5 (2016).

[378] L. Dong, Y. Yu, C. Li, S. So, and F. K. Tittel, "Ppb-level formaldehyde detection using a CW room-temperature interband cascade laser and a miniature dense pattern multipass gas cell," Opt. Express 23(15), 19821–19830 (2015).

[379] M. Graf, L. Emmenegger, and B. Tuzson, "Compact, circular, and optically stable multipass cell for mobile laser absorption spectroscopy," Opt. Lett. 43(11), 2434–2437 (2018).

[380] D. Rittenhouse, "An optical problem, proposed by Mr. Hopkinson, and solved by Mr. Rittenhouse," Am. Phil. Soc. 2, 201–206 (1786).

[381] T. Young, "On the theory of light and colours," Phil. Trans. II, 399–408 (1803).

[382] E. G. Loewen and E. Popov, *Diffraction Gratings and Applications*, in Optical Engineering Series, B. J. Thompson, ed. (Marcel Dekker Inc., 1997).

[383] P. Grodzinski, "A ruling engine used by Sir John Barton-and its products," Trans. Newcomen Soc. 26(1), 79–88 (2014).

[384] J. Fraunhofer, "Kurtzer Bericht von the Resultanten neuerer Versuche über die Gesetze des Lichtes, und die Theorie derselbem," Gilberts Ann. Phys. 74, 337–378 (1823).

[385] J. Fraunhofer, "Über die Brechbarkeit des electrishen Lichts," K. Acad. D. Wiss. zu München, April-June, 61–62 (1824).

[386] G. B. J. de Boer, C. de Weerd, D. Thoenes, H. W. J. Goossens, "Laser diffraction spectrometry: Fraunhofer diffraction versus Mie scattering," Part. Charac. 4, 14–19 (1987).

[387] M. C. Hutley, *Diffraction Gratings*, in Techniques of Physics 6, N. H. March and H. N. Daglish, eds. (Academic Press, 1982).

[388] R. S. Rasmussen, "Infrared spectroscopy in structure determination and its application to penicillin," in *Progress in the Chemistry of Organic Natural Products* 5, L. Zechmeister, ed. (Springer, 1948).

[389] W. Demtröder, *Laser Spectroscopy* (Springer, 2008).

[390] A. S. King, "Note on some effects of ruling errors in grating spectra," Astrophys. J. 17, 239–242 (1903).

[391] T. Lyman, "An explanation of the false spectra from diffraction gratings," Proc. Am. Acad. Arts Sci. 39(3), 39–47 (1903).

[392] M. Kroneberger, A. Mezger, and S. Becker, "Stray light and ghosts in catadioptric spectrometers: incorporating grating scatter measurements into simulations and ghost sensitivity into system design," Adv. Opt. Technol. 7(6), 377–386 (2018).

[393] G. F. Larson, V. A. Fassel, R. K. Winge, and R. N. Kniseley, "Ultratrace analyses by optical emission spectroscopy: The stray light problem," Appl. Spectrosc. 30, 384–391 (1976).

[394] E. B. Burgh, M. A. Bershady, K. B. Westfall, and K. H. Nordsieck, "Recombination ghosts in Littrow configuration: Implications for spectrographs using volume phase holographic gratings," Publ. Astron. Soc. Pac. 119, 1069 (2007).

[395] N. A. Finkelstein, C. H. Brumley, and R. J. Meltzer, "The reduction of ghosts in diffraction grating spectra," J. Opt. Soc. Am. 42, 121–126 (1952).

[396] J. M. Lerner, J. Flamand, J. P. Laude, G. Passereau, and A. Thevenon, "Diffraction gratings ruled and holographic-A review," in the 24th Annual Technical Symposium, Proc. SPIE 0240 (1981).

[397] Q. Zhou, J. Pang, X. Li, K. Ni, and R. Tian, "Improving the spectral resolution of flat-field concave grating miniature spectrometers by dividing a wide spectral band into two narrow ones," Appl. Opt. 54(32), 9450–9455 (2015).

[398] J. C. Knight, D. Ball, and G. N. Robertson, "Analytical inversion for laser diffraction spectrometry giving improved resolution and accuracy in size distribution," Appl. Opt. 30(33), 4795–4799 (1991).

[399] M. Dopita, J. Rhee, C. Farage, P. McGregor, G. Bloxham, A. Green, B. Roberts, J. Neilson, G. Wilson, P. Young, P. Firth, G. Busarello, and P. Merluzzi, "The wide field

spectrograph (WiFeS): performance and data reduction," Astrophys. Space Sci. 327(2), 245–257 (2010).

[400] M. M. Roth, A. Kelz, T. Fechner, T. Hahn, S. -M. Bauer, T. Becker, P. Bohm, L. Christensen, F. Dionies, J. Paschke, E. Popow, and D. Wolter "PMAS: The Potsdam Multi-Aperture Spectrophotometer. I. Design, manufacture, and performance," Publ. Astron. Soc. Pac. 117, 620–642 (2005).

[401] S. S. Wang, R. Magnusson, J. S. Bagby, and M. G. Moharam, "Guided-mode resonances in planar dielectric-layer diffraction gratings," J. Opt. Soc. Am. A 7, 1470–1474 (1990).

[402] S. S. Wang and R. Magnusson, "Theory and applications of guided-mode resonance filters," Appl. Opt. 32, 2606–2613 (1993).

[403] S. -F. Lin, C. -M. Wang, T. -J. Ding, Y. -L. Tsai, T. -H. Yang, W. -Y. Chen, and J. -Y. Chang, "Sensitive metal layer assisted guided mode resonance biosensor with a spectrum inversed response and strong asymmetric resonance field distribution," Opt. Express 20, 14584–14595 (2012).

[404] P. K. Sahoo, S. Sarkar, and J. Joseph, "High sensitivity guided-mode-resonance optical sensor employing phase detection," Sci. Rep. 7(1), 7607 (2017).

[405] D. Fattal, J. Li, Z. Peng, M. Fiorentino, and R. G. Beausoleil, "Flat dielectric grating reflectors with focusing abilities," Nat. Photonics 4, 466–470 (2010).

[406] R. Newnham and L. Cross, "Ferroelectricity: the foundation of a field from form to function," MRS Bulletin, 30(11), 845–848 (2005).

[407] A. Arnau and D. Soares, "Fundamentals on Piezoelectricity," in *Piezoelectric Transducers and Applications*, A. Arnau, ed. (Springer, 2008), pp. 1–38.

[408] C. S. Brown, R. C. Kell, R. Taylor, and L. A. Thomas, "Piezo-electric materials," Proc. IEE, Part B: Elec. Commun. Eng. 109(43), 99–114 (1962).

[409] A. Safari and E. K. Akdoğan, *Piezoelectric and Acoustic Materials for Transducer Applications* (Springer, 2008).

[410] D. DeFontaine, "Configurational thermodynamics of solid solutions," in *Solid State Physics: Advances in Research and Applications* 34, H. Ehrenreich, F. Seitz, and D. Turnbull, eds. (Academic Press, 1979).

[411] J. M. Ziman, *Models of Disorder: The Theoretical Physics of Homogeneously Disordered Systems* (Cambridge University Press, 1979).

[412] U. Rabe, M. Kopycinska, S. Hirsekorn, J. Muñoz Saldaña, G. A. Schneider, and W. Arnold, "High-resolution characterization of piezoelectric ceramics by ultrasonic scanning force microscopy techniques," J. Phys. D: Appl. Phys. 35, 2621–2635 (2002).

[413] H. Jaffe and D. A. Berlincourt, "Piezoelectric transducer materials," Proc. IEEE 53(10), 1372–1386 (1965).

[414] D. Berlincourt, B. Jaffe, H. Jaffe, and H. H. A. Krueger, "Transducer properties of lead titanate zirconate ceramics," IRE Trans. Ultrason. Eng. UE-7(1), 1–6 (1960).

[415] C. K. N. Patel and A. C. Tam, "Pulsed optoacoustic spectroscopy of condensed matter," Rev. Mod. Phys. 53(3), 517–550 (1981).

[416] C. K. N. Patel, "Opto-acoustic spectroscopy — A tool for the study of optical spectra of very transparent materials," in *Photoacoustic Effect Principles and Applications*: Proceedings of the First International Conference on the Photoacoustic Effect in Germany, E. Lüscher, P. Korpiun, H. -J. Coufal, and R. Tilgner, eds., (Springer, 1984), pp. 21–39.

[417] M. Xu and L. V. Wang, "Photoacoustic imaging in biomedicine," Rev. Sci. Instrum. 77(4), 041101 (2006).

[418] M. Lethiecq, F. Levassort, D. Certon, and L. P. Tran-Huu-Hue, "Piezoelectric transducer design for medical diagnosis and NDE," in *Piezoelectric and Acoustic Materials for Transducer Applications*, A. Safari and E. K. Akdoğan, eds., (Springer, 2008), pp. 191–215.

[419] J. M. Cannata, T. A. Ritter, W. -H. Chen, R. H. Silverman, and K. K. Shung, "Design of efficient, broadband single-element (20-80 MHz) ultrasonic transducers for medical imaging applications," IEEE Trans. Ultrason. Ferroelectr. Freq. Control 50(11), 1548–1557 (2003).

[420] A. Ramos and J. L. San Emeterio, "Ultrasonic systems for non-destructive testing using piezoelectric transducers: electrical responses and main schemes," in *Piezoelectric Transducers and Applications*, A. Arnau, ed., (Springer, 2008), pp. 413–431.

[421] J. R. Sandercock, "Brillouin scattering study of SbSI using a double-passed, stabilised scanning interferometer," Opt. Commun. 2(2), 73–76 (1970).

[422] V. Spagnolo, P. Patimisco, S. Borri, G. Scamarcio, B. E. Bernacki, and J. Kriesel, "Mid-infrared fiber-coupled QCL-QEPAS sensor," Appl. Phys. B 112(1), 25–33 (2013).

[423] R. Bechmann, "Elastic and piezoelectric constants of alpha-quartz," Phys. Rev. 110(5), 1060–1061 (1958).

[424] C. S. Tsai, "Integrated acousto-optic device modules and applications," in *Encyclopedia of Electrical & Electronics Engineering* (Wiley, 2016), pp. 1–16.

[425] V. -F. Duma, "Prototypes and modulation functions of classical and novel configurations of optical chopper wheels," Lat. Am. J. Solids Struct. 10(1), 5–18 (2013).

[426] ThorLabs, "Optical chopper system and chopper wheels" (ThorLabs, 2016). https://www.thorlabs.com/catalogpages/obsolete/2016/MC2000.pdf

[427] G. Kloos, *Applications of Lock-in Amplifiers in Optics*, in Tutorial Texts in Optical Engineering TT117, J. A. Harrington, ed. (SPIE Press, 2018).

[428] H. Osawa, T. Ohkochi, M. Fujisawa, S. Kimura, and T. Kinoshita, "Development of optical choppers for time-resolved measurements," J. Synchrotron Radiat. 24(3), 560–565 (2017).

[429] H. Osawa, T. Kudo, and S. Kimura, "Development of high-repetition-rate X-ray chopper system for time-resolved measurements with synchrotron radiation," Jpn. J. Appl. Phys. 56, 048001 (2017).

[430] P. Horowitz and W. Hill, *The Art of Electronics* (Cambridge University Press, 2015).

[431] National Instruments, "LabVIEW core 1 participant guide," (National Instruments, 2016), pp. 1–14.
http://www.ni.com/pdf/training/us/LVCore1_CourseManual_English_Sample

[432] P. Zalicki and R. N. Zare, "Cavity ring-down spectroscopy for quantitative absorption measurements," J. Chem. Phys. 102(7), 2708–2717 (1995).

[433] J. W. Hahn, Y. S. Yoo, J. Y. Lee, J. W. Kim, and H. -W. Lee, "Cavity ringdown spectroscopy with a continuous-wave laser: calculation of coupling efficiency and a new spectrometer design," Appl. Opt. 38(9), 1859–1866 (1999).

[434] H. Dahnke, D. Kleine, W. Urban, P. Hering, and M. Mürtz, "Isotopic ratio measurement of methane in ambient air using mid-infrared cavity leak-out spectroscopy," Appl. Phys. B 72, 121–125 (2001).

[435] H. Lin, Z. D. Reed, V. T. Sironneau, and J. T. Hodges, "Cavity ring-down spectrometer for high-fidelity molecular absorption measurements," J. Quant. Spectrosc. Radiat. Transf. 161, 11–20 (2015).

[436] P. Gupta, D. Noone, J. Galewsky, C. Sweeney, and B. H. Vaughn, "Demonstration of high-precision continuous measurements of water vapor isotopologues in laboratory and remote field deployments using wavelength-scanned cavity ring-down spectroscopy (WS-CRDS) technology," Rapid Commun. Mass Spectrom. 23(16), 2534–2542 (2009).

[437] B. Chen, Y. R. Sun, Z. -Y. Zhou, J. Chen, A. -W. Liu, and S. -M. Hu, "Ultrasensitive, self-calibrated cavity ring-down spectrometer for quantitative trace gas analysis," Appl. Opt. 53(32), 7716–7723 (2014).

[438] S. Zhou, Y. Han, and B. Li, "Pressure optimization of an EC-QCL based cavity ring-down spectroscopy instrument for exhaled NO detection," Appl. Phys. B 124, 27 (2018).

[439] H. Waechter, F. Adler, M. Beels, R. Matz, B. Siller, B. West, and Y. Chen, "Diverse industrial applications of cavity ring-down spectroscopy," in 2016 Photonics North (PN) (IEEE, 2016).

[440] S. A. Diddams, "The evolving optical frequency comb [Invited]," J. Opt. Soc. Am. B 27(11), B51–B62 (2010).

[441] A. Foltynowicz, T. Ban, P. Masłowski, F. Adler, and J. Ye, "Quantum-noise-limited optical frequency comb spectroscopy," Phys. Rev. Lett. 107, 233002 (2011).

[442] D. Romanini, A. A. Kachanov, N. Sadeghi, and E. Stoeckel, "CW cavity ring down spectroscopy," Chem. Phys. Lett. 264, 316–322 (1997).

[443] B. A. Paldus, C. C. Harb, T. G. Spence, B. Wilke, J. Xie, J. S. Harris, and R. N. Zare, "Cavity-locked ring-down spectroscopy," J. Appl. Phys. 83(8), 3991–3997 (1998).

[444] W. Zhang, H. Wei, X. Chen, and Y. Li, "Sensitivity improvement by optimized optical switching and curve fitting in a cavity ring-down spectrometer," Appl. Opt. 57(29), 8487–8493 (2018).

[445] M. J. Thorpe, D. D. Hudson, K. D. Moll, J. Lasri, and J. Ye, "Cavity-ringdown molecular spectroscopy based on an optical frequency comb at 1.45-1.65 μm," Opt. Lett. 32(3), 307–309 (2007).

[446] Y. R. Sun, H. Pan, C. -F. Cheng, A. -W. Liu, J. -T. Zhang, S. -M. Hu, "Application of cavity ring-down spectroscopy to the Boltzmann constant determination," Opt. Express 19(21), 19993–20002 (2011).

[447] W. Li, Y. Han, Z. Chen, H. Jiang, and K. Hamamoto, "Amplifier-assisted CRDS (cavity ring-down spectroscopy) toward compact breath sensing," Jpn. J. Appl. Phys. 58, SJJD01 (2019).

[448] Y. Chen, P. Mahaffy, V. Holmes, J. Burris, P. Morey, K. K. Lehmann, B. S. Lollar, G. Lacrampe-Couloume, and T. C. Onstott, "Near infrared cavity ring-down spectroscopy for isotopic analyses of $CH_4$ on future Martian surface missions," Planet. Space Sci. 105, 117–122 (2015).

[449] R. J. Jones, I. Thomann, and J. Ye, "Precision stabilization of femtosecond lasers to high-finesse optical cavities," Phys. Rev. A 69, 051803(R) (2004).

[450] G. Méjean, R. Grilli, C. Abd Alrahman, I. Ventrillard, S. Kassi, and D. Romanini, "A transportable spectrometer for in situ and local measurements of iodine monoxide at mixing ratios in the $10^{-14}$ range," Appl. Phys. Lett. 100, 251110 (2012).

[451] A. L. Gaeta, M. Lipson, and T. J. Kippenberg, "Photonic-chip-based frequency combs," Nat. Photonics 13, 158–169 (2019).

[452] N. Hoghooghi, R. J. Wright, A. S. Makowiecki, W. C. Swann, E. M. Waxman, I. Coddington, and G. B. Rieker, "Broadband coherent cavity-enhanced dual-comb spectroscopy," Optica 6(1), 28–33 (2019).

[453] L. E. McHale, B. Martinez, T. W. Miller, and A. P. Yalin, "Open-path cavity ring-down methane sensor for mobile monitoring of natural gas emissions," Opt. Express 27, 20084–20097 (2019).

[454] B. Martinez, T. W. Miller, and A. P. Yalin, "Cavity ring-down methane sensor for small unmanned aerial systems," Sensors 20, 454 (2020).

[455] L. Jin, V. Sonnenschein, R. Terabayashi, N. Hayashi, S. Kato, M. Yamanaka, H. Tomita, T. Iguchi, A. Sato, K. Nozawa, K. Yoshida, and N. Nishizawa, "Yb-doped fiber laser based coherent mid-infrared frequency comb at $\lambda = 4.5$ μm for CRDS application," in 2018 Conference on Lasers and Electro-Optics, OSA Technical Digest (online) (Optical Society of America, 2018), paper STh4K.4.

[456] K. K. Lehmann, "Resonance enhanced two-photon cavity ring-down spectroscopy of vibrational overtone bands: A proposal," J. Chem. Phys. 153, 089902 (2020).

[457] S. Schiller, "Spectrometry with frequency combs," Opt. Lett. 27(9), 766–768 (2002).

[458] I. Coddington, W. C. Swann, and N. R. Newbury, "Coherent dual-comb spectroscopy at high signal-to-noise ratio," Phys. Rev. A 82, 043817 (2010).

[459] B. Bernhardt, A. Ozawa, P. Jacquet, M. Jacquey, Y. Kobayashi, Th. Udem, R. Holzwarth, G. Guelachvili, T. W. Hänsch, and N. Picqué, "Cavity-enhanced dual-comb spectroscopy," Nat. Photonics 4(1), 55–57 (2010).

[460] I. Coddington, N. Newbury, and W. Swann, "Dual-comb spectroscopy," Optica 3(4), 414–426 (2016).

[461] O. Kara, L. Maidment, Tom Gardiner, P. G. Schunemann, and D. T. Reid, "Dual-comb spectroscopy in the spectral fingerprint region using OPGaP optical parametric oscillators," Opt. Express 25(26), 32713–32721 (2017).

[462] S. Coburn, C. B. Alden, R. Wright, K. Cossel, E. Baumann, G. -W. Truong, F. Giorgetta, C. Sweeney, N. R. Newbury, K. Prasad, I. Coddington, and G. B. Rieker, "Regional trace-gas source attribution using a field-deployed dual frequency comb spectrometer," Optica 5(4), 320–327 (2018).

[463] X. Ren, H. Dai, D. Li, K. Huang, M. Hu, T. Lv, M. Yan, and H. Zeng, "Mid-infrared electro-optic dual-comb spectroscopy with feedforward frequency stepping," Opt. Lett. 45(3), 776–779 (2020).

[464] G. Villares, A. Hugi, S. Blaser, and J. Faist, "Dual-comb spectroscopy based on quantum-cascade-laser frequency combs," Nat. Commun. 5, 5192 (2014).

[465] A. J. Fleisher, D. A. Long, Z. D. Reed, J. T. Hodges, and D. F. Plusquellic, "Coherent cavity-enhanced dual-comb spectroscopy," Opt. Express 24, 10424–10434 (2016).

[466] P. Honzátko, Y. Baravets, S. Mondal, P. Peterka, and F. Todorov, "Coherent sources for mid-infrared laser spectroscopy," Proc. SPIE 10142, 1014202 (2016).

[467] J. Nürnberg, C. G. E. Alfieri, Z. Chen, D. Waldburger, N. Picqué, and U. Keller, "An unstabilized femtosecond semiconductor laser for dual-comb spectroscopy of acetylene," Opt. Express 27, 3190–3199 (2019).

[468] R. Trebino, K. W. De Long, D. N. Fittinghoff, J. N. Sweetser, M. A. Krumbügel, B. A. Richman, and D. J. Kane, "Measuring ultrashort laser pulses in the time-frequency domain using frequency-resolved optical gating," Rev. Sci. Instrum. 68, 3277–3295 (1997).

[469] R. Trebino, *Frequency-Resolved Optical Gating: The Measurement of Ultrashort Laser Pulses* (Springer Science+Business Media, 2000).

[470] B. Jerez, P. Martín-Mateos, F. Walla, C. de Dios, and P. Acedo, "Flexible electro-optic, single-crystal difference frequency generation architecture for ultrafast mid-infrared dual-comb spectroscopy," ACS Photonics 5, 2348–2353 (2018).

[471] Y. Jin, S. M. Cristescu, F. J. M. Harren, and J. Mandon, "Femtosecond optical parametric oscillators toward real-time dual-comb spectroscopy," Appl. Phys. B 119, 65–74 (2015).

[472] M. Yan, P. L. Luo, K. Iwakuni, G. Millot, T. W. Hänsch, and N. Picqué, "Mid-infrared dual-comb spectroscopy with electro-optic modulators," Light Sci. Appl. 6, e17076 (2017).

[473] G. Ycas, F. R. Giorgetta, E. Baumann, I. Coddington, D. Herman, S. A. Diddams, and N. R. Newbury, "High-coherence mid-infrared dual-comb spectroscopy spanning 2.6 to 5.2 μm," Nat. Photonics 12, 202–208 (2018).

[474] M. Yu, Y. Okawachi, A. G. Griffith, N. Picqué, M. Lipson, and A. L. Gaeta, "Silicon-chip-based mid-infrared dual-comb spectroscopy," Nat. Commun. 9, 1869 (2018).

[475] P. J. Schroeder, R. J. Wright, S. Coburn, B. Sodergren, K. C. Cossel, S. Droste, G. W. Truong, E. Baumann, F. R. Giorgetta, I. Coddington, N. R. Newbury, and G. B. Rieker, "Dual frequency comb laser absorption spectroscopy in a 16 MW gas turbine exhaust," Proc. Combust. Inst. 36, 4565–4573 (2017).

[476] I. Pupeza, M. Huber, M. Trubetskov, W. Schweinberger, S. A. Hussain, C. Hofer, K. Fritsch, M. Poetzlberger, L. Vamos, E. Fill, T. Amotchkina, K. V. Kepesidis, A. Apolonski, N. Karpowicz, V. Pervak, O. Pronin, F. Fleischmann, A. Azzeer, M. Žigman, and F. Krausz, "Field-resolved infrared spectroscopy of biological systems," Nature 557, 52–59 (2020).

[477] K. Wang, H. Pu, and D. -W. Sun, "Emerging spectroscopic and spectral imaging techniques for the rapid detection of microorganisms: an overview," Compr. Rev. Food Sci. Food Saf. 17, 256–273 (2018).

[478] K. Balskus, S. Schilt, V. J. Wittwer, P. Brochard, T. Ploetzing, N. Jornod, R. A. McCracken, Z. Zhang, A. Bartels, D. T. Reid, and T. Südmeyer, "Frequency comb metrology with an optical parametric oscillator," Opt. Express 24(8), 8370–8381 (2016).

[479] M. S. Alshaykh, J. D. McKinney, and A. M. Weiner, "Radio-frequency signal processing using optical frequency combs," IEEE Photon. Technol. Lett. 31(23), 1874–1877 (2019).

[480] M. Piccardo, M. Tamagnone, B. Schwarz, P. Chevalier, N. A. Rubin, Y. Wang, C. A. Wang, M. K. Connors, D. McNulty, A. Belyanin, and F. Capasso, "Radio frequency transmitter based on a laser frequency comb," Proc. Natl. Acad. Sci. 116(19), 9181–9185 (2019).

[481] R. A. McCracken, J. M. Charsley, and D. T. Reid, "A decade of astrocombs: recent advances in frequency combs for astronomy [Invited]," Opt. Express 25(13), 15058–15078 (2017).

[482] N. Picqué and T. W. Hänsch, "Mid-IR spectroscopic sensing," Opt. Photonics News 30(6), 26–33 (2019).

[483] J. L. Klocke, M. Mangold, P. Allmendinger, A. Hugi, M. Geiser, P. Jouy, J. Faist, and T. Kottke, "Single-shot sub-microsecond mid-infrared spectroscopy on protein reactions with quantum cascade laser frequency combs," Anal. Chem. 90, 10494–10500 (2018).

[484] M. Karpov, M. H. P. Pfeiffer, J. Liu, A. Lukashchuk, and T. J. Kippenberg, "Photonic chip-based soliton frequency combs covering the biological imaging window," Nat. Commun. 9, 1146 (2018).

[485] H. -H. Lu, A. M. Weiner, P. Lougovski, and J. M. Lukens, "Quantum information processing with frequency-comb qudits," IEEE Photon. Technol. Lett. 31(23), 1858–1861 (2019).

[486] H. Lu, Z. Li, J. Wang, H. Meng, and J. Zha, "Two-way optical time and frequency transfer over a 20-km fiber link based on optical frequency combs," IEEE Photonics J. 11(1), 7201707 (2019).

[487] B. Spaun, P. B. Changala, D. Patterson, B. J. Bjork, O. H. Heckl, J. M. Doyle, and J. Ye, "Continuous probing of cold complex molecules with infrared frequency comb spectroscopy," Nature 533, 517–520 (2016).

[488] K. Balskus, Z. Zhang, R. A. McCracken, and D. T. Reid, "Mid-infrared 333 MHz frequency comb continuously tunable from 1.95 to 4.0 μm," Opt. Lett. 4(17), 4178–4181 (2015).

[489] K. Iwakuni, T. Q. Bui, J. F. Niedermeyer, T. Sukegawa, and J. Ye, "Comb-resolved spectroscopy with immersion grating in long-wave infrared," Opt. Express 27(3), 1911–1921 (2019).

[490] A. V. Muraviev, V. O. Smolski, Z. E. Loparo, and K. L. Vodopyanov, "Massively parallel sensing of trace molecules and their isotopologues with broadband subharmonic mid-infrared frequency combs," Nat. Photonics 12, 209–214 (2018).

[491] H. Timmers, A. Kowligy, A. Lind, F. C. Cruz, N. Nader, M. Silfies, G. Ycas, T. K. Allison, P. G. Schunemann, S. B. Papp, and S. A. Diddams, "Molecular fingerprinting with bright, broadband infrared frequency combs," Optica 5(6), 727–732 (2019).

# APPENDIX A

## THE BEER-LAMBERT LAW WITH ATMOSPHERIC AEROSOLS

In atmospheric applications, the aerosol optical depth (AOD) is a dimensionless quantity that represents a measurement of the atmospheric transparency. The differential form is:

$$d\tau_c = n \ \sigma \ \cos(\theta) \ ds$$

Where $\theta$ is the angle with respect to the normal, s is the optical path, $\sigma$ is the cross-section, and $n$ is the number density. For a normal incidence, the optical depth can be expressed in term of a column density $N$ as:

$$\tau_c = \int_0^z n \ \sigma \ dz = N \ \sigma$$

Atmospheric studies use the optical depth to investigate cloud thickness. Satellite sensors, MODIS for example, measures the spectral reflectance which is used then to determine cloud properties such as the effective radius and the optical depth. The thermal infrared bands obtained from this satellite can also be used to provide atmospheric properties. Vertical temperature changes are studied based on the MODIS bands in the visible and infrared spectral regions.

Recall the Beer-Lambert law from Section 2.1.3. This simple absorption law is more complicated for atmospheric measurements due to the scattering of light from different molecules present in the atmosphere. In terms of the optical depth $\tau_x = N_x \ \sigma_x$, the Beer-Lambert law for atmospheric measurements can be written as:

$$I = I_o\, e^{-m\,(\tau_{aer} + \tau_{gas} + \tau_{NO_2} + \tau_{H_2O} + \tau_{O_3} + \tau_R)}$$

Here, $m = \dfrac{1}{\cos(\theta)}$ is the air mass factor, $\theta$ is the zenith angle to the Earth's normal at the observation site, $R$ refers to Rayleigh scattering from molecular nitrogen and molecular oxygen, $aer$ to aerosols, $gas$ to uniformly mixed gases ( oxygen and carbon dioxide mainly), and other terms refer to absorption by the indicated gas molecules. Since the density of absorbing molecules is not constant along any path of length $z$ in the atmosphere, the modified Beer-Lambert law for atmospheric applications has the following form:

$$T = \frac{I}{I_o} = e^{-\int \alpha'\, dz} = e^{-\sigma \int n\, dz}$$

Quantitative analysis based on Beer-Lambert Law are widely applied in various areas of science and industry.

# APPENDIX B

## REVIEW OF ELECTROMAGNETIC RADIATION AND THE WAVE EQUATION

The integral form of Maxwell's equations in SI units [368] is as follows:

$$\oiint E \cdot dS = \int \frac{\rho}{\varepsilon_o} \, dV$$

$$\oiint B \cdot dS = 0$$

$$\oint E \cdot d\ell = - \frac{d}{dt} \iint B \cdot dS$$

$$\oint B \cdot d\ell = \mu_o I + \mu_o \varepsilon_o \frac{d}{dt} \iint E \cdot dS$$

Here, $E(r, t)$ is the electric field, $B(r, t)$ is the magnetic field, $I$ is the current, $\varepsilon_o$ is the electric permittivity of free space, and $\mu_o$ is the magnetic permeability of free space.

Using Gauss's law and Stokes theorem for a vector field $F(r)$:

$$\oiint F \cdot dA = \int \nabla \cdot F \, dV$$

$$\oint F \cdot dS = \int \nabla \times F \cdot dA$$

We arrive at the differential form of Maxwell's equations:

$$\nabla \cdot E = \frac{\rho}{\varepsilon_o}$$

$$\nabla \cdot B = 0$$

$$\nabla \times E = - \frac{\partial B}{\partial t}$$

$$\nabla \times B = \mu_o J + \mu_o \varepsilon_o \frac{\partial E}{\partial t}$$

The divergence and the curl operators are defined as follows:

$$\nabla = \frac{\partial}{\partial x} \hat{\imath} + \frac{\partial}{\partial y} \hat{\jmath} + \frac{\partial}{\partial z} \hat{k}$$

$$\nabla \cdot A = \frac{\partial A_x}{\partial x} + \frac{\partial A_y}{\partial y} + \frac{\partial A_z}{\partial z}$$

$$\nabla \times A = \begin{vmatrix} \hat{x} & \hat{y} & \hat{z} \\ \dfrac{\partial}{\partial x} & \dfrac{\partial}{\partial y} & \dfrac{\partial}{\partial z} \\ A_x & A_y & A_z \end{vmatrix}$$

Using the following vector identity:

$$A \times (B \times C) = (A \cdot C)B - (A \cdot B)C$$

we get as a result:

$$\nabla \times (\nabla \times B) = \nabla(\nabla \cdot B) - \nabla^2 B = -\nabla^2 B$$

And from Maxwell's equations we obtain:

$$\nabla \times (\nabla \times B) = \mu_o \varepsilon_o \frac{\partial}{\partial t}(\nabla \times E) = \mu_o \varepsilon_o \frac{\partial}{\partial t}\left(-\frac{\partial B}{\partial t}\right)$$

resulting in the wave equation:

$$\nabla^2 B - \mu_o \varepsilon_o \frac{\partial^2 B}{\partial t^2} = 0$$

Similarly for E, we obtain:

$$\nabla^2 E - \mu_o \varepsilon_o \frac{\partial^2 E}{\partial t^2} = 0$$

The speed of light in vacuum $c$ is related to the electromagnetic constants $\mu_o = 4\pi \: X \: 10^{-7} \: F/m$ and $\varepsilon_o \approx \frac{1}{36\pi} \: X \: 10^{-9} \: H/m \: \approx 8.854 \: X \: 10^{-12} \: H/m$ (in MKS units) such that $c = \frac{1}{\sqrt{\mu_o \varepsilon_o}} = 299792458 \: m/s \approx 3 \: X10^8 \: m/s$.

The Poynting vector describes the flow of electromagnetic power, which is orthogonal to both E and B:

$$S = \frac{1}{\mu_o} E \: X \: B$$

In the presence of charges and currents, the following constitutive relations describe the response of bound charges and currents to the applied fields:

$$D = \varepsilon_o E + P$$

$$H = \frac{1}{\mu_o} B - M$$

where $P(r,t)$ is the polarization field, $M(r,t)$ is the magnetization field, $D = \varepsilon E$ is the electric displacement field, $H = \frac{B}{\mu}$ is the magnetic field , $\varepsilon$ is the permittivity of the material, and $\mu$ is the permeability of the material.

The differential form of the Poynting theorem describes the energy transfer in terms of the energy flux and the rate of work done by the fields on a charged object, where $S = E \: X \: H$ , is:

$$-\frac{\partial u}{\partial t} = \nabla.S + J.E$$

$$u = E.D + B.H = \frac{1}{2} \left( \varepsilon_o E^2 + \frac{1}{\mu_o} B^2 \right)$$

The energy density associated with an electric field is denoted by $u_E$:

$$u_E = \frac{1}{2}\,\varepsilon_o\,E^2$$

and the energy density associated with a magnetic field is denoted by $u_B$:

$$u_B = \frac{1}{2\,\mu_o}\,B^2$$

and their summation gives:

$$u = u_E + u_B$$

## C.1 Basic Concepts

The piezoelectric effect is explained by the theory of ferroelectrics, which depends of Landau theory of phase transformations [409]. Landau theory uses the concept of "order parameter", which is based on order-disorder transformation arising from the change in the symmetry of the crystal. The order parameter represents the broken symmetry resulted from a transformation from a disordered phase of high-symmetry to an ordered phase of low symmetry [410, 411]. According to Landau, the Helmholtz free energy of this transformation can be expressed as a Taylor series expansion of the order parameter. In general, any variable of the system present at the phase transition point can be the order parameter. The spontaneous polarization is the order parameter in the case of ferroelectrics [409].

Let us consider the thermodynamic formalism of a simple transformation from a nonpolar cubic phase to a uniaxial ferroelectric phase upon cooling [409]. In this case, the free energy functional is an even function of the form:

$$\Delta A_L(P, T) = \frac{1}{2}\alpha P^2 + \frac{1}{4}\beta P^4 + \frac{1}{6}\gamma P^6 + \cdots$$

where $P$ is the polarization, $T$ is the temperature, and $\alpha$, $\beta$, and $\gamma$ are the expansion parameters as a function of temperature. Typically, only $\alpha$ is considered the temperature-dependent parameter, and it has the form of a reciprocal Curie-Weiss Law:

$$\alpha = \frac{T - T_c}{\varepsilon_o C}$$

where $C$ is the Curie-Weiss constant, $T_c$ is the Curie-Weiss temperature, and $\varepsilon_o$ is the permittivity of free space. The spontaneous polarization $P_S$ of the uniaxial ferroelectric phase can be determined by the thermodynamic equilibrium condition $\frac{\partial \Delta A_L}{\partial P} = 0$ as:

$$P_S^2(T) = \frac{-\beta + \sqrt{(\beta^2 - 4\alpha\gamma)}}{2\gamma}$$

which results in spontaneous strains.

Piezoelectric materials are commonly used around us. They are found in items of everyday life such as microphones, electric lighters, vehicle seat belt locks, and electronic toothbrushes. Applications in industry, medical diagnosis, environmental and underwater sensors, and musical instruments are broad [412]. This is a consequence of the various advantages these materials have.

A piezoelectric crystal has a rapid response, and it operates over a wide range of frequencies, which makes it a key element in broadband ultrasonic systems. When used in sensors, the output voltage does not depend on the size of the crystal. Furthermore, these materials are highly stable and are available in different sizes and shapes. Quartz crystals and barium titanate ceramic, for example, can be provided in any shape or size to meet the requirement of an application. Disadvantages include relative sensitivity to temperature and to extreme humidity levels (higher than 85%), and the need for an external circuit with high impedance to amplify the low output signal of the transducer.

Quartz crystals are natural piezoelectric materials. Rochelle salt, also known as potassium sodium tartrate, is made from natural components and was the first piezoelectric

311

material to be discovered [406]. Whereas, ammonium dihydrogen phosphate and lithium sulfate are artificial synthetic crystals [413]. Barium titanate is a popular man-made polarized ceramic.

Ceramic, in general, does not exhibit the piezoelectric effect, but it can be manufactured with a special treatment of polarization to meet this requirement [414]. This treatment gives polarized ceramic crystals the advantage of operating at low voltage levels and at high temperatures ~ $3000^o C$. However, natural quartz is considered the mostly used crystal in PZTs. This rises from its high resistivity and low temperature sensitivity comparing to other piezoelectric materials. It also shows linearity over a broad range of vibration frequencies, enabling static calibration.

Applications of PZTs spread over a variety of areas in scientific, industrial, and medical instrumentation and research. In condensed matter studies, pulsed photoacoustic spectroscopy is a technique that uses a pulsed laser emitted on a sample, and senses the thermal changes in the gas layer, which is in contact with the sample, to observe any cooling or heating effects [415, 416]. This techniques depends on the transient acoustic waves generated by the absorption of optical pulses. The high peak power of laser pulses allow for high sensitivity and for detection of nonlinear absorption in liquids or solids.

Medical imaging systems based on the photoacoustic effect are used for diagnosis of several diseases [417]. It is well-known that the ultrasound is the safest and the most commonly used medical imaging technique. For different diagnoses, transducers with specific characteristics are developed to meet the requirement of each imaging system [418].

Broadband ultrasonic-imaging transducers were designed and fabricated by Cannata and co-workers for medical imaging applications [419]. The center frequency of the single-element lithium niobate ($LiNbO_3$) transducers are in the range $20 - 80$ Hz, which results in high sensitivity that improves the SNR of the image and allows for deeper penetration.

In industry, certain procedures are performed for quality control of products. One of the popular technique is the non-destructive testing (NDT) technique, in which high frequency ultrasonic waves are used. In most of those applications, PZTs of pulse-mode operation are used to generate and detect the ultrasonic waves. The wave propagates in the fabricated material and encounters mechanical discontinuities. This results in scattering, reflection, and attenuation effects that can be analyzed allowing for the assessment of the internal structure of the material [420].

In spectroscopic experiments, applications of PZTs mainly involve scanning the length of the optical cavity [9, 370]. Sandercock studied the elastic constant of SbSI crystal in the neighborhood of a ferroelectric transition [421]. He used a piezo-electrically scanned double-pass interferometer to investigate the back scattering from this non-transparent material.

A recent innovative system applies the quartz-enhanced photoacoustic spectroscopy (QEPAS) technique for trace gas sensing [422]. The system is based on an external cavity quantum cascade laser (EC-QCL) coupled with a mid-IR fiber. To demonstrate the detection capabilities of the system, they have selected $SF_6$ as a target gas. Effective QCL fiber coupling resulted in transmission of almost the whole laser beam

~ 94.4%, which allowed for high sensitivity of the spectroscopic system, 50 parts per trillion, in a measurement time equal to one second. This result corresponds to $2.7 \times 10^{-10} \ W \ cm^{-1} \ Hz^{-\frac{1}{2}}$ normalized noise-equivalent absorption.

## C.2 Mathematical Approach

In a simple approach to the mathematical formulation of the piezoelectric effect, we start with the demonstrations made by the brothers Curie [407]. Denote the applied stress by $T$ and the piezoelectric strain coefficient by $c_S$. Then, the piezoelectric polarization vector can be written as:

$$P_{pz} = c_S \, T$$

In the reverse piezoelectric effect, the brothers Curie verified that the produced strain in the piezoelectric material due to an applied electric field is equal in ratio to the produced polarization due to an applied stress in the direct effect. Denote the magnitude of the applied electric field by $E$, then the produced strain takes the form:

$$S_{pz} = c_S \, E$$

Using the elastic properties of the piezoelectric material, these expressions can be rewritten as:

$$P_{pz} = c_S \, T = c_S \, c_e \, S = \ c_P \, S$$

$$T_{pz} = c_e \, S_{pz} = c_e \, c_S \, E = c_P \, E$$

where $c_e$ is the elastic constant associated with the applied strain $T = c_e \, S$, and $c_P$ is the piezoelectric stress constant. A compliance coefficient duo to material deformation under stress can be introduced such that $S = s \, T$.

314

Let us consider the contribution of the piezoelectric effect to the elastic properties of the material. The material stiffness increases under the piezoelectric effect. When the material experiences a strain $S$, an elastic stress $T = c_e S$ will be generated and a piezoelectric polarization $P_{pz} = c_P S$. An internal electric field, of the following form, will be created in the material due to this polarization:

$$E_{pz} = \frac{P_{pz}}{\varepsilon} = \frac{c_P S}{\varepsilon}$$

where $\varepsilon$ is the dielectric constant of the material. As a result, this electric field produces a stress $T_{pz} = c_P E_{pz}$ against the deformation. Adding the two contributions, the strain $S$ generates a stress given by:

$$T = T_e + T_P = c_e S + c_P E_{pz} = c_e S + c_P \frac{c_P S}{\varepsilon} = \left( c_e + \frac{c_P{}^2}{\varepsilon} \right) S = \bar{c} S$$

where $\bar{c}$ is the piezo-electrically stiffened constant. As can be seen, an increase of the elastic constant $c_e$ of the material duo to the piezoelectric effect increases its stiffness [407]. The piezoelectric and elastic constants of alpha-quartz were determined by Bechmann with a high accuracy [423].

Consider now a material of a dielectric constant $\varepsilon$ under the effect of piezoelectricity, where the material is placed between two electrodes. Applying an external electric field causes an electric displacement in the material towards the electrodes. This results in a free surface charge density on the electrodes of magnitude $D = \varepsilon E$ given by:

$$\sigma = \sigma_o + \sigma_d = \varepsilon_o E + \chi E = (\varepsilon_o + \chi) E = \varepsilon E$$

where $\sigma_o$ is the vacuum charge density, $\varepsilon_o$ is the vacuum dielectric permittivity, $\sigma_d$ is the charge density induced by the dielectric effect, and $\chi$ is the material dielectric susceptibility.

If the material is piezoelectric, the electric field also produces a strain $S_{pz} = c_S E$, which causes a deformation in the structure of the material. And because of the material polarization, the stain $S_{pz}$ increases the charge density by $P_{pz} = c_P S_{pz} = c_P c_S E$. If the electric field is maintained constant, the piezoelectric polarization $P_{pz}$ increases the electric displacement of free charges so that the total is:

$$D = \varepsilon E + P_{pz} = \bar{\varepsilon} E$$

where $\bar{\varepsilon} = \varepsilon + c_P c_S$ is the effective dialectic constant with the piezoelectric contribution contained.

The electric field applied on the material and the piezoelectric nature of the material both contribute to the internal stress in this material. As we discussed, the electric field causes a deformation in the material described by the strain $S_{pz}$, which introduces an elastic stress of magnitude $T_e = c_e S_{pz}$. On the other hand, the applied field exerts a force on the internal structure of the material producing a stress $T_{pz} = c_P E$. The direction of this stress is opposite to that of the elastic stress $T_e$. And since $T_{pz}$ is the major stress in the material, it tends to recover its structure. Therefore, the internal stress in the material can be obtained from:

$$T = c_e S_{pz} - c_P E$$

In some cases when the two strains are equal, the material will be static and strained. In practice, a varying field is commonly applied, which results in a dynamic displacement caused by the variable strain. As a result, the medium in contact with the piezoelectric material experiences a perturbation [407, 409]. This electromechanical phenomenon based on piezoelectricity is used in transducers, actuators, and sensors.

## APPENDIX D

## LOCK-IN AMPLIFIERS

In experiments, lock-in amplifiers can be used to avoid the frequency range associated with considerable $1/f$ noise. This noise is frequency-dependent and must be considered cautiously. For this purpose, the circuit of a lock-in amplifier has an electronic unit that includes a low-pass filter and a multiplier. After the input signal, with the accompanying noise, is multiplied to the reference signal, the filter allows some frequencies to pass and blocks off the unwanted higher frequencies in the output signal. Filters and amplifiers of a lock-in device are located at the "multiplication and integration unit" [331, 427]. Before this unit is the reference channel, which is responsible for generating and adjusting the reference signal. This channel is composed of a phase shifter and a phase-lock loop.

Periodic modulation is performed based on the input signal and the reference to maintain the frequency and phase of the reference signal. Since the output is a DC signal, the phase difference between the signal and the reference should stay constant in time. For this synchronization to be achieved, a voltage-controlled oscillator (VCO) is used in the phase-lock loop, which is one of the main parts of this instrument [430]. In this loop, the reference signal is generated and locked to the internal local oscillator. All this takes place in the lock-in unit in advance of amplification and integration. The instrument is called a "lock-in amplifier" based on this feature.

The operation of the phase-lock loop is illustrated in Figure 108. At the phase-checking stage, an error signal is generated to address the phase matching between the signal and reference. This error signal is proportional to the difference in phase. The AC part of the error signal is blocked since we only inquire the DC part [331].
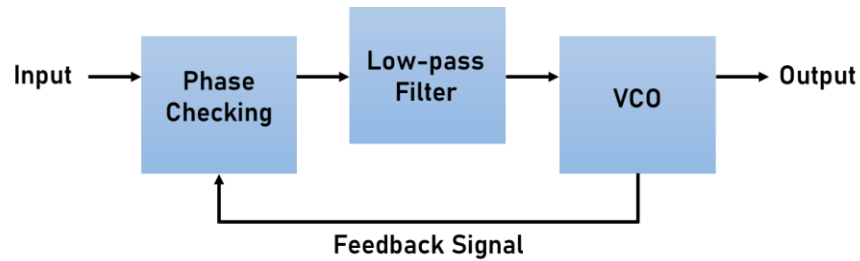


Figure 108 A schematic of the operation of a phase-lock loop inside a lock-in amplifier.

After that, the output of the low-pass filter goes to the VCO, which uses the filtered signal to tune its frequency with correspondence to the input signal. Let us consider that the phase of the input signal is $\varphi_1$ and the phase of the reference signal is $\varphi_2$, then the frequency of the VOC is chosen such that:

$$\omega_{VOC} = \omega_o + K.(\varphi_1 - \varphi_2)$$

where $\omega_o$ is a characteristic frequency of the VOC, and $K$ is a constant that indicates proportionality. The term with the phase difference $\Delta\varphi = \varphi_1 - \varphi_2$ is fed back to the loop, and phase-checking is performed again. If a phase difference $\Delta\varphi \neq 0$ is detected, the low-pass filter sends a nonzero output to the VCO. The sign of the feedback signal, which includes $\Delta\varphi$, decides whether the VCO has to oscillate faster or slower. According

to this change in the oscillation, the phase of the reference signal is adjusted. The loop continues to perform until $\Delta\varphi = 0$ is obtained at the phase-checking stage. This result means that the frequency of the VCO is equal to that of the input signal.

Let us discuss a simple example of a sinusoidal input signal of the form:

$$S = A_1 \sin(\omega t + \varphi)$$

and a reference signal of the form:

$$R = A_2 \sin(\omega t)$$

where $A_1$ and $A_2$ are the amplitudes of the input signal and the reference signal, respectively, and $\varphi$ is the phase difference between the two signals. Denote the noise contribution to the input signal as $N$, and the time constant of the averaging process of the low-pass filter as $\tau$, then the output signal of a lock-in amplifier can be written as:

$$V_{out} = \frac{1}{\tau} \int_0^\tau (S + N). R \, dt = \frac{1}{\tau} \int_0^\tau S. R \, dt + \frac{1}{\tau} \int_0^\tau N. R \, dt$$

The noise term is suppressed to zero by the filter, which is considered a hidden advantage of lock-in amplifiers [427]. The product in the signal term is handled using the following trigonometric identity,

$$\sin(x) \sin(y) = \frac{1}{2} \left[ \cos(x - y) - \cos(x + y) \right]$$

which gives:

$$S. R = A_1 A_2 \sin(\omega t + \varphi) \sin(\omega t) = \frac{A_1 A_2}{2} \left[ \cos(\varphi) - \cos(2\omega t + \varphi) \right]$$

Then, the output voltage after filtering yields:

$$V_{out} = \frac{1}{\tau} \int_0^\tau S. R \, dt = \frac{A_1 A_2}{2\tau} \int_0^\tau \cos(\varphi) \, dt - \frac{A_1 A_2}{2\tau} \int_0^\tau \cos(2\omega t + \varphi) \, dt$$

320

For simplicity, a rectangular function is considered for the low-pass filter, but in practice, the transfer function is more complicated [331]. In the second term of our result, we have a periodic function. Integrating this function over a sufficiently long time gives a zero because the negative part will cancel the positive one. In the first term, the integration over time is a constant equal to $\tau$. As a result, we have:

$$V_{out} = \frac{A_1\, A_2}{2}\, \cos(\varphi)$$

Similarly, we can consider the case when the frequencies of the input and reference signals are different. Let the reference signal be:

$$R = A_2 \sin(\Omega t)$$

Making use of the trigonometric equality mentioned above, and the following trigonometric equalities,

$$\sin(x + y) = \sin(x)\cos(y) + \cos(x)\sin(y)$$

$$\cos(y)\sin(x) = \frac{1}{2}\,[\sin(x - y) + \sin(x + y)\,]$$

the product of $S$ and $R$ gives:

$$S.R = A_1\, A_2\, \sin(\omega t + \varphi)\, \sin(\Omega t)$$

$$= A_1\, A_2\, [\sin(\omega t)\cos(\varphi)\sin(\Omega t) + \cos(\omega t)\sin(\varphi)\sin(\Omega t)]$$

$$= \frac{A_1\, A_2}{2}\, \cos(\varphi)\,[\cos(\omega - \Omega)t - \cos(\omega + \Omega)t\,]$$

$$+ \frac{A_1\, A_2}{2}\, \sin(\varphi)\,[\sin(\omega - \Omega)t + \sin(\omega + \Omega)t\,]$$

Under integration, the terms with periodic functions cancel out, and the only term which contributes to the output is the nonzero DC part at $\omega = \Omega$:

$$V_{out} = \frac{1}{\tau} \int_0^\tau S.R \, dt = \frac{A_1 A_2}{2\tau} \cos(\varphi) \int_0^\tau \cos(0) \, dt = \frac{A_1 A_2}{2} \cos(\varphi)$$

Notice that the output voltage of the more general case is the same as the one obtained before for input and reference signals with the same frequency [427].

In conclusion, a lock-in amplifier is a device that receives an input signal, with the noise associated with it, as an input voltage:

$$V_{in} = V_o \sin(\omega t + \varphi) + V_{noise}$$

and provide a DC output voltage proportional to the amplitude of the input signal, and related to the phase shift as follows:

$$V_{out} \propto V_o \cos(\varphi)$$

Applications of lock-in detection to non-periodic signals involve an optical chopper, as discussed previously in Sections 3.4 and 3.5. Chopping the incoming signal at a constant rate creates a periodic behavior. This will produce a signal that carries information on the phase and frequency of modulation, which then serves as a reference in the lock-in amplifier. A variety of applications of lock-in amplifiers can be found in various fields.

APPENDIX E

THE LABVIEW SOFTWARE


An introductory description of the LabVIEW program is provided in this appendix based on LabVIEW Core 1 Participant Guide offered by National Instruments for LabVIEW training [431]. When LabVIEW is launched, one can select a saved project or open a new project. After choosing a project, a "Project Explorer" window appears. This window includes "Project Root," "My computer," "Dependencies," and "Build Specifications." Through this window, the developer can see the VI files in that particular project. A VI is a major element of LabVIEW environment, and it consists of three main parts; a front panel window, a block diagram, and an icon/connector pane [431].

The Front Panel is the user interface window. By clicking anywhere on this window, a small window containing the "Controls" and "Indicators" will appear. The Controls are interactive inputs, and the Indicators are interactive outputs. Knobs and push buttons are examples of Controls, whereas a graph is an example of an Indicator.

When the LabVIEW software is used with instruments, the Controls can simulate the input devices and transfer the data to the Block Diagram of the associated VI. On the other hand, the Indicators simulate the output devices and displays the data generated by the Block Diagram.

The data type of Controls and Indicators can be a string, a Boolean, or a numeric. A string consists of ASCII characters, so it is used for text inputs and outputs. Whereas,

data that only have two possible values are represented by a Boolean control, e.g. ON and OFF, or a Boolean indicator, e.g. True or False conditions.

Numeric values can be integers or real numbers. LabVIEW has different representations of Numeric data types that the developer can choose from, such as signed integers, unsigned integers, and floating point. The number of bits that the program uses to store the Numeric value can also be specified. This option offers the user to choose the appropriate number of bits, for each Numeric value in his program, and save usage and storage space in the memory.

Modern, Silver, System, and Classic are different control palettes that the LabVIEW has. Each palette contains a different set of user interface building objects. The toolbar of the Front Panel allows the programmer to edit and run the VI. The Block Diagram also has a toolbar that allows for running the program and offers several debugging options. Components of the Block Diagram are Functions, Structures, Constants, Nodes, Terminals, Wires, SubVIs, Icon, and Connector Pane.

Functions or "Function Nodes" are fundamental elements of operation in LabVIEW. In the Block Diagram, Nodes are objects that have inputs and outputs, or either inputs or outputs. Comparing to text-based programming languages, LabVIEW Nodes are equivalent to operators, statements, and subroutines.

Terminals are entrance and exit ports, through which data is exchanged between the Front Panel and the Block Diagram. Wires transfer data between different objects in the Block Diagram. If there is an error in connecting different objects, a broken wire with

"×" mark on it will appear between the two objects. In this case, the programmer cannot run the VI unless the error is fixed.

At the upper right corner of the Front Panel, The Icon of the VI is located. The Icon is a graphical representation of the VI, and it can be edited by the programmer to reflect the main operation of the VI. The Connector Pane maps the locations of the input and the output terminals of an object. Since these terminals are connected to Controls and Indicators on the Front Panel, the Connector Pane is not accessible from the Block Diagram.

In text-based programming languages, the programmer can recall a sub-function, which has a programming code written in a separate program file, to perform a certain operation within another function. Whereas in LabVIEW, the sub-functions which can be used within the VI are called SubVIs. Each SubVI has its own Front Panel and Block Diagram, which is analogous to a sub-function that has its specific programming code in a text-based language. In addition, each SubVI has an Icon that represents it in the main VI. One type of commonly used SubVIs is the Express VI, which can be configured with a dialog box. On the Block Diagram, a SubVI appears as an Icon, while Express VIs appear as an Icon with a blue field around it.

LabVIEW has a large number of objects, and each one of them has specific terminals. The question mark tool located at the toolbar in LAbVIEW can be used to open the Context Help window. This window displays the specified Icon, all its terminals, and the wire connections. In LabVIEW, different colors are used for wires to indicate the type of data expected at different terminals. Examples of LabVIEW projects are available on

the NI Example Finder. When this window opens, it allows the developer to search for an example or browse an example. These examples cover a wide range of tasks including test, control, design, or measurement [431]. One can use the LabVIEW software instead of a hardware device to perform certain tasks for many experiments in engineering and science.

MIRROR REFLECTIVITY

The high reflectivity of the mirrors used in the multipass cell is tested in our laboratory based on the method explained here. We simply add a beam splitter (BS) in the path of the laser beam emitted from our mid-IR frequency comb source, as illustrated in Figure 109 below. Having only one hole for the beam to enter and exit the cell means that the beam follows almost the same path when it exits the cell. Therefore, the BS serves to transmit the beam as it enters the cell and reflect the output beam which has the information about the reflectivity. Using a pinhole helps to align the beam before entering the multipass cell.

In this measurement, we only used 60% of the total optical power that can be emitted from the mid-IR comb source ($0.6 \, P_{total} \approx 200 \, mW$). Since the beam travels for a distance before it arrives at the BS, we measure its power at that position and found it close to $100 \, mW$. After splitting at the BS, we measure the power of the transmitted beam to be around $70 \, mW$, which is the power of the beam incident into the multipass cell ($P_o$). The power of the reflected part from the incidence side is measured to be around $30 \, mW$. This indicates, experimentally, that the BS we are using is a $70/30$ splitter in the mid-IR.

After a total number of $580$ passes inside the multipass cell, the beam exits the cell through the same hole. The power of the output beam after reflection from the BS is around $1.6 \, mW$. Considering the 30% reflectivity of the BS, the power of the output beam

$(P)$ from the multipass cell has to be around $5\ mW$. Comparing this value to the incident

power, we can estimate the reflectivity of our mirrors based on this expression:

$$\frac{P}{P_o} \approx (A.R.D)^N$$

where $P_o$ is the incident power, $P$ is the output power, $N$ is the total number of reflections

on the mirrors, $A$ indicates absorption losses, $D$ is for diffraction losses, and $R$ refers to

reflection losses. Ignoring absorption and diffraction terms sets both $A$ and $D$ to 1. Then,

we can estimate the reflectivity using our experimental measurements, $P_o = 70\ mW$, $P = 5\ mW$, and $N = 279$, and we get $R \geq 0.9955$.
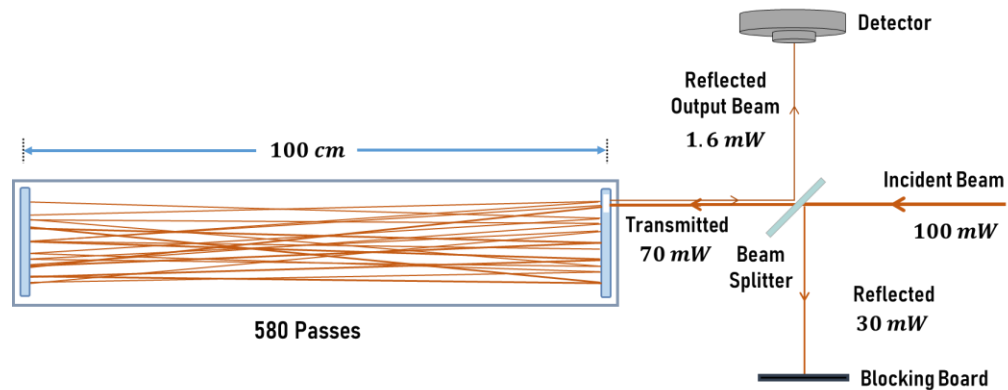


Figure 109 An illustration of the method used to measure the reflectivity of the mirrors.